HOT ISOSTATIC PRESSING OF SILICON NITRIDE BASED CERAMICS

Kevin Paul Plucknett

A thesis submitted for the degree of Doctor of Philosophy

March 1990

University of Warwick

Department of Physics
University of Warwick
United Kingdom

ABSTRACT

Several techniques have been developed for the encapsulation, and subsequent hot-isostatic pressing (HIPing), of silicon nitride (Si_3N_4) based ceramics. Green-state and densified billets of silicon nitride were vacuum encapsulated in either glass tube or powder. Glass powder encapsulation allows complex shaped ceramic pieces to be HIPed. A selection of silicon nitride compositions were HIPed to near-theoretical density (>97% T.D.) after encapsulation in either Pyrex glass tube or powder. The silicon nitride compositions studied included single yttria (Y_2O_3) additive materials that cannot be densified by conventional pressureless sintering, hence the requirement for pressurised sintering. Similar ceramic compositions were also densified using the commercial ASEA HIP process for comparison.

The bulk ceramic microstructure was generally similar to pressureless sintered type materials, with a complete α- to β-Si_3N_4 transformation, although a finer microstructure and lower matrix phase volume were apparent.

The ceramic/encapsulant interaction during HIP was generally assessed using a boron nitride (BN) interlayer. When a thick layer (> 50 μm thickness) was retained after HIP negligible interaction was apparent. A thin silicon oxynitride (Si_2N_2O) surface layer was observed to form with thinner interlayers. Penetration of the molten encapsulant glass through the porous BN layer occurs during HIP, leading to an increase in the Si^{4+} and O^{2-} concentration at the ceramic surface and the subsequent re-precipitation of Si_2N_2O in preference to β-Si_3N_4. Direct penetration of the encapsulant glass into the porous ceramic occurs in the absence of a BN barrier layer and a similar encapsulant dependent compositional modification was observed.

Sub-surface ceramic contamination by boron was apparent in isolated samples HIPed in a Pyrex-type glass at ASEA. Interaction between the encapsulant and ceramic did not significantly affect the post-HIP surface oxidation rate, when compared with the bulk material.

ACKNOWLEDGEMENTS

The research presented in this thesis was conducted in the Department of Physics between October 1985 and December 1988. The work described is my own except where specifically noted in the text, and the contribution of these people is gratefully acknowledged. I wish to thank Professor S.B. Palmer and Dr H. Mykura for the provision of laboratory facilities at Warwick, Rolls-Royce plc (Leavesden) for financial support, and Dr A. Hepworth for access to laboratory facilities at T and N Technology Ltd., Rugby. Dr B. Rickinson, Lance Tidbury and Andrew Cartledge are thanked for their assistance and experience in hot-isostatic pressing conducted at HIP Ltd., Chesterfield.

I am especially grateful to Professor M.H. Lewis for general supervision and guidance during this research and to Drs D. Holland and G. Leng-Ward for further technical assistance. In addition I would like to thank the excellent departmental technical staff, especially Gerry Smith and Steve York for tuition in electron microscopy techniques and maintenance of the equipment, and Bill Jones, Pat Beecroft and Dan Lee for assistance in the mechanical workshops.

A special acknowledgement must be made to my former research colleagues, Drs V.S.R Murthy and Steve Mason, Nick Butler, John Fernie, Markys Cain, Steve Ketchion, Ian Tuersley, Mark Pharaoh, Olwen Pullum and Li Jie for technical assistance, discussions and providing a lively and enjoyable working environment during my time at Warwick.

Finally special thanks go to: Rolf Howarth, for his friendship and considerable help in the typing and formatting of this thesis, my father and my late mother for their patience and support over the years, and Sharen Bowman for her companionship, understanding and just being there.

Table of Contents

List of Figures

List of Tables

CHAPTER ONE

INTRODUCTION: SILICON NITRIDE CERAMICS

1.1 ENGINEERING CERAMICS

The operational limits for the current generation of 'superalloy' metals are approaching rapidly and interest has been focussed on possible non-metallic materials for their replacement, for example as major components in advanced gas turbine engines. The potential of the non-oxide silicon based ceramics for fabrication of components such as turbine blades and inlet nozzles, with high operating temperatures, has motivated much interest. Current gas turbines are limited to an operational ceiling temperature of ~1050°C [1], above which material properties such as creep and oxidation deteriorate catastrophically. Silicon nitride offers the possibility of component usage at temperatures up to 1400°C. Improvements on this operating temperature are possible with silicon carbide, however the material shows inferior resistance to thermal shock and brittle fracture. Silicon nitride has, because of an excellent combination of properties (Table 1.1), become the target material for integration into gas turbine design since the early 1970's, following the initiative of the U.S. Government's Advanced Research Projects Agency (ARPA) [2].

Theoretical studies investigating the expected increases in gas turbine efficiency by the implementation of silicon nitride components have forecast that, with an engine working temperature of ~1370°C, efficiency would be improved by one fifth [3] and the fuel consumption could be halved [1]. Fuel savings attainable for several different applications are presented in Table 1.2 [4]. These potential savings added up to a total of around half a billion barrels of oil in 1980, approximately $17.5 billion in financial terms [4]. Further potential benefits of increased operating temperatures through ceramic component introduction include the use of cheaper, low grade fuels, reduced exhaust pollution and a reduction in component weight (reducing stress and inertia). The natural

Material	Density ($g\,cm^{-3}$)	Flexural strength (MPa) Room temp	High temp	(°C)	Decomposition Temperature (°C)	Thermal Expansion ($\times 10^{-6} K^{-1}$)
silicon nitride						
RBSN	2.7-2.8	210	380	(1375)	1900 (D)	2.8
HPSN	3.1-3.2	700	330	(1375)	1900 (D)	3.0
SSN	3.1-3.3	650	275	(1375)	1900 (D)	3.2
HIPSN	3.2-3.3	700	500	(1400)	1900 (D)	~ 3.0
silicon carbide						
SSiC	3.1-3.2	700	700	(600)	2723 (D)	4.8
RBSiC	2.7-2.8	300	300	(600)	2723 (D)	4.4
HPSiC	3.2-3.3	655	520	(1375)	2723 (D)	4.5
PSZ	5.7-6.0	700-1000	500	(600)	2680 (M)	–
LAS	2.3	60-75	60-75	(600)	1199 (M)	–
h.s. Steel	7.8	1500	850	(600)	1500 (M)	12
Aluminium	2.7	370	–	–	660 (M)	23

Notes:

RBSN	Reaction-Bonded Si_3N_4
SSN	Sintered Si_3N_4
HPSN	Hot-Pressed Si_3N_4
HIPSN	Hot-Isostatically Pressed Si_3N_4
SSiC	Sintered SiC
RBSiC	Reaction-Bonded SiC
HPSiC	Hot-Pressed SiC
PSZ	Partially Stabilised Zirconia
LAS	Lithium aluminosilicate

Table 1.1 Typical properties of selected structural materials (summarised from references [4,9,44,76])

abundance of silicon and nitrogen (together with carbon) presents a strong contrast to the economic and physical barriers that must be overcome to obtain high temperature 'superalloy' constituents (including chromium, nickel, cobalt and tungsten), deposits of which are in short supply and strategically placed.

Technology	System configuration	Reduction in fuel use	Component operating temperature
Gas Turbines			
Automotive	~150hp, single shaft engine	27%	1370°C
Truck	~350hp, two shaft engine	17%	1240°C
Industrial/Ship	~1000hp, three stage engine	10%	1370°C
Diesel Engines			
Truck	~500hp, adiabatic turbo-compound engine	22%	1210°C
Ind. Heat Recovery Recuperator	SiC high-temperature heat-exchanger	42%	1300°C

Table 1.2 Projected energy savings from the implementation of ceramic technology (summarised from reference [4])

National ceramic research and development expenditure has consequently increased heavily in the last decade, particularly in Japan and the United States [5] (Table 1.3a). A further breakdown of U.S. federal funding, purely for structural ceramics (Table 1.3b), reveals a relative increase ahead of inflation [5].

The continual advances made in silicon nitride fabrication methods, together with the development and improvement of other technical ceramics, over the past 15 years has given the ceramic engineer a vast choice of materials such that each can be tailored for a specific application. Component selection can thus be made, depending on mechanical strength, corrosion resistance, complexity of shape and cost.

Silicon nitride is currently being integrated into a prototype automotive gas turbine by the Nissan Motor Co. [6]. Also in Japan, Kyoto Ceramic Co. have investigated the use of sintered silicon nitride ceramic components in several different diesel engine designs [7]. Parts fabricated initially included the piston cap, cylinder liner spacer and headplate. Later diesel components such as pistons and tappets were tested [6]. In 1984 Daimler-Benz demonstrated a ceramic gas turbine powered passenger car, the culmination of nine years of research and development initiative [8], whilst in the U.S. Ford have considered

Country	Year			
	1975	1981	1982	1983
United States	35.2	46.1	47.7	50.0
Japan	11.0	17.4	18.5	20.2
West Germany	7.7	10.1	10.4	10.5
France	5.3	6.9	7.6	7.6
United Kingdom	6.0	7.1	–	–

Table 1.3a National expenditure on ceramic research and development (billion US dollars, from reference [5])

Funded body	Financial year				
	1983	1984	1985	1986	1987
Dept. of Energy	20.1	27.1	27.5	27.7	30.2
NASA	3.0	2.5	5.4	4.5	4.6
National Science Foundation	2.9	3.3	3.6	3.6	3.7
National Bureau of Standards	–	–	–	2.2	3.0
Dept. of Defence	16.6	19.9	18.0	21.4	17.0
Total	42.6	50.8	54.5	59.4	58.5

Table 1.3b US federal funding for structural ceramic technology (million US dollars, from reference [5])

a selection of differing materials for advanced heat engine components and are already producing sintered silicon nitride turbocharger rotors, pre-combustion chambers and rocker arm tips [9,10]. However, the confident implementation of ceramic components in all potential areas of application will not be possible until ceramics have consistent and reproducible target properties.

1.2 SILICON NITRIDE CRYSTAL STRUCTURE

Silicon nitride exists in two hexagonal crystallographic modifications, α and β [11,12], which differ in that the distance of the lattice parameter c of the α-form is approximately twice that of the β-form (Table 1.4).

	Lattice parameter (nm)	
	a	c
α-Si_3N_4	0.7753	0.5617
β-Si_3N_4	0.7608	0.2911

Table 1.4 Lattice parameters for the two crystalline forms of silicon nitride

β-Si_3N_4 consists of covalently bonded SiN_4 tetrahedra joined at each corner such that each nitrogen atom is shared by a further three tetrahedra (fig. 1.1). The β-Si_3N_4 structure, with a Si_6N_8 unit cell, derives from the phenacite type Be_2SiO_4 structure (with Si and N atoms replacing Be and O respectively [14,15]) and consists of Si_3N_4 layers alternating in the stacking sequence ABAB... in the c direction.

α-Si_3N_4 has a similar structure to β-Si_3N_4 with the exception that every third and fourth layer is inverted through 180° about the c-axis giving a stacking sequence ABCD. This rotation/inversion has the effect of doubling the unit cell size ($Si_{12}N_{16}$) to a=0.7753 and c=0.5617nm.

α-Si_3N_4 becomes increasingly unstable with respect to the β-form with increasing temperature and β-Si_3N_4 is believed to be more thermodynamically stable above 1500°C. The transformation that occurs from α to β-Si_3N_4 is reconstructive and can be performed via either volatilisation/condensation or solution/reprecipitation processes. The latter mechanism requires the presence of a liquid (at the processing temperature) to promote 'liquid phase sintering'. The transformation of β to α-Si_3N_4 has been reported once although has yet to be confirmed [16].

Silicon nitride possesses a unique combination of thermal and mechanical properties. Si-N covalent bonding means that it has a high elastic modulus and a high strength to weight ratio because of its low molecular mass. It shows a high resistance to thermal shock and a low thermal expansion coefficient. Silicon nitride has a high decomposition

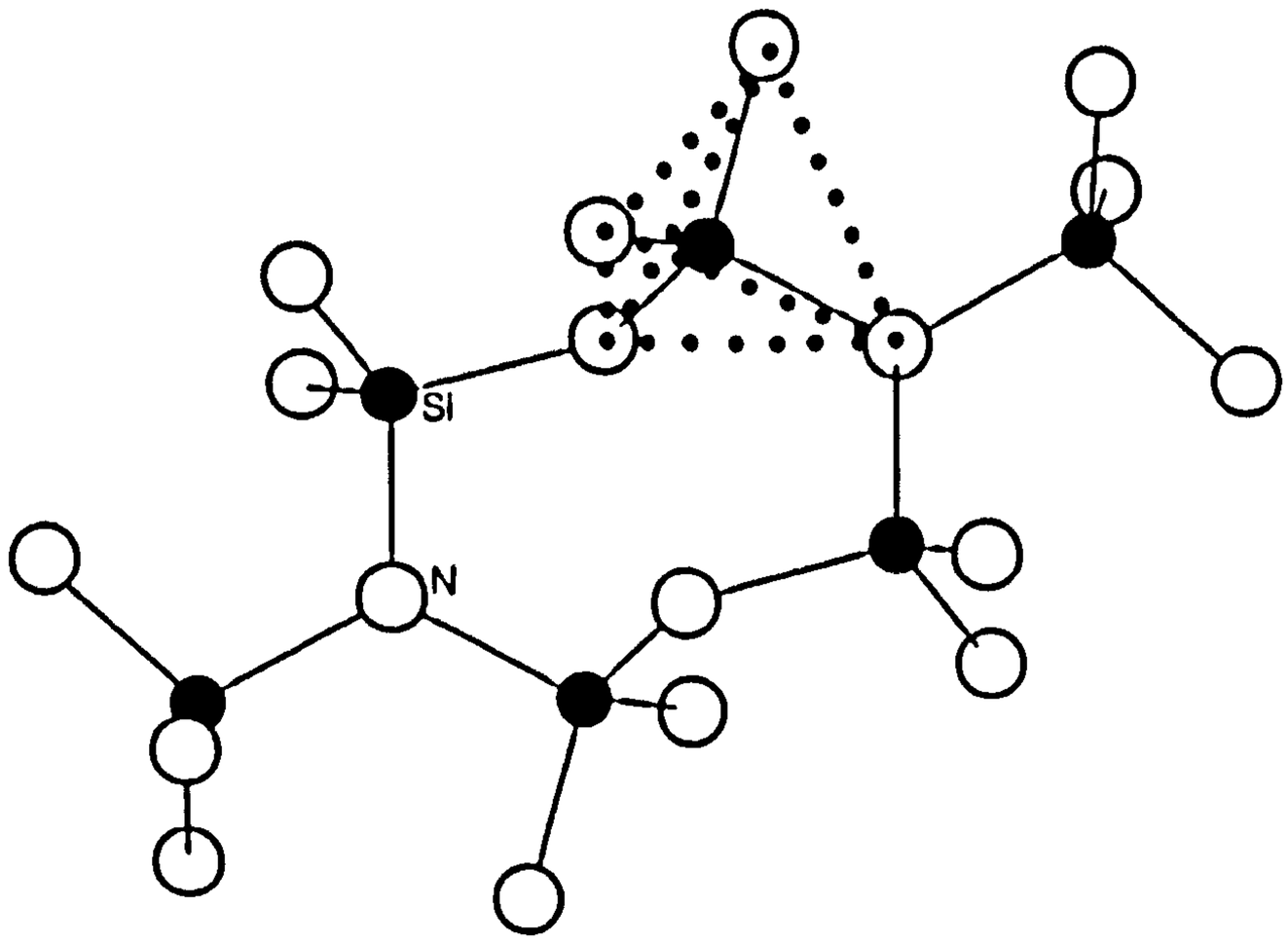

Figure 1.1 The crystal structure of β–Si_3N_4

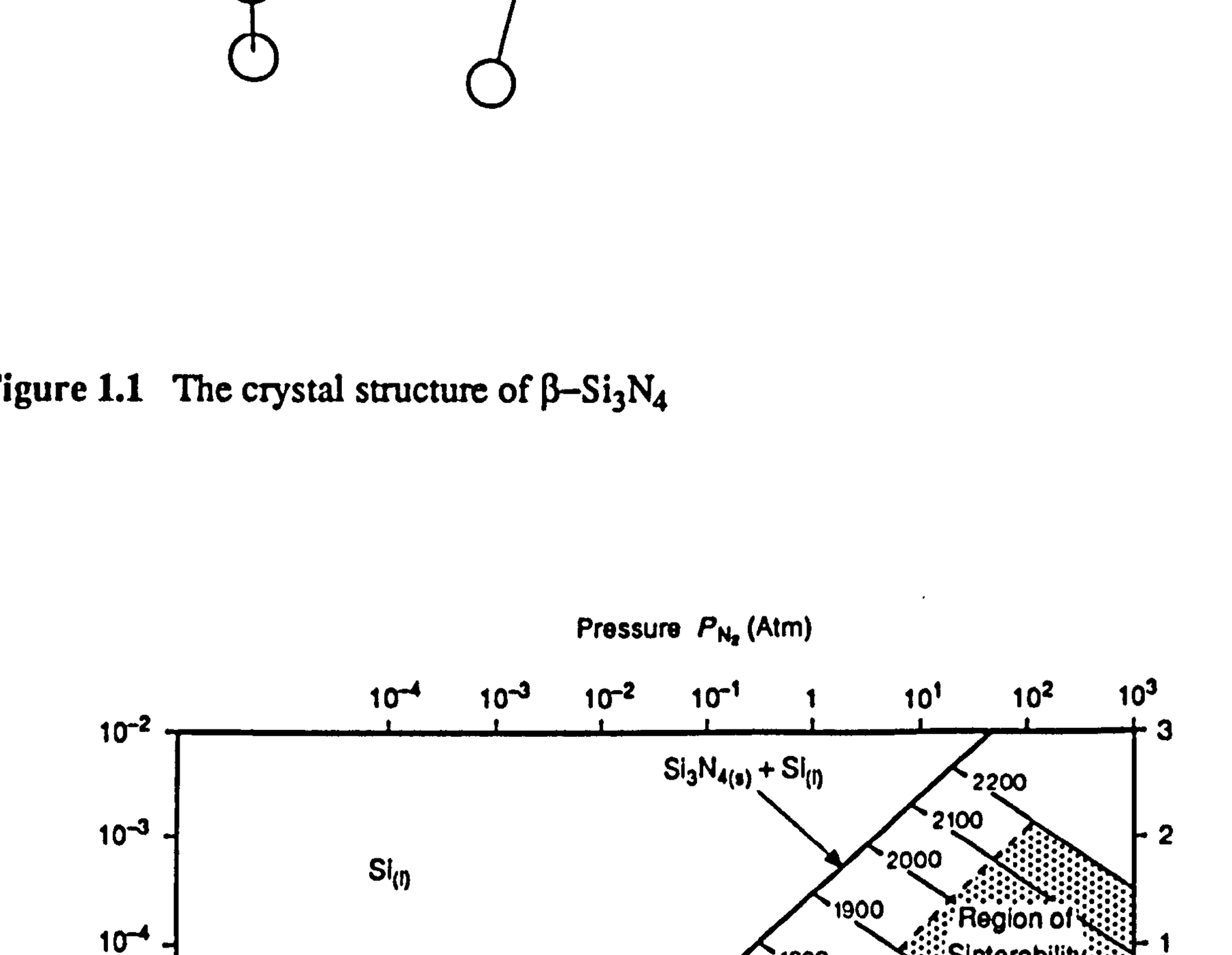

Figure 1.2 The vapour pressure of silicon (P_{Si}) in equilibrium with silicon nitride as a function of nitrogen pressure and temperature (after reference 17).

temperature (~1900°C) and, in the α-form, good resistance to oxidation due a semi-protective silica surface layer that forms in oxygen atmospheres.

However, the covalent bonding nature of the solid means that the self-diffusivity of atoms is low and the densification of pure Si_3N_4, by conventional sintering means, does not occur below the decomposition temperature.

1.3 FABRICATION AND PROPERTIES OF Si_3N_4 CERAMICS

The highly covalent bonding nature of silicon nitride necessitates the use of very high sintering temperatures to achieve material consolidation. However, silicon nitride decomposes at 1900°C under a pressure of 0.1 MPa N_2 following the reaction:

$$Si_3N_{4(s)} \rightleftharpoons 3Si_{(l)}+2N_{2(g)}$$

Consideration of the Si and N_2 equilibrium partial pressures, shown in figure 1.2, reveals the tendency for Si_3N_4 decomposition to be suppressed at higher nitrogen pressures [17].

The requirement for the production of silicon nitride components has led to the development of several differing fabrication routes.

1.3.1 Reaction Bonding

Silicon powder is the starting material used to fabricate reaction bonded silicon nitride (RBSN). The powder is consolidated (via cold-isostatic pressing (CIP), slip casting or injection moulding) and this is generally followed by a pre-sintering step (~1000°C) in an inert atmosphere to provide a machineable preform with requisite porosity. Pre-sintering is followed by nitridation (at ~1400°C) over several days. RBSN microstructure is dominated by a high volume of macro- and microscopic porosity (with micropores in the size range 0.01-1 μm diameter and macropores ranging from 1 μm to 50 μm), with the main material phase being α- and β-Si_3N_4, unreacted Si and impurities. Only small dimensional changes occur during nitridation (± 0.1%) so the process is particularly suited to mass production of complex shaped components where little final machining is

required. Densities in the range 70-88% of theoretical are typical of this processing method. The mechanical properties of RBSN are heavily determined by the high porosity level resulting in low strength (from high flaw concentration) and a reduction in the oxidation resistance (from the increased exposed surface area).

1.3.2 Hot Pressing

Hot pressed silicon nitride requires the use of a sintering aid, typically MgO, Y_2O_3 or CeO_2 (1-5 wt.%), to achieve full density [18-21]. The sintering additives react with SiO_2 or silicon oxynitride, present on the surface of α-Si_3N_4 powders, to form a secondary liquid phase [22,23]. Densification thus proceeds via the liquid phase sintering process described by Kingery [24], following the mechanisms; particle rearrangement, solution-diffusion-precipitation, coalescence, which are shown schematically for hot pressed silicon nitride in figure 1.3. Fine Si_3N_4 powder, with sintering aid(s), is uniaxially die pressed (using graphite dies) under a pressure of 25-40 MPa and a temperature of 1650-1800°C for a period between one and four hours [21]. HPSN is a high strength material which exhibits little degradation in strength at temperatures up to 1000-1100°C. However softening of the mainly amorphous grain-boundary phase at temperatures above 1100°C produces a dramatic reduction in ultimate strength and oxidation resistance. The uniaxial nature of hot pressing promotes a certain degree of anisotropy in material properties (up to 20%) due to preferred orientation of the elongated β-crystals perpendicular to the pressing direction [26,27].

Ultimately HPSN is limited in applications because only simple shapes can be formed. Expensive diamond machining is therefore required to produce complex shapes from the extremely hard densified material.

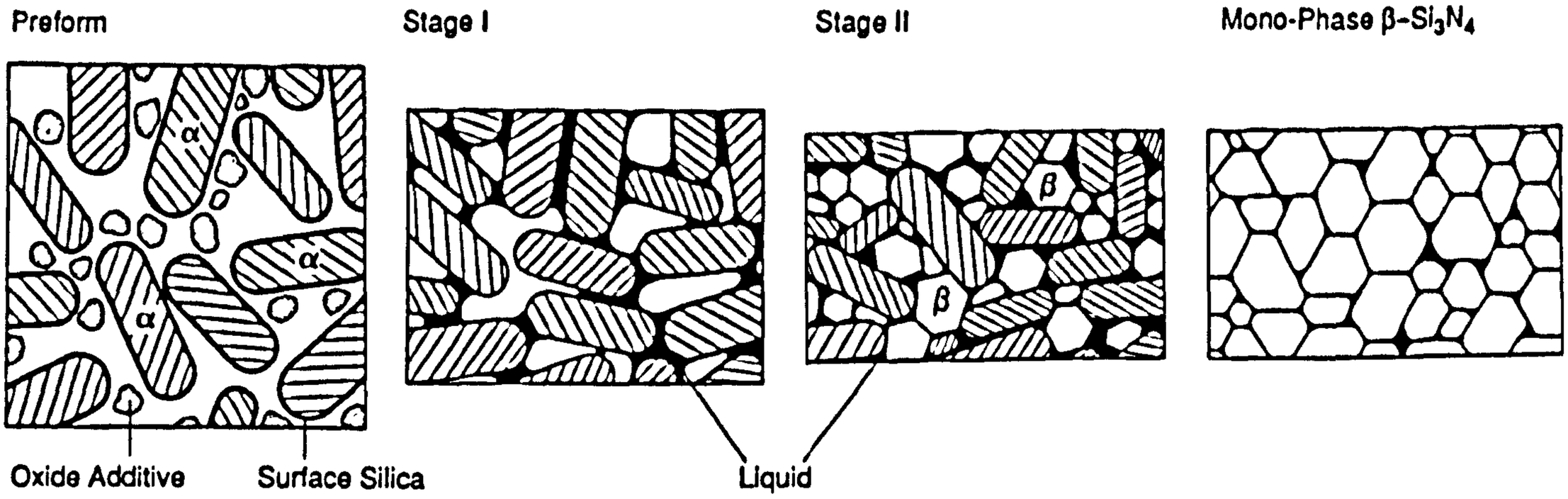

Figure 1.3 Schematic diagram of the densification of silicon nitride by hot-pressing, following stages I and II of the liquid phase sintering process (after reference 25).

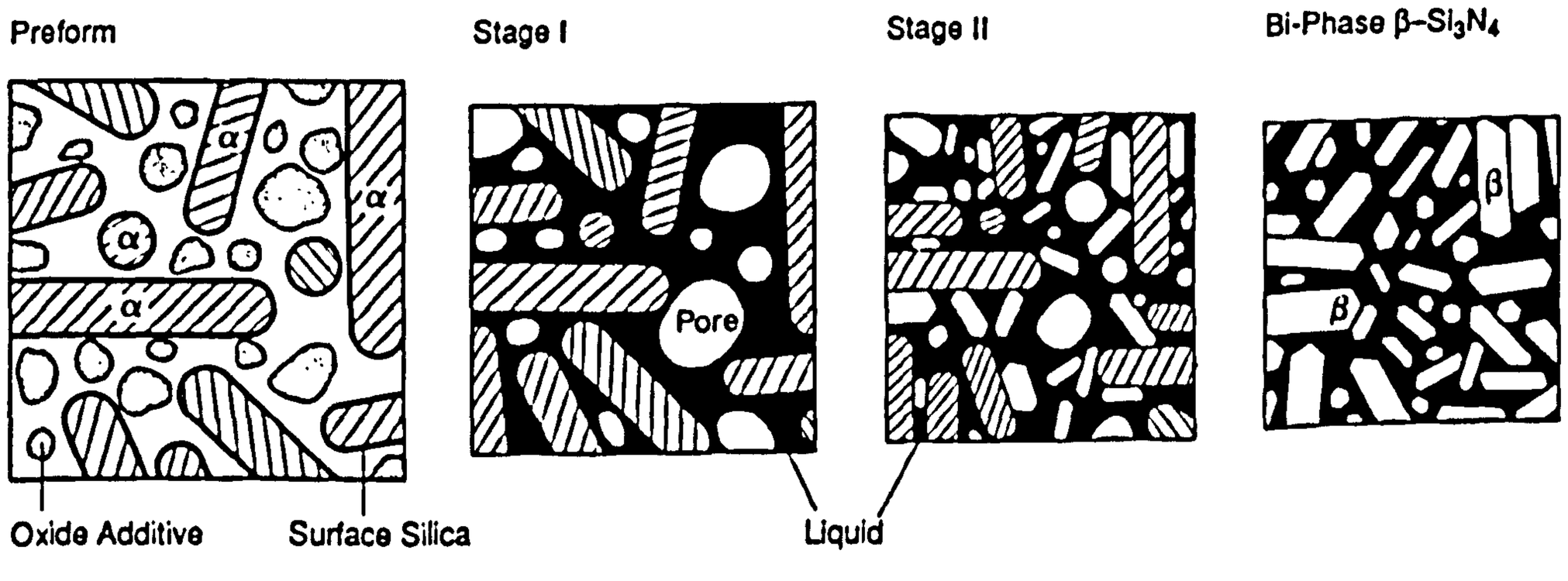

Figure 1.4 Schematic representation of the liquid phase sintering process during pressureless sintering, demonstrating the use of an increased liquid volume relative to hot-pressing (after reference 25).

1.3.3 Pressureless Sintering and the Si-Al-O-N's

The need to produce densified, complex-shaped, silicon nitride components that possess high strength, and require a minimum of diamond machining, has promoted the development of a further fabrication technique, pressureless sintering. The consolidation of pressureless sintered silicon nitride (SSN) is again via the liquid phase sintering process (fig. 1.4).

Early attempts at conventional pressureless sintering resulted in material of approximately 90% density [28]. The rate of sintering (densification) versus dissociation (thermal decomposition) of silicon nitride were such that low densities and high weight losses occurred. Mitomo [29] and Priest *et al* [30] independently sintered silicon nitride with MgO additives to near theoretical density, with little weight loss, using a nitrogen over pressure (~1 MPa). Giachello *et al* [31] sintered similar composition specimens using a silicon nitride powder bed, producing comparable results.

It was noted that the density of specimens sintered with MgO additions in a silicon nitride powder bed was lower at the surface than in the bulk material, producing a 'skin' approximately 1 mm thick. Analysis revealed that the surface 'skin' was devoid of MgO. Further loss of MgO from the specimen occurred when the sintering temperature or time was increased. The use of a mixed powder bed of composition 50% Si_3N_4, 10% MgO and 40% BN (to prevent the powder bed sintering) reduced the problem. A combination of pressure and the use of a protective powder bed produced the best results [32]. Pompe has demonstrated that Y_2O_3 and Al_2O_3 additive species also migrate during sintering in a study of the influence of powder beds [33].

The densification kinetics of silicon nitride are highly dependent on the amount and type of sintering aid used. The variation in viscosity of MgO and Y_2O_3 eutectic liquids, for example, determines the rate controlling process during sintering [34], shown in the Kingery model. MgO forms a lower viscosity eutectic liquid (with surface silica) than

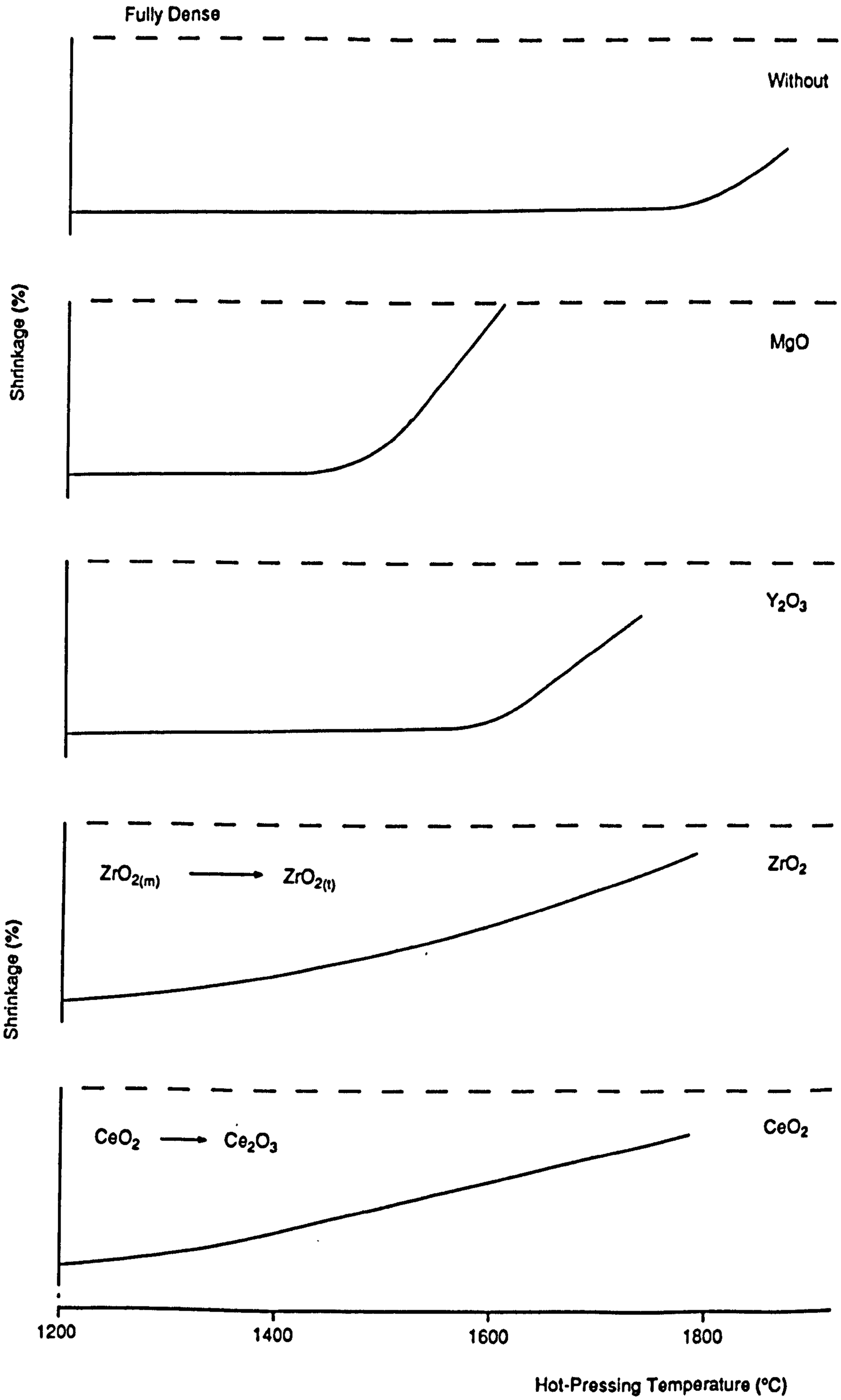

Figure 1.5 A representation of the densification of hot-pressed Si_3N_4, with differing oxide additives, as a function of temperature.

Y_2O_3. For pressureless sintering complete densification, with only partial α-β transformation, occurred with MgO additions. Incomplete densification, with total α-β transformation, was obtained withY_2O_3 additions.

The variation of densification with oxide additive is compared in figure 1.5 [35]. The eutectic liquid softening temperatures for Y_2O_3, ZrO_2 and CeO_2 are higher than for MgO, and therefore higher densification rates only occur at greater temperature, when the liquid is less viscous.

Multi-component sintering aids have been examined more recently. The most favoured additive combinations are Y_2O_3 with Al_2O_3, Al_2O_3 with MgO and Y_2O_3 with MgO [32-37]. The use of mixed additions results in a lowering of the eutectic liquidus temperature (ie. Y_2O_3-Al_2O_3-SiO_2 at 1445°C) relative to the pure binary oxide (Y_2O_3-SiO_2 1660°C) allowing greater final densities to be obtained. In the early 1970's Oyama in Japan [38] and Jack in England [19], independently discovered that Al^{3+} ions could be directly substituted for Si^{4+} provided that there was a simultaneous replacement of N^{3-} by O^{2-} to maintain charge neutrality. These Si-Al-O-N ceramics, so called because of the elements present in the major phase, are based on substituted forms of α- and β-Si_3N_4 (labelled α′- and β′-Si_3N_4 respectively). The general β′- solid solution composition is given by the formula:

$$Si_{6-z}Al_zO_zN_{8-z}$$

where the substitution level, z, varies from 0 to approximately 4.2 [39].

Initially only Al_2O_3 additions were used to produce β′, but Lumby *et al* [40] successfully used AlN which was generally added in the form of a Si-Al-O-N polytype. The four component Si_3N_4-SiO_2-Al_2O_3-AlN is shown in figure 1.6a. The Si-Al-O-N system representation (together with the five component Y-Si-Al-O-N Janecke Prism representation) is described in greater depth in reference [13] and the Y-Si-Al-O-N system is shown schematically in figure 1.6b,c.

a

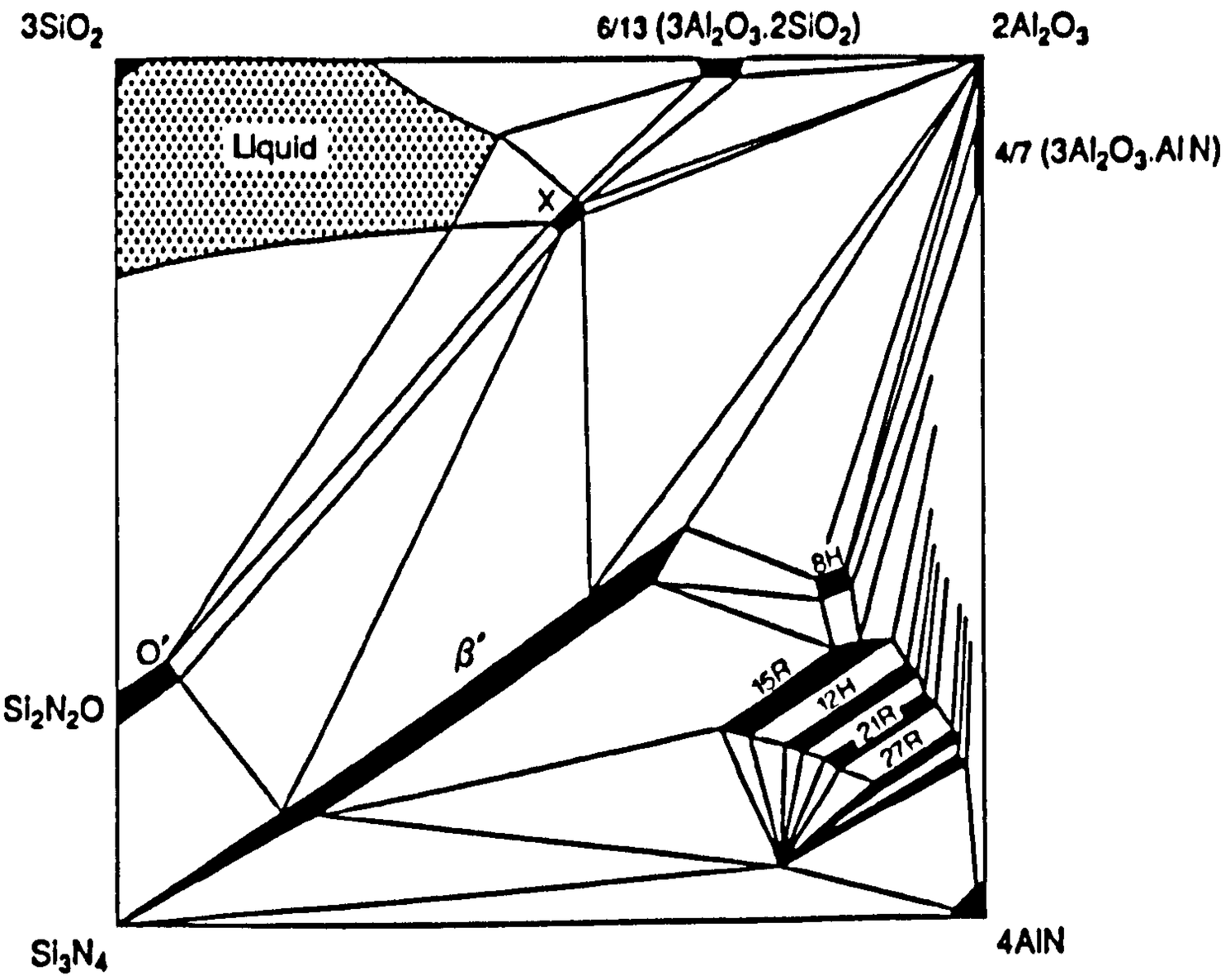

b

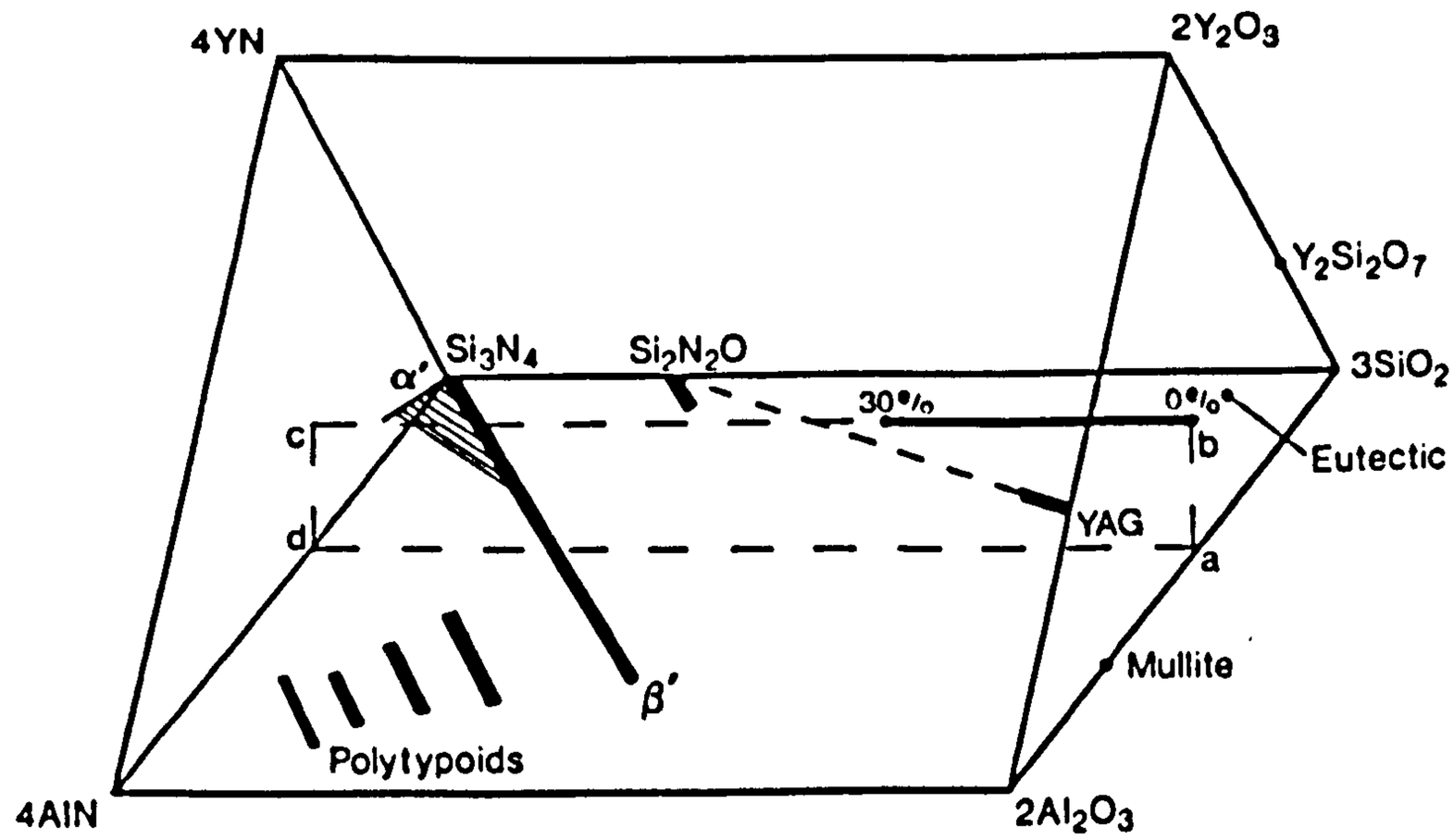

c

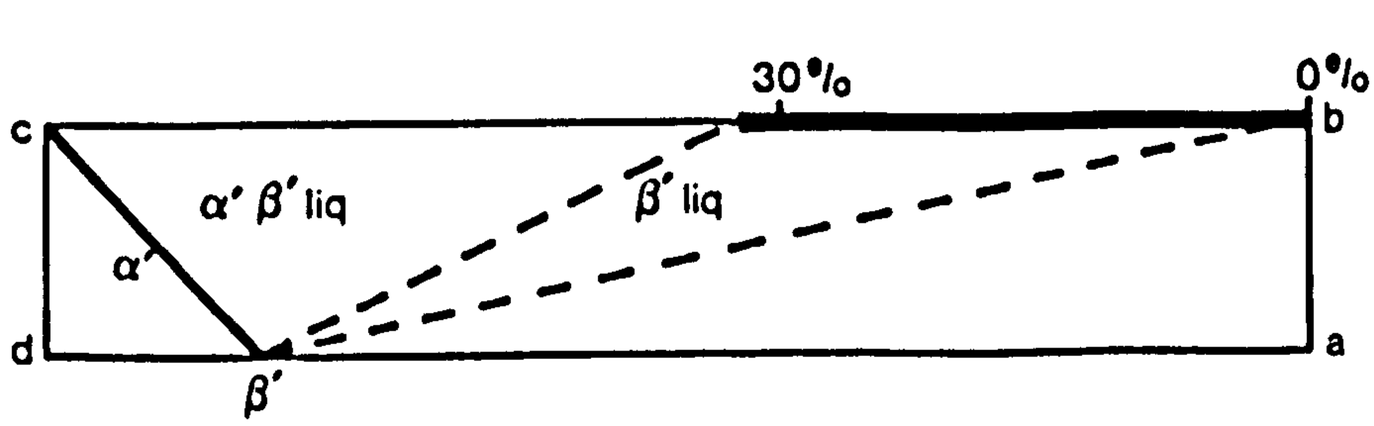

Figure 1.6 a) The four component Si_3N_4–SiO_2–Al_2O_3–AlN system at 1700°C (after reference 13). b) The Janecke Prism representation of the five component Y-Si-Al-O-N system, illustrating the relationship between major crystalline ceramic phases and sintering liquid composition. c) The cross section 'abcd', through the Y-Si-Al-O-N system, demonstrates the emergence of α'–Si_3N_4 under conditions of high nitrogen concentration.

Careful compositional control of the starting powder constituents for Si-Al-O-N ceramics allows a high percentage of incorporation of Al and O in the β′ major phase, which results in the retention (after sintering) of a low volume glass residue at grain boundary triple junctions, improving the creep resistance of densified ceramics [40]. The flexibility allowed by the Si-Al-O-N alloy route also offered the advantage of tailoring the residual glass phase present after sintering so that a post-sinter heat treatment can be incorporated to produce crystallisation of the glass to a more refractory phase. This method has been used to fabricate ceramic materials with a Y-Si-Al-O-N matrix that have been completely crystallised to yttrium aluminium garnet (YAG) and which possess excellent high temperature mechanical properties [41-43]. However, instability of the YAG phase in oxidising atmospheres above 1320°C leads to severe environmental degradation of these materials [44].

The role of the grain boundary phase in all densified Si_3N_4 based ceramics is of great importance and the potential requirement is for a stable intergranular phase under oxidative and corrosive atmospheres up to a temperature of 1450°C. Therefore careful consideration must be made to the starting powder morphology and purity, together with tailoring of the overall ceramic chemistry to enhance material properties.

1.4 Si_3N_4 STARTING POWDER REQUIREMENTS

Investigation of silicon nitride powders has revealed the requirement for specific powder properties to obtain full density ceramic articles. A high α-Si_3N_4 content (>90%) is desirable to obtain elongated β-grains [45]. Equiaxial α-powder grains allow higher 'green' densities to be obtained and hence greater shape retention during sintering [46]. Decreasing the powder size (ie. increasing the specific surface area) results in an increased sinterability for a constant oxygen content [46]. However, in practice, the oxygen level is found to increase thus requiring an increase in sintering aid to maintain an overall balanced composition, which tends to reduce the densification effect due to the

powder size. The impurity content of the starting powder is also extremely important to the ultimate properties of the densified ceramics, with elements such as iron or aluminium, which segregate to the residual glass phase, acting as glass modifiers by reducing the liquid viscosity, hence degrading high temperature properties. These impurities can also lead to the formation of inclusions, which tend to reduce the overall material strength [47-49]. The presence of free carbon in the starting powder leads to a reaction with the surface oxygen, subsequently impairing sintering liquid formation.

Three principal commercial production routes exist for silicon nitride powder.

1. Nitridation of silicon between 1200 and 1400°C using an iron catalyst:

$$3Si_{(s)}+2N_{2(g)} \longrightarrow Si_3N_{4(s)}$$

2. Carbothermal reduction of silica in a nitrogen atmosphere using readily available source materials such as rice husks:

$$3SiO_{2(s)}+6C_{(s)}+2N_{2(g)} \longrightarrow Si_3N_4+6CO_{(g)}$$

3. Thermal decomposition of precipitated silicon diimide:

$$SiCl_{4(l)}+6NH_{3(g)} \xrightarrow{0^\circ C} Si(NH)_{2(s)}+4NH_4Cl_{(g)}$$

$$3Si(NH)_{2(s)} \xrightarrow{1200^\circ C} Si_3N_{4(s)}+2NH_{3(g)}$$

A summary of the powder properties for these production routes is shown in Table 1.5 [50,51].

Fabrication route	Specific surface area (m^2g^{-1})	Impurity content (wt. %)			Crystallinity (%)	$\frac{\alpha}{(\alpha+\beta)}$ (%)	Morphology
		O	C	Σ Fe,Al,Ca			
Si nitridation (1)	8 - 25	1.0 - 2.0	0.14 - 0.4	0.07 - 0.15	100	95	Equiaxed
Carbothermal reduction (2)	4.8	1.6	1.05	0.06	100	95	Equiaxed and rod-like
Diimide precipitation (3)	9.1	1.4	0.1	0.006	100	86	Equiaxed

Table 1.5 Typical properties of Si_3N_4 powders manufactured by the principle commercial production routes (from references [50,51])

1.5 Si_3N_4 PROPERTY DESIGN

1.5.1 Stability of Si_3N_4 Ceramics in Oxidising Environments

The oxidation behaviour of silicon nitride ceramics is of vital importance to the ceramic engineer as the majority of potential applications involve extended usage in hostile environments. Essentially two oxidation reactions occur for silicon nitride:

1. Active oxidation, occurring under extremely low oxygen potentials, leads to an overall specimen weight loss (from the formation of gaseous SiO) and proceeds via either

$$Si_3N_{4(s)} + O_{2(g)} \longrightarrow 3SiO_{(g)} + 2N_{2(g)}$$

occurring in the presence of a gaseous oxygen atmosphere, or

$$Si_3N_{4(s)} + 3SiO_{2(s)} \longrightarrow 6SiO_{(g)} + 2N_{2(g)}$$

which arises from reaction with non-gaseous oxygen sources, for example the SiO_2 oxide scale formed in passive oxidation.

2. Passive oxidation occurs in conditions of high oxygen potential (eg. normal atmospheres) and leads to the formation of amorphous SiO_2, with either gaseous or diffusive N_2 loss, and an overall weight gain following the reaction:

$$Si_3N_{4(s)} + 3O_{2(g)} \longrightarrow 3SiO_{2(s)} + 2N_{2(g)}$$

Generally the oxidation rate is parabolic in nature, approximating to

$$W^n = kt + \text{constant} \qquad (1.1)$$

where W is the extent of oxidation at time t, n the oxidation exponent and k is a rate constant [52,53]. Parabolic high temperature oxidation behaviour indicates a diffusion controlled rate determining process, first theoretically predicted by Wagner [52]. Deviations from parabolic behaviour can generally be attributed to time-dependent composition variations of the oxide scale, non-parabolic thick film oxidation mechanisms or, trivially, incorrect determination of the oxidation level.

Predictably, passive oxidation is of the most interest to investigators as component usage will require operation under atmospheric conditions at elevated temperatures. Several mechanisms have been proposed as the rate controlling process for oxidation of silicon nitride including the in-diffusion of O^{2-} and, more notably, the out-diffusion of cationic species, present in the grain boundary phase as either sintering additives (eg. Mg^{2+} or Y^{3+}) or impurities (eg. Ca, K) [54,55]. A diffusion couple between surface SiO_2 (formed by direct oxidation of Si_3N_4 at the sample surface) and the intergranular glass (or partially crystalline) residue has been proposed [54]. Out-diffusion of cationic elements has also been observed experimentally in the form of a gradient of depleted sub-surface elements [54-56]. The rate of oxide scale evolution was shown to be dependent upon the type and amount of intergranular phase present [56-59], by altering the viscosity of this phase thus changing the materials oxidation resistance. Cubiccioti and Lau also proposed a further modification to the oxidation mechanism, with out-diffusing ions generally lowering the viscosity of the surface silica melt and hence increasing the solubility of Si_3N_4 within the melt with a consequent increase in the oxidation kinetics. Generally increasing the MgO additive level in dense silicon nitride is detrimental to the oxidation resistance, however yttria-based additive systems present the possibility of crystallising the glassy intergranular phase to a more refractory one.

Fully crystalline β′-Si-Al-O-N/YAG ceramics have been shown to possess excellent resistance to passive oxidation at temperatures up to 1300°C, however above 1320°C the YAG reverts to a liquid by reaction with the surface SiO_2 oxide film [44] causing a drastic increase in the oxidation rate.

Heath annealed a low 'polytypoid addition' Si-Al-O-N material producing a β'-Si_3N_4/α-$Y_2Si_2O_7$/YAG ceramic with excellent oxidation resistance to a temperature of 1300°C, however a reduction in the SiO_2 oxide scale viscosity by outdiffusing Al^{3+} cations (from β-Si-Al-O-N and YAG) drastically increases the oxidation rate at 1350°C [44].

Although silicon nitride ceramics with a crystalline yttrium disilicate intergranular phase have been demonstrated to possess excellent resistance to oxidation, careful compositional selection is required when preparing materials in the Y-Si-O-N system (fig. 1.7). Lange demonstrated that certain quaternary Y-Si-O-N phases, which crystallise either during fabrication or the initial oxidation stage suffer from large molar volume changes upon oxidation at relatively low temperatures (Table 1.6), which can eventually lead to specimen disintegration [60]. It is therefore important to prevent the nucleation of these phases upon specimen annealing (eg. by obtaining an overall compositional balance within the Si_3N_4-Si_2N_2O-$Y_2Si_2O_7$ compatibility triangle) (fig. 1.7). Similar problems arise with oxynitride secondary phases in both the Ce-Si-O-N and Zr-Si-O-N systems [60].

Crystalline phase	Oxidation product	Volume change
$Y_2Si_3O_3N_4$	$Y_2Si_2O_7 + SiO_2$	+30%
$YSiO_2N$	$0.5\ Y_2Si_2O_7$	+12%
$Y_5(SiO_4)_3N$	$0.75\ Y_{4.67}(SiO_4)_3O + 0.75\ Y_2SiO_5$	+ 4%

Table 1.6 Molar volume changes of unstable quaternary Y-Si-O-N phases upon oxidation (from reference [60])

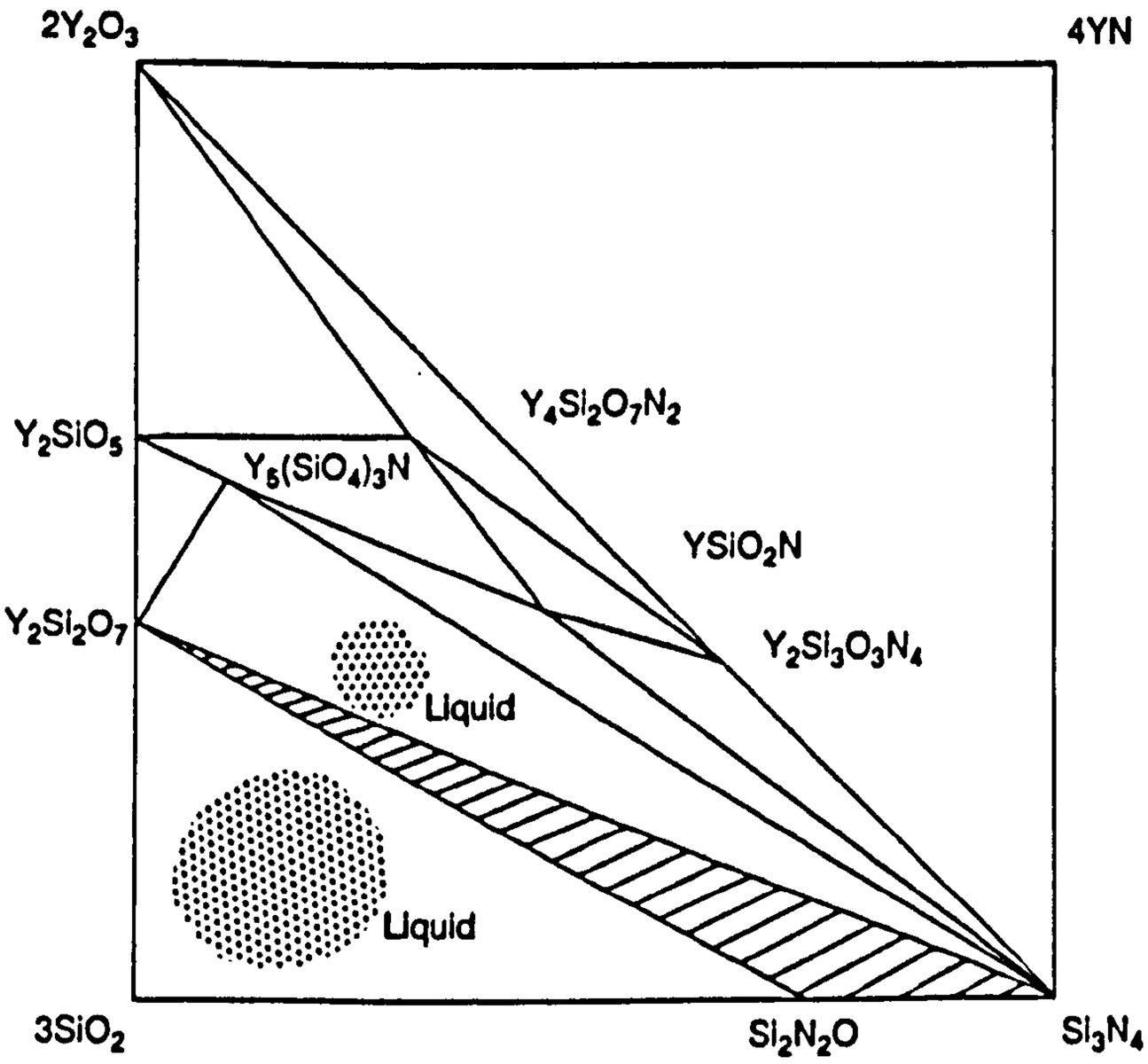

Figure 1.7 The Si_3N_4–SiO_2–Y_2O_3–YN phase system at 1550°C (after reference 170).

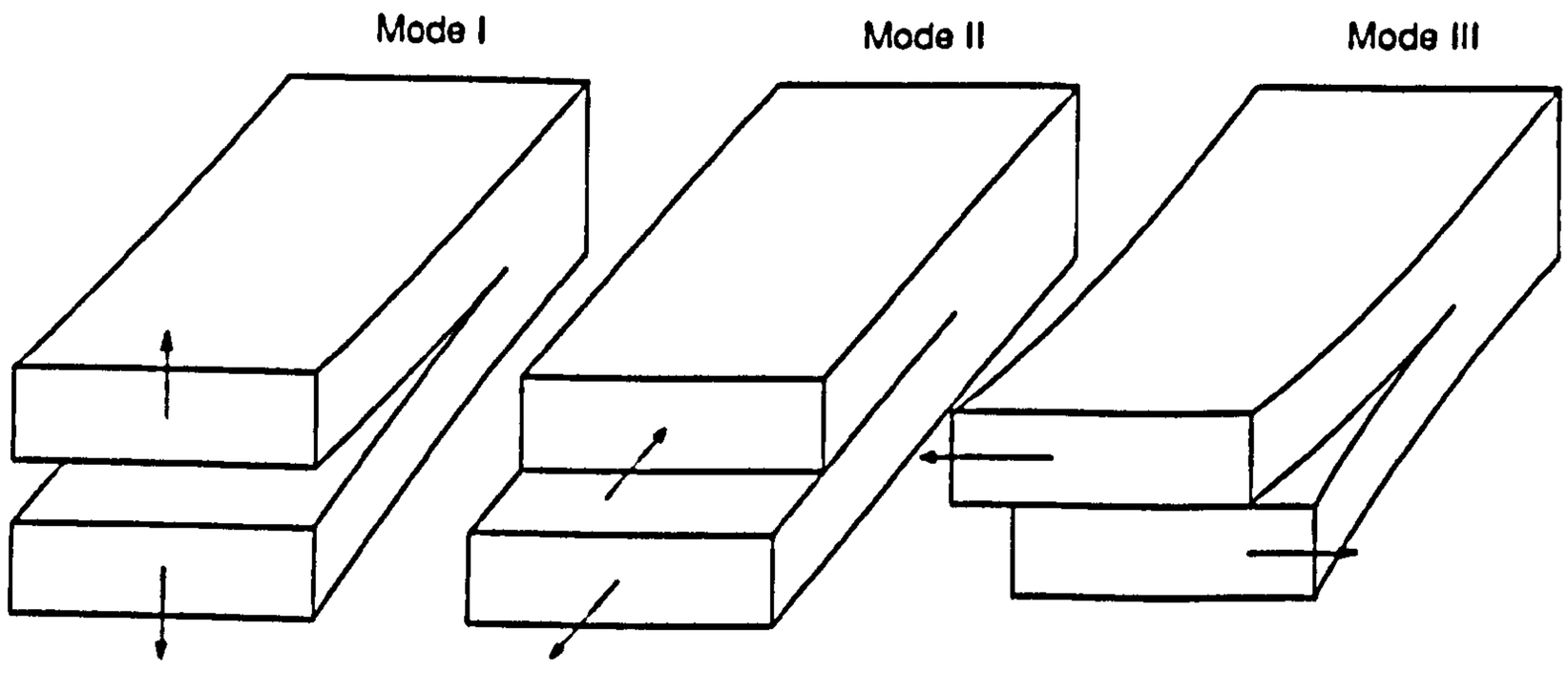

Figure 1.8 The three fundamental fracture modes for brittle materials: I (opening mode), II (sliding mode), and III (tearing mode).

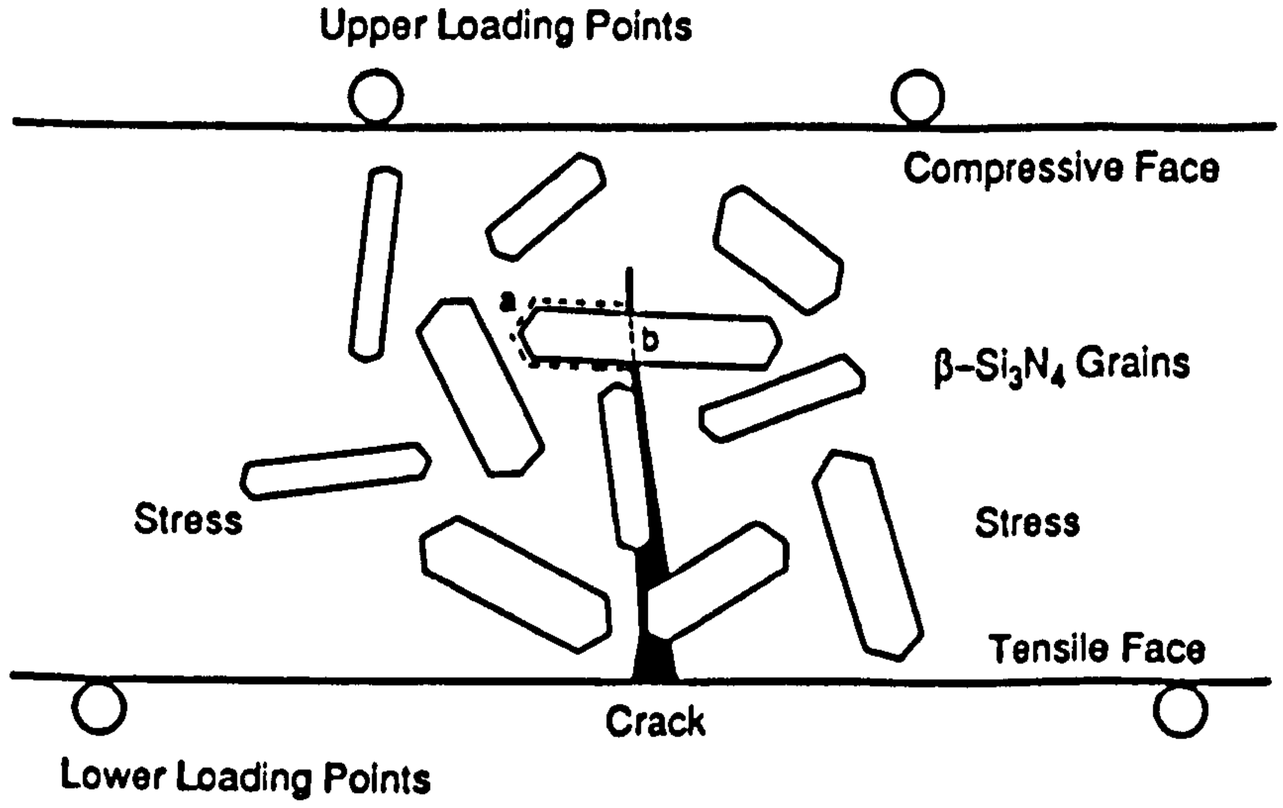

Figure 1.9 Schematic representation of the influence of interlocking β–Si_3N_4 grains on crack propagation. In the example shown further propagation of the crack can occur: either a) parallel to the applied stress, energetically unfavourable, or b) through the β–Si_3N_4 grains. Both of these crack routes enhance the fracture toughness (K_c) (after reference 73).

1.5.2 Mechanical Behaviour of Si_3N_4 Ceramics

As previously stated, ceramics have yet to be fully accepted as engineering materials because of their brittle nature and relative unpredictability (cf. metals). The concept of fracture mechanics initially arose to determine why engineering components failed at applied stresses below the calculated critical applied stress for that material.

Initial investigation of this behaviour was examined both practically and theoretically by Inglis [61] and Griffith [62]. It was proposed that fracture arose from microscopic (or macroscopic) surface flaws, or cracks, and that the applied stress (σ_n) was effectively increased at a crack tip. Griffith derived an expression relating the applied stress to the concentrated stress (σ_c) at the crack tip:

$$\sigma_c = \sigma_n 2\sqrt{a/r} \tag{1.2}$$

where a is the crack/flaw length and r is the tip radius. However, the notch model proved unsuitable for atomically sharp cracks, further energy considerations were thus developed assuming [62]:

1. The free energy of the (cracked) material and the specific applied forces do not increase during elongation of the crack.

2. Energy dissipation during crack extension only arises via the formation of two surfaces (thermodynamic surface energy γ).

This methodology led to the now familiar Griffiths relation describing the failure stress:

$$\sigma_f = \frac{1}{Y}\left(2E\frac{\gamma}{a}\right)^{1/2} \tag{1.3}$$

where E is the Youngs modulus, a the crack length and Y is a geometrical factor which relates the flaw/specimen geometries and the loading configuration. In reality other energy dissipative mechanisms exist during crack propagation, most

notably plasticity and sub-critical crack growth.

A generalisation of the Griffith equation, derived by Irwin [63], suggested that crack elongation will occur provided the strain energy release rate (G) is greater than or equal to the rate of dissipated energy upon further crack formation,

$$\sigma_f = \frac{1}{Y}\left(\frac{EG_c}{a}\right)^{1/2} \tag{1.4}$$

A 'stress intensity factor' (K) can be defined for a general applied stress level σ_a to a crack of length a:

$$K = \sigma_a Y a^{1/2} \tag{1.5}$$

If the stress intensity K exceeds a critical value K_C, catastrophic failure of the stressed material will result. K_C therefore determines the fracture toughness of the specific material.

Three fundamental crack propagation modes exist for ceramic materials (fig. 1.8). Crack extension studies of brittle materials are generally conducted using the mode I (crack opening) method, ie. under simple tensile loading. Several experimental methods have been devised for K_C determination, and details of these techniques are described in references [64-68]. At the critical point of failure of a material it was shown that K_{IC} and G_{IC} are related by the equation [69]

$$G_{IC} = (1 - \mu)\,\pi\,\frac{K_{IC}^2}{E} \tag{1.6}$$

where μ is the bulk modulus of the material. K_{IC} and G_{IC} both provide a measurement of the resistance to crack propagation within the material, ie. indicating the 'fracture toughness' of that material.

1.5.3 Factors Affecting Fracture Toughness

There are several factors that have been reported to affect the K_C value of a particular material. Silicon nitride possessing a fine, interlocking needle-like β- grain structure has been shown to exhibit high values of fracture toughness [70,71]. Additionally a reduction of the overall grain size, whilst maintaining a constant aspect ratio, also tends to increase K_C [71]. However, it has also been reported that K_C is independent, or even increases with increasing grain size [72] for some other ceramic materials.

It was suggested that, for high aspect ratio β grains, many are aligned perpendicular to the stress axis [73] (fig. 1.9). The crack therefore has to continue either via the tortuous intergranular route (grain 'pull-out') or by transgranular fracture, both mechanisms produce an effective increase in K_C. This behaviour is analogous to the pull out/crack deflection toughening mechanism defined for composite materials [74,75].

The volume and viscosity of the secondary phase present in densified silicon nitride are also of great importance in determining the strength and toughness. Increasing the secondary phase volume, for a constant composition, has been shown to enhance K_C, primarily through an increase in β- grain aspect ratio [76]. The composition of the sintering aid(s) and the processing have been shown to affect both the aspect ratio and grain size [45,46,77-79]. Additionally K_C can be increased or decreased by porosity [80], with an enhancement of toughness by small pores and a reduction by large pores. Finally it should be noted that the test method is a further parameter involved in K_C determination [81].

1.6 CERAMIC COMPOSITION ENGINEERING

The principle silicon nitride densification techniques described in this chapter, hot-pressing and pressureless-sintering, both suffer from specific limitations. It is possible to fabricate hot-pressed silicon nitride with an excellent combination of material properties (strength, oxidation resistance etc.), however the mechanical behaviour is anisotropic and, more importantly, the process is limited to relatively simple shapes. Conversely, pressureless-sintering allows the consolidation of complex shaped parts. Unfortunately the presence of a large secondary glass volume is a limiting factor to the applications of these ceramics. This limit can be extended by post-sinter crystallisation of the glass phase, a method that has been utilised for commercial Y-Si-Al-O-N ceramics [42,82], producing a ceramic material with a maximum operating temperature of approximately 1300°C. For further improvements in operating temperature it is desirable to fabricate silicon nitride based materials with a matrix glass that can be devitrified to a phase that is stable with respect to SiO_2.

Crystalline phases compatible with SiO_2 include the tri-valent metal disilicate compounds (eg. $Y_2Si_2O_7$ and $Nd_2Si_2O_7$). However, fabrication of ceramics that can be annealed to give stable disilicate matrices requires the use of a binary SiO_2-M_2O_3 eutectic matrix composition (where M is a tri-valent metal ion). The high viscosity of these binary glasses at typical sintering temperatures requires the use of pressurised sintering to obtain complete consolidation. The most promising pressure-sintering method currently available is hot-isostatic pressing, utilising pressures up to 200MPa, and it is this fabrication technique that forms the major aspect of research conducted during the current programme.

1.7 CURRENT PROGRAMME OBJECTIVES

The principle objectives of this research programme were:

1. Comparison of the pre- and post- HIP microstructure and properties of a range of sintered silicon nitride ceramics.

2. Development of glass encapsulation techniques for the HIP processing of advanced silicon nitride compositions. The fabrication routes investigated, described in chapter five, included encapsulation in both glass tube and powder. The temperature and pressure conditions of HIPing silicon nitride were to be determined and the subsequent densification behaviour assessed.

3. Microstructural examination of glass encapsulated HIPed silicon nitride together with investigation of the influence of the encapsulant material on the near surface microstructure of these densified ceramics. Assessment of the oxidation behaviour of HIPed silicon nitride, specifically examining variation in properties arising from interaction between the ceramic and encapsulant.

CHAPTER TWO

HOT ISOSTATIC PRESSING OF SILICON NITRIDE: A REVIEW

2.1 INTRODUCTION

Hot Isostatic Pressing (HIP) is a technique that involves the use of both high isostatic (tri-axial) pressure and temperature to assist densification of specimens by the simultaneous processes of sintering and mechanical consolidation. The HIP process is used to bond or form materials resulting in high or full density and hence negligible porosity. During HIPing the specimens are placed within a furnace contained in a pressure vessel (fig. 2.1) [83]. Pressure application occurs via an inert gas, typically argon, helium or nitrogen. Temperature and pressure conditions vary markedly depending on the materials, typically temperatures between 500 and 2200°C with pressures up to 200 MPa [83].

2.2 HISTORICAL BACKGROUND

Hot Isostatic Pressing is essentially a combination of two previously established techniques, hot pressing and cold isostatic pressing (CIP). The first documented application of uniaxial hot pressing, in 1883, was in the production of metal bonded diamond tools [84]. Subsequently the method has been utilised in the formation of cemented carbides, heavy metal compounds and hard or refractory compounds [85]. Associated problems of hot pressing have been described in detail in section 1.3.2, but briefly they are: die life, contamination of pressed items by the die, and a restriction in the complexity of geometry of pressed parts.

Madden [86] first devised a cold isostatic compaction technique to obtain uniform and defect-free tungsten compacts. Madden's process overcame the majority of problems that had previously plagued the compaction of fine, non-ductile powders, such as

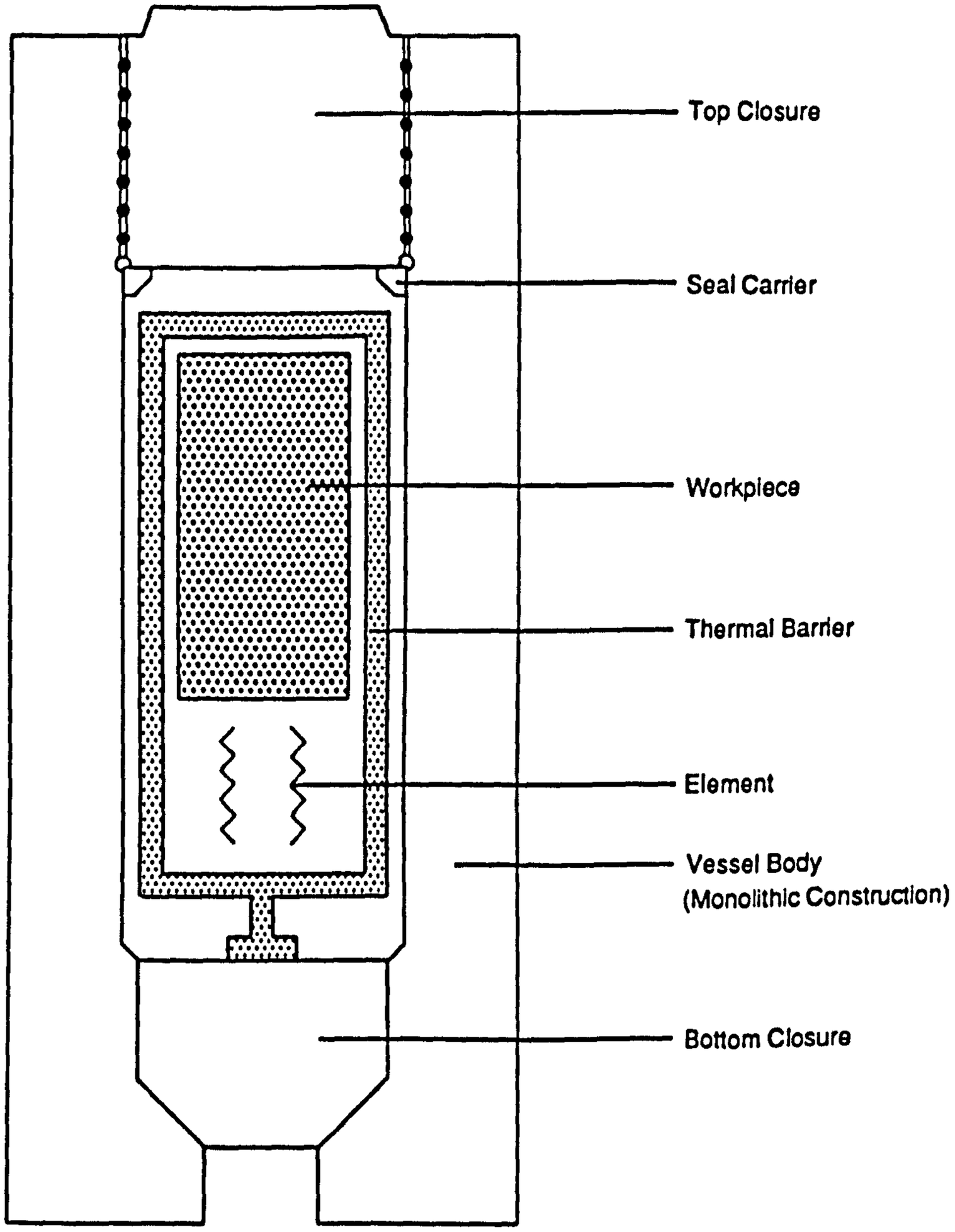

Figure 2.1 Simplified schematic diagram of HIP vessel and workpiece (after reference 83).

cracking, laminations, lack of green strength and non-uniformity of properties. Methods for the isostatic compaction of ceramic articles were described in patents taken out by Jeffrey [87,88] and Daubenmeyer [89] in the early 1930's. Among the ceramic articles fabricated by Jeffrey were grinding media and spark-plug insulators. The advent of World War II moved development of CIP techniques from the laboratory to large scale production with emphasis placed on metals and explosives. Further development was slow, especially in the field of powder metallurgy, however increased interest was generated in the compaction of ceramic powders. Today CIP is a standard fabrication technique for forming complex shaped articles (and more simple shapes) in the fields of powder metallurgy and traditional/advanced ceramics, and for diverse materials such as polymers (eg. PTFE), pharmaceuticals and foodstuffs [90].

The hot isostatic pressing process, or gas pressure bonding as it was originally known, was first devised at Battelle Laboratories, Columbus, Ohio in 1955 [91]. It was developed as a method to bond components on small Zircoloy-clad fuel elements whilst maintaining dimensional control. The first HIP system used was of the hot wall type, and consisted primarily of a stainless steel vessel, in the form of a high pressure tube. The steel vessel had an overall length of 3 ft and internal and external diameters of 3/16 in and 9/16 in respectively.

One end of the tube was closed by welding, whilst a high pressure valve was threaded to the other. The specimens were inserted into the tube and a line was then attached from the valve to a helium cylinder. The system was subsequently pressurised to 14 MPa (2000 psi), and the closed end was inserted into a heat treatment furnace at ~800°C (1500°F) for a period ranging between 24 and 36 hours [92]. Excellent Zircoloy to Zircoloy and Zircoloy to core bonds were produced by this route, although the processing time was excessive.

The limitations of the hot-wall type system, with respect to size, processing temperature and pressure, led to the production of an alternative cold-wall hot-isostatic press. This

system utilized a forged stainless steel vessel with internal dimensions of 0.23m diameter and 1.20m length and was pressurised by a 70 MPa compressor. A ceramic tube furnace with a wound heating element, and insulated with ceramic brick, was used to heat the specimen. However [93] problems occurred with temperature stability through the vessel, with the system taking an extreme period to reach equilibrium. The furnace design was therefore revised to incorporate a slotted ceramic tube with a cromel heating element, positioned in a stainless steel can. Fibrous insulation was tightly packed between the furnace and the inner can. This system achieved a maximum temperature of 830°C and pressure of 70 MPa for a short period [94]. Gradual refinements were performed to this system, leading to research into compaction of MgO and Al_2O_3 [94] and the cladding of zirconium hydride with various stainless steels [95]. Over the following years many minor improvements were made in HIP system design, particularly with a view to increasing the furnace volume and the system operating conditions (increasing temperature and pressure). In the mid 1960's Battelle conducted a heat flow study, to both model and experimentally determine flow patterns within the HIP furnace [96]. Confirmation was obtained of convectional gas flow through the furnace and vessel.

Further developments at the Battelle Institute between 1965 and 1970 included [94]:

1. Compaction of powdered tungsten (in the form of spherical granules) to obtain a fully dense structure.

2. A technique to outgas specimen containers prior to compaction. Further modifications were thus made to the HIP system design at Battelle, by incorporating an inverted container furnace to remove, or at least minimise, convective heat flow within the furnace and therefore maintain a stable hot zone.

3. The development of a rapid, automated process system. Samples to be processed were heated in an external furnace and hot-loaded into the HIP chamber, processed

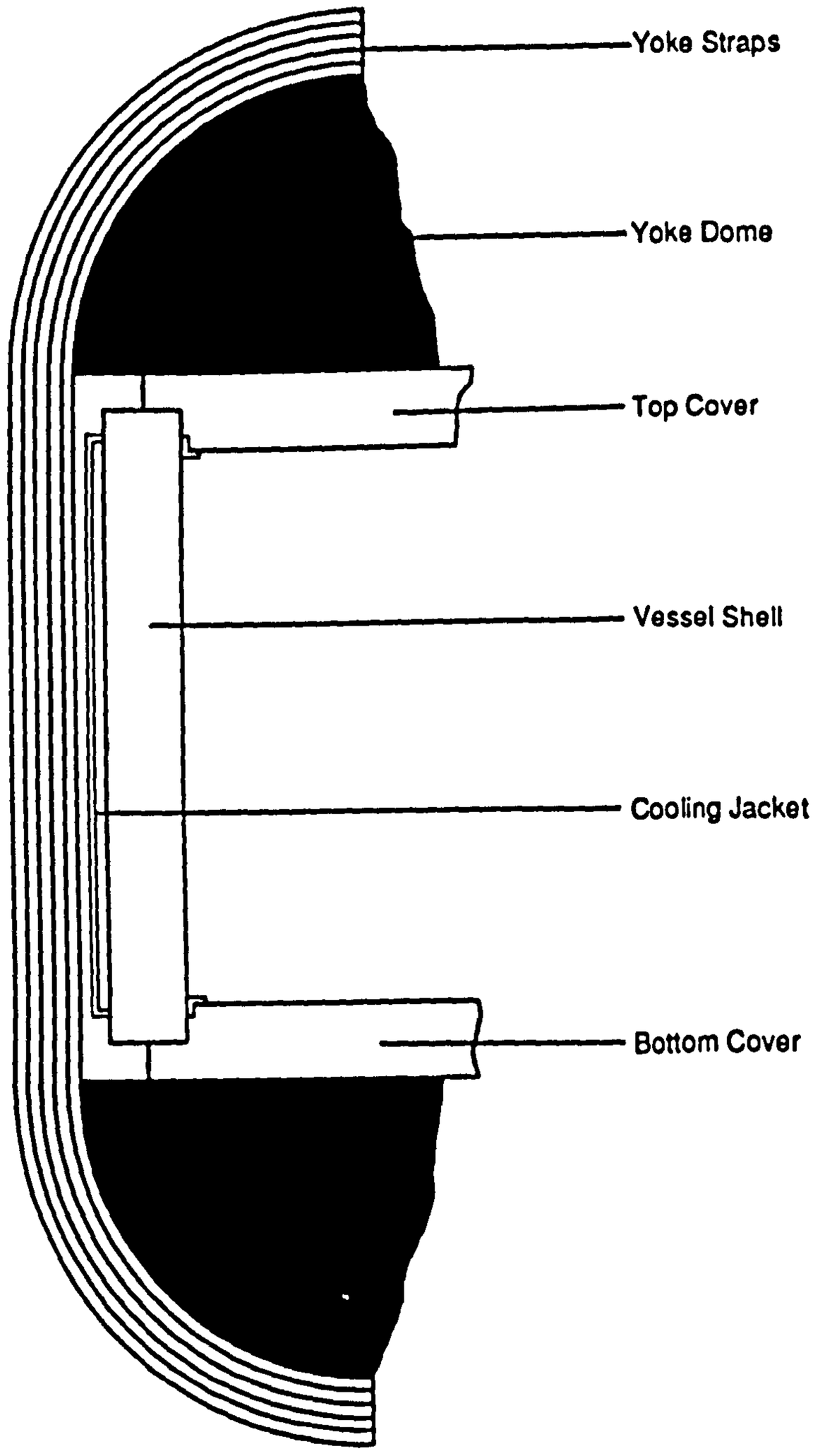

Figure 2.2 Autoclave Engineers (AE) IsoFrame assembly (after reference 83).

(rapid compaction) and hot-unloaded.

4. The conducting of high pressure melting and casting within the HIP system.

5. Development of a 'plug-in' furnace design which could be exchanged for another furnace in the HIP system without manual disconnection.

The safety aspects of HIP production have been improved with the 'yoke' type assembly used by Autoclave Engineers (AE), with the AE Isoframe (fig. 2.2), and ASEA, with the Quintus frame. Both of these systems allow transmission of axial loads, arising from the internal pressure vessel, to the yoke. Thus, only radial and tangential stresses are transmitted to the shell. Typically these systems are top loaded, with a threadless lid which allows a more rapid 'turn-over' time. An ASEA Quintus system is shown in figure 2.3, together with a schematic representation.

In the early 1970's ASEA and Stora Kopparberg announced the introduction of one of the first commercial processes utilising HIP production in the fabrication of tool steels [98], the ASEA-STORA process. This technique involved the encapsulation and HIP of powdered tool steel alloys in pre-shaped mild steel cannisters. At approximately the same time Battelle and other laboratories were investigating further development in the areas of powder consolidation, defect healing and rejuvenation of fatigue damaged components, with development of the first 'net-shape' powder consolidation (of complex shaped beryllium articles) via HIP [99].

Continued development of HIP equipment and applications has occurred throughout the last two decades, most notably in the processing of ceramics. HIP systems with increased temperature and pressure capabilities have been introduced for the densification of these materials. However they have tended to be less reliable and improvements must be obtained for the future large scale fabrication of ceramics.

One of the most promising ceramics for HIP processing is silicon nitride, and it is this

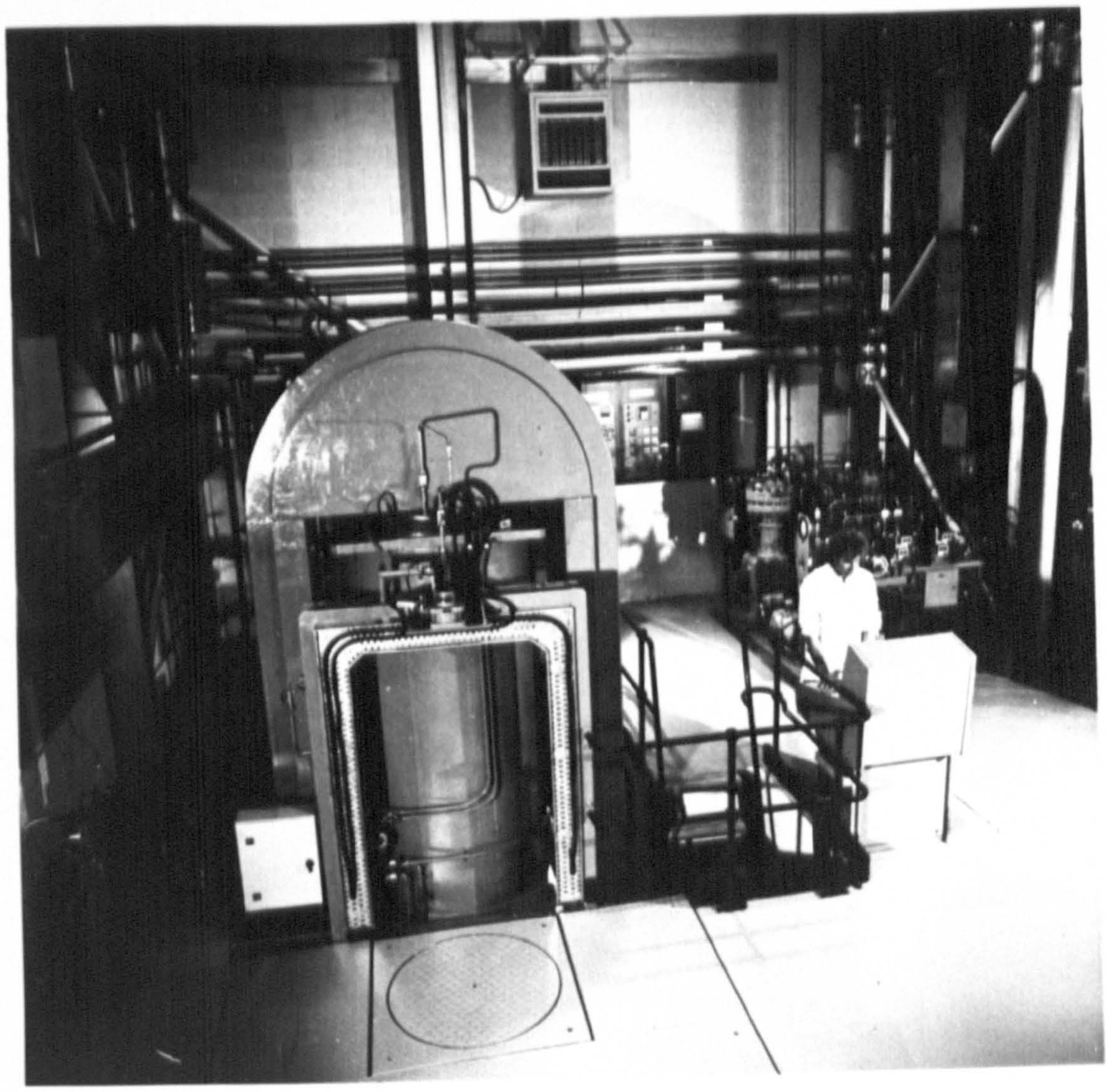

Figure 2.3 a) ASEA Quintus HIP system (Courtesy of HIP Ltd., Chesterfield).
b) Schematic representation of ASEA Quintus system (after reference 83).

b

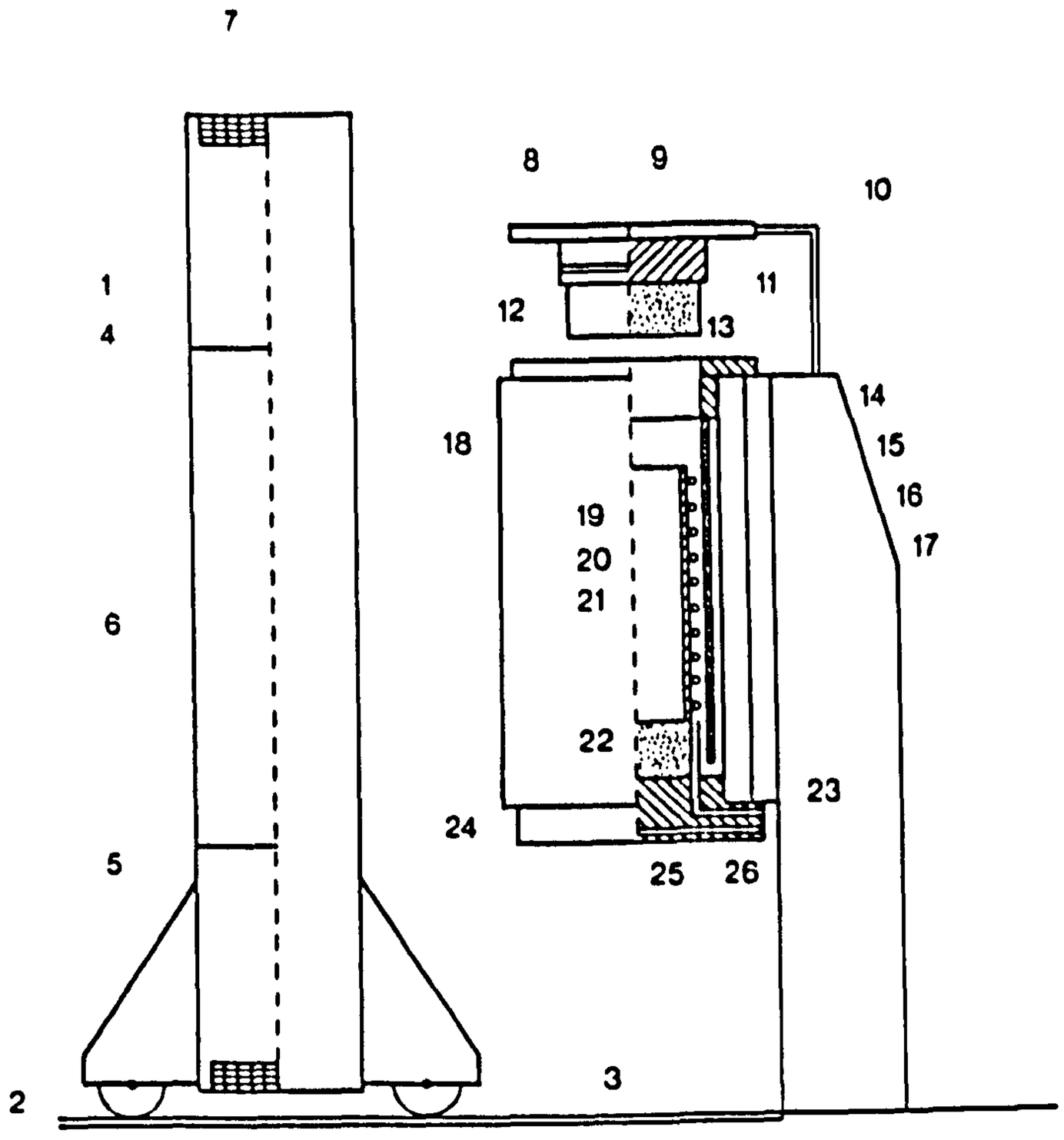

Key

1. Press Stand
2. Support Wheels
3. Support Rails
4. Upper Yoke
5. Lower Yoke
6. Spacers
7. Prestressed Strip Sheath (Yoke Straps)
8. Vessel Top Cover
9. Upper Sealing Ring
10. Pivotable Operating Rod
11. Top Cover Closing Face
12. Top Cover Insulation
13. High-pressure Cylinder Seal
14. High-pressure Cylinder Strip Sheath
15. High-pressure Cylinder Inner Tube
16. Furnace Insulating Sheath
17. High-pressure Vessel Stand
18. High-pressure Vessel
19. Furnace
20. Heating Elements
21. Heating Elements Support
22. Lower Insulating Support
23. Lower Sealing Ring
24. End Closure
25. Gaseous Pressure Inlet
26. Electrical Connecting Channel

material that has been the focus for the present program.

2.3 HOT-ISOSTATIC PRESSING (HIP) OF Si_3N_4

The major fabrication routes for dense silicon nitride, hot-pressing and pressureless sintering, both suffer serious drawbacks when a complex shaped component is required for use at high temperatures (~ 1400°C), and these are summarised in sections 1.3.2 and 1.3.3. The HIP processing of silicon nitride offers many potential advantages, as described by Larker *et al* in 1977, and as such presented itself as a viable economic alternative [100]. The potential benefits summarised by Larker are:

1. Dense silicon nitride can be produced without any additives (using Si_3N_4 powder with ~ 0.6wt.% metal impurities).

2. Fully isotropic properties are observed.

3. A high modulus of rupture is recorded at elevated temperature, together with a consistently high Weibull modulus.

4. Particularly good creep resistance.

Four routes for the HIP densification of silicon nitride have been outlined by Larker [101] and are shown in figure 2.4. Starting with silicon nitride powder, as opposed to free silicon, it can be seen that two alternatives exist;

1. A 'green' state ceramic article is formed and then vacuum encapsulated prior to HIP.

2. Sintering of the 'green' state material to a state of closed porosity, i.e. removing all the surface connecting porosity (typically >93% of theoretical density). The sintered ceramic is then HIPed without encapsulation to a higher density.

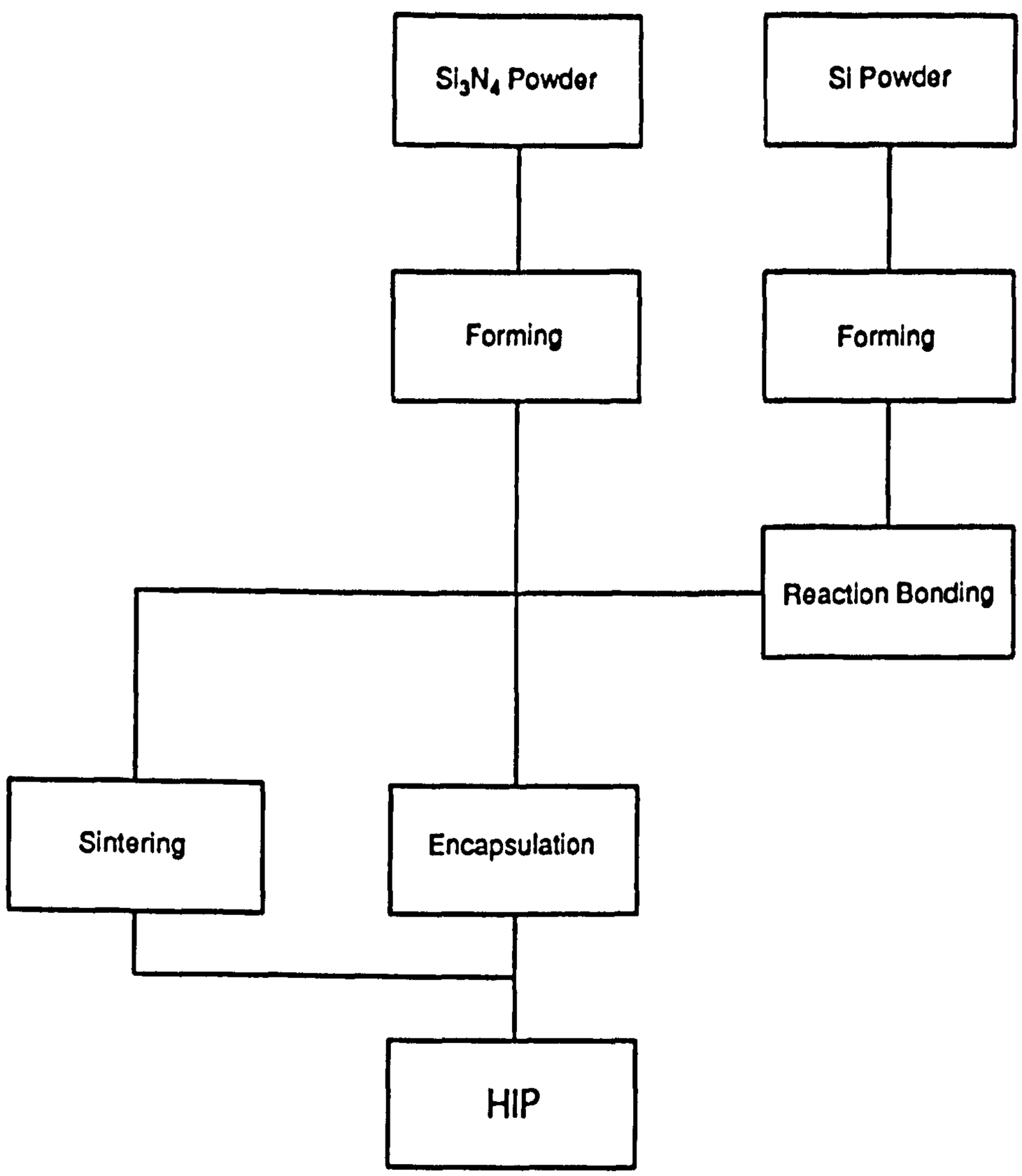

Figure 2.4 Summary of the four principle routes for HIP densification of silicon nitride ceramics (after reference 101).

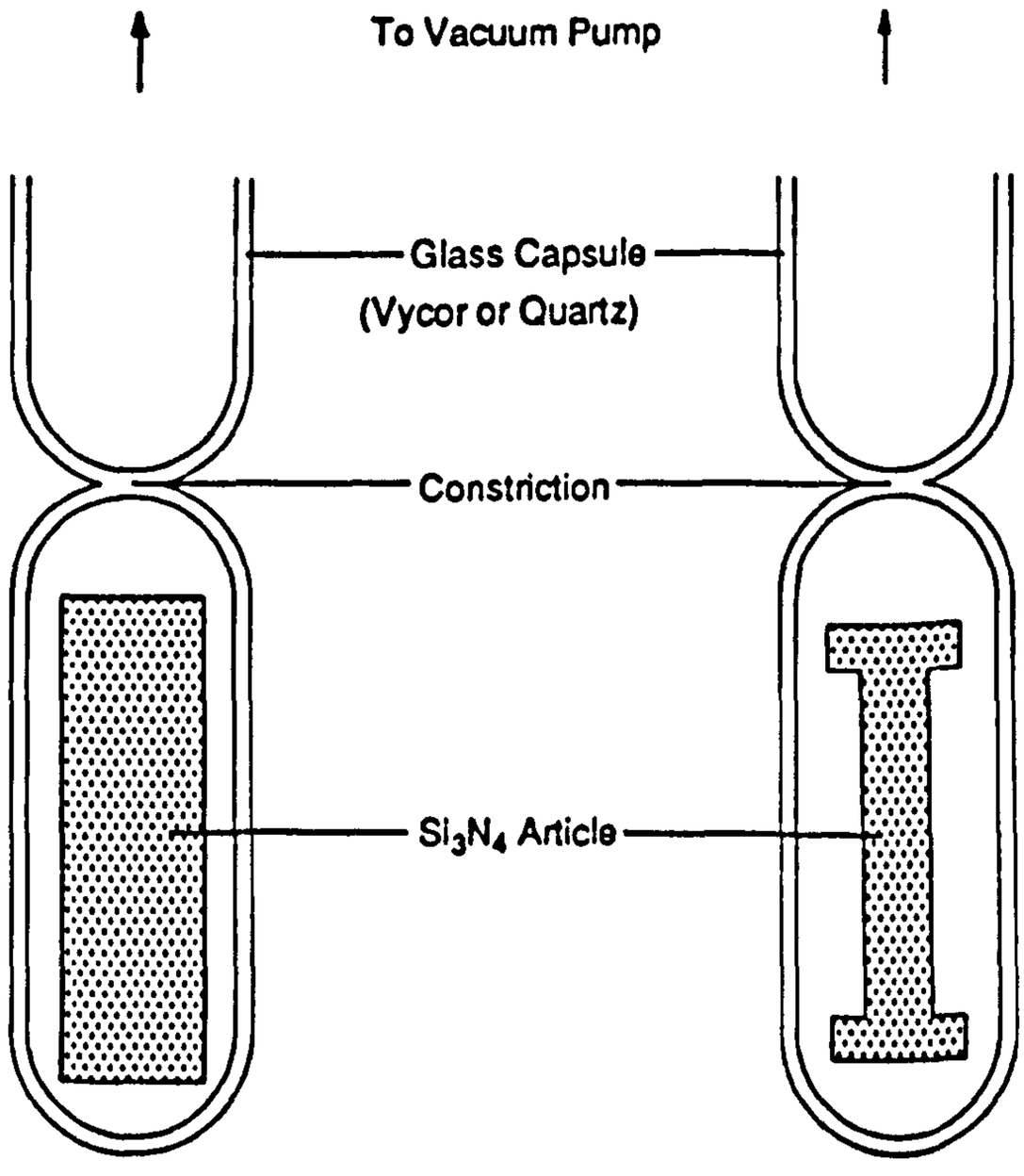

Figure 2.5 ASEA SiO_2 (or Vycor) encapsulation representation.

The silicon starting powder routes are essentially identical to those for silicon nitride, however nitriding (reaction bonding) of the formed silicon body is required prior to encapsulation or sintering.

2.4 GLASS ENCAPSULATION

2.4.1 Simple Tubular Encapsulation

The porous nature of 'green' state ceramic articles (typically 60-65% of theoretical density) requires the use of an impermeable barrier layer that totally envelopes the ceramic during HIP processing. This encapsulant layer prevents penetration of the pressure-transmitting gas into the ceramic article. If gas ingress into the ceramic does occur, for example, from encapsulant failure, the gas pressure acting within the interconnecting porosity of the ceramic will counteract the densification process. Obviously the gas pressure will be highest during the hold period of the HIP cycle.

Initial investigation of the HIP densification of silicon nitride was conducted in Sweden by Adlerborn and Larker of ASEA Aktiebolag [100,102-104]. A preformed body of silicon nitride was placed in an open ended, oversized capsule of SiO_2 or borosilicate glass [102], which is then placed in a conventional furnace at 100°C and evacuated to 0.1 Pa for 8 hours using a vacuum pump attached to the open end of the capsule (fig. 2.5). The capsule was then backflushed with nitrogen to atmospheric pressure and sealed. Following sealing, the capsule is heated in the furnace to 1250°C, at which point the glass softens and becomes deformable, and it is then transferred to the HIP vessel (pre-heated to 1250°C). Temperature and pressure were then ramped up to the hold conditions, a pressure between 200-300 MPa and temperature between 1700-1800°C. These conditions were held for a minimum of two hours. The pressurising gas used was either argon or helium. Density values of greater than 99.5% of theoretical were obtained using additive-free or low weight percent magnesia additions with the silicon nitride powder. Other sintering additives were also investigated, including CeO_2, Ce_2O_3,

BeO, Y_2O_3 and La_2O_3 [100]. After HIPing the encapsulant glass was removed by sandblasting. Commercial silicon nitride, HIPed to full density without additives (typically with ~ 0.6% metal oxide impurities), possessed a high degree of strength retention (~ 55%) over the temperature transition range from RT to 1370°C. However the room temperature modulus of rupture of this material was ~ 75% of that obtained with typical modern two phase Si-Al-O-N type materials, such as LCS 201 (Lucas Cookson Syalon, Solihull), because of the more equiaxed β- grain morphology that results from sintering in the presence of negligible liquid volume (arising only from silicon nitride impurities and surface SiO_2).

The potential of silicon nitride utilising purely Y_2O_3 additions (with ~ 0.3 wt.% metal oxide impurity) was revealed in this early research by Larker [100]. Excellent resistance to steady state creep was observed with a 5 wt.% Y_2O_3 addition. The densification of silicon nitride with varying levels of Y_2O_3 sintering aid is shown in figure 2.6.

This encapsulation method, however, was limited to relatively simple 'turned' glass shapes as the high stress imparted on thin, flat parts by the folding and conforming of the encapsulant glass tended to distort the ceramic pieces during processing.

A further development of this method, allowing the fabrication of more complex shapes, involved packing the silicon nitride article to be HIPed in SiO_2 powder within a borosilicate glass capsule, typically Pyrex [104], represented in figure 2.7. This patent describes the process for encapsulation using a number of different glasses with softening points in the range 500°C to 1300°C (lead silicate through to pure silica). The use of an inner glass powder that softens at a higher temperature than the capsule allows the formation of an intermediate composition/viscosity region between the two glasses. Experimentally Adlerborn found the presence of this layer to be necessary as the Pyrex tends to 'run off' at temperatures in excess of 1000°C and the inner silica powder will not soften until ~ 1250°C. This technique allows greater flexibility than that previously

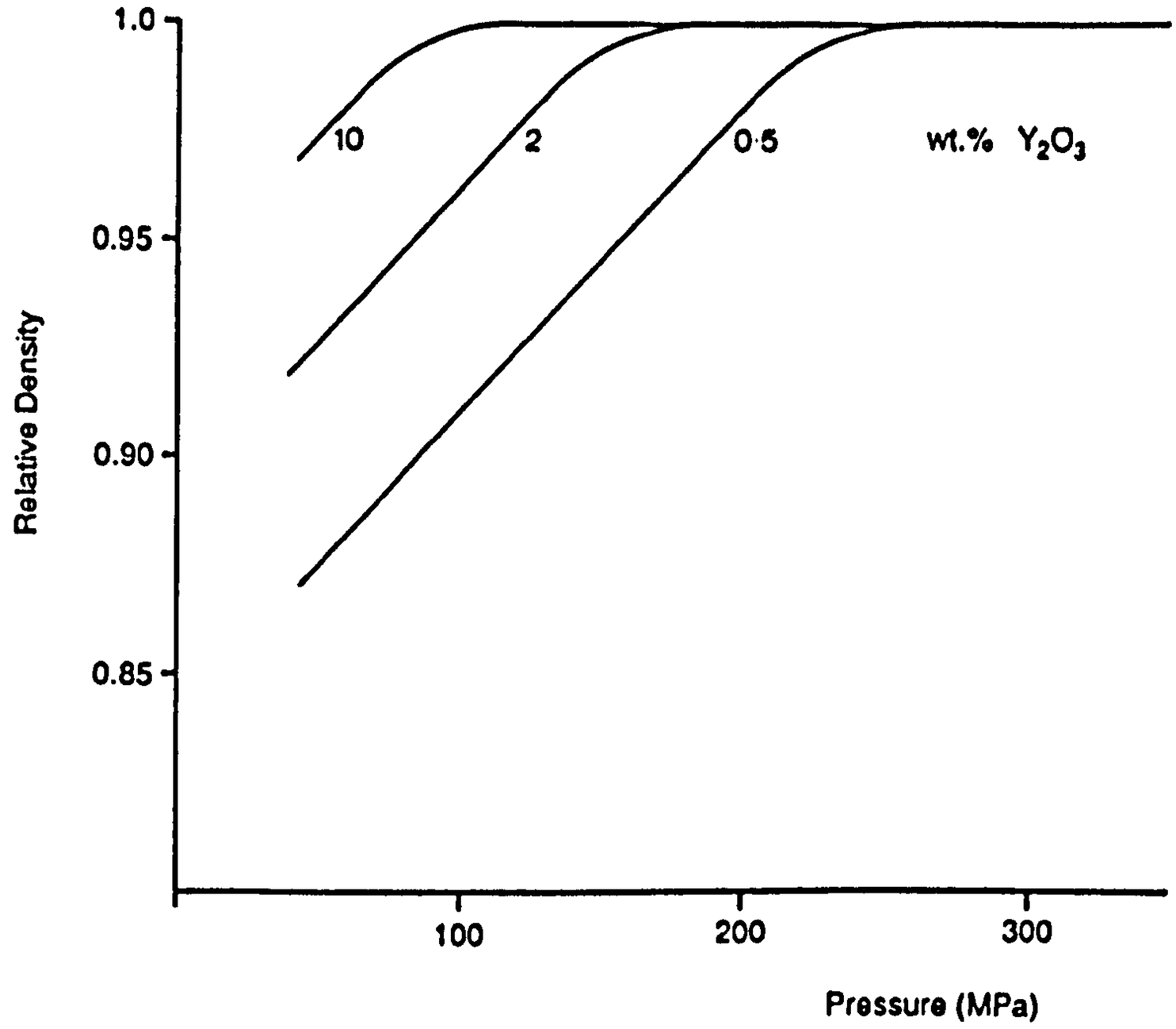

Figure 2.6 The densification behaviour of silicon nitride powder (0.3 wt.% impurity) as a function of Y_2O_3 additive level and applied pressure, with HIPing conducted at 1750°C (after reference 100).

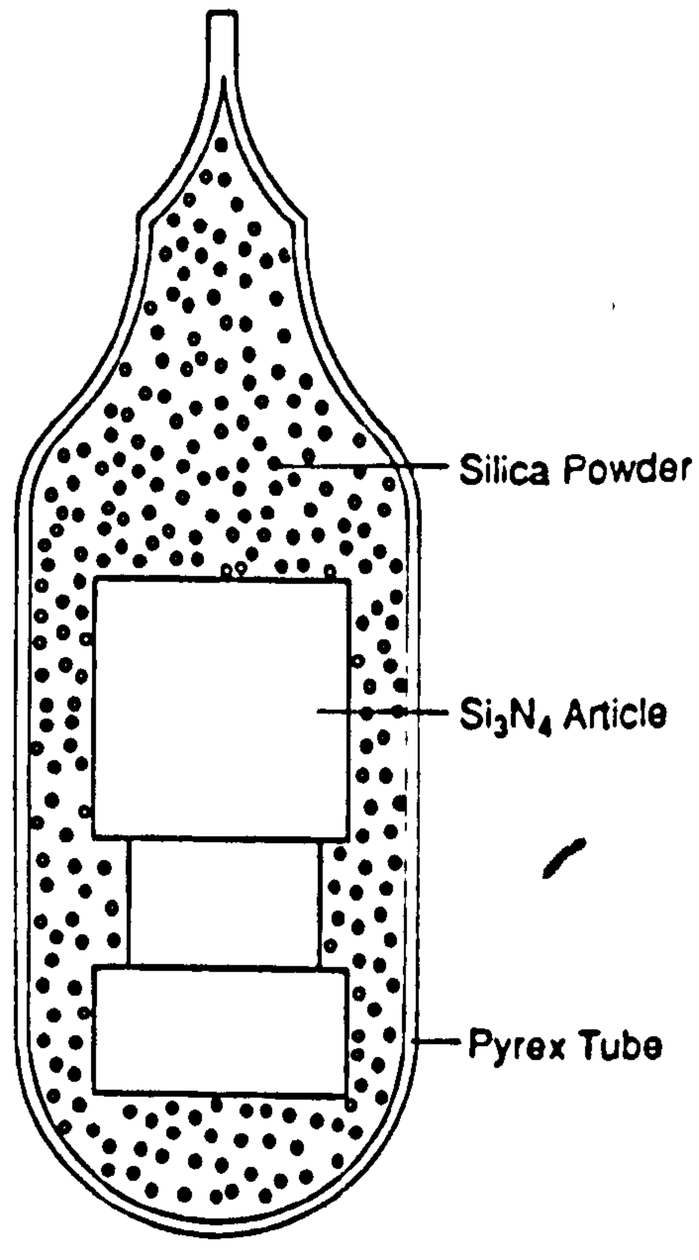

Figure 2.7 Schematic representation of ASEA encapsulated specimen, for relatively complex shapes (after reference 104).

described due to the lower pressure application point during the HIP cycle of ~ 600°C (cf. 1250°C for pure SiO_2) and is also inherently cheaper with respect to encapsulant costs.

In Germany, Heinrich and Bohmer examined the effect of varying the additive level for RBSN encapsulated in SiO_2 tube [106], using MgO or Y_2O_3 additions [71,107]. Full density was achieved when a Y_2O_3 level greater than 0.7 wt.% (0.5 wt.% for MgO) was used. Superior oxidation resistance was demonstrated when compared to hot-pressed materials available at that time [108]. Increasing the Y_2O_3 additive content was found to increase both the fracture strength at room temperature [71] by the formation of a more elongated and interlocking β-Si_3N_4 grain morphology, and the creep resistance at elevated temperature.

Similar densification and microstructural results were obtained by a research team at Osaka, studying SiO_2 encapsulated HIPing of both additive free [109] and metal nitride fluxed silicon nitride [110]. More recently the Osaka research group have used a Pyrex tubular encapsulation technique, investigating the diffusion bonding of sintered alumina and silicon nitride ceramics (producing Si_3N_4-Si_3N_4 and Al_2O_3-Si_3N_4 bonds), with little degradation of hardness across the bond interface [111], and to fabricate high density, additive free silicon nitride [112]. A summary of the HIP conditions and property attainment of the research described in this section is presented in Table 2.1.

Encapsulating Material	HIP conditions Temp (°C)	Pressure (MPa)	Time (hrs)	Properties Density (% TD)	MOR (MPa)	Additives (wt. %)	Reference
High-silica capsule inside borosilicate capsule	1300 –1900	100 –200	2	86-98	–	0.5-3.2 Y_2O_3 or 3.7 YN or 4.0 AlN	[109]
Fused silica	1750	100	1	100	346 (1370) 539 (1225) 665 (RT)	None (low purity) Si_3N_4	[100]
Fused silica	1750	100	1	100	554 (1370)	Y_2O_3	[100]
SRBSN in Vycor tube	1750	207	1	>95	628 (1375) 780 (RT)	3 or 5 or 7 or 9 Y_2O_3	[177]
Fused silica	1750	1–200	1	75-100	200-800 (RT)	0.5-5.0 MgO or 0.7-7.0 Y_2O_3	[107]

Table 2.1 Summary of HIP conditions and material properties attained using glass encapsulated HIP processing

2.4.2 Glass Powder Encapsulation

The desire to fabricate more complex shaped parts, for instance integrated turbine blisks, led to further investigation at ASEA into methods of near-net shape encapsulation via the use of a glass powder. Identical problems are present for glass powder encapsulation as for simple tubular encapsulation with the addition that the encapsulant glass powder must be sintered to form a gas impermeable layer prior to pressure application.

The initial encapsulation development involved the application of two porous layers of powdered glass to the silicon nitride article shown in figure 2.8 [113-115]. The inner coating was transformable (partially by interdiffusion with the outer layer) at a temperature below that required for densification of the silicon nitride, typically using Vycor or a high silica content glass. The outer porous layer was transformable, to a continuous glass envelope, at a temperature below the inner layer. Pyrex or aluminium silicate powdered glass was generally used in this instance. The patent noting this

a

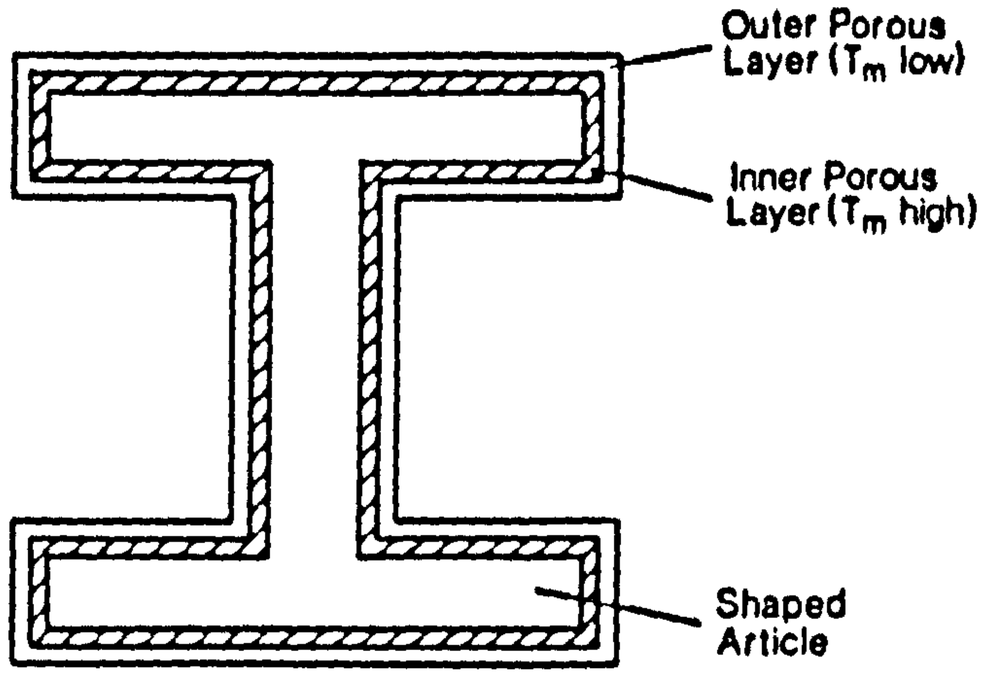

b

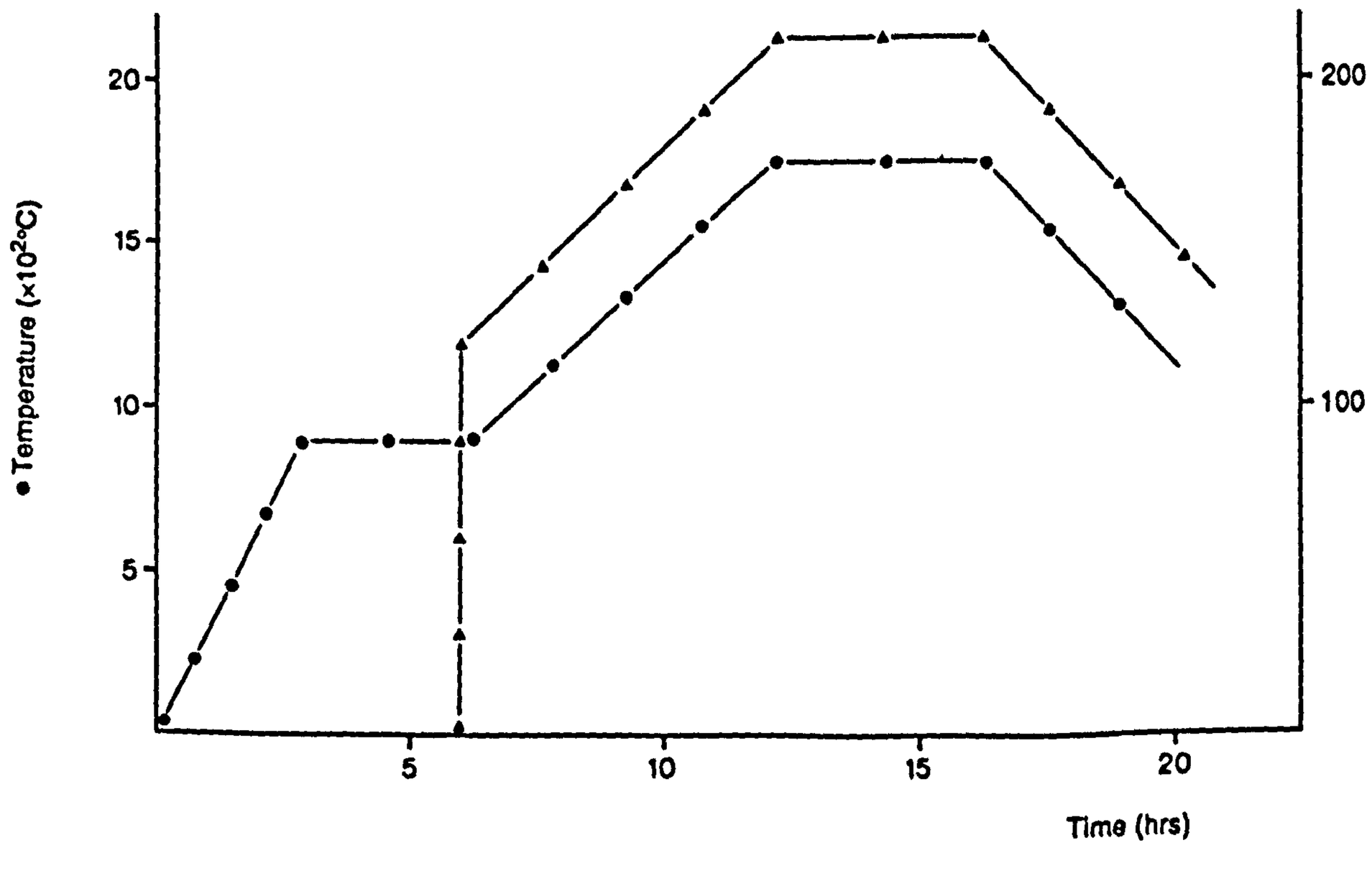

Figure 2.8 a) Representation of ASEA glass powder, dip coated silicon nitride sample where T_{melt} (outer layer) < T_{melt} (inner layer) < $T_{sinter}(Si_3N_4)$ (after reference 113). b) Typical HIP cycle for glass powder encapsulated silicon nitride (after reference 113).

encapsulation method also covers the use of high melting point powdered metals (for example molybdenum or tungsten) for use as an inner encapsulant layer, although it is questionable if this route was of practical use for silicon nitride. Both of the porous glass layers are applied to the ceramic by dip coating in aqueous suspensions of the glass particles, giving layer thicknesses in the range 0.5 - 1 mm, or alternatively by a thermal spraying technique.

After coating, the ceramic articles were outgassed at room temperature within the HIP system, for a period determined by the sample volume. The temperature is then increased, with continued evacuation, to fully melt the outer porous layer. This route allows the development of an intermediate viscosity encapsulant glass whilst maintaining a layer impervious to the gas pressure medium. Initial gas pressure application was performed after the transformation of the outer layer, which lies within the range 600 - 1100°C (depending on the glass composition) with the inner layer being transformed within the range 1300 - 1600°C. Hot-isostatic pressing would then be conducted using helium or argon with an applied pressure greater than 100 MPa (generally between 200 - 300 MPa) and at a temperature above 1600°C (but less than 1900°C) for either pure silicon nitride or silicon nitride mixed with a sintering aid. After the HIP cycle is completed the encapsulant glass is removed by sand blasting.

Metallic and ceramic materials have been processed using this technique, with the choice of encapsulant glass compositions being dependent on the predicted HIP temperature.

A questionable extension of this process [116] described the removal of the encapsulant glass at the HIP temperature (after sintering) by reducing the applied pressure to approximately 0.001 MPa, thus allowing partial dissociation of the densified silicon nitride article and the subsequent formation of nitrogen gas which forced the glass away from the ceramic surface (allowing easy removal after cooling). However it is probable that this method of decapsulation would ultimately produce silicon nitride with a finite free - Si residue and entrapped nitrogen bubbles within the intergranular glass.

A simplification of the glass powder coating encapsulation route has been described in a series of ASEA patents and publications [117-124], where the encapsulant is formed from a glass powder bed (or frit). The article to be HIPed is situated in the glass powder, within a shaped crucible (typically graphite) as shown in figure 2.9. A barrier layer of boron nitride is used between the glass and the crucible to facilitate easy removal and prevent any reaction occurring (ie. graphite oxidation/erosion by the oxide encapsulant).

A range of boron containing glasses were specified, ranging from 2 to 70 weight percent B_2O_3, including Pyrex with a coefficient of thermal expansion approximately equal to that of silicon nitride over the temperature range 20 - 500°C. It is desirable that the glass particles are transformed to a viscous melt at a relatively low temperature (ideally ~ 1100°C) to prevent dissociation of silicon nitride. The encapsulant melting is conducted under vacuum. Alternatively a low nitrogen gas pressure may be utilised (at a pressure greater than the partial pressure of nitrogen in Si_3N_4 at this temperature) allowing the use of a higher melting temperature glass such as Vycor. Full pressure is applied, in both instances, when the melted gas has a suitably high viscosity (a maximum of 10^6 poises). After this point the HIP cycle can be conducted as previously described.

Where a high B_2O_3 content is used for encapsulation, greater than 50 weight percent, it was presumed that a boron nitride barrier layer is formed on the ceramic surface via an *in situ* reaction between B_2O_3 and Si_3N_4 at approximately 1000°C. The boron nitride layer was believed to prevent penetration of the low viscosity glass into the silicon nitride surface porosity at elevated temperatures.

After HIPing, when using a high B_2O_3 containing glass, the encapsulant glass could be removed by hot water or steam, by hydrolysis of B_2O_3. Alternatively, when using a high melting point glass the HIPed ceramic was hot transferred to a high temperature furnace and heated to ~ 1800°C, the glass then gradually ran off the ceramic under the effect of gravity.

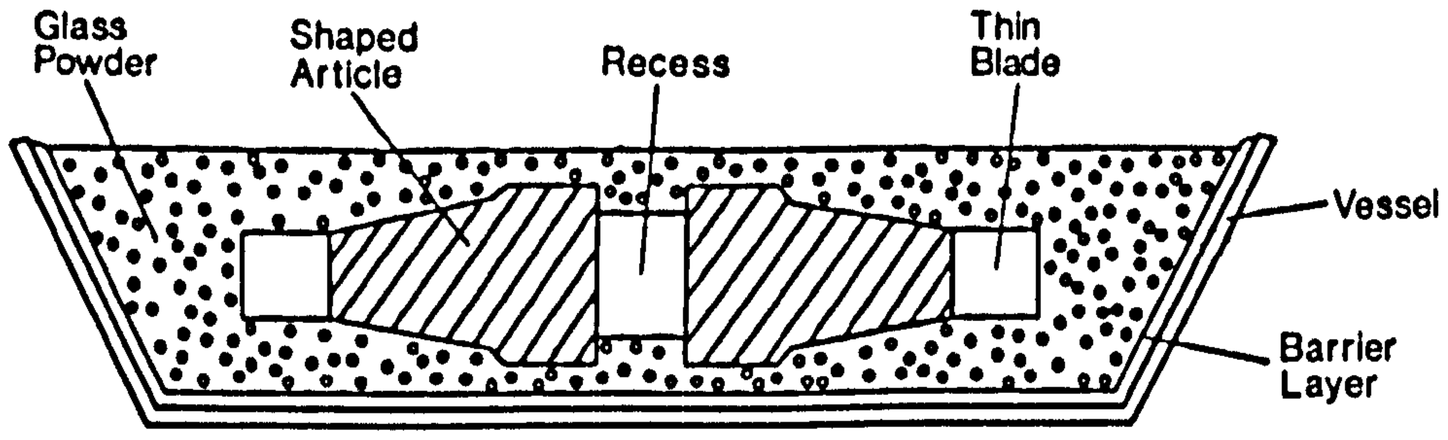

Figure 2.9 Schematic diagram of ASEA glass powder bed encapsulated silicon nitride. Melting of the glass powder occurs prior to gas pressure application (after reference 117).

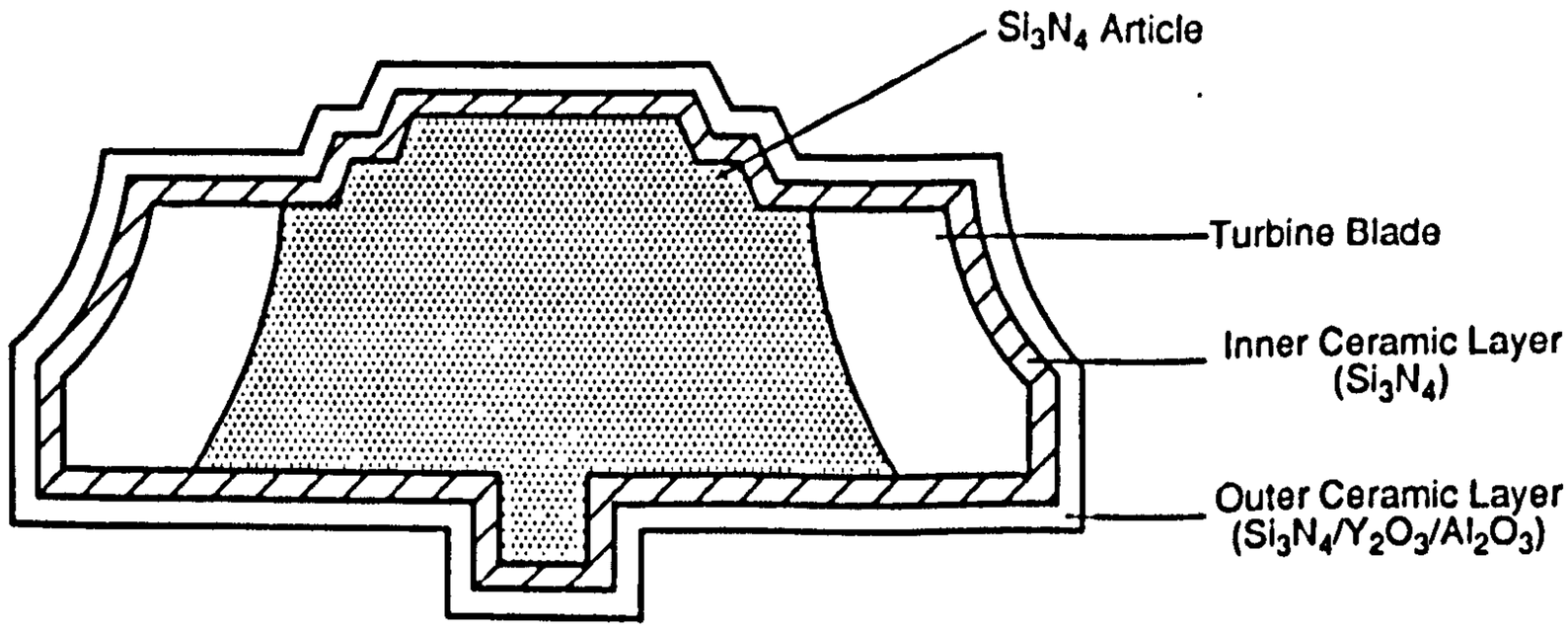

Figure 2.10 Schematic representation of complex shaped encapsulated silicon nitride, utilising a sintered silicon nitride encapsulation layer (after reference 125).

A silicon nitride based encapsulant for HIPing of complex-shaped silicon nitride articles (with 0-4 wt.% Y_2O_3) has been described by Heinrich and Bohmer [125]. The encapsulant was applied in two layers by dip-coating in silicon nitride suspensions (fig. 2.10). Initially the shaped article, typically an individual gas turbine blade, is sintered in a nitrogen atmosphere at 1700-2000°C for 10 minutes. The sintered blade (~80% TD) is then immersed in a 50 wt.% Si_3N_4/50 wt.% iso-propanol suspension and dried to remove the solvent. A layer thickness of approximately 1 mm is applied by this route. A second layer is then applied via a similar route. The powdered content of the second layer comprises 80 wt.% Si_3N_4, 15 wt.% Y_2O_3 and 5 wt.% Al_2O_3. After drying, the coated blade was sintered in N_2 at 1820°C for 10 minutes, producing an outer impermeable coating. The article is then HIPed in argon at 1750°C and ~200 MPa. The capsule is removed by sandblasting.

Recently the patented ASEA process has been utilised to densify a range of silicon nitride based ceramics, using Y_2O_3 or Nd_2O_3 sintering additives, with a high retention of strength (~450 MPa at 1400°C) and excellent resistance to oxidation at 1450°C [76,126]. To maintain a compositional balance, within the compatibility triangle, concurrent additions of SiO_2 were made to increasing Y_2O_3 or Nd_2O_3 levels, thus allowing devitrification of the glassy second phase to $Y_2Si_2O_7$. It was noticed that increasing the Y_2O_3 or Nd_2O_3 content improved the room temperature fracture toughness, primarily because of the greater β-Si_3N_4 aspect ratio, enhancing K_{IC} by the mechanism described in section 1.5.3. In Sweden Ekstrom and co-workers have HIPed various mono-phase Si-Al-O-N ceramics to near theoretical density. Si-Al-O-N materials with a substitution level (z) varying from 0.25-4.5 were produced using Y_2O_3 or Nd_2O_3 additions [127-130].

The flexibility associated with glass-encapsulated HIP has allowed the fabrication of dense silicon nitride composites utilizing either silicon carbide or silicon nitride whisker reinforcement [131-135]. Generally a small additive volume is used, either Y_2O_3 or Y_2O_3 and Al_2O_3, however some authors have reported the HIP densification of additive-

free composites at temperatures of ~1900°C [133,134].

The HIP densification behaviour of high purity silicon nitride without additives has been examined by several workers [136-140]. Full densification only arises with a processing temperature in excess of 1900°C, with a pressure of greater than 180 MPa [138-140]. The microstructure of these HIPed ceramics consists principally of equiaxed β-Si_3N_4, although small amounts of Si_2N_2O were reported by Nezuka *et al* [138]. High-resolution transmission electron microscopy of additive-free silicon nitride monolithic and composite materials has demonstrated the presence of a small volume residual amorphous phase at grain boundary triple junctions [134,138]. A similar amorphous residue has been observed at the grain boundaries of HIPed silicon nitride with a crystalline $Y_2Si_2O_7$ matrix phase, illustrated in figure 2.11 [126]. The residue viscosity in composite ceramics densified without additives is likely to be lower than the monolithic equivalents as the current generation of SiC and β-Si_3N_4 whiskers have a high impurity level relative to the 'matrix' α-Si_3N_4 powder. This behaviour may lead to enhanced transformation kinetics for whisker loaded materials (when compared to additive-free monoliths).

Glass powder bed encapsulation has been shown to be suitable for the mass production of densified ceramics, with a maximum processing capacity of over 26 000 components in one HIP cycle [124].

Further to the current patents covering the ASEA glass powder encapsulation process, a boron nitride multilayer coating has been developed, and patented, to prevent or minimise interaction between the ceramic and encapsulant [141]. An initial boron nitride layer is applied to the green ceramic article by spraying on an acetone-based slurry. The applied layer thickness is approximately 200 μm. A second layer is then applied, composed of boron nitride and a glass viscosity modifier (normally silicon nitride/carbide). Further repeated layers are then applied if required. Articles are then

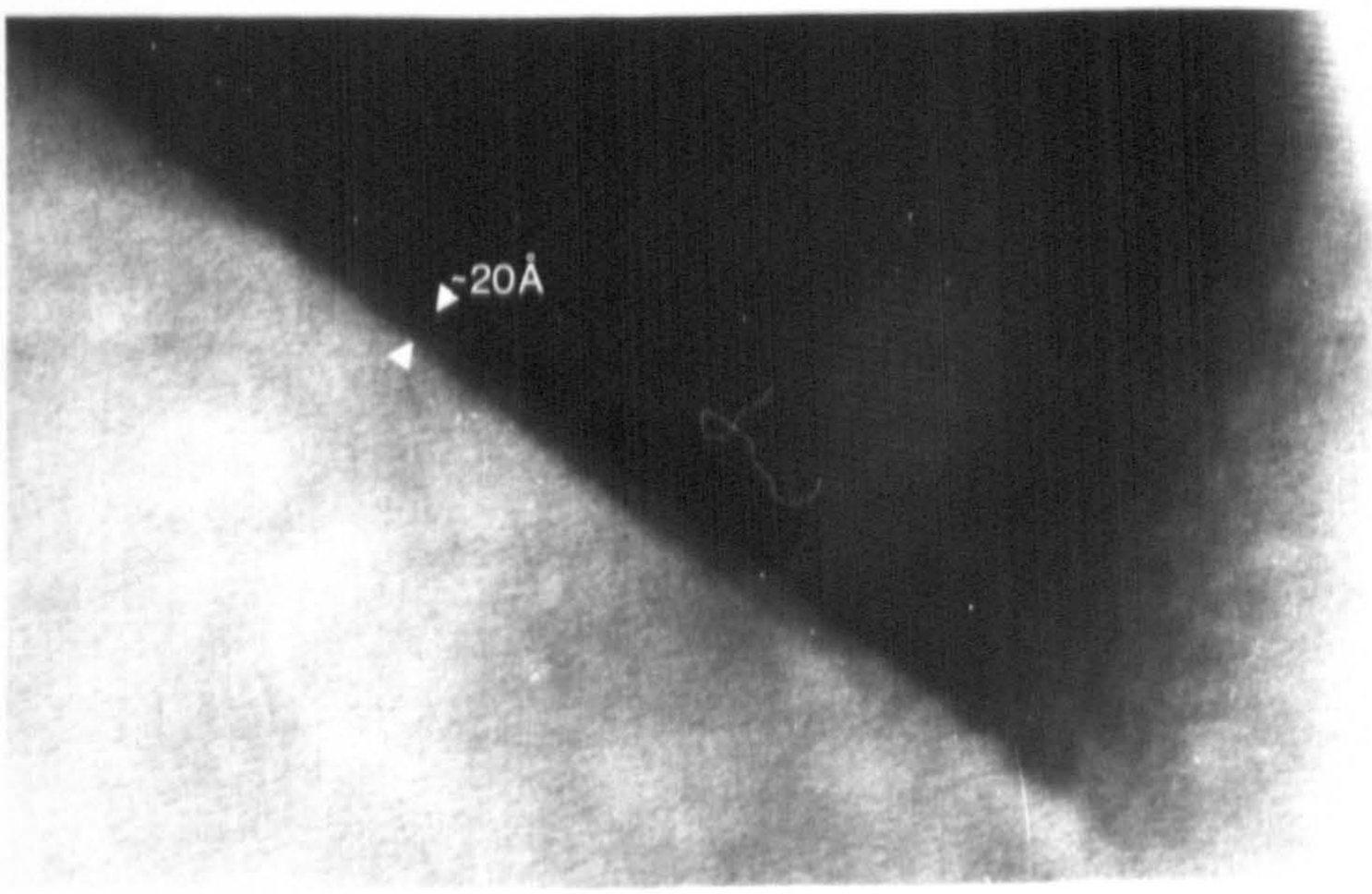

Figure 2.11 High Resolution Transmission Electron Micrograph of amorphous residue present at grain boundaries in HIPed silicon nitride (Courtesy Dr G. Leng-Ward).

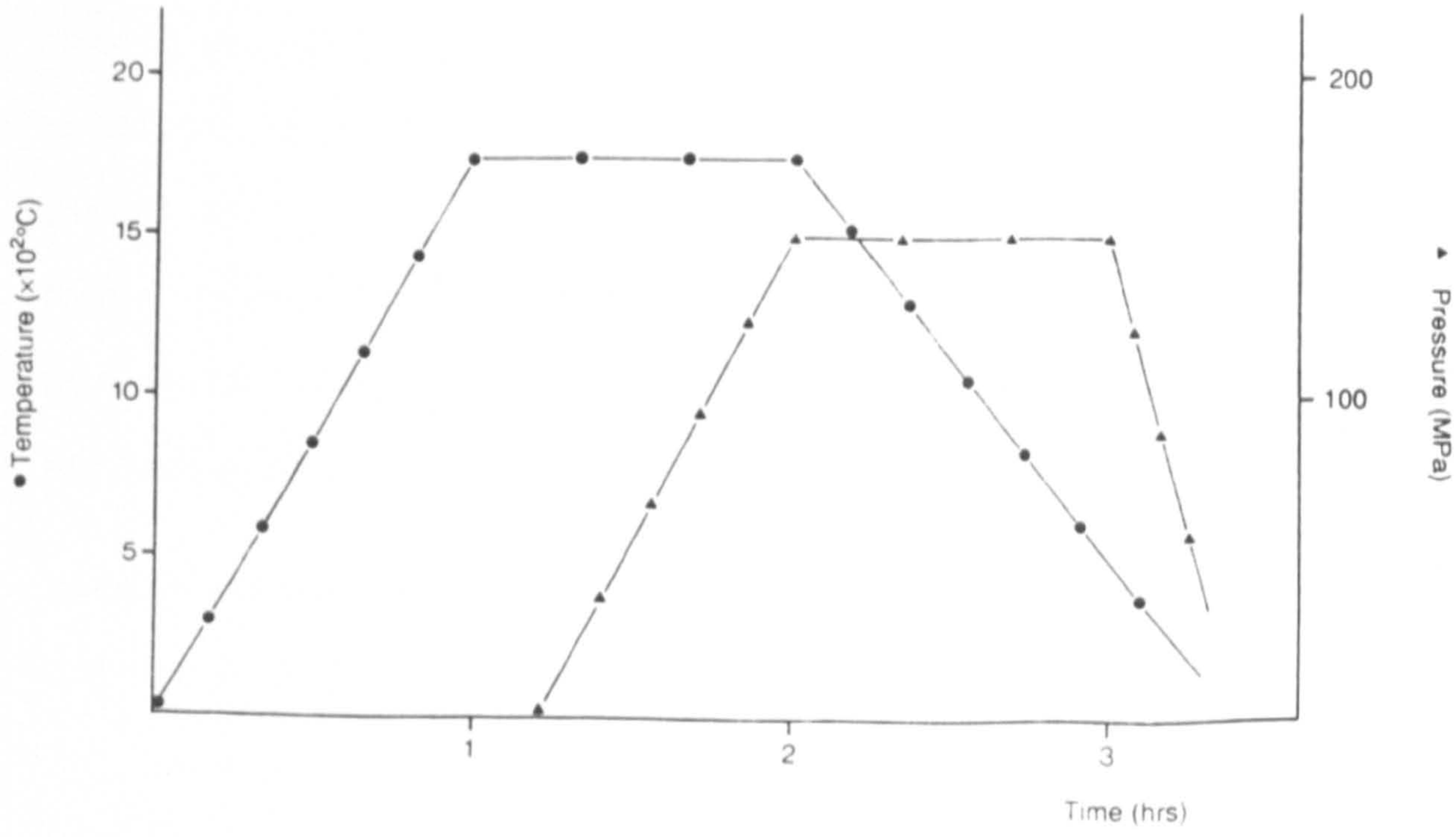

Figure 2.12 Typical temperature/pressure cycle used during the sinter-HIP densification of silicon nitride (after reference 152).

encapsulated in a glass powder bed and HIPed as previously described. This patent describes the problems occurring with the standard boron nitride-type barrier layer which generally does not completely prevent penetration of the encapsulant glass through to the ceramic because of a certain retained porosity within the layer. The potential encapsulant/ceramic interaction and any possible effect on the ultimate densified material properties has not yet been discussed by other investigators, and thus forms part of the focus of the current work.

2.5 REFRACTORY METAL ENCAPSULATION

Currently the only investigated alternative encapsulation route to those previously described involves vacuum welding a refractory metal cannister around the shaped 'green' state ceramic material. Typical metals used include tantalum [142-145] and molybdenum [21], both melt at a temperature greater than 2700°C. Molybdenum 'canning' was used for the encapsulation and subsequent HIPing of relatively low purity commercial silicon nitride powder without sintering aids [21]. Compaction was performed using both hydraulic (up to 1300°C) and gas HIPing. High densities > 95% of theoretical were obtained without additives, and the α - β transformation was reported to occur as low as 1150°C. Near theoretical density silicon nitride was obtained when a Y_2O_3 additive level of 5 wt.% was used (however high impurity levels of Al, Fe, C and 'free' Si were present in the starting powder), and the samples were HIPed for one hour at 200 MPa and 1725°C [142]. The HIPed materials possessed a high percentage flexural strength retention, and minimal fracture toughness variation when examined at 1400°C relative to hot-pressed silicon nitride (with Y_2O_3 or $BeSiN_2$) under investigation at that time. Further study of the HIPed 5 wt.% Y_2O_3 based ceramic revealed a considerable improvement in compressive creep resistance to the hot-pressed materials [143].

Although complex shaped metallic cannisters have been produced, the encapsulation costs are high relative to glass encapsulation, particularly with respect to the raw

materials involved. Further limitations of this technique include the flexibility regarding net shape applications and the reliability (leaking) of the sealed cannisters during HIPing. A summary of the HIP processing conditions and material properties obtained after metal canning are given in Table 2.2.

Encapsulating Material	HIP conditions Temp (°C)	Pressure (MPa)	Time (hrs)	Properties Density (% TD)	MOR (MPa)	Additives (wt. %)	Reference
Molybdenum	1550-1620 1760	140 275	1 1	80 89-95		None (low-purity Si_3N_4)	[21]
Tantalum	1725	200	1	99	449 (1400) 636 (RT)	5 Y_2O_3	[142,143]
Tantalum	1800	90	1¾	95		10 Y_2O_3	[144]

Table 2.2 Summary of metal canning encapsulation conditions and properties

2.6 SINTER-HIP

For successful densification of 'green' state ceramics it has been shown that a gas-impermeable barrier is required. However, an alternative to this technique, as outlined by Larker [100], involves HIPing a pre-sintered ceramic. A major requirement of this route, which removes the intermediate encapsulation stage, is that a state of closed porosity must be obtained after the pre-sintering stage to attain near-theoretical density after HIPing. To date, little has been published on the capsule-free HIPing of silicon nitride. Initial investigation in Japan revealed that density increases occurred only when the sintered density was greater than 93% theoretical and that higher densities and strengths were obtained with nitrogen as the pressurising gas (relative to argon) [176]. Argon HIPing produced near surface porosity formation, probably from silicon nitride dissociation.

A thorough examination of the pre-sinter/HIP route has been conducted by Ziegler and Wotting [146,147]. After HIPing, little noticeable rearrangement of β-Si_3N_4 grains was

observed, although grain coarsening was detected, generally producing a degradation in strength. This effect was most obvious in microstructurally anisotropic samples, fabricated by uniaxial hot-pressing followed by HIP, except when a high residual α-Si_3N_4 content is present after hot-pressing as the α-Si_3N_4 is subsequently isotropically precipitated during HIP [147]. The overall increase in strength, arising from an increase in density, was thus found to be limited, although generally the Weibull modulus and fracture toughness were improved.

Nitrogen dissolution, presumably in the intergranular phase, in sintered silicon nitride subjected to capsule-free HIP was observed by Hirota *et al* [148]. A nitrogen increase of up to 0.6 wt.% occurred near the sample surface after a 14 hour HIP run. Subsequent high temperature heat treatment evolved pores in the HIPed samples via nitrogen evolution. A similar effect often occurs upon heat treatment of high nitrogen content oxynitride glasses [149].

Recent investigation of the sinter/HIP route has included the fabrication and testing of silicon nitride cutting inserts [150], possessing superior toughness and inferior wear resistance to Al_2O_3 composite tools, and the role played by the powder bed during capsule-free HIPing [151]. In Spain, Castro and co-workers have sinter-HIPed silicon nitride, with mixed Y_2O_3/Al_2O_3 additions, to near-theoretical density (> 98% TD) [152,153]. Higher densities were obtained when using a nitrogen pressure medium relative to argon. A typical sinter-HIP temperature/pressure cycle is shown in figure 2.12.

2.7 THE DENSIFICATION AND DIMENSIONAL STABILITY OF MATERIALS FABRICATED VIA HIP: THEORETICAL ASPECTS

The densification behaviour of ceramics during HIPing is very complex as several mechanisms assist consolidation [154]. The external applied gas pressure is transmitted throughout the ceramic body via contact forces between particles which, after an initial

elastic deformation, lead to rearrangement and an overall increase in the packing density. As the contact pressure increases, plastic deformation and fracture occurs creating area contacts between some particles. Eventually further particle yielding does not arise, and densification will only continue through time-dependent diffusive/creep processes. Generally the later stage densification mechanisms are slow, however with silicon nitride an additional mechanism contributing to densification arises, liquid phase sintering, which promotes consolidation via the dissolution of α-Si_3N_4 in a transient liquid phase followed by reprecipitation as β-Si_3N_4.

Each densification mechanism also shows a differing dependence on both the material and processing parameters (ie. grain size, HIP temperature and pressure etc.) [155]. Generally the densification rate is increased most efficiently by using a finer grain size allied with an increased processing temperature, however care is required to avoid unwanted secondary reactions occurring in some ceramic systems at elevated temperatures.

Although the qualitative effect of the densification and dimensional stability of green state ceramic materials, HIPed to full density, has been examined to a moderate extent [122], the theoretical aspects have been relatively ignored. Larker has derived an expression relating the contact force per unit area for adjoining particles to the external applied pressure [123]. The model is simplified by the choice of identical spheres in a dense, randomly packed formation. The effective pressure acting at a point of particle can be determined (surface tension is included as the additional driving force) by relating the total surface contact area of one particle to the average contact force arising from the external applied pressure P_{gas}. Larker showed that the effective particle contact pressure during the initial stages of consolidation (ie. the relative density $D < 0.9$) can be expressed as:

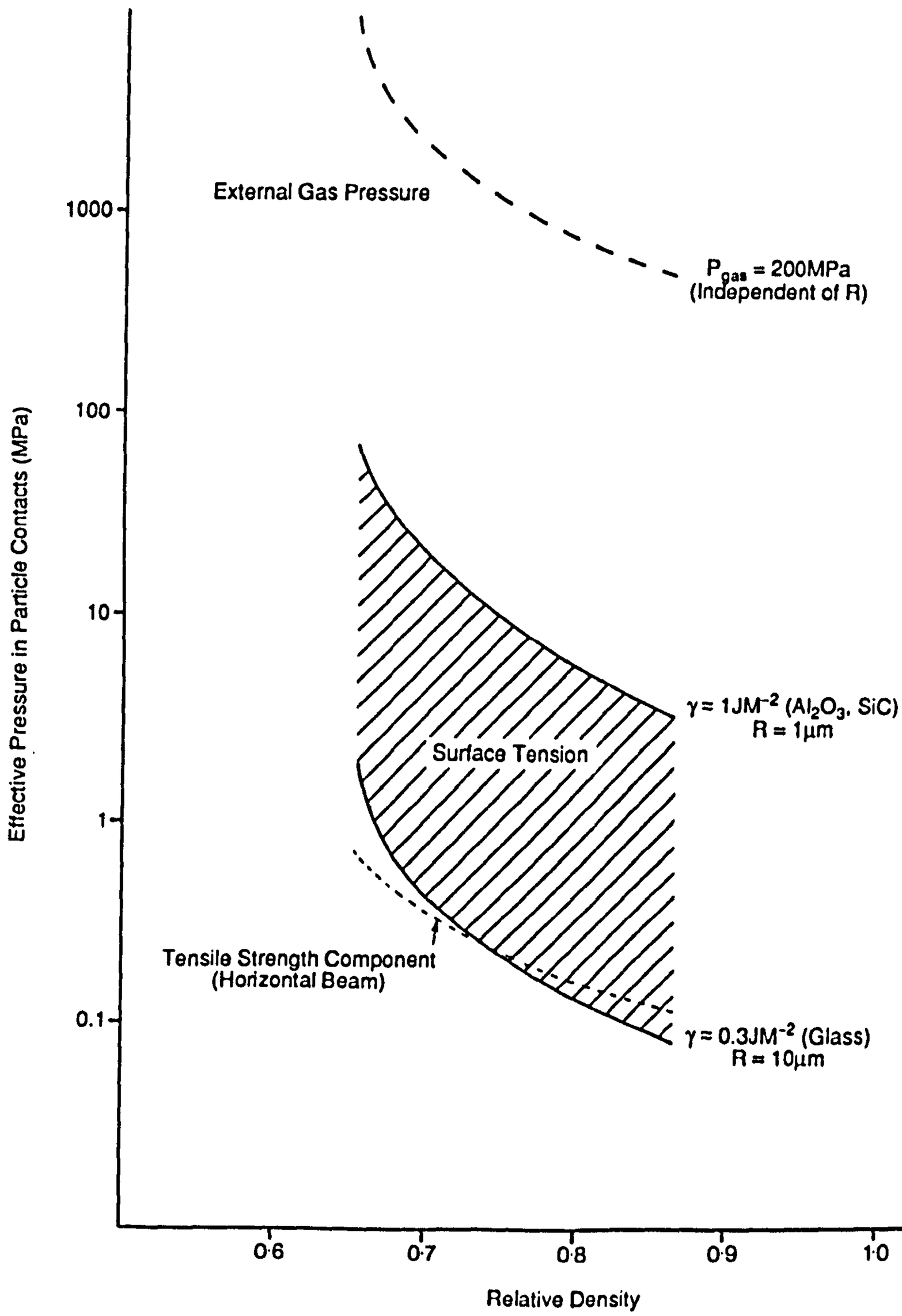

Figure 2.13 Representation of the densification driving force (effective particle contact pressure) arising from external gas pressure and surface tension. An example of the tensile stress component in a horizontal beam of Si_3N_4, to simulate a turbine blade (beam of height 5mm and length to height ratio 10), is also shown (after reference 123).

$$P = \frac{\gamma\,(2-3(D-D_o)^{1/3})}{R(D-D_o)} + \frac{\pi\,P_{gas}}{4(D-D_o)\,[10(D-D_o)+1]} \qquad (2.1)$$

where γ is the surface energy, R the initial particle radius and D_o the initial relative density.

The first part of equation 2.1 represents the surface tension component (applicable to any sintering process), whilst the second describes the influence of the external applied pressure. It can be seen that the only variable in equation 2.1 is the relative density (D) and hence it is possible to analyse the relative importance of both components on the densification driving force (particle contact pressure). A series of curves can thus be produced for specific processing conditions relating the relative density (D) to the effective particle contact pressure (P), shown in figure 2.13 [123]. Typical values of HIP gas pressure (100-200 MPa) and surface tension (1 Jm^{-2} for glass) are used in this analysis. The lower surface tension value is assumed for silicon nitride with a glassy second phase. Elementary tensile stress analysis of a horizontal beam (employed as a model of a turbine blade attached to a hub), of length l and height h, allowed the tensile stress due to gravity to be calculated by Larker using:

$$\sigma_{max} = \frac{3\,g_o\,\rho_b\,l^2}{h} \qquad (2.2)$$

where ρ_b is the beam density and g_o the normal acceleration (9.81 ms^{-2}). Figure 2.13 reveals that, for specific beam dimensions, the tensile stress curve position is comparable to the lowest values of the surface tension component of equation 2.1. Therefore in the absence of an applied external pressure (eg. for pressureless sintering) sagging of the beam is likely. However, with the addition of an external HIP pressure, the risk of sagging is effectively removed by the considerably higher stress induced by the isostatically applied gas.

Another factor affecting the dimensional stability of HIPed ceramics is the presence of a thermal gradient within the powder body during densification, arising from the poor

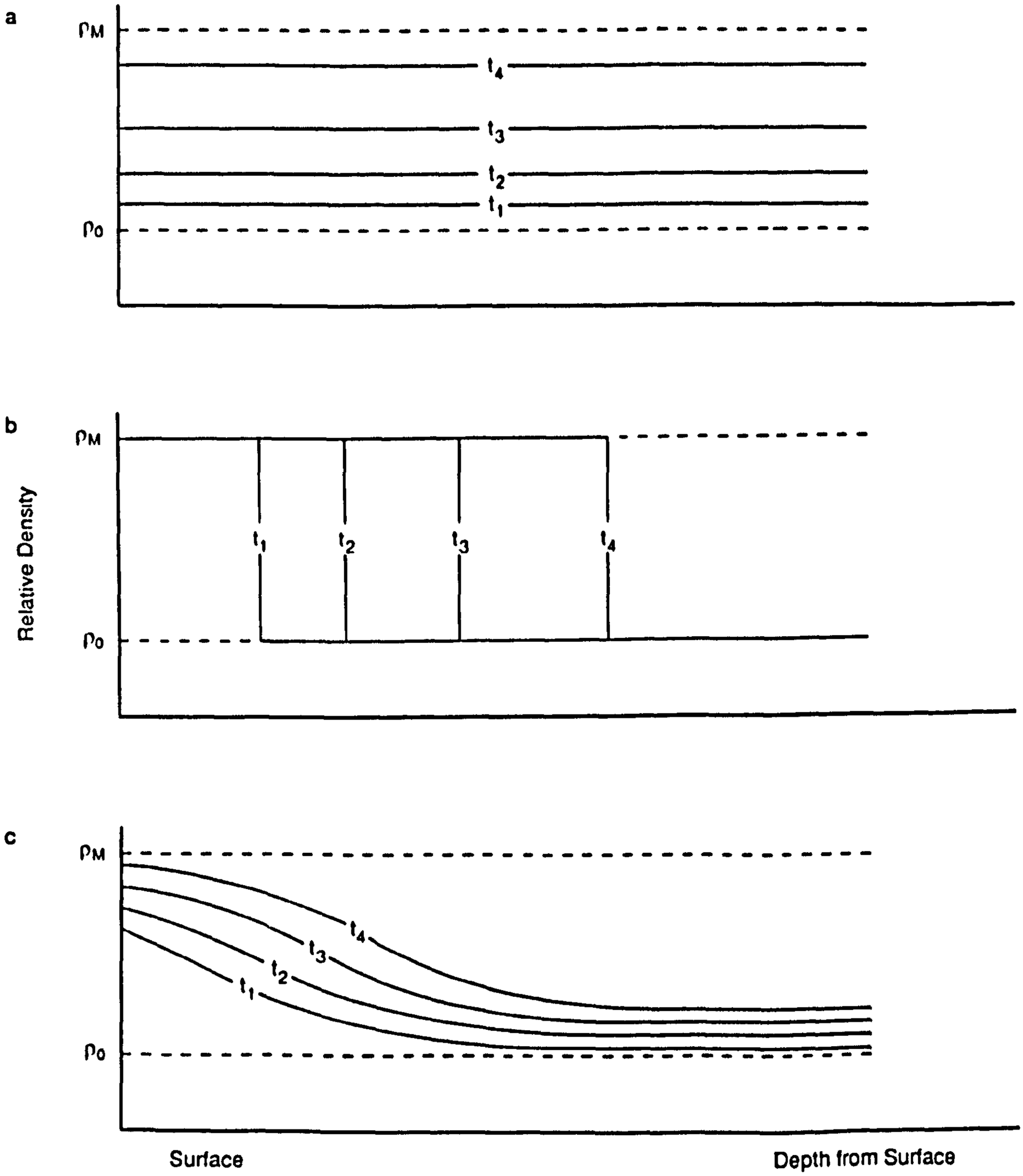

Figure 2.14 Typical series of curves demonstrating the relationship between HIPed density distribution and distance from specimen surface (where time $t_1<t_2<t_3<t_4$), for a) homogeneous densification, b) an extremely sharp densification front, and c) a typical, experimentally observed densification front.

thermal conduction of finely milled ceramic powders [154]. Li *et al* have shown that the density of a HIPed material can vary as a function of time, depending upon the depth from the specimen surface [156].

Typical density-distance profiles for powder consolidation in the presence of a 'densification front' are shown in figure 2.14, together with comparable profiles arising from homogeneous densification [156]. Small localised pressure variations through the body are also likely to be present, although the effect is thought to be less influential on densification [157]. Aren and Navara presented several models describing the shape changes that arise during HIPing of geometrical powder compacts following two limiting mechanisms [157,158]:

1. Homogeneous densification, with a uniform temperature throughout the powder body.

2. The formation of a sharp densification front at the specimen surface, assuming that heat transfer from the surface to the bulk is highly dependent on the material density such that

$$\lambda_{HD} \gg \lambda_{LD}$$

where λ_{HD} and λ_{LD} represent the high and low density heat transfer coefficient respectively.

The final densification product of a theoretical one dimensional wall will ultimately be identical for both mechanisms (fig. 2.15). The case for a two dimensional body is more complicated (fig. 2.16a). The densification front will move into the bulk perpendicular to the surface so that, at the centre of an edge, a densified region similar to figure 2.15a will be observed. However, at the corner, two fronts will converge (at an identical angle to the original corner) as shown in figure 2.16b. It can be seen that the initial and final corner areas are related by

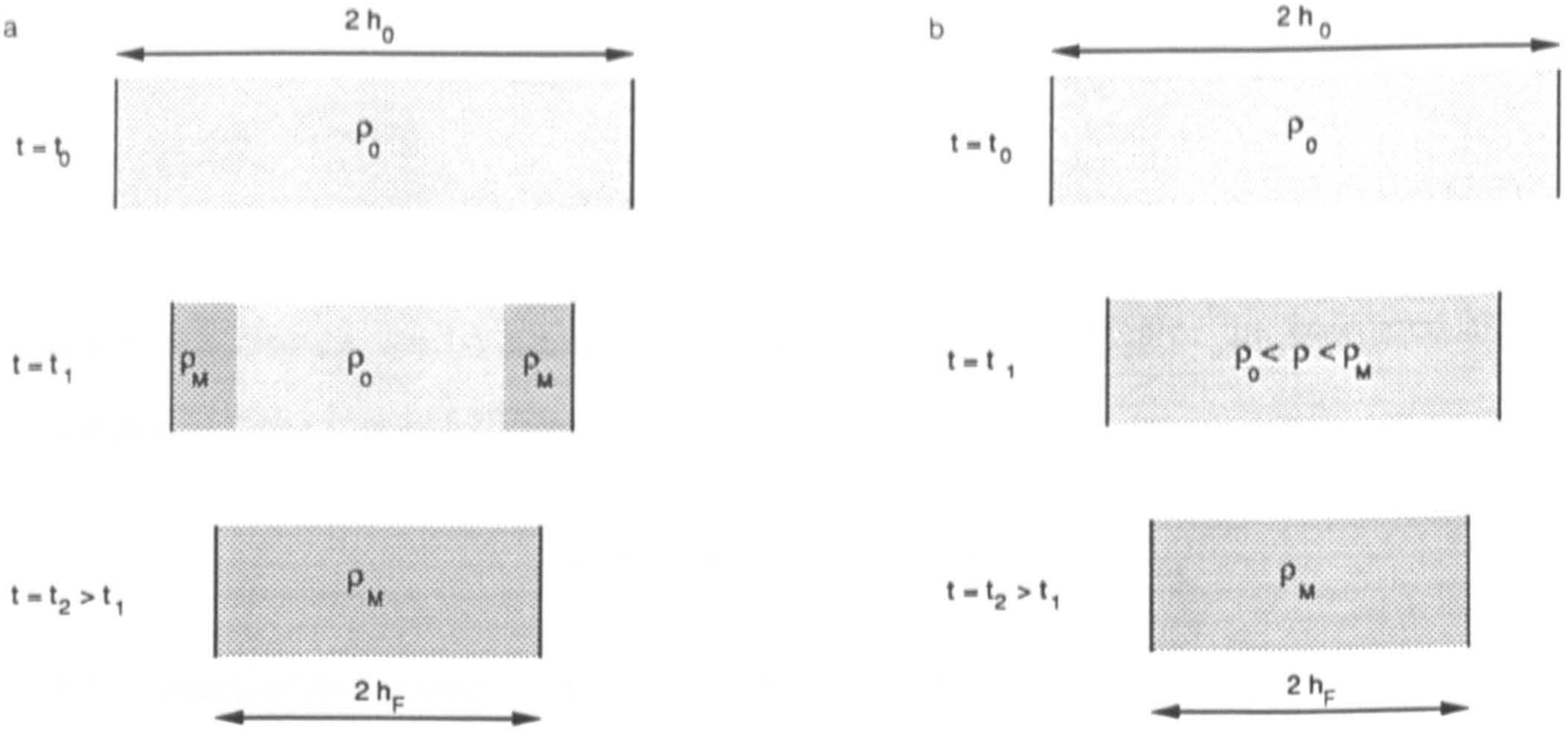

Figure 2.15 The behaviour of a theoretical one-dimensional body, during the two densification extremes: a) in the presence of a sharp densification front, and b) homogeneous densification (after references 157, 158).

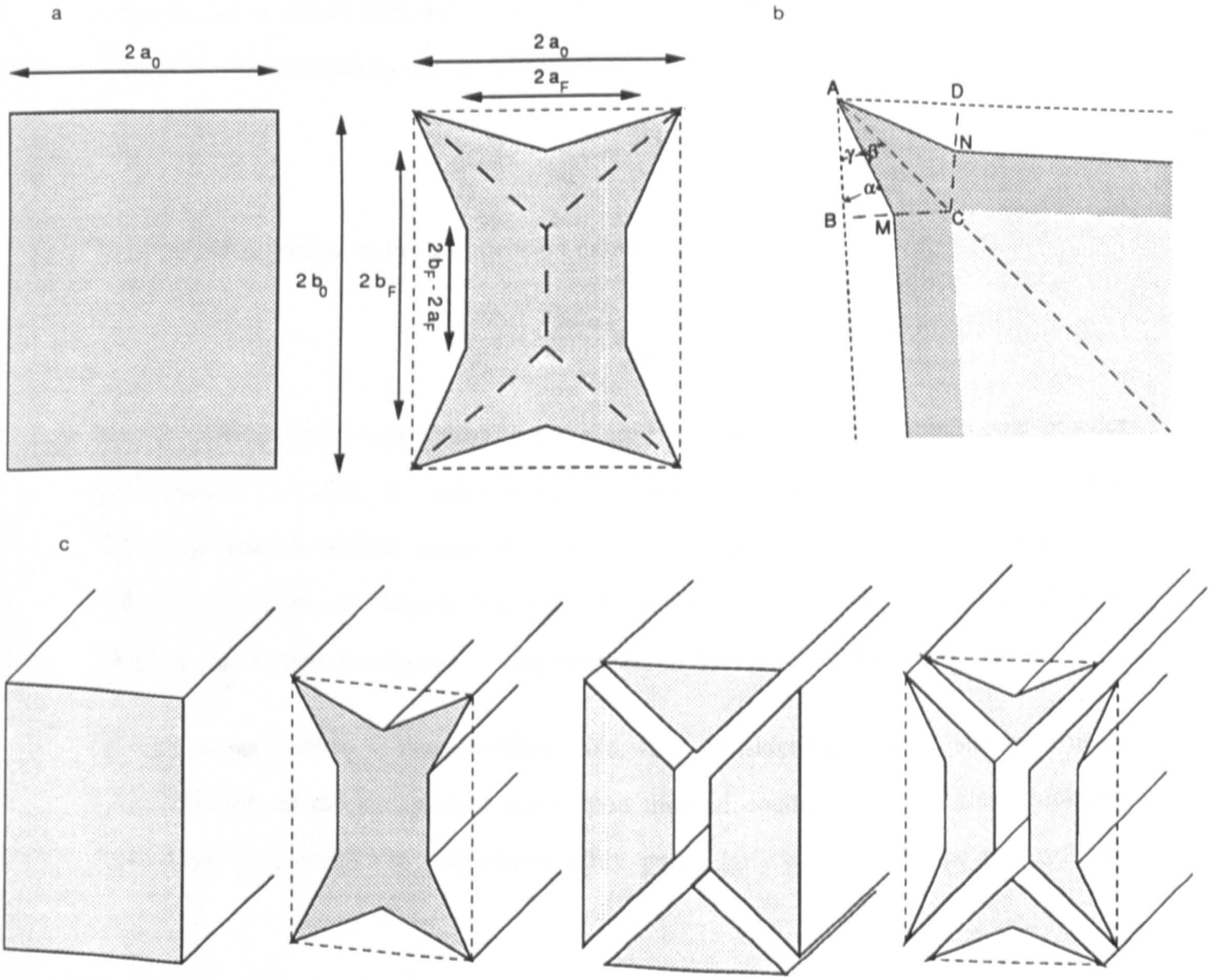

Figure 2.16 a) The behaviour of a theoretical two dimensional powder during densification in the presence of a sharp densification front. b) Geometrical considerations demonstrate the formation of a ''star-arm''. c) The behaviour of an infinitely long rectangular bar, following densification with a sharp densification front (after references 157, 158).

$$\frac{AMCN}{ABCD} = \frac{\rho_o}{\rho_m} \tag{2.3}$$

and a relationship can be determined between the corner angles of the powdered and densified bodies (2α and 2β respectively):

$$\beta = \alpha - \tan^{-1}\left(\frac{\rho_m - \rho_o}{\rho_m}\tan\alpha\right) \tag{2.4}$$

The densification behaviour of an infinitely long rectangular powder bar is shown in figure 2.16c. In the ideal case of homogeneous densification simple geometric considerations show that:

$$\frac{a_f}{a_o} = \frac{b_f}{b_o} = \left(\frac{\rho_o}{\rho_m}\right)^{1/2} \tag{2.5}$$

It can be easily shown that, with a sharp densification front, the minimum cross-sectional dimension is expressed by the equation:

$$\frac{a_f}{a_o} = \frac{\rho_o}{\rho_m} \tag{2.6}$$

with the other minimum finite dimension expressed as:

$$\frac{b_f}{b_o} = \frac{a_o(\rho_o/\rho_m) + (b_o - a_o)}{b_o} \tag{2.7}$$

Similar dimensional relationships to these are obtained for a three dimensional powder body model [157,158]. It should be remembered that the models derived by Aren and Navara present an extreme example in the form of a sharp densification front. In reality a considerably shallower thermal gradient will be witnessed, leading to slight curvature of flat faces rather than the sharp faceting observed in the model [159,160].

Further complications to these models arise when considering complex shaped articles and the effect of the encapsulant glass upon thermal conductivity (the glass thickness around the sample will also vary considerably, particularly with a 'frit' type encapsulant).

2.8 HIP ECONOMICS

The application of HIP to the commercial processing of silicon nitride has yet to become a reality. However, HIP is already an established fabrication route for hard metal materials, particularly for the removal of porosity in WC-Co alloys [161,162]. HIPing has also been utilised commercially for the processing of materials such as titanium, superalloys and powder metals [163]. In Germany HIP has been utilised to produce electronic ceramics, including multilayer capacitors and magnetic tape heads [163].

The increasing need to fabricate materials at higher temperature has led to the production of large volume HIP furnaces which are capable of operation at temperatures up to 2200°C with the incorporation of graphite furnace components. Industrial Materials Technology (IMT), USA, is currently operating a 310MPa HIP unit, with a 41 cm diameter working zone and temperature capability of 2200°C for processing superalloy and ceramic components [163]. ASEA Cerama AB are presently operating HIP units ranging in operational volume from 5 to 600 litres [164], with the smaller units capable of 2000°C and 300 MPa, and the larger presses 1800°C and 160 MPa. ASEA are currently producing turbocharger rotors for the American market, at a component cost of US $ 6-8 [164] and high tolerance silicon nitride high speed bearings for use in jet planes [164,165]. Cost prediction at ASEA has revealed the potential for an approximate cost as low as US $ 0.55/kg for 'cladded' HIPing of steel based products.

In addition to the reduced component cost, further consideration of HIP processing must be made with regard to flexibility and consistency. Glass encapsulated HIPing allows the possibility of joining two, complex shaped, ceramic articles provided that enclosed cavities are avoided [165]. Sagging of the ceramic powder body is essentially eliminated during HIP and a uniform density (± 0.001 gcm^{-3}) can be obtained throughout individual processed articles [166].

Although HIP development of ceramic materials is still in its infancy, the potential

benefits for fabrication of dense ceramics have already been demonstrated. Ultimately, HIP will continue to gain approval as a production technique for advanced structural ceramics and, as costs are reduced, and powder and 'green' state processing methods improve, HIP will become a 'standard' production route for high temperature materials.

CHAPTER THREE

GENERAL EXPERIMENTAL TECHNIQUES

3.1. INTRODUCTION

This chapter describes the experimental techniques used for the characterisation and testing of all ceramics investigated during the current study. The composition and fabrication of these materials is also discussed.

3.2. MATERIAL FABRICATION

3.2.1. Material Composition and Preparation

The materials used during the current research program have been supplied by Lucas-Cookson Syalon Ltd (LCS), Solihull, and T & N Technology Ltd (T&N), Rugby.

A commercially available matrix-crystallised Y-Si-Al-O-N ceramic (type 201) was supplied by LCS. The LCS Type 201 ceramic utilizes Y_2O_3 and 21R (an AlN polytypoid) as additions to aid densification. The mixed powders were ball-milled, using alumina media, in isopropyl alcohol to ensure that both a fine particle size and a homogeneous dispersion of the sintering additives were obtained. There is approximately 3 wt.% alumina 'pick up' during milling. The milled powders were then dried and cold-isostatically pressed in rubber containers. The compacted powder billets were then placed in a boron nitride powder bed and sintered in a graphite resistance furnace for a period of four hours. Sintering was conducted in a nitrogen atmosphere at a temperature between 1800 and 1850°C. The pressureless sintered billets were then heat-treated (in an extension of the sintering cycle) to achieve matrix crystallisation. A two-step 'nucleation' (1250°C for 7 hours) and 'growth' (1400°C for 5 hours) schedule was used for this purpose.

The majority of the silicon nitride ceramic compositions provided by T&N were in the 'green' state. However, a limited amount of material was initially provided in a densified form, as pressureless sintered (SSN) and sintered reaction bonded silicon nitride (SRBSN). Anzon* α-Si_3N_4 starting powder was used for the SSN, whilst Starck†, Kemanord‡ and Pilamec§ P84 Si powders were used for the SRBSN samples provided. The starting powder compositions are presented in Tables 3.1a,b. The additives used for both SSN and SRBSN materials were 10 wt.% Y_2O_3, 2 wt.% MgO and 2 wt.% Cr_2O_3 (referred to as A1), and these were added prior to milling. The silicon nitride (and silicon) based powder mixtures were attritor milled in propanol for three hours using steatite media. After milling the mixed powders are dried and cold-isostatically pressed in rubber containers.

Si_3N_4 powder	Phase-analysis	Impurities (%)						Specific surface area (m^2g^{-1})
		Free Si	Al_2O_3	CaO	C	Fe_2O_3	O	
Anzon	>90% α-Si_3N_4	<0.5	0.26	0.05	0.20	0.22	1.0-1.5	7.3

Table 3.1a Powder specifications of Anzon α-Si_3N_4 starting powder

Si powder	Phase-analysis	Impurities (%)					Specific surface area (m^2g^{-1})
		Al	Fe	Ca	C	O	
Pilamec P84	~97% Si	0.70	1.94	0.13	–	–	–
Kemanord	–	0.07	0.07	0.01	0.06	~0.2	0.4
Starck	>98% Si	0.2	0.4	0.1	–	0.4	–

Table 3.1b Specifications for a selection of commercial Si powders used in composition A1

---

* Cookson Ceramics and Antimony Ltd., Tyne and Wear, England

† H.C. Starck, Berlin, W.Germany

‡ Kemanord, Sweden

§ Supplied by Willan Metals Ltd, Rotherham

The pressed silicon powder billets are then pre-sintered in an argon atmosphere to produce a semi-dense machinable material (all machining can therefore be performed prior to nitriding). Nitridation is conducted at 1300-1400°C in flowing nitrogen. The nitrided (reaction bonded) specimens were then pressureless sintered at 1750°C for two hours in a nitrogen atmosphere. The pressed silicon nitride billets were pressureless-sintered for two hours, again in a nitrogen atmosphere. A range of temperatures, from 1600-1750°C, were employed.

Two compositional variations of SSN A1 were also mixed by T&N, referred to as A2 (with additions of 10 wt.% Y_2O_3 and 2 wt.% MgO), and A3 (with just a single 10 wt.% Y_2O_3 addition). These compositions (using Anzon α-Si_3N_3 powder) were supplied, complete with further A1, in the 'green' state billet form. All three 'green state' compositions were used for the developmental stage of the glass encapsulation/HIP investigation (described in Chapter 5) and both A1 and A2 sections were also used for pressureless-sintering/HIP fabrication.

3.2.2. Revised 'Single' Additive Compositions

The desire to tailor a ceramic composition that allows near complete crystallisation of the second (glassy) phase after sintering led to the development of a 'second generation' of ceramic compositions. An initial series of seven potential compositions were devised as part of a series of single additive ceramics for use in a parallel HIP fabrication programme conducted at Warwick University [76,167]. A constant Si:Y ratio was chosen for all compositional variants studied here, with the O:N ratio systematically altered by replacing silicon nitride with either silica (SiO_2) or silicon oxynitride (Si_2N_2O). A summary of the seven compositions is presented in Table 3.2, with identification of the individual powder constituents given in weight percent and subsequently calculated in equivalent percent (with eq.%Y = 3[Y]/(3[Y]+4[Si]) and eq.%N = 3[N]/(3[N]+2[O])).

	Weight %				Element					
	Y_2O_3	Si_3N_4	SiO_2	Si_2N_2O	Y	Si	O	N	eq.%Y	eq.%N
B1	5.0	95.0	–	–	0.065	2.952	0.202	3.866	1.62	96.65
B2	5.0	93.0	2.0	–	0.65	2.951	0.297	3.802	1.62	95.04
B3	5.0	91.0	4.0	–	0.65	2.951	0.395	3.737	1.63	93.42
B4	5.0	87.0	8.0	–	0.65	2.951	0.592	3.606	1.65	90.14
B5	5.0	90.0	–	5.0	0.65	2.951	0.269	3.821	1.62	95.51
B6	5.0	85.0	–	10.0	0.65	2.951	0.338	3.775	1.63	94.37
B7	5.0	70.0	–	25.0	0.66	2.951	0.547	3.636	1.64	90.89

Table 3.2 Additive level for ASEA HIP ceramics B1 to B7

Compositions (B2 to B7) were devised to lie within the Si_3N_4-$Y_2Si_2O_7$-Si_2N_2O compatibility triangle, with B1 tailored to lie on the Si_3N_4-$Y_2Si_2O_7$ tie-line (fig. 3.1). This diagrammatic representation is only reliable if the oxygen content of the α-Si_3N_4 powder is both consistent and accurate, and hence high purity UBE SNE10 α-Si_3N_4 was used as the starting powder. UBE SNE10 has been found to possess a uniform particle size and a low, constant oxygen content (quoted at ~1.03 wt.%, equivalent to a silica impurity content of ~1.93 wt.%). The oxygen level upon receipt of the UBE powder was more typically 1.2 wt.% [168]. Powder specifications are shown in Table 3.3. The silicon nitride powder was mixed with the sintering aids in batches of 1 kg and attritor milled in propanol for 16 hours using HIPed Si_3N_4 milling media. After milling the mixed powders were dried and cold-isostatically pressed in rubber containers, producing 'green' state billets with approximate dimensions of 11 cm length and 2.5 cm diameter. Billets of all seven compositions were used for HIPing at ASEA Cerama (Chapters 5 and 6) and sections of B1, B2 and B5 were utilised in the glass encapsulation/HIP aspect of the current programme (Chapters 5 and 6) conducted at HIP Ltd., Chesterfield.

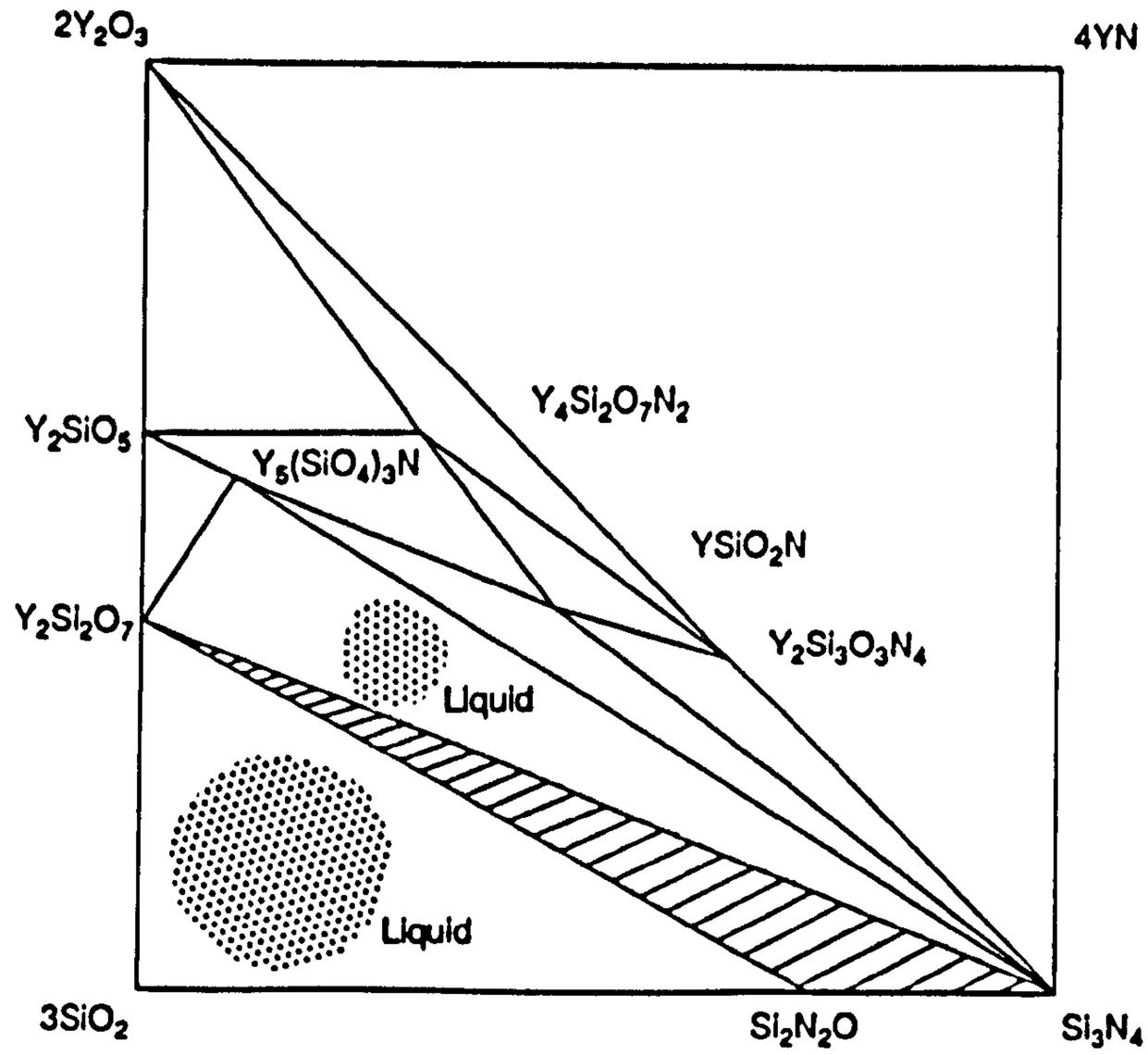

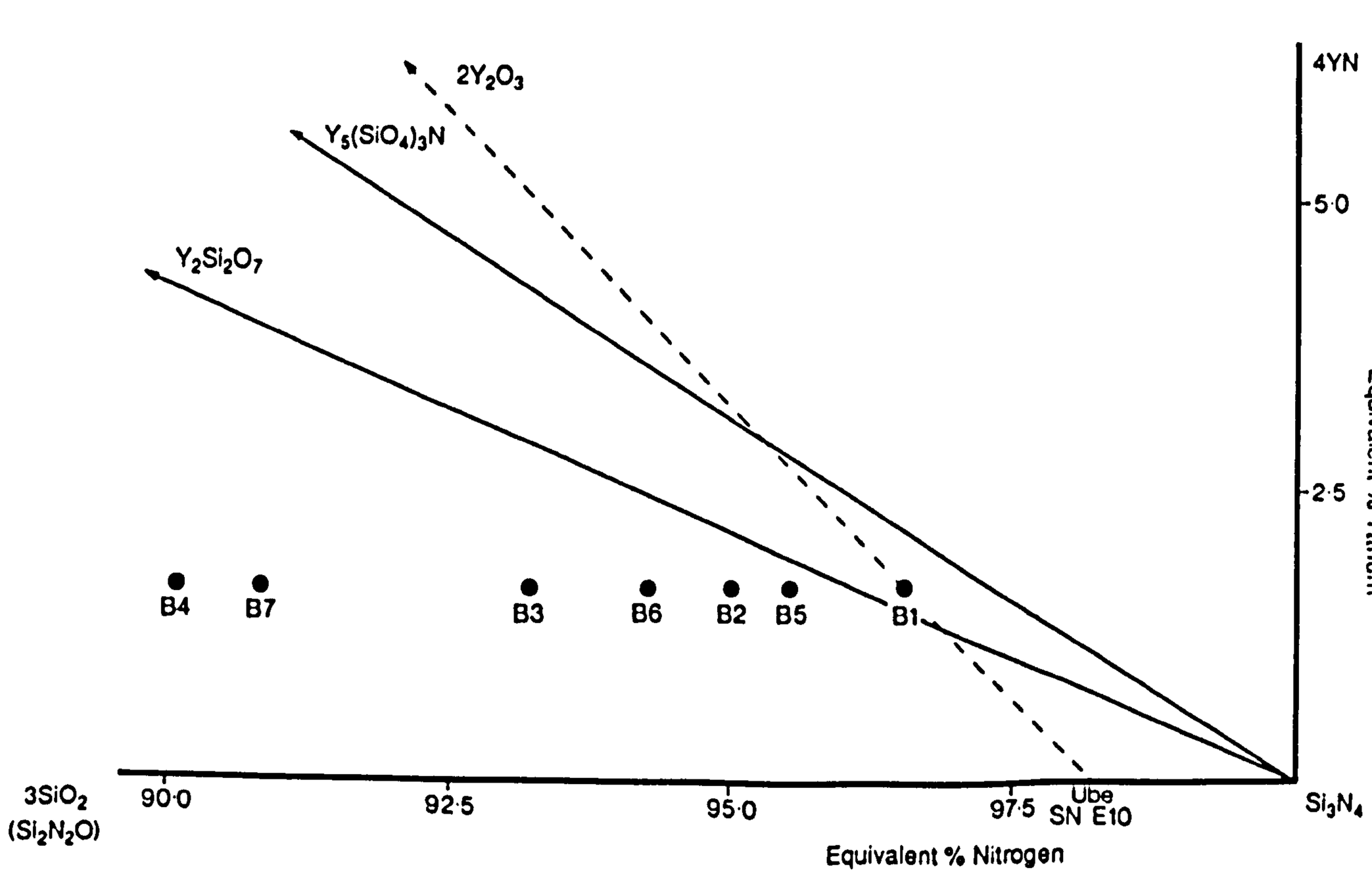

Figure 3.1 The Si_3N_4-SiO_2-Y_2O_3-YN phase system, showing the compositions B1 to B7 plotted on the enlarged Si_3N_4 corner of the diagram.

UBE SNE10		
Impurities	N	38.7%
	O	1.3%
	Cl	50 ppm
	Fe	50 ppm
	Ca	<50 ppm
	Al	<50 ppm
Specific surface area		12 m^2/g
Degree of crystallinity		~100%
$\beta/(\alpha+\beta)$		2%

Table 3.3 UBE SNE10 powder characteristics

Two further 'single' additive compositions were also supplied; the first with a 7.3 wt.% Nd_2O_3 (an equivalent molar percentage to B1) and a mixed 2.25 wt.% Y_2O_3 / 4.00 wt.% Nd_2O_3 additive material. The use of Nd_2O_3 or a Y_2O_3/Nd_2O_3 additive mixture will lower the matrix liquidus temperature by up to 60°C relative to pure Y_2O_3 additions.

3.2.3. Pressureless Sintering Procedure

Pressureless sintering of silicon nitride ceramics used in the current study was conducted within a vertical tube type furnace. Initially an RF induction furnace was used. The construction of this furnace type has been described previously by Bayliss [169] and Butler [171]. Induction heating is provided by an RF coil surrounding the furnace and connected to a Raydyne generator (capable of 30 kW at 450 kHz). A maximum sintering temperature of ~1850°C can be obtained with this system, with a typical heating rate of $10°Cmin^{-1}$. A natural 'furnace cool' was used after sintering.

Later, a tube furnace utilising molybdenum disilicide ($MoSi_2$) heating elements was used. This system used a Saffil insulating furnace box through which the alumina tube was situated. The Super Kanthal $MoSi_2$ elements have a maximum operating temperature of 1800°C, although continuous usage can be maintained at 1700°C. The furnace can be run under inert atmosphere (either nitrogen or argon) or in air. A vacuum

facility is also incorporated into this system. Further details of the furnace construction can be obtained in [172].

Sections of 'green' state A1 and A2 were dry-cut to form rectangular billets using a resin-bonded diamond peripheral saw (of approximate dimensions 10 × 10 × 20 mm). Additionally, cylindrical billets of composition A1 (of dimension 10mm diameter by 15mm length) were produced by grinding on an Elliot Universal grinder. The billets were packed in a powder bed, of composition 50 wt.% BN, 45 wt.% Si_3N_4 and 5 wt.% MgO, within a graphite crucible. Pressureless sintering was conducted in a nitrogen atmosphere at temperatures between 1250 - 1750°C for two hours.

Cylindrical billets of compositions A3 and B1 were prepared by grinding on an Elliot Universal grinder, to an approximate size of 10mm diameter by 15mm length. The billets were packed in a 50 wt.% BN / 50 wt.% Si_3N_4 powder bed within a graphite crucible. Sintering was again conducted in a nitrogen atmosphere. Sintering temperatures between 1550 and 1700°C were employed with a hold period of two hours.

3.2.4. Hot Isostatic Pressing

Examination of glass encapsulation techniques (described in Chapter 5) were conducted using a laboratory scale HIP unit at H.I.P. Ltd, Chesterfield. The laboratory unit was constructed by Autoclave Engineers (AE) Inc, USA. The AE system is shown in figure 3.2. This system utilizes the AE Isoframe assembly shown in figure 2.2 (Chapter 2) for improved safety at high pressure.

Heating is provided by graphite resistance elements which are isolated from the heat insulating base by BN pads. The HIP furnace unit is shown in figures 3.3 a,b. The HIP chamber dimensions are a length of 120 mm with a 75 mm diameter. Temperature control is maintained with the aid of several W-5%Re/W-26%Re (type C) thermocouples, which monitor the chamber temperature during a HIP cycle. Pressure

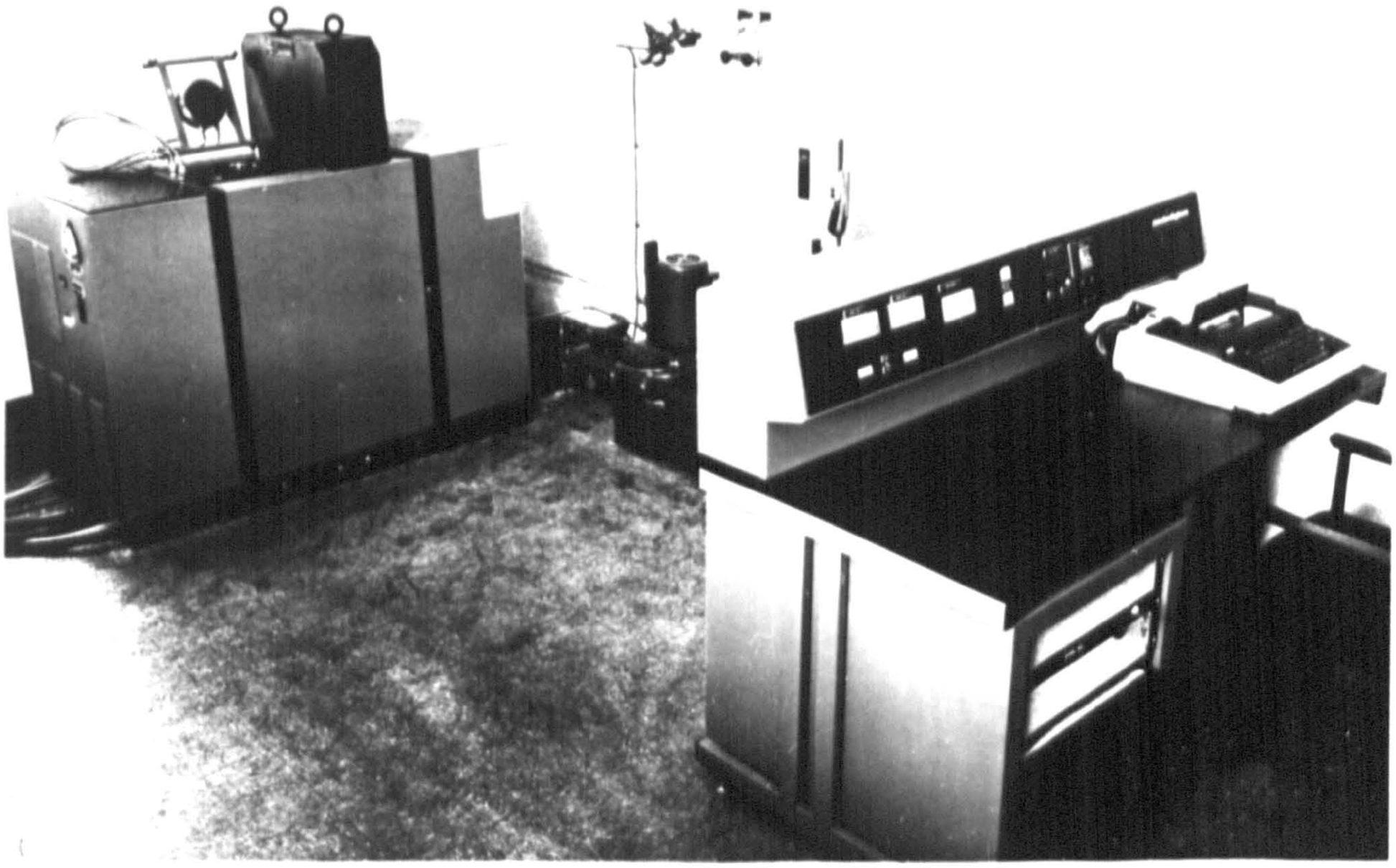

Figure 3.2 The Autoclave Engineers (AE) laboratory scale HIP unit at HIP Ltd., Chesterfield (Courtesy of HIP Ltd.)

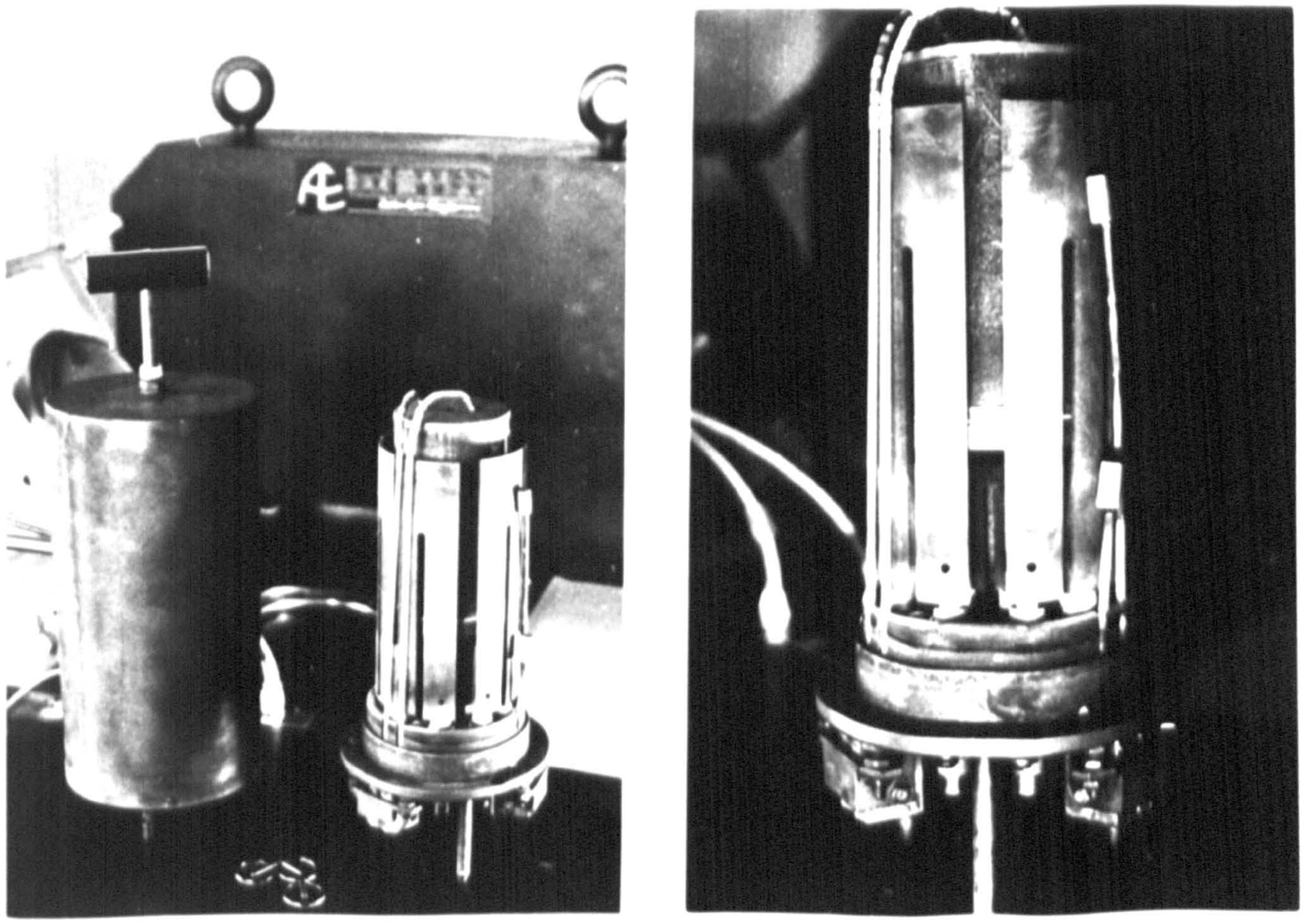

a

Figure 3.3 a) The furnace unit used in the AE laboratory HIP system (Courtesy of HIP Ltd., Chesterfield). b) Schematic representation of the HIP furnace construction.

b

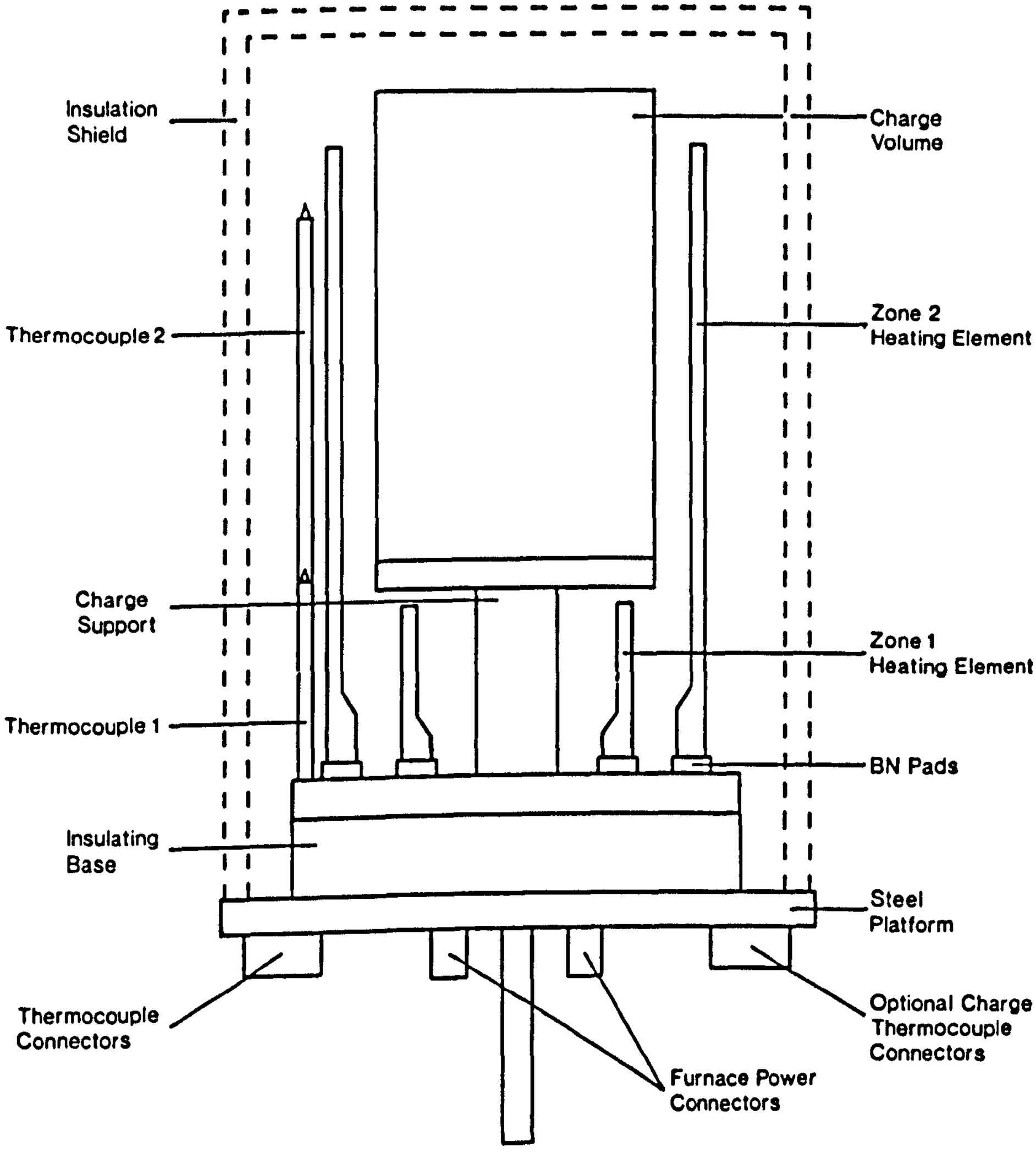
Insulation Shield
Charge Volume
Thermocouple 2
Zone 2 Heating Element
Charge Support
Zone 1 Heating Element
Thermocouple 1
BN Pads
Insulating Base
Steel Platform
Thermocouple Connectors
Optional Charge Thermocouple Connectors
Furnace Power Connectors

application within the HIP chamber can be made using either nitrogen or argon gas. During the current programme nitrogen gas was used exclusively for the sinter-HIP processing of non-encapsulated silicon nitride and for the initial silica and Pyrex encapsulation examination.

To increase the working life of the graphite furnace components a nitrogen/argon gas mix was preferred, and this was used during the latter stages of the glass encapsulation stage of this programme. Initially the chamber is pressurised with nitrogen (when using a gas mix) and, as the temperature is increased, the pressure is also increased by the addition of argon such that approximately 5-10% nitrogen is retained at the processing temperature. Details of the encapsulation techniques derived during the current research are documented in chapter 5.

3.3. MICROSTRUCTURAL EVALUATION

3.3.1. Density Measurement

The density measurement of specimens with negligible surface porosity (ie. >90% TD) was performed using an Archimedian immersion method in methanol. Specimens were weighed in air and in methanol, with the bulk density subsequently calculated using the equation:

$$\rho_{spec} = \rho_{meth} \frac{M_a}{(M_a - M_m)} \qquad (3.1)$$

where ρ_{spec} is the specimen density, ρ_{meth} the density of methanol, M_a the mass of the specimen in air and M_m the specimen mass when immersed in methanol. Approximate theoretical densities were calculated using a simple rule of mixtures law from the starting constituent percentages and densities (summarised in Table 3.4).

Material	Density ($g\,cm^{-3}$)
Si_3N_4	3.19
Y_2O_3	5.03
MgO	3.58
SiO_2 (am)	2.2
Si_2N_2O	2.85
Cr_2O_3	5.21
Nd_2O_3	7.24

Table 3.4 The densities of the various silicon nitride starting constituents

The density of ceramic samples that contain a high degree of interconnecting porosity was assessed by immersion in mercury using a Doulton Densiometer with a Mettler digital balance, provided by T&N Ltd. The use of mercury, a poor wetting agent, prevents penetration of the liquid into the interconnecting porosity within the specimen. Sample densities were calculated from the equation:

$$\rho_{spec} = \rho_{Hg}\frac{w_1}{w_2} \tag{3.2}$$

where w_1 is the specimen weight in air, w_2 is the weight immersed in mercury less the weight of the densiometer saddle (used to physically hold specimens within the mercury, thus preventing the specimen floating) and ρ_{Hg} is the density of mercury.

3.3.2. X-Ray Diffraction

The densification of crystalline phases in all ceramic materials examined was conducted using the well established technique of X-ray diffraction [173]. Generally, specimens were ground flat (with SiC paper) prior to analysis in a standard Philips diffractometer. Spectra were taken using CuK_{α_1} radiation, of wavelength 1.5405Å, at a scanning rate of $½^{o}\,2\theta\,min^{-1}$ for 10 to 60^{o} 2θ and recorded on a standard single pen chart recorder.

3.3.3. Electron Microscopy

Samples prepared for examination in the Scanning Electron Microscope (S.E.M.) were cut to size using an annular diamond bladed saw and then mounted in a conducting bakelite resin block. A ¼ μm surface finish was obtained on S.E.M. samples after grinding (with wet SiC paper) and polishing with diamond lapping paste. A thin conductive carbon or gold coating was evaporated onto the sample to prevent it charging in the S.E.M. electron beam.

Microstructural examination was performed with a Cambridge Instruments Stereoscan S250, equipped with a solid state back-scattered electron detector (K.E. Developments). X-ray microanalysis was conducted using the `ZAF 4` facility on a Link 860 EDX analyser (later replaced with a Link AN10000 system). The facility for light element analysis ($5<z<12$) was available with the incorporation of a thin window (beryllium)/windowless detection system. The Link AN10000 system also allows the determination of ceramic phase volume percentages, using the `X-Ray Mapping` and `Digipad` routines.

Specimens prepared for the transmission electron microscope (T.E.M.) were cut using the annular diamond saw to a thickness of approximately 0.5 mm. These specimens were then ground to a thickness of approximately 0.2 mm (200 μm) and polished on one side to a surface finish of ¼ μm. Discs of 3 mm diameter were cut from the polished sections using an ultrasonic drill fitted with a 3 mm diamond impregnated cylindrical bit. The unfinished side of the disc was then 'dimpled' (using a South Bay Technology dimpler) to a centre thickness of ~ 30 μm using 6 μm diamond paste. Finally the dimpled surface was polished to ¼ μm using diamond paste. A 5 kV argon ion beam was used to further thin the dimpled specimens until a small hole has appeared in the specimen and an electron-transparent region peripheral to this hole is obtained. After 'ion beaming', T.E.M. specimens were carbon coated.

JEOL 100C 100kV and 2000FX 200kV T.E.M.s were used for microstructural examination of these specimens. Energy dispersive X-ray analysis was performed on the 100C with an EDAX 9100 analyser.

3.4. MATERIAL PROPERTY ANALYSIS

3.4.1. Oxidation Resistance Determination

Specimens subjected to oxidative heat treatment were ground and polished on the major oxidation surface to a finish of 6 μm. During oxidation each specimen was sited on two silicon carbide knife edge supports, held in place in notches in an inverted section of mullite tube. Oxidation of individual specimens was performed in a horizontal (alumina) tube furnace, with each being inserted and removed from the heat treatment furnace at a constant rate (~200°C min^{-1}), primarily to prevent thermal shock of the alumina tube.

A high volume, high thermal mass furnace was used for the simultaneous oxidation of several specimens at identical temperature, which were inserted into the furnace at 1000°C with the temperature subsequently ramped to hold. The oxide scale development for silicon nitride based materials was examined via S.E.M. of specimens sectioned perpendicular to the major oxidation face (finished to 0.25 μm).

Where specimen size allowed the crystalline phase content of the oxide scale was determined by X-ray diffraction. Oxidation kinetics were determined by oxide scale thickness measurement, with the rate exponent (n) calculated using the relation:

$$d^n = kt \tag{3.3}$$

where d is the scale thickness, t the oxidation time and k the oxidation rate constant [52].

3.4.2. Modulus of Rupture (MOR) and Fracture Toughness (K_{IC}) Determination

MOR test bars were cut from densified billets using a Jones and Shipman surface grinder equipped with a diamond coated peripheral slitting wheel (with dimensions 50 × 3.5 ×

3.5 mm) and machined to size (3.0 × 3.0 mm cross section) using a diamond grinding wheel. The individual test bars were then surface finished to ~ 1μm by P.S. Marsden Ltd., Nottingham.

K_{IC} test bars were cut from pre-sintered ceramic billets of ceramics A1, A3 and B1 using an annular diamond saw (to a size of 3.2 × 3.2mm cross-section). Testing was performed using the single-edged notched beam (SENB) technique [64,65], which is particularly applicable because of the high porosity level of the pre-sintered materials. An analogue clock gauge was utilised to accurately measure the notch depth, cut in the tensile face of each bar using the annular diamond saw to a depth of 1 mm (~30% of specimen width). The depth of the machined notch was verified with a travelling microscope. K_{IC} test bars were also cut from 'green' state silicon nitride (ρ< 60% TD), using the annular diamond saw, to assess the potential 'green' machining strength (section 5.10). Bar and notch dimensions were identical to those previously described.

Mechanical testing was performed on an Instron 1122 using a (0-500kg) compression/tension load cell. Room temperature fracture toughness and flexural strengths were determined using a four point bend jig, with a 10mm outer span and 3mm inner span. All mechanical testing was conducted using a cross-head speed of 0.5 $mm\,min^{-1}$.

3.4.3. Equations for Calculation of MOR and K_{IC}

M.O.R. (fracture stress) values were calculated using the standard formula for four-point bend testing:

$$\sigma_F = \frac{3 P_F d}{B W^2} \qquad (3.4)$$

where P_F is the failure load (Newtons), B is the specimen height, W the specimen width and d is a geometrical factor. The variable d is determined by the four-point bend jig dimensions such that:

$$d = \frac{L - I}{2} \tag{3.5}$$

with L the jig outerspan and I the innerspan. All material dimensions are in metres.

The 'reliability' of each material was determined via calculation of the Weibull Modulus [174]. This quantity is related to the flaw size distribution within the material. A summary of the calculation involved in determining the Weibull Modulus is found in reference 174.

Fracture toughness (K_{IC}) values were calculated using the equation [175]

$$K_{IC} = \frac{3P_F d}{BW^2} a^{½} \left[3.86 - 6.15\left(\frac{a}{W}\right) + 2.17\left(\frac{a}{W}\right)^2 \right]^{½} \tag{3.6}$$

where a is the specimen notch depth, and the other variables are as in equation 3.4.

CHAPTER FOUR

THE EFFECT OF POST-SINTER HIP'ING UPON THE MICROSTRUCTURE AND PROPERTIES OF DENSIFIED SILICON NITRIDE CERAMICS

4.1. INTRODUCTION

The majority of research investigating HIPing as a consolidation technique for silicon nitride has involved the use of an impermeable gas barrier to isolate the ceramic body from the external pressurising gas. A gas barrier is required because HIPing is generally performed on green state silicon nitride pieces which contain a high volume of interconnecting porosity. Gas penetration into the porosity, which would inhibit densification, is therefore prevented by the gas impermeable barrier (typically a refractory glass or metal canister). Glass encapsulation has formed the major point of interest of this thesis and is described in Chapters 5 and 6.

One alternative to this encapsulation process is to provide an *in situ* gas barrier, formed by pressureless sintering the green state ceramic to a state of closed porosity. It is therefore understandable that only ceramics with a relatively low (< 1500°C) matrix eutectic temperature can be processed in this manner (eg. ceramic A1 and the commercially available Syalon LCS 201) and the sinter-HIP technique is not suitable for the single-additive ceramics typified by compositions B1 to B7 (described in section 3.2.2).

This chapter assesses the effect of a post-sinter HIP treatment upon the microstructure of ceramics A1 and LCS 201. Additionally the influence of HIP upon the room temperature mechanical properties of ceramic LCS 201 is examined. It is probable that HIP of the densified LCS 201 ceramic will produce a general improvement in material reliability due to the removal of bulk micropores.

4.2. THE MICROSTRUCTURE OF AS-RECEIVED Si_3N_4 CERAMICS

4.2.1. Densification Behaviour of A1

As received, densified A1 ceramics were provided in two forms:

1. Four variations of the A1 based SSN and SRBSN materials (described in section 3.2.1) were provided in the form of broken test bars, of 3 × 3 mm cross-section (sintered at BCRA, Stoke-on-Trent). Each test bar had been cut from the bulk section of a large densified billet. Densities for these materials could not be directly assessed by immersion because of the low mass of each section. Densities were thus calculated by analysis of the porosity level, which was performed using the image analysis facility on the Link AN10000 system (with data obtained from integration of grey levels), and are shown in Table 4.1.

2. Complete billets (10 × 10 × 60 mm) of SSN composition A1 sintered at a range of temperatures between 1600 and 1750°C (sintered at BCRA). Densities of these billets, measured by immersion in methanol, are also presented in Table 4.1.

	Sintering temp (°C)	ρ	%TD
SSN	1750	3.25 (*)	97.9
P84 SRBSN	1750	3.18 (*)	95.8
Starck SRBSN	1750	3.17 (*)	95.8
Kemanord SRBSN	1750	3.18 (*)	95.8
SSN	1600	3.15	94.8
SSN	1725	3.19	96.1
SSN	1750	3.27	98.5

Note: (*) measured by SEM volume percentage porosity

Table 4.1 Densities of SSN and SRBSN samples sintered at BCRA

In addition to the as-received ceramics, sections of 'green' state composition A1 were pressureless sintered in a nitrogen atmosphere at temperatures between 1400 and 1700°C

for two hours. Comparison of these sintered densities (Table 4.2) with the as-received materials reveals a slight decrease in the relative density. Full details of the processing route for the as-received ceramics were not available making it difficult to ascertain the reason for density variation. However, it may be assumed that a gaseous (nitrogen) overpressure was utilised at BCRA when considering the optimisation of conditions used for (one atmosphere) pressureless sintering at Warwick (described in detail in section 3.2.3).

Sintering temp (°C)	ρ	%TD
1400	1.75 (*)	52.7
1500	2.49	75.0
1600	2.70	82.0
1700	2.99	90.1

Note: (*) Sample cracked during sintering

Table 4.2 Densities of ceramic A1 sintered at Warwick

4.2.2. The Microstructure of A1 Based Ceramics

The microstructural development of ceramic A1 (SSN) has been most easily observed in the series of 'green' state specimens pressureless sintered at temperatures between 1400 and 1700°C. Sections of composition A1 were cut to a size of 10 × 10 × 20 mm prior to sintering in a 5 wt.% MgO/45 wt.% Si_3N_4/50 wt.% BN powder bed.

Pressureless sintering of ceramic A1 (SSN) at 1400°C produced only a minimal transformation of α- to β-Si_3N_4 (<20%). After sintering at 1500°C a high proportion of α- to β-transformation had occurred with the exception of the extreme bulk ceramic, where a lower transformation percentage was apparent.

A complete transformation of α- to β-Si_3N_4 was observed for all sintering temperatures of 1600°C or greater. A coherent β-Si_3N_4/glass microstructure was apparent for all fully

a

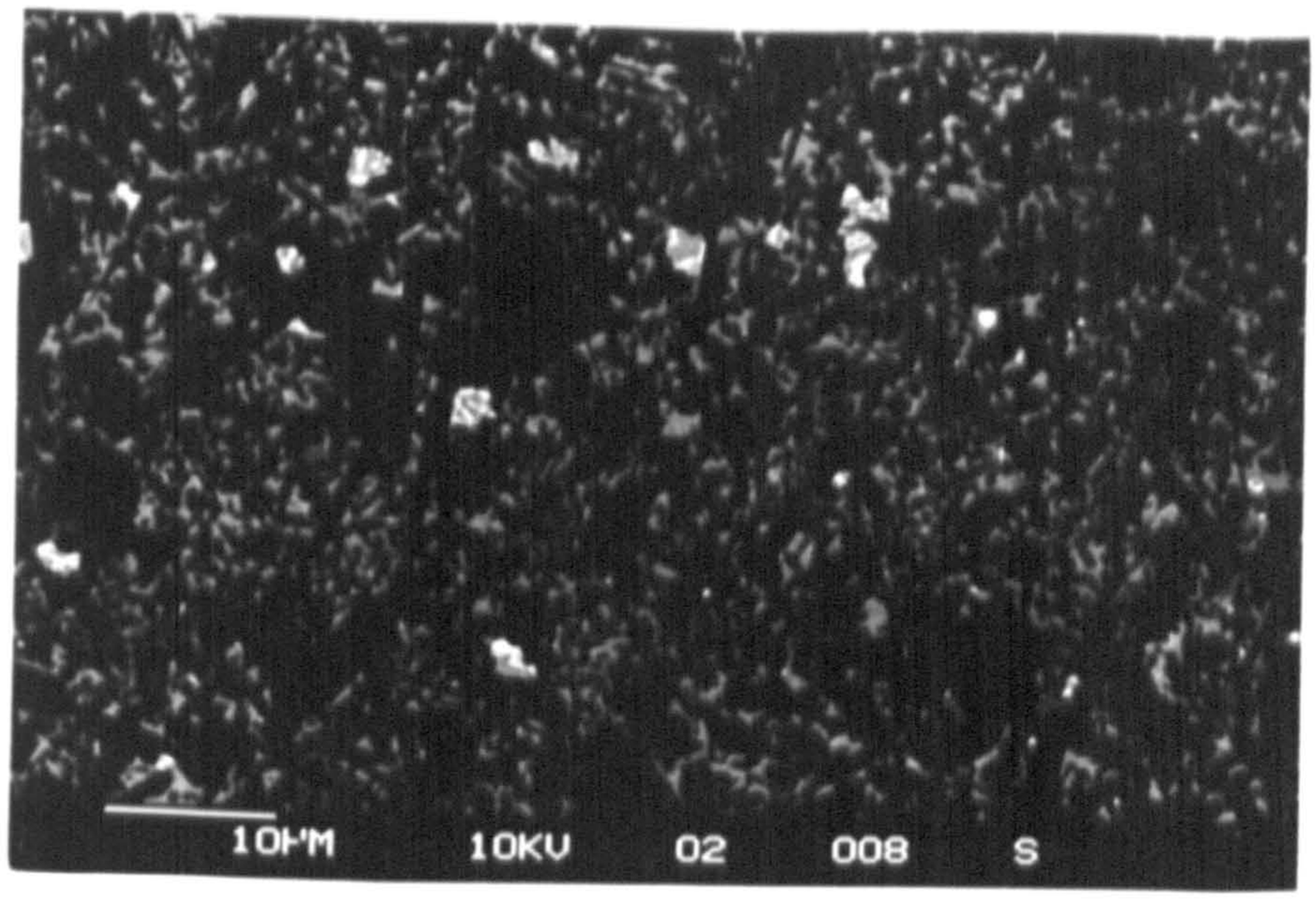

b

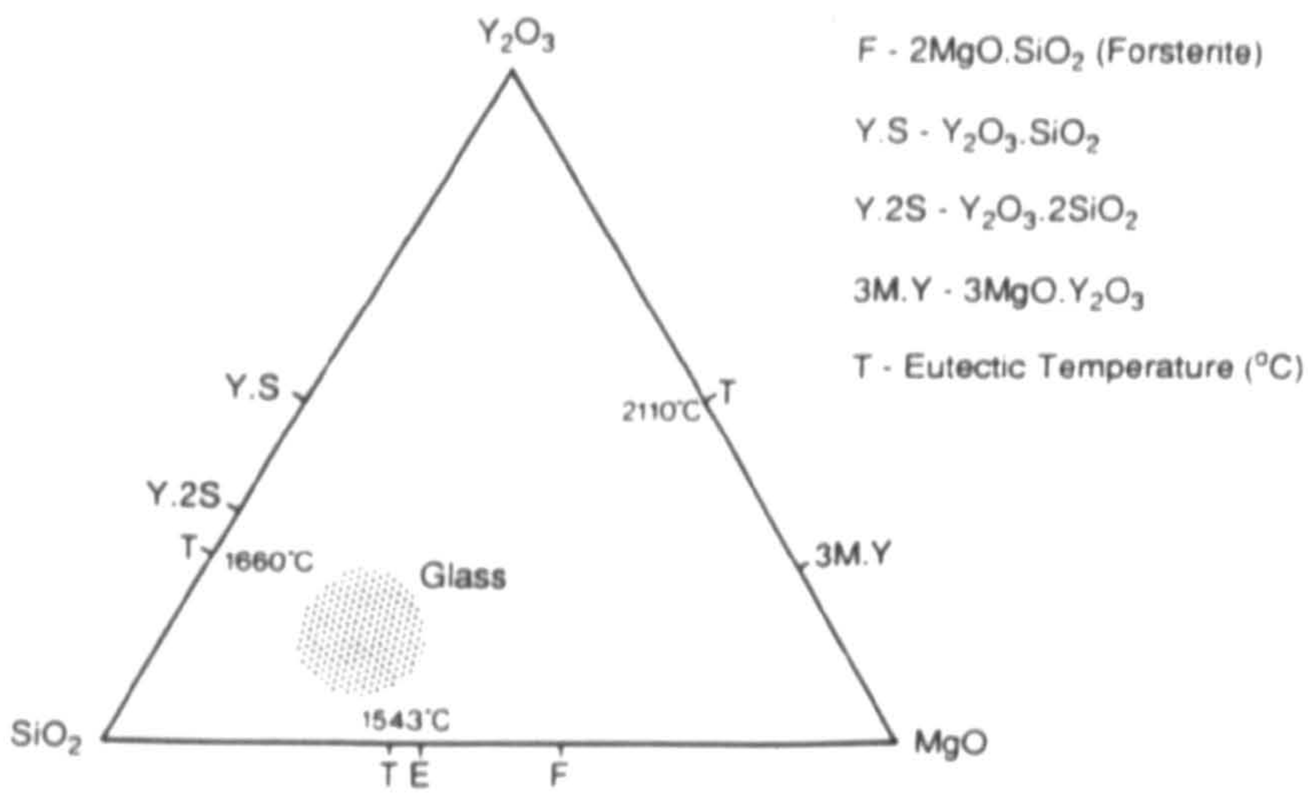

c

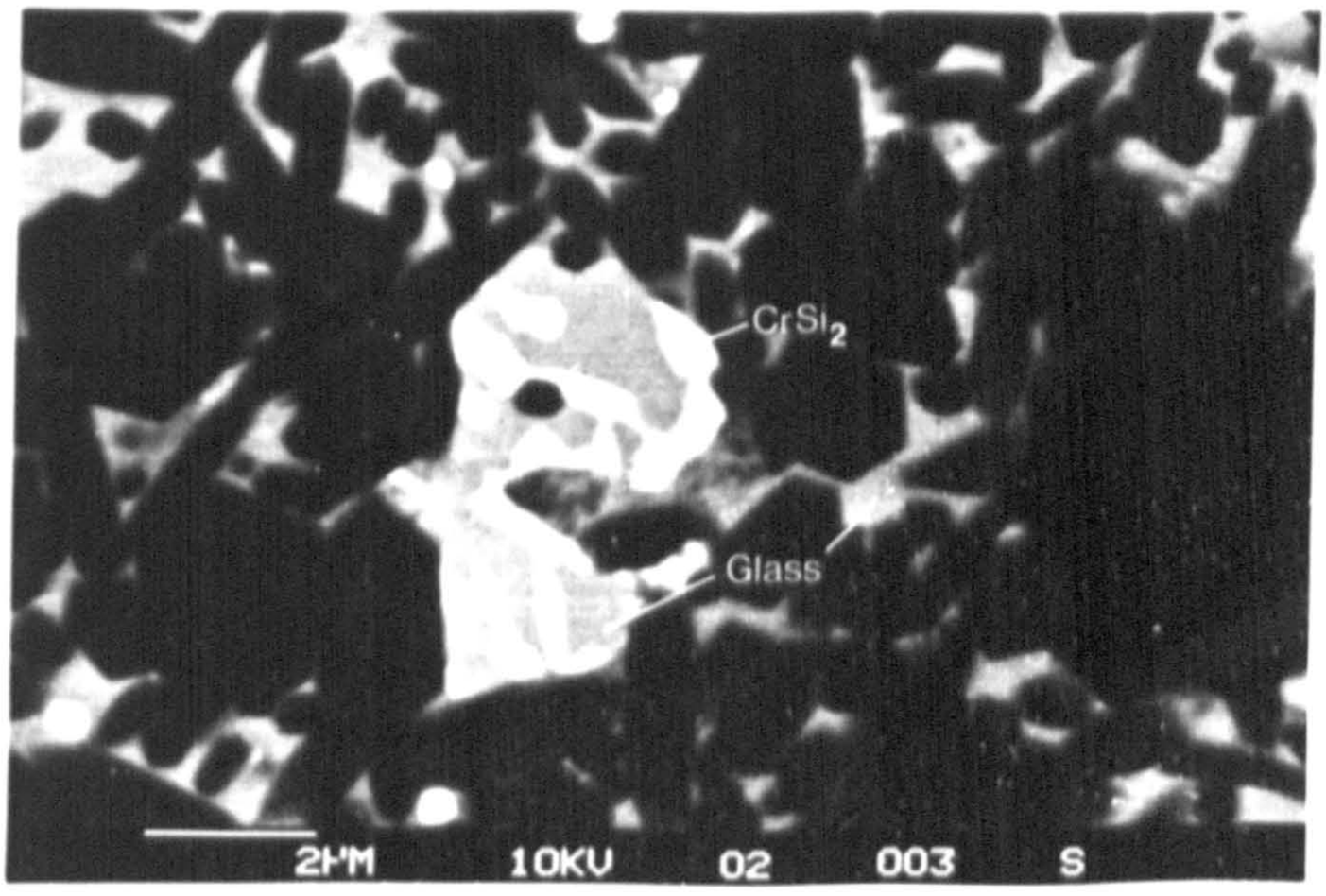

Figure 4.1 a) SEM micrograph of the bulk microstructure of ceramic A1 pressureless-sintered at 1750°C. b) Intergranular matrix composition for densified ceramic A1. c) Chromium silicide present in ceramic A1.

transformed specimens, with hexagonal β-Si_3N_4 grains present within a continuous glassy intergranular phase of ~17% volume (fig. 4.1a). The average glass composition was determined to be approximately

$$Si_{3.5}Y_{2.0}Mg_{1.0}O_{11.0}$$

by X-ray microanalysis (fig. 4.1b). A further phase, homogeneously distributed throughout the densified material, was analysed as chromium silicide (of general stoichiometry $CrSi_2$). The chromium silicide morphology was granular at the higher sintering temperature and generally each isolated region was a Cr-silicide/Y-Mg-silicate glass mixture (fig. 4.1c). $CrSi_2$ possesses a hexagonal crystal structure.

A low level of MgO depletion was observed in some isolated regions of the near surface microstructure (< 50μm from the specimen surface). This behaviour demonstrates the high mobility of Mg^{2+} species at the processing temperature, with a measured loss of this specific additive to the mixed powder bed (presumably occurring at areas of lower Mg concentration within the powder bed).

Crystallisation of the matrix phase was not observed by XRD or TEM (fig. 4.2). Some isolated chromium silicide regions contained a finite iron content, probably arising from impurities in the silicon nitride starting powder, which can be directly substituted for chromium. Some areas of unreacted Cr_2O_3 additions were retained in the bulk of the ceramic sintered at 1600°C, as isolated regions of pure oxide/silicide mixtures.

The chromium silicide phase was actually a mixture of two compositions, mainly $CrSi_2$ and a small volume of analysed composition CrSi (not observed via XRD). The formation of chromium silicide ($CrSi_2$ and CrSi) during sintering can be predicted by considering the thermodynamics of reaction. Cr_2O_3 does not form a liquid with SiO_2 below 2200°C in the pure binary system [178] although no literature is available for the mixed Cr_2O_3-Y_2O_3-MgO-SiO_2 system. Negita demonstrated that, for an oxide to be utilised as a sintering additive, the free energy of formation of the oxide from the pure

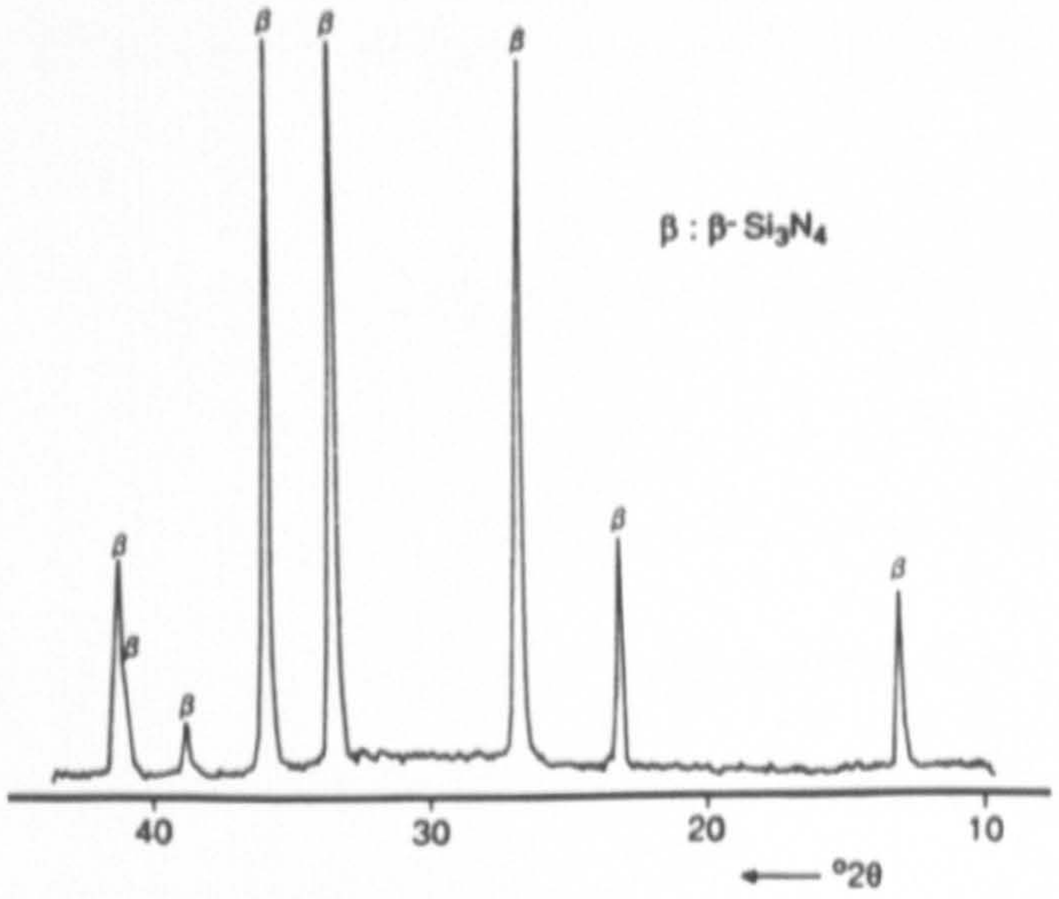

Figure 4.2 XRD and TEM demonstrate the retention of a glass intergranular phase after sintering.

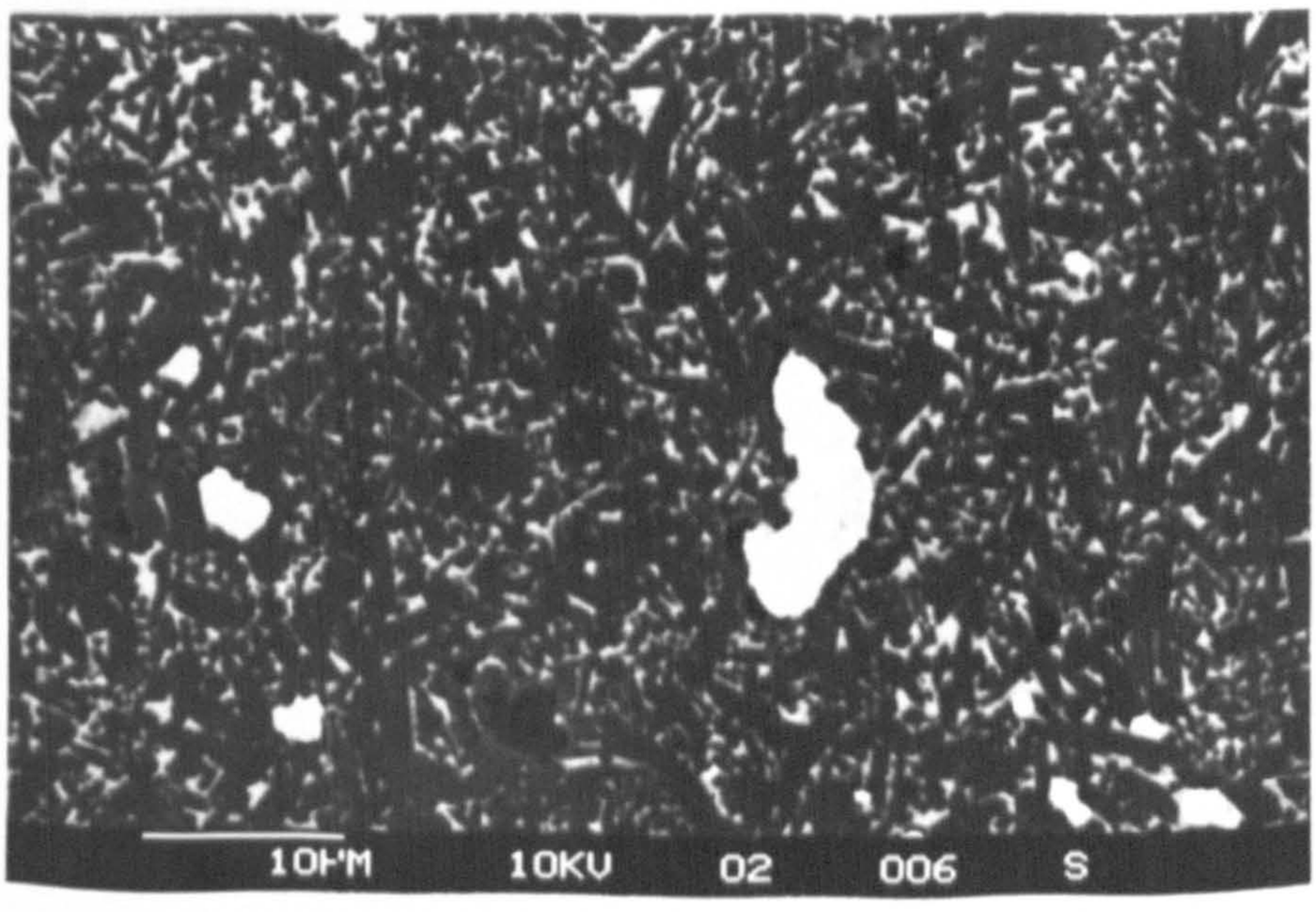

Figure 4.3 SEM micrograph of the bulk microstructure of SRBSN variant of ceramic A1 (using Kemanord Si powder).

metal must be more negative than the free energy of oxidation of silicon nitride [179]. The formation of chromium silicide occurs following the decomposition of Cr_2O_3 via reaction with Si_3N_4 :

$$3Cr_2O_3 + 4Si_3N_4 \longrightarrow 6CrSi_2 + 4½O_2 + 8N_2$$

or

$$3Cr_2O_3 + 2Si_3N_4 \longrightarrow 6CrSi + 4½O_2 + 4N_2$$

Neither chromium silicide is actually stoichiometrically 'pure', containing up to 25 atomic % oxygen. The silicide phases are believed to be defect structures similar to those observed for iron silicide [180].

4.2.3. Microstructural Variation of Sintered Reaction-bonded A1 Ceramics

The microstructure of SRBSN variants of composition A1 were generally similar to the pressureless sintered equivalent (fig. 4.3). However the β grain aspect ratio was lower for the SRBSN materials. A small volume (1-2 vol.%) of 'free' silicon was observed in the SRBSN ceramics, which was residual from the nitriding stage. A small increase in bulk porosity was apparent in the SRBSN processed ceramics relative to the SSN materials.

4.2.4. The Microstructure of Pressureless-Sintered Ceramic A2

It was apparent that, after pressureless-sintering at temperatures up to 1700°C, the densification level of samples of ceramic A2 was not as high as ceramic A1. A relationship between density and sintering temperature was not observed with the sample sintered at 1600°C having a higher density than that processed at 1700°C.

EDX microanalysis of the sintered samples and green state A2 revealed a considerably lower average magnesium level than composition A1 (using essentially identical additives), with a high variation in magnesium concentration from one area to another. The intergranular matrix phase was primarily a binary Y_2O_3-SiO_2 liquid in most regions

with small amounts of MgO in the remaining areas.

This composition was not studied any further, except for the Pyrex encapsulated HIP investigation (Chapters 5 and 6), because of the high degree of inhomogeneity that had arisen from mixing at T&N Ltd.

4.2.5. The Microstructure of a Commercial Y-Si-Al-O-N Ceramic: LCS 201

LCS 201 is a commercial grade high nitrogen content Si-Al-O-N ceramic which has a crystalline second phase rather than the more typical glassy second phase of the AED ceramics (A1).

The bulk microstructure consisted predominately of fine elongated β'-Si_3N_4 grains of substitution level $Z = 0.46$, giving a β' composition of

$$Si_{5.54}Al_{0.46}O_{0.46}N_{7.54}$$

(fig. 4.4a). A bimodal grain size distribution was observed, with an average aspect ratio of about 2:1 and β' grains in the size range 1 to 5μm. A small volume (~ 5 vol.%) of α'-Si_3N_4 was also present in the bulk ceramic, with a composition of

$$Y_{0.5}Si_{10.6}Al_{1.4}O_{1.4}N_{14.6}.$$

α' formation is typical in high nitrogen content Si-Al-O-N's, with yttrium acting as an α' stabilising element [181,182]. The crystalline intergranular phase was primarily yttrium-aluminium garnet, comment referred to as YAG ($Y_3Al_5O_{12}$), although small amounts of the Y-Si-O-N quaternary phase N-α-wollastonite were detected (fig. 4.4b). The presence of YAG as the main crystallisation product arises from the high 21R Si-Al-O-N polytypoid content in the starting material, moving the overall matrix composition towards the garnet phase field.

The as-received surface microstructure consisted of a uniform layer, – 25-30μm thick, of α'-Si-Al-ON crystals of approximate composition

a

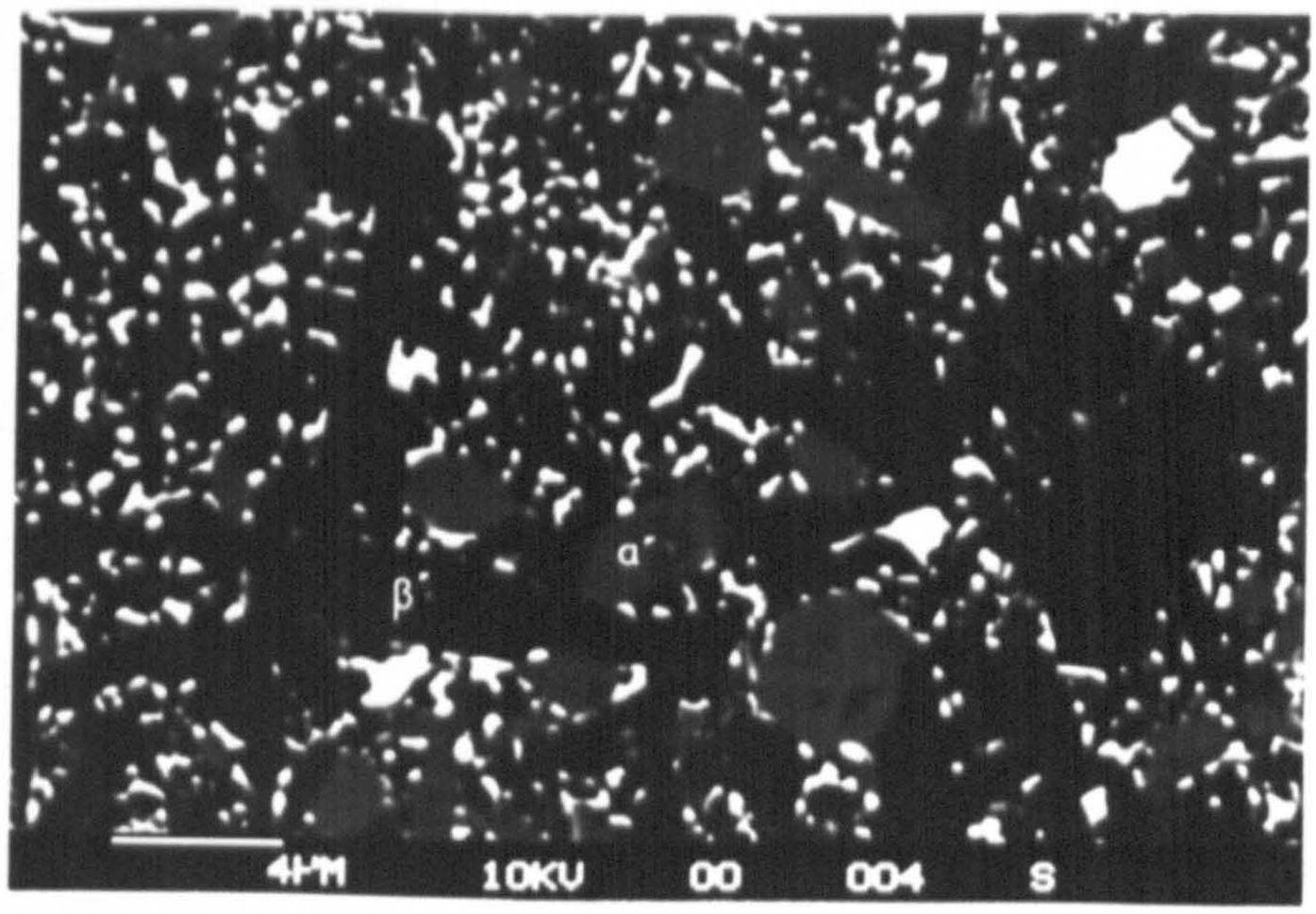

b

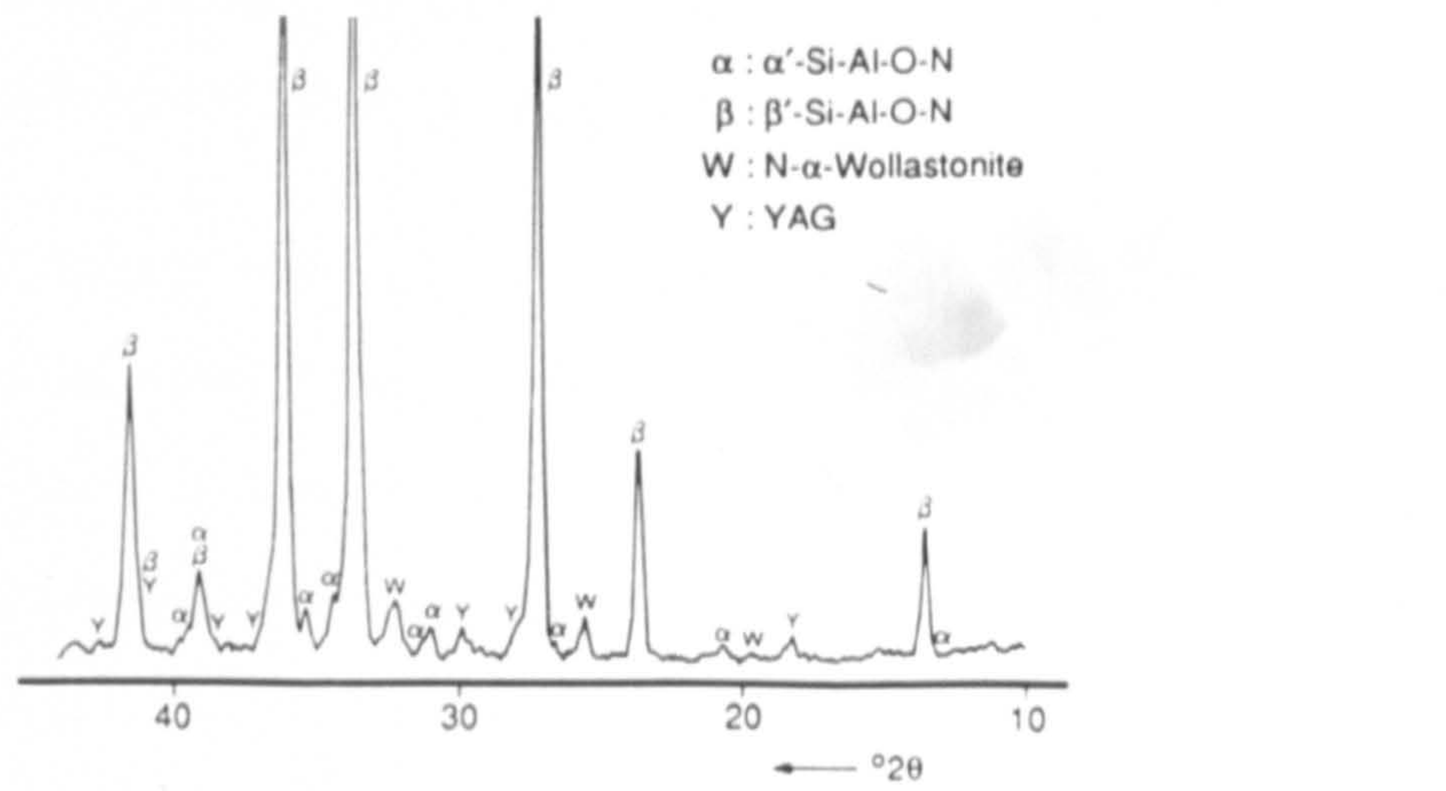

c

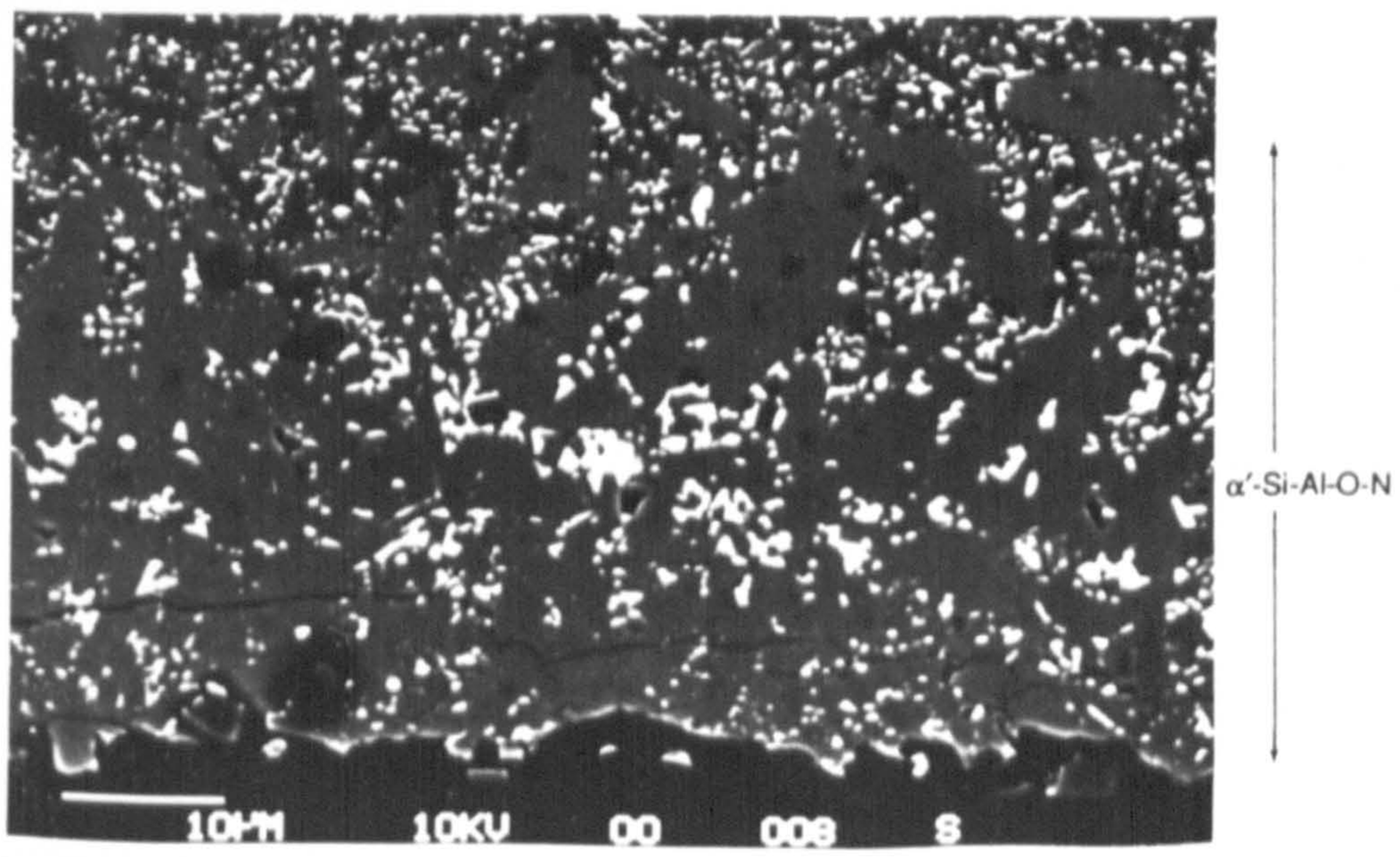

Figure 4.4 a) SEM micrograph showing the bulk microstructure of the commercial LCS 201 type ceramic, demonstrating α'-Si-Al-O-N re-precipitation. b) XRD demonstrates the formation of YAG and the Y-Si-O-N quaternary phase N-α-wollastonite. c) SEM micrograph of the as-received surface microstructure showing the formation of a uniform α'-Si-Al-O-N layer.

$$Y_{0.62}Si_{10.26}Al_{1.74}O_{1.75}N_{14.25}$$

(fig. 4.4c). The α′ grains, up to 15μm in length, were of similar aspect ratios to those in the bulk ceramic. A lower matrix phase volume was present within the α′ layer.

4.3. THE EFFECT OF HIP PROCESSING UPON THE MICROSTRUCTURE OF PRESSURELESS-SINTERED Si_3N_4

4.3.1. The Densification Behaviour of Si_3N_4 Ceramics Subjected to Post-Sinter HIPing (A1, LCS 201)

The variation of pre- and post-HIP density of ceramic A1 (SSN) with sintering temperature, prior to HIPing, is shown in figure 4.5. It can be seen that full densification is not obtained, after HIP, for any of the sintering conditions used. It is also clear the highest sintered densities show the smallest density increase after HIP.

The post-HIP density of the LCS 201 ceramic was essentially unchanged from the as-received ceramic, which is already near to the theoretical density, however it is believed that HIP may help to close the few isolated micro-pores remaining in the as-received ceramic, thus improving the material reliability (this is assessed via Weibull modulus determination for LCS 201, described in section 4.4.1).

4.3.2. Microstructural Variation after HIP (A1, LCS 201)

The bulk microstructures of sections of ceramic A1, pressureless-sintered at 1400°C - 1700°C and HIPed for one hour at 1750°C and 130MPa, are shown in figure 4.6. Little change (except porosity volume) is observed in the final microstructures, despite the initial variation (with predominately α-Si_3N_4 in the sample sintered at 1400°C and a complete α- to β- transformation occurring when sintered at 1700°C).

XRD demonstrated a complete α- to β-Si_3N_4 transformation for all sinter-HIPed A1 specimens. The bulk intergranular matrix glass composition was essentially unchanged

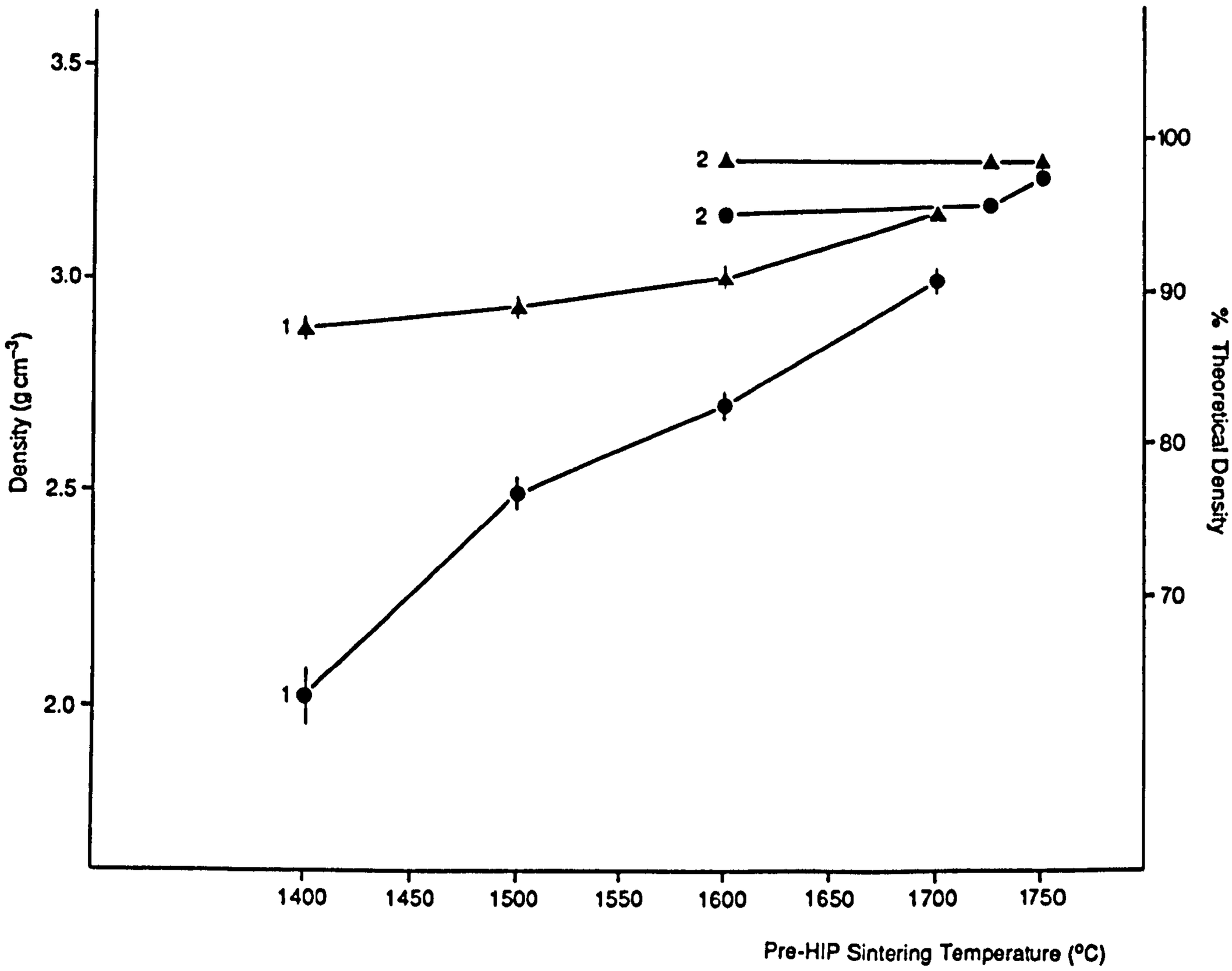

Figure 4.5 The variation of pre- and post-HIP density for ceramic A1 (SSN) as a function of the pre-HIP sintering temperature. Filled circles indicate the pre-HIP sintered density whilst the filled triangles show the post-HIP density of the same samples. Series 1 samples were pressureless sintered at Warwick and series 2 samples were over-pressure sintered at BCRA, Stoke-on-Trent. HIPing of all samples was conducted at 1750°C.

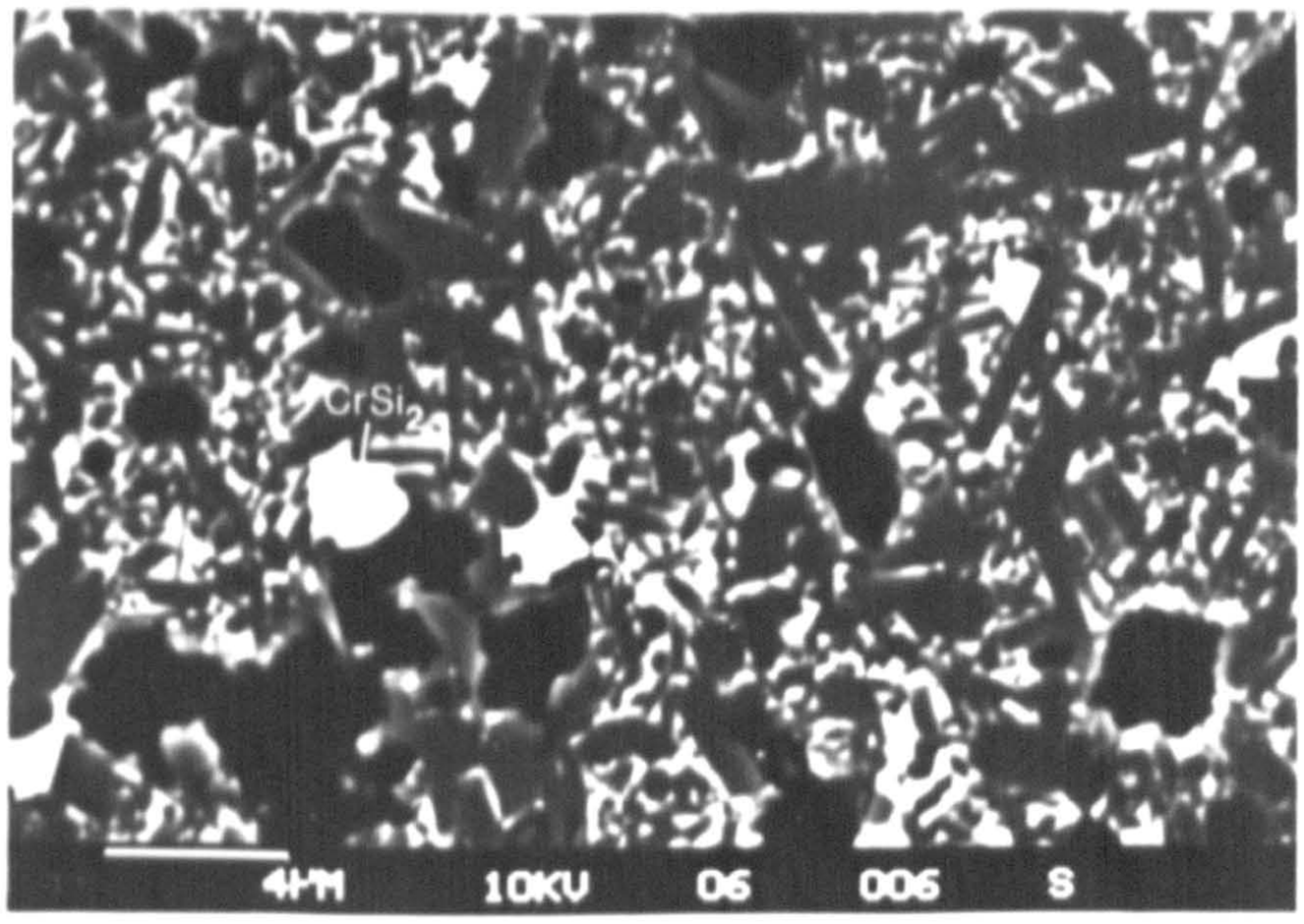

1400 °C

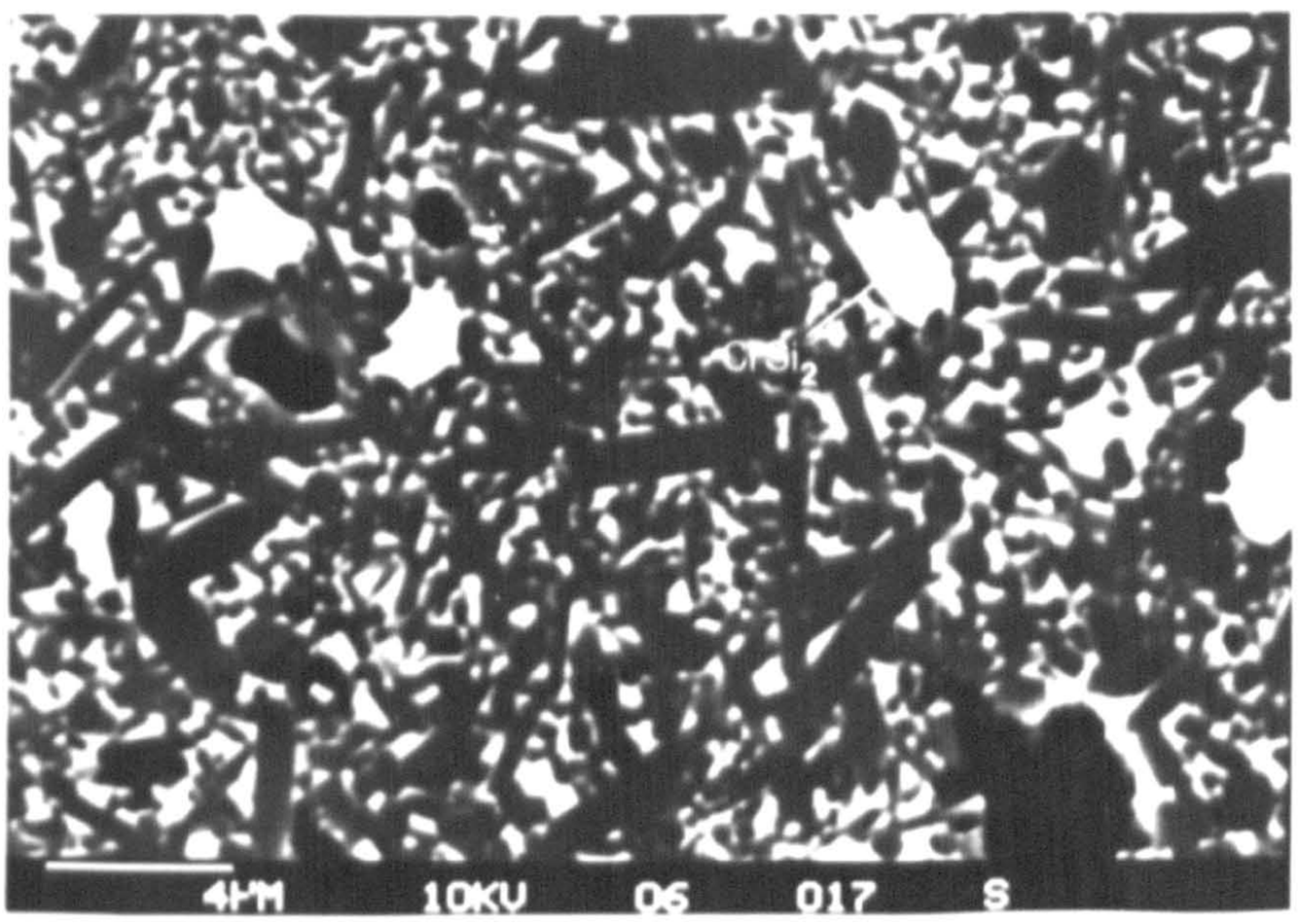

1700 °C

Figure 4.6 SEM micrographs showing the microstructural variation of HIPed A1 (SSN) with initial sintered density.

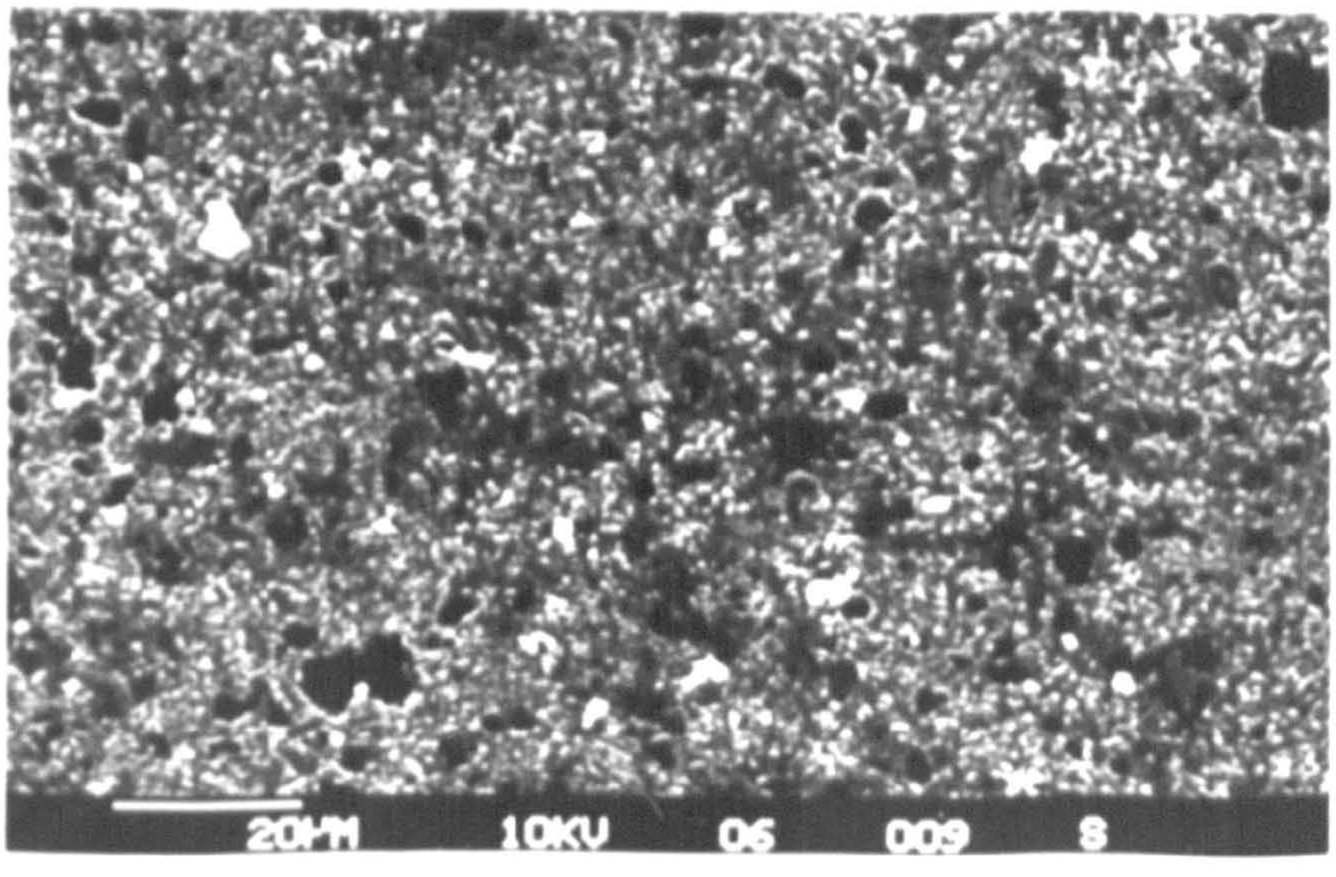

Figure 4.7 SEM micrograph showing the bulk pore morphology after sintering at 1400°C for 2 hours, followed by HIP.

after HIP, although some nitrogen dissolution in the glass of the lower pre-HIP density samples can be expected. This does not appear to effect the β- grain morphology, which is similar for all HIPed A1 samples and comparable to the as-received, pressureless-sintered ceramic (section 4.2.2). The bulk-pore morphology after HIP was generally spherical in appearance (fig. 4.7).

The near surface matrix composition was essentially identical to the bulk material, with only minimal loss of Mg^{2+} cations in some isolated regions, due to the use of a 'protective' $BN/Si_3N_4/MgO$ powder bed during the HIP of ceramic A1. Some variation in chromium silicide stoichiometry was apparent in the subsurface region (to an average depth of ~50μm in the A1 samples sintered below a temperature of 1600°C). An approximate measured Cr:Si ratio of 3:1 was detected in this subsurface region, corresponding to the cubic chromium silicide form (Cr_3Si). Additionally some regions of (predominately) pure chromium (with up to 10% Si) were observed. The regions are believed to be mixed Cr_3Si/Cr areas. It is believed that the chromium silicide phase becomes increasing unstable as the glass phase nitrogen content is increased, via dissolution of the pressure transmitting medium. The driving force and mechanism of this interaction is not understood and will not be discussed further.

The bulk microstructure of the LCS 201 ceramic was similar to the as-received material, with (~ 5 vol.% α′-Si-Al-O-N, and 8-9 vol.% matrix phase (fig. 4.8a). XRD demonstrated the reversion of the predominately YAG crystalline matrix to a Y-Si-Al-O-N glass (fig. 4.8b). Heath demonstrated that YAG reversion, in inert atmosphere, occurs at 1525°C [44]. A subtle increase in β′-grain coarseness was apparent in the bulk ceramic, coupled with a slightly more equiaxed β′ structure. A considerable increase in α′-Si- Al-O-N grain size was apparent at the as-received surface of HIPed LCS 201, with preferential grain coarsening apparent (with a marked reduction in the percentage of fine α′-grains present in the α′/matrix layer), shown in figure 4.9a. A higher α′- aluminium (and yttrium) level was observed in the surface layer with an approximate composition of

a

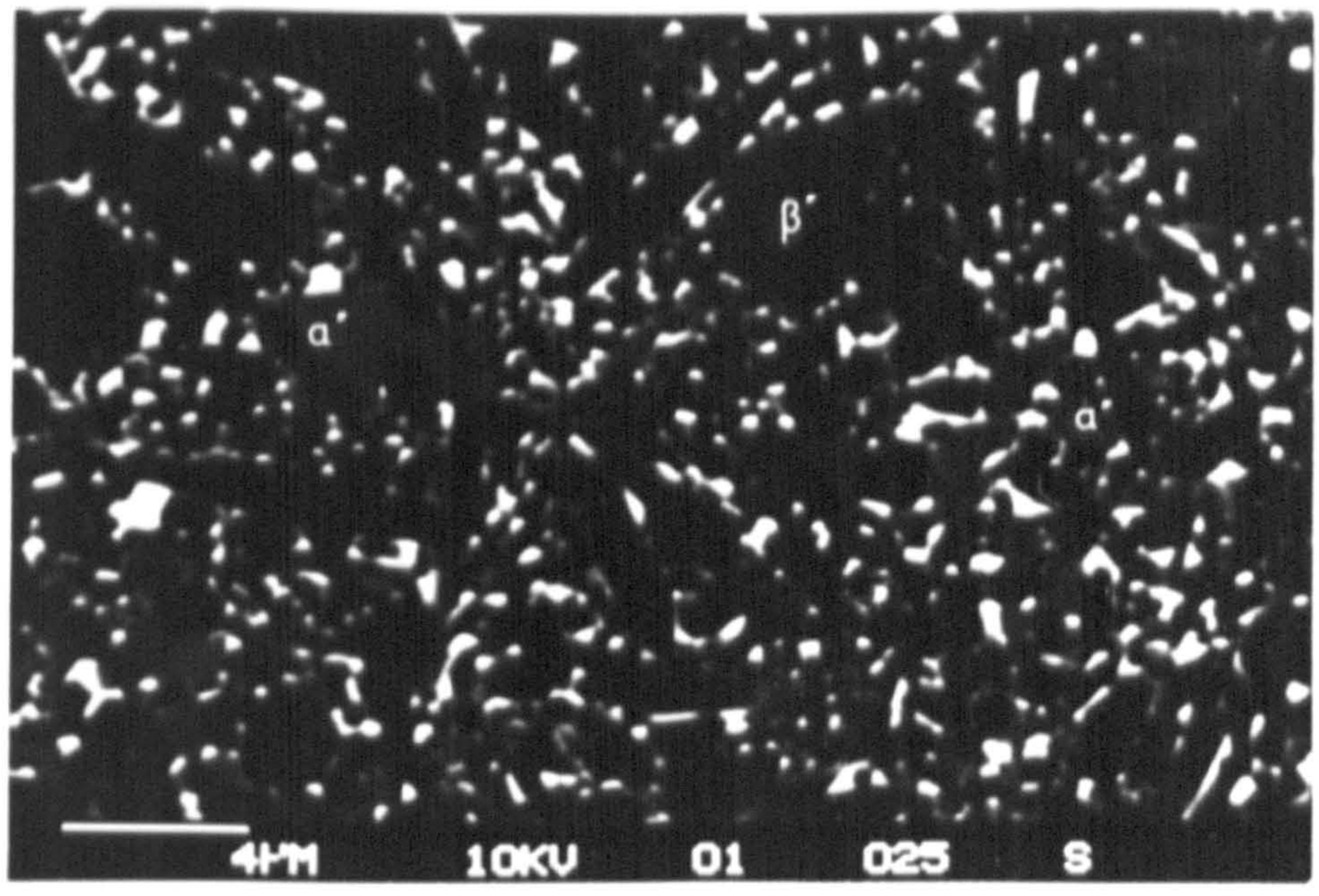

b

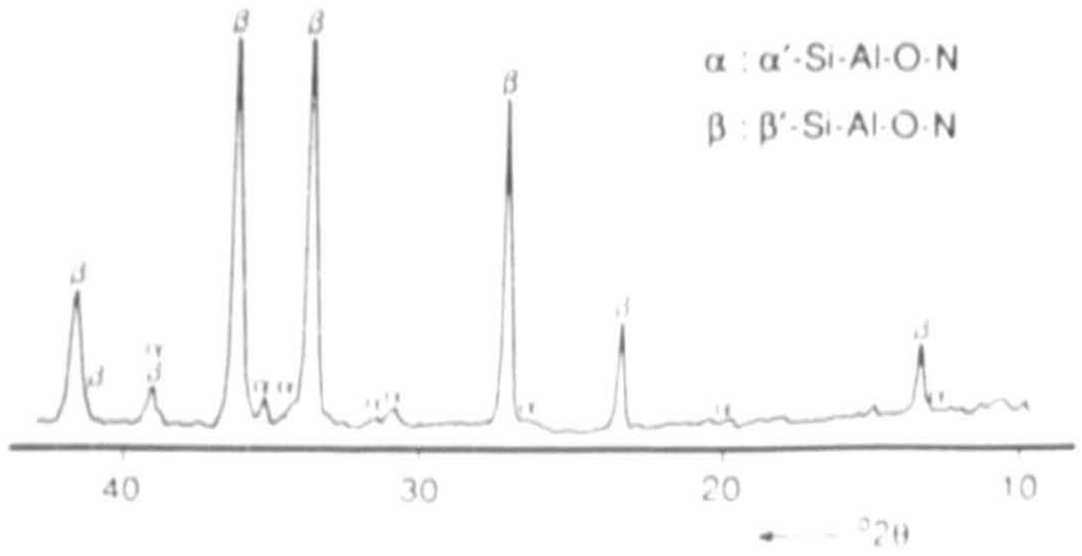

Figure 4.8 a) SEM micrograph of the bulk microstructure of HIPed LCS 201 showing α′ retention. b) XRD demonstrates a reversion of the YAG matrix to glass.

a

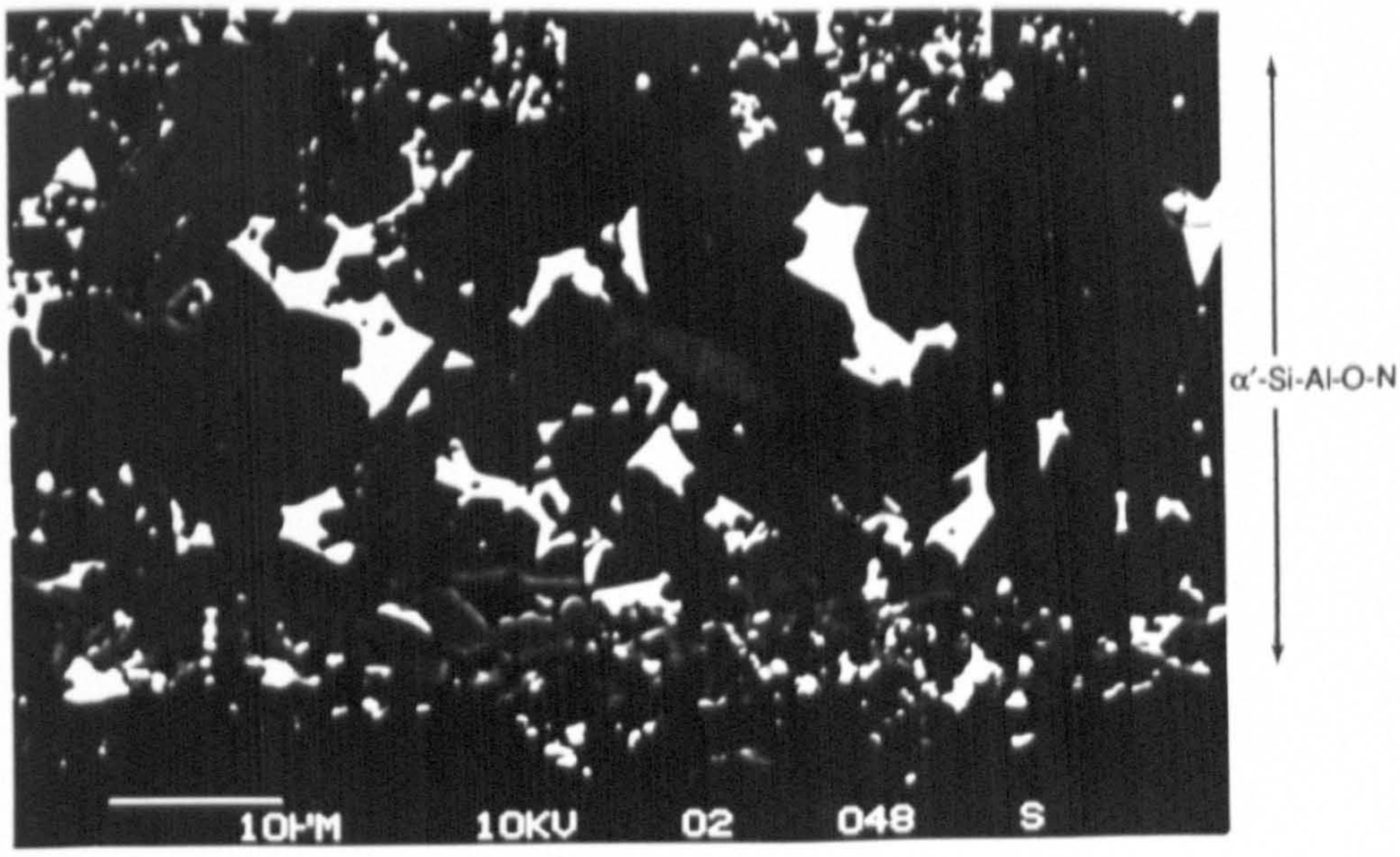

b

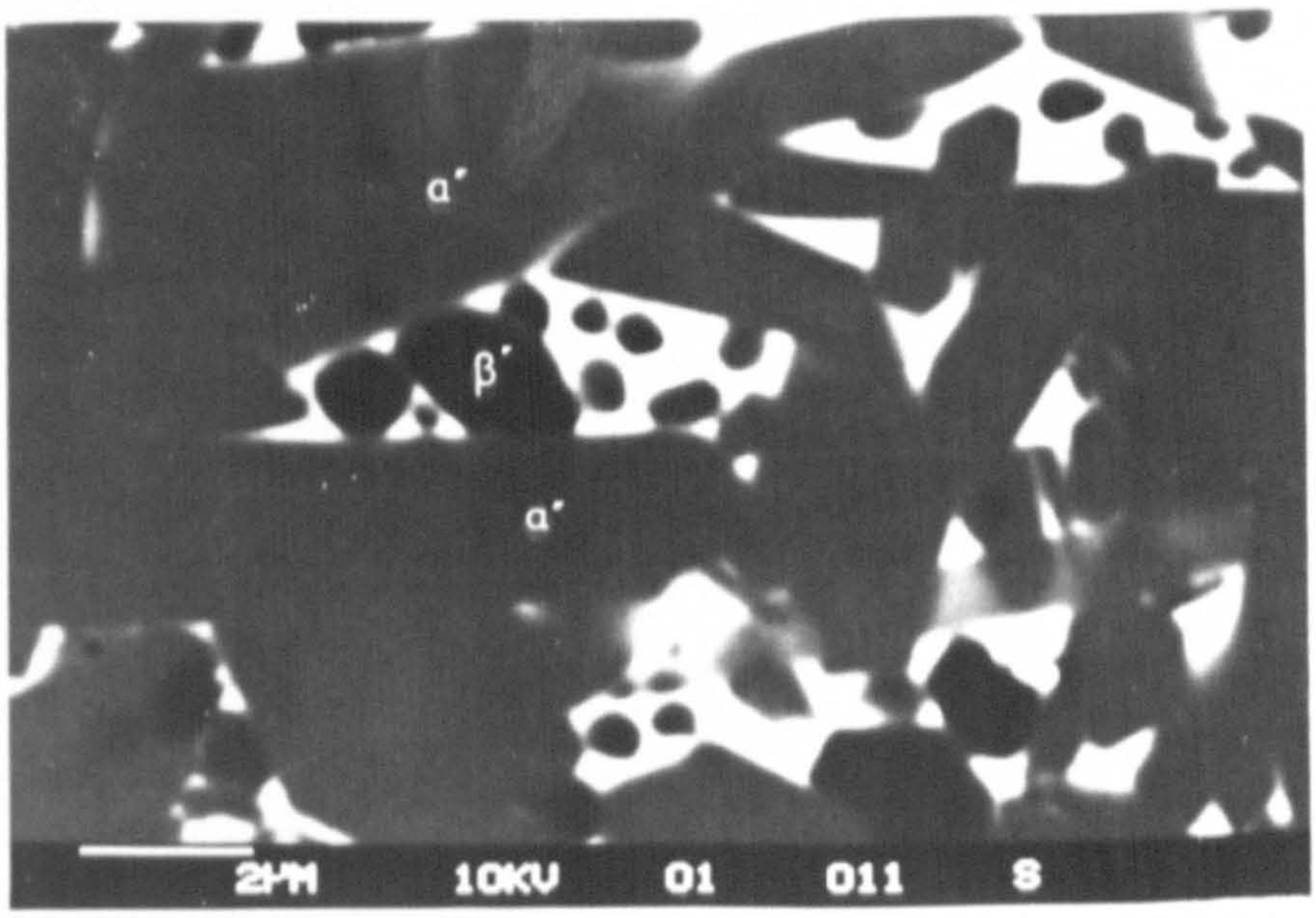

Figure 4.9 a) SEM micrograph of the surface microstructure of HIPed LCS 201, showing a considerable increase in α' grain size. b) SEM micrograph of β' grain formation between the larger α' surface grains.

$$Y_{0.7}Si_{10.2}Al_{1.8}O_{1.8}N_{14.9}$$

calculated from the formula devised by Jack [182]. This is a higher α′ substitution level than previously reported for LCS 201 type ceramics [183], and this effect may arise from the high nitrogen pressure at the ceramic surface increasing the matrix nitrogen content (via dissolution). An increased level of α′ stabilizing yttrium was also apparent in the surface α′ layer. The matrix phase in the α′ surface layer had a stoichiometry approximating to $Y_2Si_2O_7$, although levels of aluminium were detected (fig. 4.9a). No crystalline matrix phase was detected via XRD and it is believed that the matrix phase in a nitrogen rich glass, of lowered Al concentration, from loss to the higher substitution α′ grains. Further evidence for this behaviour is observed in the precipitation of fine β′ grains between the large α′-Si-Al-O-N grains during cooling (fig. 4.9b).

A high degree of preferred growth orientation was observed, via XRD, in the α′ surface layer, with growth parallel to the (100) plane, with only weak XRD peaks detected for the α′ surface layer and considerably stronger peaks recorded for perpendicular planes, (001) etc.

The α′ grain structure below the surface was similar to the bulk material, although generally a larger grain size was apparent.

A thin (3-5μm thick) mainly α′-Si-Al-O-N layer was formed at the exposed surface of the bulk microstructure after HIP (ie. originally β′/YAG as opposed to coarse α′ grain structure), with the subsurface microstructure generally similar to the bulk ceramic.

4.3.3. The Microstructural Stability of Sinter-HIPed Silicon Nitride at Elevated Temperature

Sections of the sinter-HIPed ceramics A1 and LCS 201 were heat-treated (at 1650°C for 2 hours in an inert N_2 atmosphere) to examine the microstructural stability after HIP. Hirota *et al* reported evidence of gaseous nitrogen evolution from the ceramic matrix

phase after HIP for 14 hours at 1750°C / 126MPa [148].

No obvious evidence of gaseous pore formation was apparent in any of the HIPed ceramic sections studied here after post-HIP heat treatment at 1650°C. The pore formation observed by Hirota was generally fine scale even after a 14 hour HIP treatment. Although this particular effect requires further study it is believed that excessive gas evolution will not occur unless long HIP durations have been used.

4.4. THE EFFECT OF POST-SINTER HIP TREATMENT UPON THE PROPERTIES OF LCS 201 SILICON NITRIDE

4.4.1. Modulus of Rupture (MOR)

Values of MOR and Weibull modulus were derived for three processing variations of LCS 201 (presented in Table 4.3). Post-HIP heat-treatment was identical to the standard schedule of 1250°C for seven hours, followed by 1400°C for five hours.

Processing route	MOR (MPa)	Weibull modulus (m)	Statistical frequency
1. As-received (sinter+H.T.)	693±85	15	9
2. As-received +HIP (*)	780±85	14	16
3. As-received +HIP+HT	681±29	27	8

Note: (*) Glass matrix

Table 4.3 Summary of the modulus of rupture (MOR) values obtained for various LCS 201 ceramic variants

The data obtained for Weibull modulus calculation is presented in figure 4.10. It can be seen that a significant improvement in the Weibull modulus was obtained for the HIP plus heat-treatment samples. Further research in this area is required as the statistical

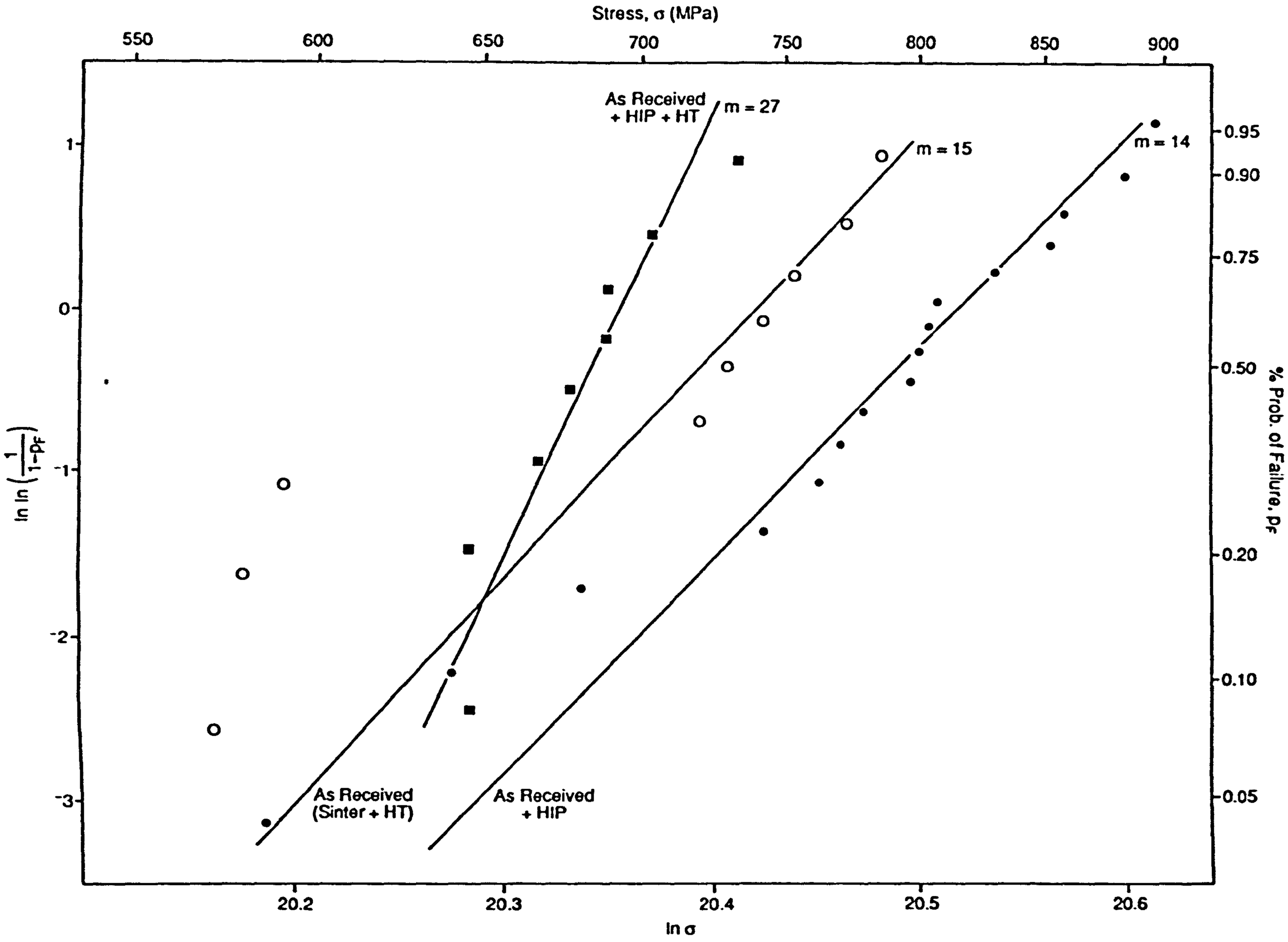

Figure 4.10 Weibull modulus determination for HIPed LCS 201 based ceramics, including the as-received material.

representation is small, with only eight breaks. The slight reduction in overall MOR for this sample may be attributed to an overall (subtle) grain-coarsening effect in the ceramic microstructure or to the retention of residual stresses after the crystallisation heat-treatment. Ziegler *et al* also reported an overall increase in the Weibull modulus but negligible variation in strength [147]. The improvement in Weibull modulus can be attributed to a general micro-pore removal. This reliability improvement should also be observed for the HIPed LCS 201 prior to heat-treatment. It can be seen from Table 4.3 that this is not in fact the case. However, examination of the individual fracture stress results revealed three values below 700MPa (more than 100MPa less than average). Ignoring these values, due to either $FeSi_2$ inclusions or surface machining flaws reducing the fracture strength, improved the recorded Weibull modulus to $m \approx 19$, and reduced the standard deviation error to half its original value.

An improvement in Weibull modulus can be obtained by post-sinter HIP processing, following the mechanism of micro-pore removal or size reduction. Ultimately though improvements in reliability will be limited by processing inhomogeneities, particularly inclusions, which cannot be removed by HIP consolidation, and surface machining damage.

4.4.2. Oxidation Behaviour

The reversion of YAG to glass during HIP meant that the oxidation behaviour of HIPed LCS 201 was generally identical to the β′/glass materials studied by Heath [44], and as such will only be discussed briefly.

The oxidation kinetics of HIPed LCS 201 were determined from oxide scale thickness measurement of sections heat treated at 1300°C and 1350°C for a range of times up to 100 hours (fig. 4.11). Understandably the oxidation rate was considerably greater (below 1350°C) than β′/YAG materials. Comparison with the oxidation scale thicknesses observed by Heath during heat treatment of β′/glass ceramics showed them to be

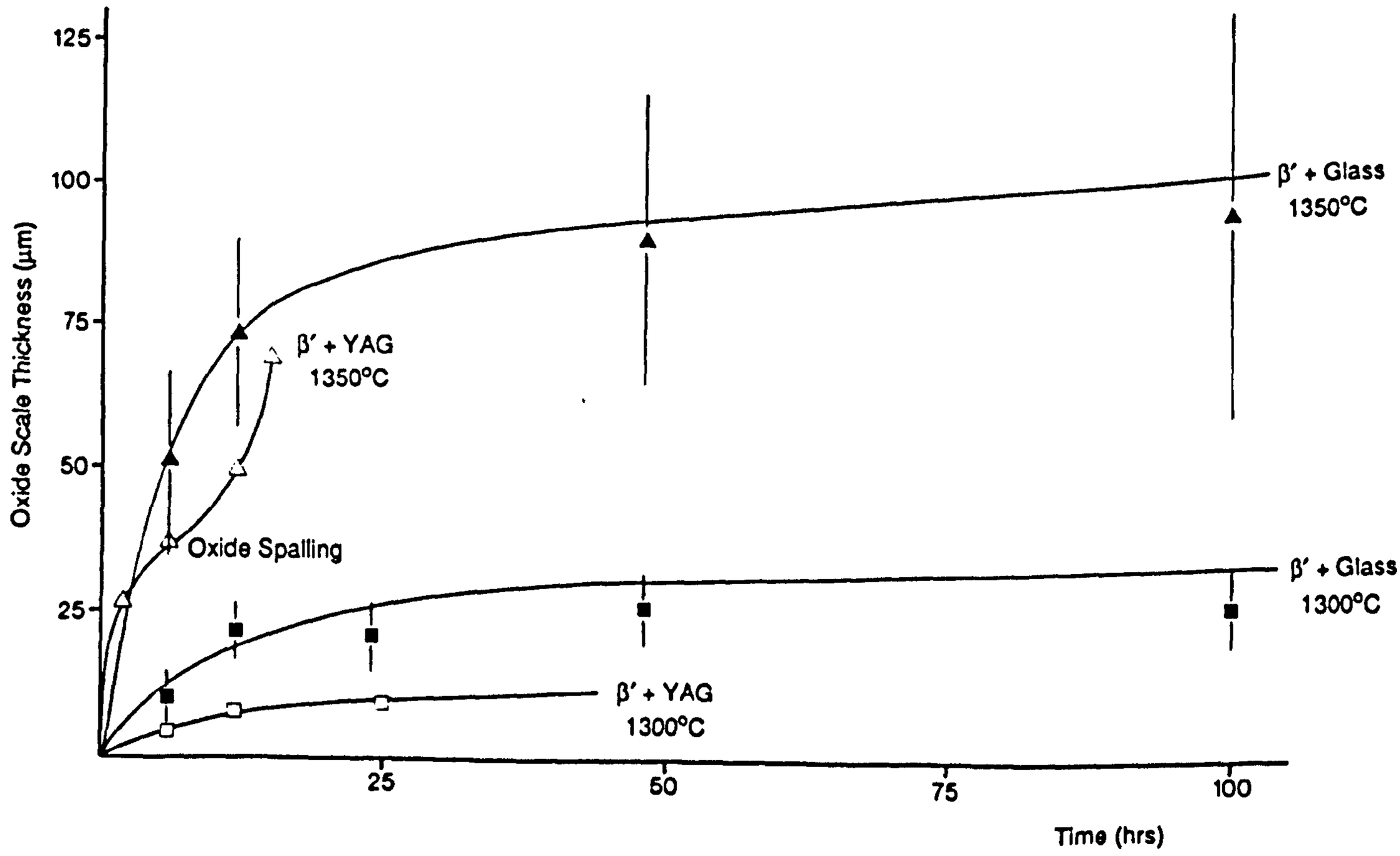

Figure 4.11 Oxidation kinetics measurement of HIPed ceramic LCS 201 (at 1300°C and 1350°C) together with curves for the typical as-received β′/YAG material (after Heath [44]). Regions of severe oxide spalling in the HIPed ceramic were ignored.

generally identical to those measured for the HIPed, reverted YAG, LCS 201. It is apparent that the potential problem of nitrogen dissolution in the surface matrix phase during HIP does not have a significant long range effect upon the bulk intergranular matrix composition or viscosity. This behaviour is generally consistent with the observations regarding surface α′ growth which is relatively short range (to a total depth of 20 - 30μm, including subsurface α′ volume increase). If considerable nitrogen dissolution was apparent in the bulk LCS 201 ceramic it may be expected to increase the matrix glass viscosity, which would tend to reduce the post-HIP oxidation rate as material transport would be slower.

4.5. DISCUSSION: SINTER-HIP DENSIFICATION

The failure of sinter-HIP samples to achieve full density was not predicted prior to processing, as it is possible to 'over-pressure'-sinter identical ceramics to near theoretical density. Ziegler *et al* also observed a similar failure to attain complete consolidation after sinter-HIP processing, even for silicon nitride ceramics where 95% TD < ρ_{sinter} < 100% TD [147]. Hirota *et al* did not achieve theoretical density for silicon nitride (with Al_2O_3 and MgO additives) until a HIP cycle duration of six hours was exceeded [148]. Two differing mechanisms were proposed by these authors. Ziegler proposed that β-'grain-interlocking' occurs at high densities inhibiting further densification. This mechanism is questionable as Ziegler utilised the glass-encapsulated HIP process to fully densify identical compositions. Similar complete consolidation was obtained for glass encapsulated HIP of ceramic A1 during the current programme. Hirota measured a high proportion of gaseous nitrogen dissolution in the grain boundary matrix phase after extended HIP, which considerably altered the glass viscosity by systematically nitriding grain boundary SiO_2 to Si_3N_4.

At present no mechanism can be proposed to fully explain the incomplete densification. In the lower sintered density samples of ceramic A1 it is clear that N_2 gas pressure build-up in the interconnecting porosity inhibits full densification, with spherical pore formation apparent.

It is possible that the state generally referred to as 'closed-porosity' (> 93% TD) is not quite as described, with a finite amount of fine scale surface connecting porosity, alternatively nitrogen dissolution in the sub-surface matrix phase may allow in-diffusion to internal pores leading to the creation of internal pore-pressure despite the apparent 'closed-porosity' state. Nitrogen dissolution in the sub-surface of sinter plus HIP ceramics has been observed during the current programme, in the form of microstructurally modified surface and sub-surface zones. Further investigation is required to quantify the effect of nitrogen dissolution upon the ceramic microstructure and properties.

Sinter plus HIP processing did not improve the room temperature mechanical properties of LCS 201 by any significant amount. The Weibull modulus of HIPed/heat-treated LCS 201 was observed to be greater than that recorded for the as-received ceramic. However, further study of this behaviour is required as only a small statistical group was examined. Additionally negligible improvement was apparent for the β′/glass (HIPed) LCS 201.

A partial improvement in Weibull modulus for near theoretically dense silicon nitride can be obtained by post-sinter HIPing following the closure of residual micropores. However HIP cannot remove processing inhomogeneities such as inclusions and post-HIP strengths will still be partially dependent upon the mechanical surface state.

Although sinter-HIP has been widely accepted as a consolidation method in the powder metallurgy industry, very little information has been published regarding the sinter-HIP densification of silicon nitride. The need to optimise processing variables to obtain near theoretical density will be an important factor in deciding the future applicability of this technique. It is possible that the greatest benefits will be obtained when using a lower gas pressure in combination with an increased processing temperature, such that the counteraction of densification (via applied gas pressure acting within the ceramic interconnecting porosity) in inhibited.

CHAPTER FIVE

THE DEVELOPMENT OF GLASS ENCAPSULATION TECHNIQUES FOR THE HOT ISOSTATIC PRESSING OF SILICON NITRIDE

5.1. INTRODUCTION

The continuing desire to advance the current operational temperature and lifetime of advanced silicon nitride based ceramics has moved the emphasis of silicon nitride based research at Warwick University away from the pressureless sintered Si-Al-O-N type materials, with an operational ceiling temperature of ~1300°C, towards materials utilising a high viscosity, low volume intergranular phase. Such refractory second phases are generally based on either Y_2O_3-SiO_2 or Nd_2O_3-SiO_2 binary systems which offer the potential for use at temperatures up to 1400°C for extended periods. However, full densification of these materials is impossible via conventional pressureless sintering. Therefore pressure-assisted sintering, or as it is more commonly known hot-isostatic pressing (HIP), is required to obtain dense ceramic articles. Two simultaneous densification processes occur during HIPing, sintering and mechanical shear consolidation, allowing a reduction in the required processing temperature, often by >200°C (although dependent on material). However, the HIP consolidation of 'green' state ceramic articles (typical density ~65% T.D.) requires the use of an impermeable gas-barrier around the ceramic to prevent HIP gas ingress.

This chapter summarises the development of glass encapsulation routes for simple and more complex shaped ceramic articles using a variety of glass tube and powder compositions.

5.2. THE DERIVATION OF SiO_2 GLASS ENCAPSULATION METHODS

5.2.1. Silica Encapsulation Techniques and HIP Processing

Cold isostatically pressed billets of A1 ceramic (SSN) were cut into rectangular test bars of approximate dimensions 8 × 8 × 20 mm prior to encapsulation in fused silica tubing (Hereaus*). The tubing has an outside diameter (OD) of 15 mm with 0.5 mm wall thickness (WT). Lengths of ~320 mm were cut using a Tyslide peripheral diamond saw and subsequently heated at the centre of the length using an oxygen/natural gas torch, whilst rotating on a glass working lathe. When the heated area has attained its softening temperature the tube is pulled gently either side of the heated zone giving two 160 mm lengths, each sealed at one end. However, the glass thickness at the sealed ends is reduced by this process (fig. 5.1a).

The shaped preforms were placed in the tubes, which were then partially necked on the lathe, leaving the preform in an unsealed ampoule 60 mm in length at the end of the tube (fig. 5.1b). The partially necked tubes were evacuated to a pressure of 2×10^{-5} torr, using a Genevac rotary/diffusion pump system, and out-gassed for 3-4 minutes with an oxygen/natural gas hand torch at a temperature in excess of 500°C (fig. 5.1c). The out-gassing procedure was repeated until there was no loss in vacuum when the preform was heated. The ampoules were then sealed using the hand torch (fig. 5.1d).

Later specimens were shaped into solid cylinders, using an Elliot Universal grinder, for encapsulation in larger dimension silica tubing of dimensions 25 mm OD with 1.4 mm WT. These specimens were sealed as before with the exception of the initial sealing of one end. This was carried out using a gravitational flow method, heating the tubing but allowing it to deform under gravity and surface tension (fig. 5.2). Necking of the silica tube occurs, and thus it can be pulled to give two sealed ends of increased wall thickness.

---

* Supplied by Hereaus, West Germany

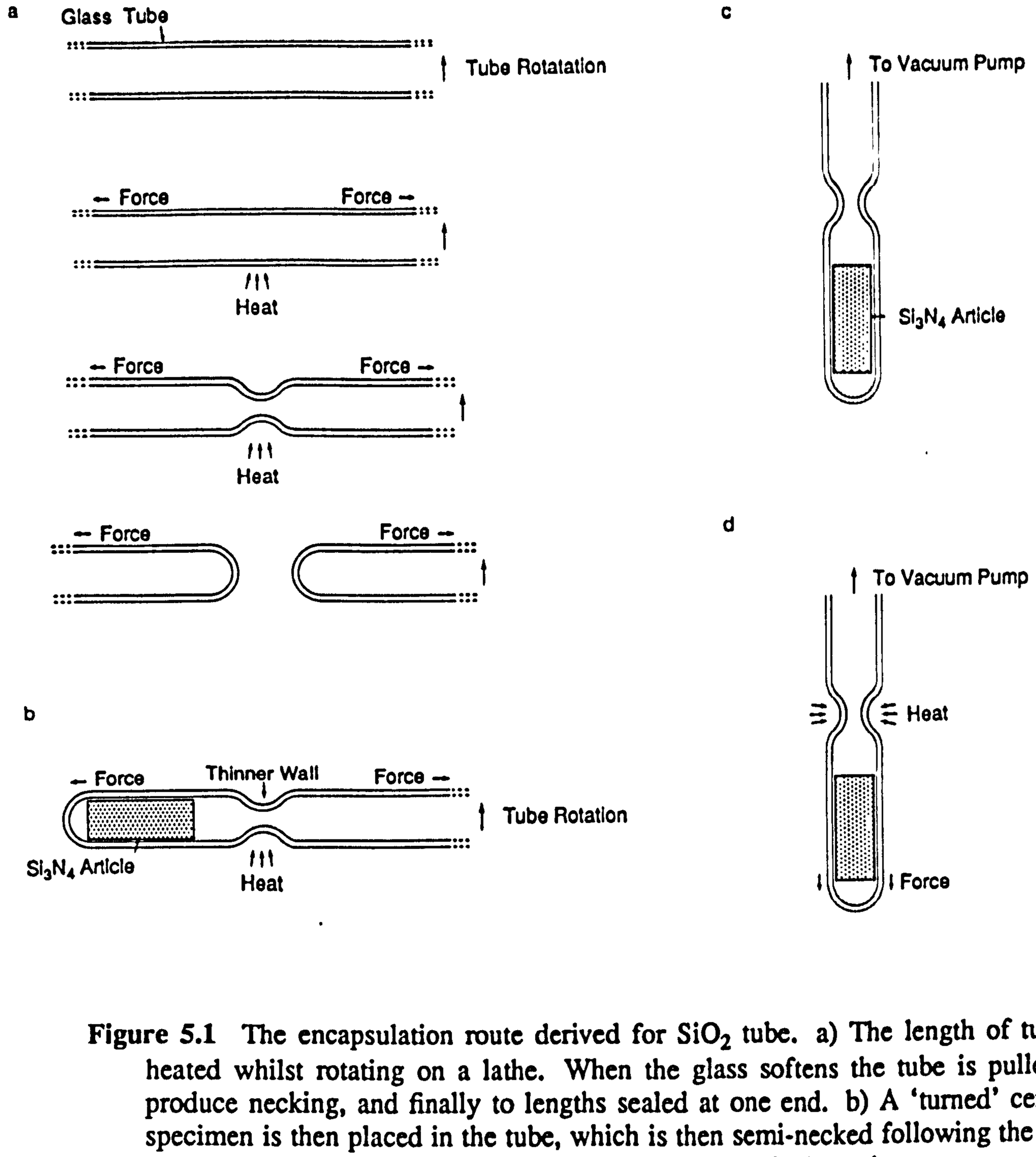

Figure 5.1 The encapsulation route derived for SiO_2 tube. a) The length of tube is heated whilst rotating on a lathe. When the glass softens the tube is pulled, to produce necking, and finally to lengths sealed at one end. b) A 'turned' ceramic specimen is then placed in the tube, which is then semi-necked following the route described in a). c) After necking the tube is attached to the vacuum system, outgassed and d) finally sealed.

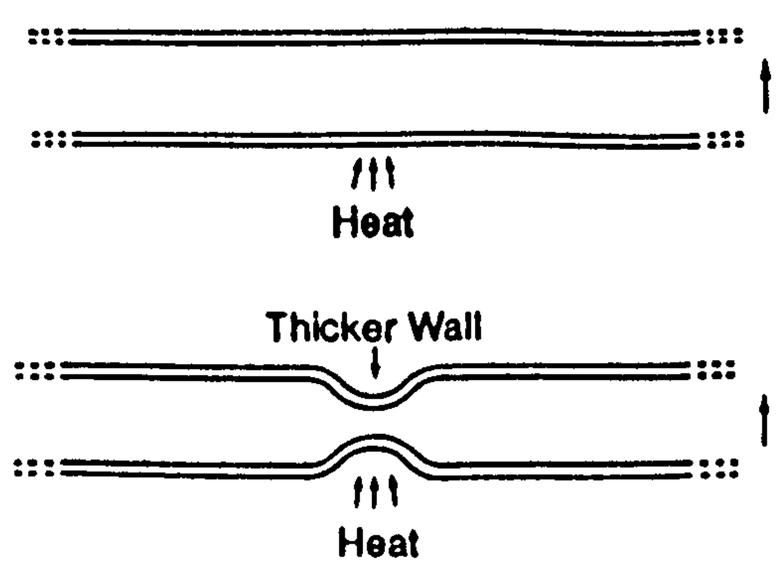

Figure 5.2 Static necking technique used for later examples to increase the glass thickness at the sealed ends.

Matrix crystallised Lucas 201 ceramic was also encapsulated in silica using this method. Two pieces of 201 were sealed into an ampoule with the intention of forming a HIP bond between them. The contact surfaces were ground flat to a surface finish of 10-20 μm. The 201 pieces were shaped by grinding to give a tight fit within the tubing and thus ensure contact between the faces.

HIPing was conducted in a laboratory scale Autoclave Engineers Inc. HIP unit (described in section 3.2.4). Encapsulated specimens were contained within a graphite crucible (fig. 5.3a), and supported by boron nitride powder to prevent any reaction between the silica and graphite. The HIP cycle devised for silica encapsulated specimens is shown in figure 5.3b. Nitrogen gas pressure application is delayed until the temperature has ramped to 1300°C, the approximate softening point of silica. Temperature and pressure are then ramped up (at $10^{\circ}C\,min^{-1}$) to the hold conditions, 1750°C and 107 MPa for one hour. A natural furnace cool was used after HIPing to prevent crystallisation of the intergranular glass phase.

5.2.2. Densification Behaviour of Silica Encapsulated Si_3N_4 (A1, LCS 201)

Silica encapsulated A1 billets were HIPed to 83-84% TD. Failure to obtain full density was caused by fracture of the silica ampoules during the initial ramp stage of the HIP cycle (prior to pressure application), allowing ingress of high pressure nitrogen gas into the porous billet during the hold period of the cycle. The high pressure gas acting within the interconnecting porosity of the ceramic can therefore be observed to inhibit densification as a comparable composition can be consolidated (>90% TD) via pressureless sintering

Optical and scanning electron microscopy revealed a high degree of porosity in the bulk material, decreasing near to the surface, indicating a temperature gradient acting through the specimen during HIPing. LCS 201 is already near theoretical density and there was negligible increase after silica tube encapsulated HIP.

a

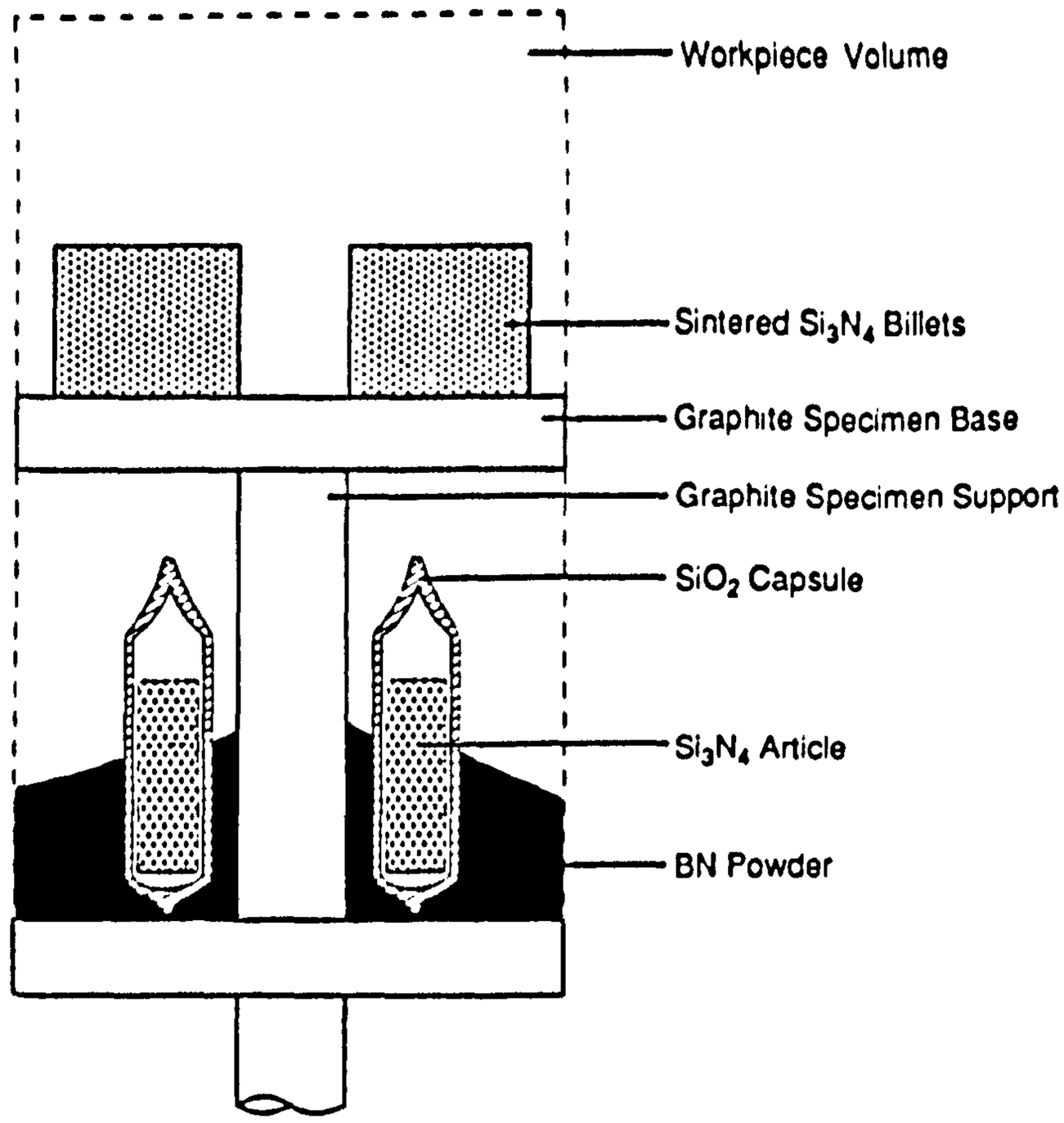

b

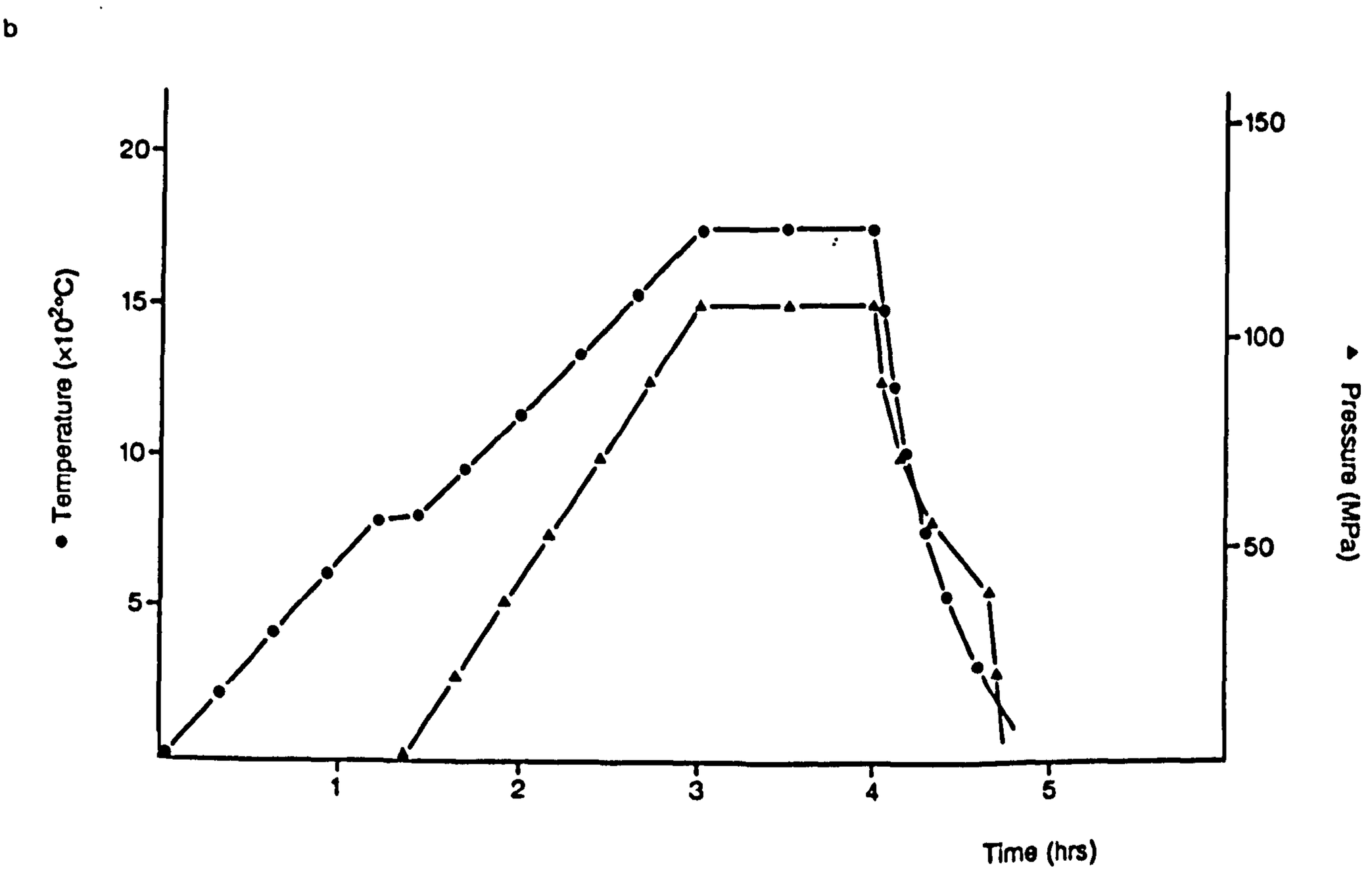

Figure 5.3 a) Schematic representation of the furnace/specimen placement during HIP processing of SiO_2 encapsulated specimens. Also included are sinter-HIP samples (described in chapter 4). b) Temperature/pressure cycle derived for HIP processing of SiO_2 encapsulated specimens.

5.3. PYREX GLASS TUBE ENCAPSULATION

5.3.1. Pyrex Encapsulation Techniques and HIP Processing

To solve the problems associated with the silica tube encapsulation method, Pyrex glass was chosen. The variation of the softening point and working temperature range for various easily obtainable glasses is shown in figure 5.4. The lower softening temperature of Pyrex tubing allows it to be manipulated more easily than SiO_2 when using the glass working lathe. A further advantage is the potential to lower the gas pressure application temperature (by >600°C) during the HIP processing of Pyrex encapsulated specimens. Care must be taken to prevent overheating the tubing during the encapsulation process. If overheating occurs small bubbles form in the molten glass, these are believed to be bubbles of oxygen given off during the decomposition of the borate additive in Pyrex.

Cylindrical billets of each of the powder compositions for HIPing were produced by grinding on an Elliot Universal grinder with a peripheral diamond wheel. The dimensions of each billet were approximately 20 mm length × 50 mm diameter. To prevent, or reduce, any reaction between the Pyrex encapsulant tubing and the billet, they were initially dip-coated in a slurry produced by mixing boron nitride powder and acetone. This mixture, however, had a tendency to 'flake off' when the compact was placed in the tubing and worked on the lathe. A more viscous boron nitride/collodion (in amyl acetate) composition was finally used because of its apparent success in isolating ceramic articles from the graphite die in hot-pressing fabrication. A 200-300 μm thick BN coating applied by painting in a slurry form. It was necessary to bake the coated billets prior to encapsulation to avoid burn-off of the organic components in the coating mixture. Baking was performed in a preheated fan assisted oven at 250°C for 12 hours.

Heavy wall Pyrex tubing was used for billet encapsulation, with dimensions of 26 mm outside diameter and 1.4 mm wall thickness. The Pyrex tube (Corning*) was delivered

* Supplied by Camlab, Cambridge

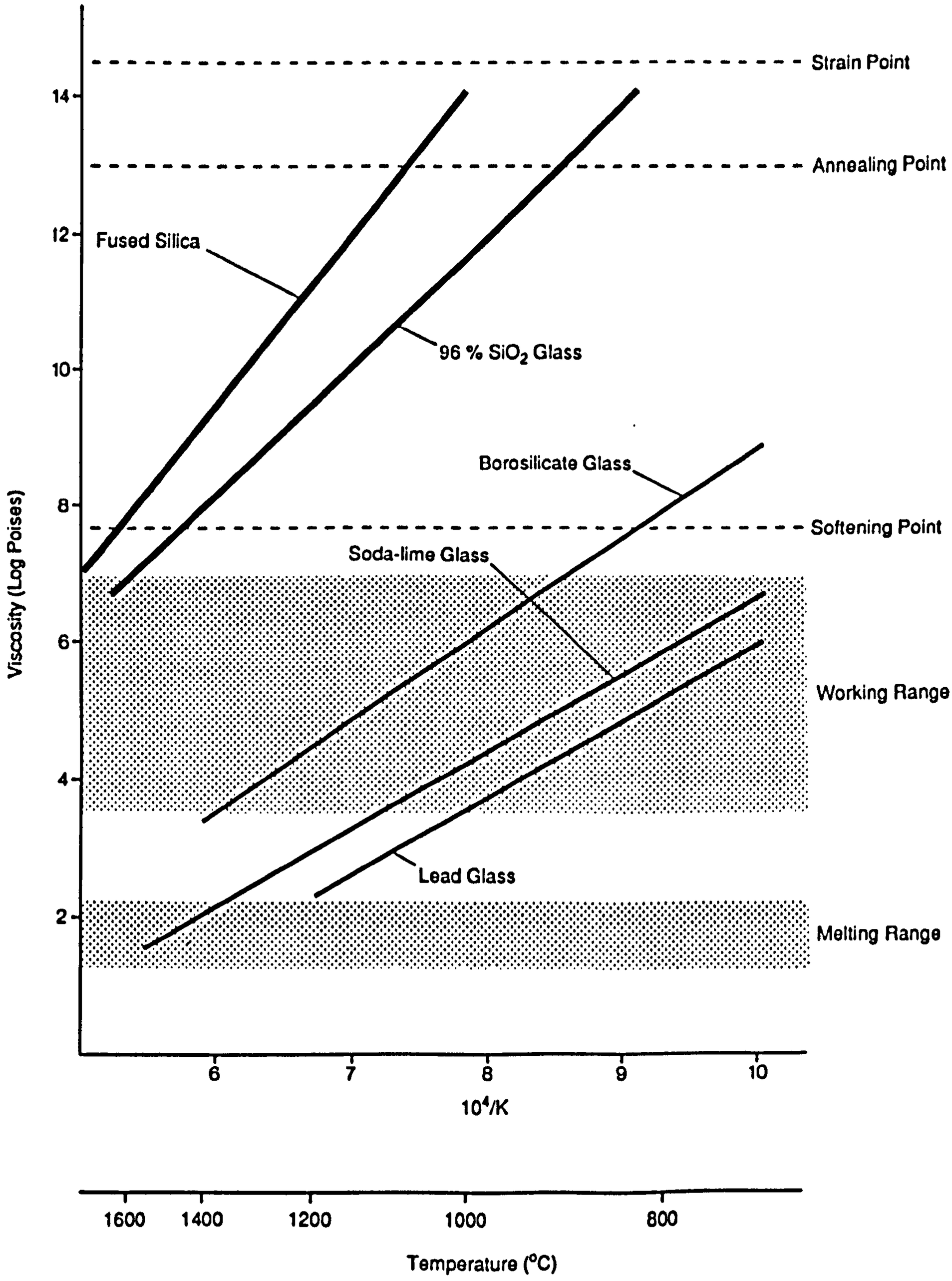

Figure 5.4 The variation in viscosity of certain glasses as a function of temperature. The annealing temperature is defined as the point at which the atomic mobility is sufficient to permit stress relief within 15 minutes; this corresponds to a viscosity of 10^{13} poises.

in 1500 mm lengths which were cut into three equivalent sections using a peripheral diamond saw. Boron nitride coated samples of silicon nitride were encapsulated in Pyrex tube using the following summarised route (similar to that shown in figures 5.1 and 5.2):

1. The 500 mm tube lengths are rotated on the glass working lathe and heated in the centre using an oxygen/natural gas torch. As the glass softens the centre of the tube begins to constrict under the combined influence of gravity and the surface tension of the glass. Gently pulling the ends of the rotating tube during the initial stage of softening aids this behaviour. When the glass viscosity is sufficiently reduced the tube constriction will close totally and the tube is pulled to produce two separate lengths, sealed at one end. The wall thickness of the sealed end is considerably increased using this static necking (typically from 1.4 to 4-5 mm) and, with continued heating, the sealed ends are made flat. The contact area of the ceramic billet on the sealed region of the tube is therefore increased and thus the risk of capsule failure from puncture by the sharp edges of the billet is considerably reduced. An 'oxygen free' natural gas flame is then used to reduce the thermal stresses that have occurred in the heated regions of the tube (relative to the unsoftened regions).

2. A coated silicon nitride billet is placed in the length of tube (~250 mm long), which is then attached to the glass working lathe. The lathe was tilted to an angle of ~20° to prevent the billet moving up the tube from the sealed end. Whilst held on the lathe the Pyrex tube is heated at a point ~100 mm from the sealed end (i.e. 30-40 mm from the top of the 50 mm long billet) and allowed to gradually constrict to an approximate internal diameter of 5 mm. Once the tube diameter is sufficiently reduced in the heated zone the heat source is removed and the glass allowed to cool.

3. The necked tube (containing the ceramic billet) is then attached to a Genevac vacuum pump. The semi-encapsulated billet was evacuated to 2×10^{-5} Torr and kept under vacuum at room temperature for a period of 12 hours. Hot-evacuation

was initially conducted using an oxygen/natural gas hand torch, with the billets repeatedly heated to a temperature of 200-300°C until no loss of vacuum occurs.

4. Once hot-evacuation has been completed, and with the tube still under vacuum, the necked section of the tube is sealed using the hand torch. This procedure is conducted by heating the necked region and, when the glass begins to soften, gently twisting the ampoule below. Continued twisting (and heating of the necked region) closes the internal tube diameter until it eventually seals and the enclosed ampoule can then be drawn from the length of tube.

5. With the ampoule removed from the tube the sealed end can be gently annealed using a natural gas flame on the hand torch. Some of the sealed Pyrex ampoules were found to have developed small cracks around the sealed area due to static fatigue of the glass. This occurred hours, or sometimes days, after sealing. An annealing process was devised and applied to all ampoules after this discovery. Heating and cooling rates for the annealing cycle were both 6°C per minute with a hold time of 60 minutes at the annealing temperature (560°C for Pyrex)

Compositions A1 and A2 were encapsulated in Pyrex Ampoules using this method, together with smaller boron nitride coated sections (20 mm length × 20 mm diameter) of compositions B1, C1 and C2, which were encapsulated together in a single ampoule. A re-usable graphite crucible was used to contain each ampoule, with the ampoule suspended in a BN powder bed to prevent contact with the graphite (fig. 5.5a). A revised HIP cycle was devised for the Pyrex encapsulated specimens, because of the lower softening point of Pyrex relative to silica. The HIP equipment is described in detail in section 3.2.4. The pressure application temperature was lowered to approximately 600°C for Pyrex, with the pressure application medium again being N_2 gas. The HIP cycle used is shown in figure 5.5b, with the pressing conditions being 1750°C at 130 MPa for one hour. A heating rate of 10°Cmin^{-1} was used during the initial stage of the HIP cycle. A natural furnace cool was used after HIP to prevent crystallisation of the matrix phase on

a

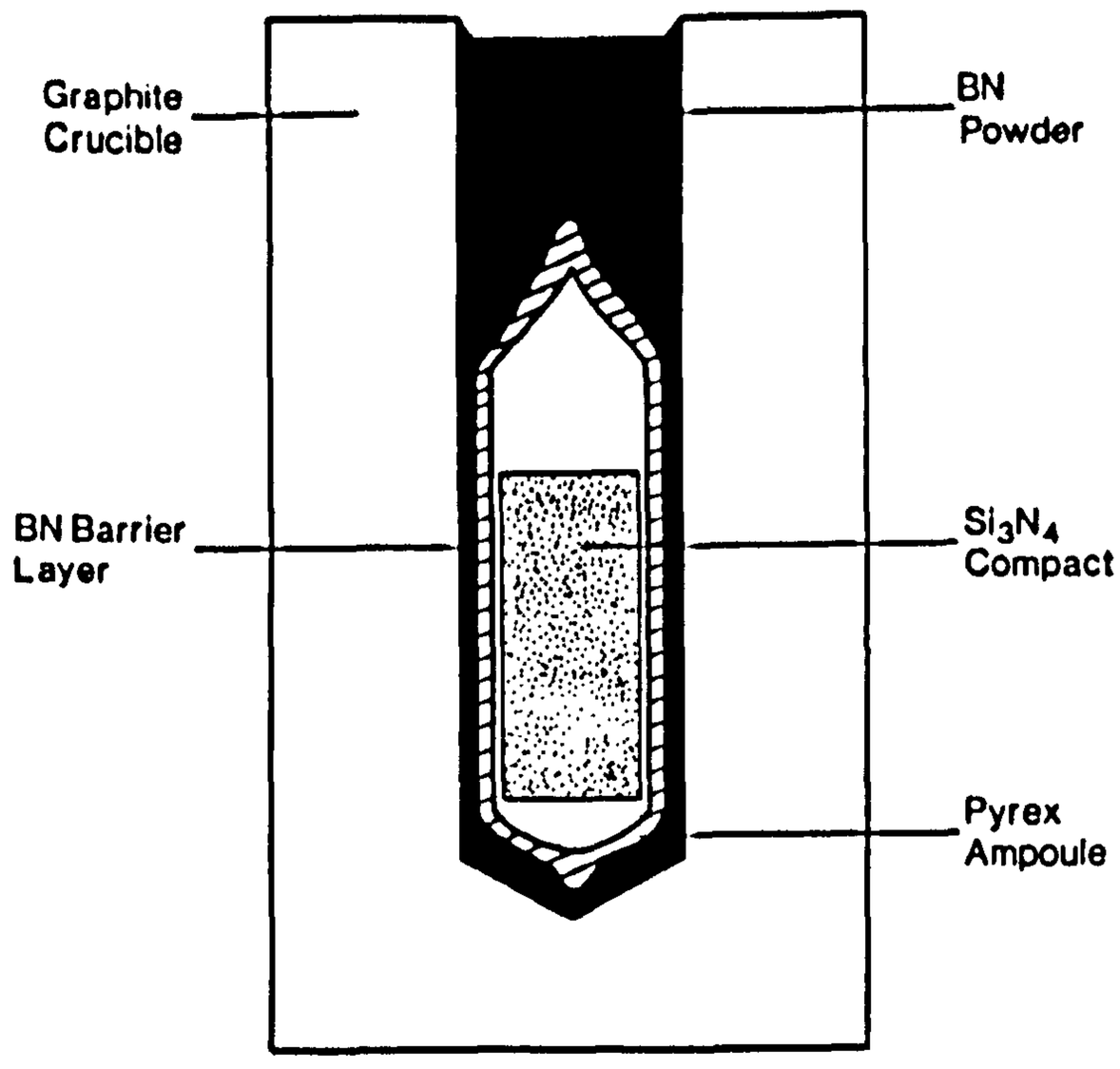

b

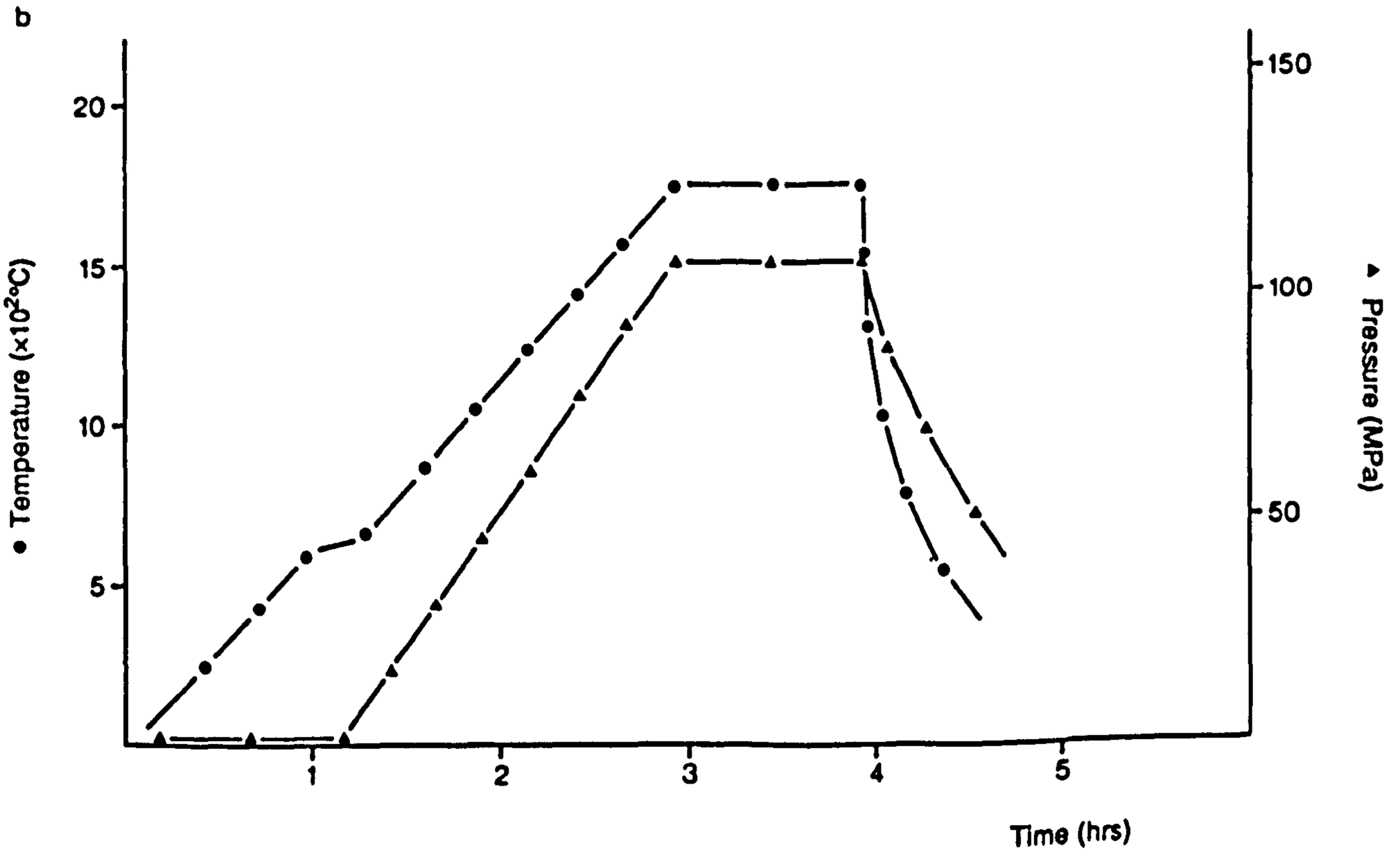

Figure 5.5 a) Schematic diagram of the specimen/crucible representation for initial Pyrex encapsulation technique. b) Revised HIP temperature/pressure cycle for Pyrex encapsulation.

cooling.

After HIP the ampoules were removed from the graphite crucible and sectioned using an annular diamond saw. The densities of the A1 and A2 specimens were found to be 2.97 and 2.95 gcm^{-3} respectively (~ 88% TD). The microstructure of these partially densified materials is briefly described in section 6.4.1. It was clear, from optical microscope examination of a cross section through the top of the billet, that both A1 and A2 billets had fallen slightly sideways during densification, puncturing the evacuated ampoules from the inside (fig. 5.6). This problem arose during an early stage of the hold period of the HIP cycle, when the encapsulant glass viscosity was lowest. A similar effect was observed for ceramics B1, C1 and C2, with comparable densities obtained.

Further sections of compositions A1 to A3 were cut and prepared as before, however a heavier gauge of Pyrex tubing was used (26 mm diameter with 2.0 mm WT) for encapsulation and the billet height to diameter ratio was reduced to 40 mm × 20 mm. Encapsulation was conducted following the previously described method with the exception that hot-outgassing was conducted using a vertical tube furnace. A steel frame was designed to hold the furnace around the semi-encapsulated billet whilst the length of tube is attached to the vacuum pump (fig. 5.7a,b). A stepped outgassing cycle was used (fig. 5.8), with each semi-encapsulated billet outgassed at 150°C, 300°C and finally 450°C with a two hour hold time at each temperature. After outgassing the furnace is lowered away from the Pyrex tube which, when cool, is sealed as previously described. The ampoule is then annealed at 560°C.

The initial specimen processed, of composition A3, was contained within a graphite crucible, shown in figure 5.9a. The sealed Pyrex ampoule was embedded in a coarse (0.25-0.50 mm) silica powder (Quintus Quartz). The silica powder, acid washed to remove the impurity Fe_2O_3 content, was used to increase the Pyrex viscosity at the ampoule/powder interface. A collodion (in amyl acetate)/boron nitride mixture was used to coat the internal walls of the graphite crucible, which was then baked at 400°C for 12

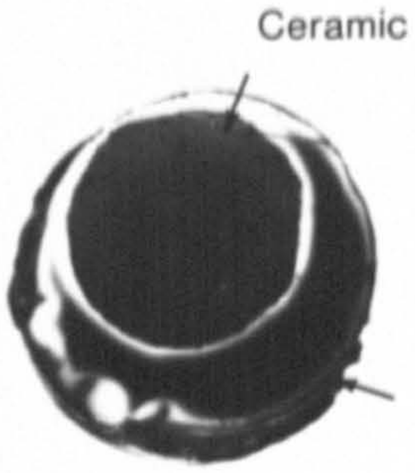

Figure 5.6 Cross-section through composition A2, demonstrating capsule puncture by the ceramic.

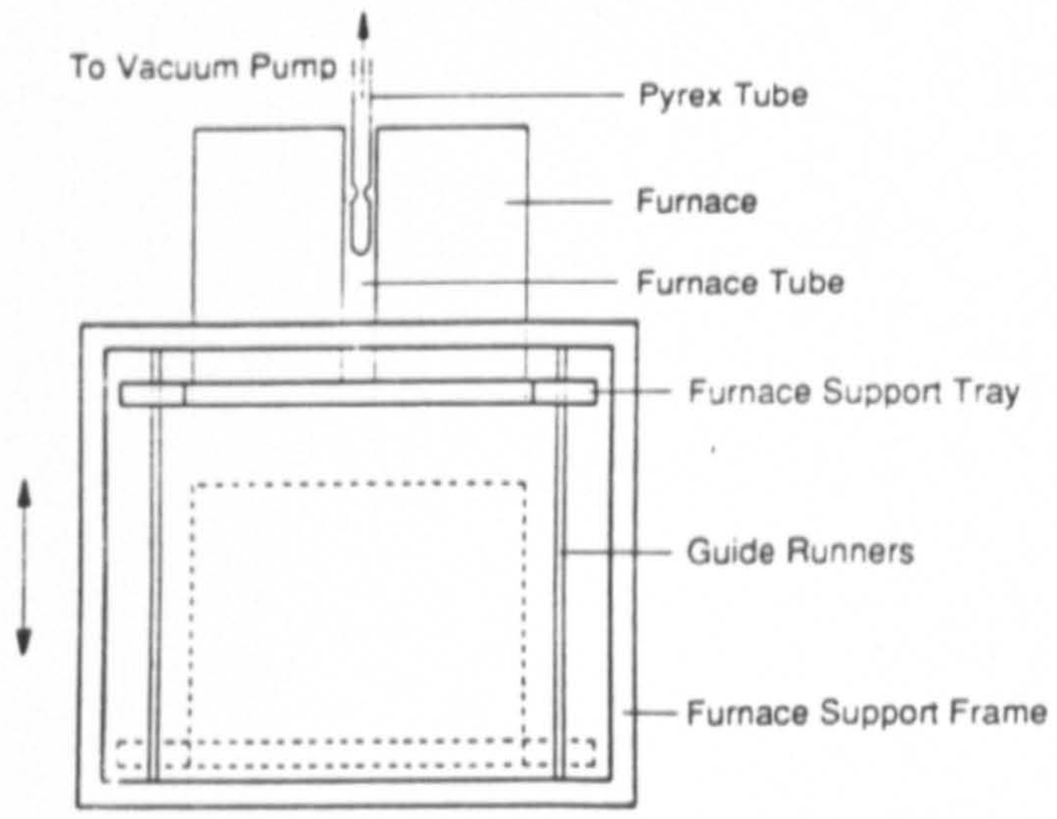

Figure 5.7 The height adjustable furnace, allowing hot-outgassing of encapsulated samples.

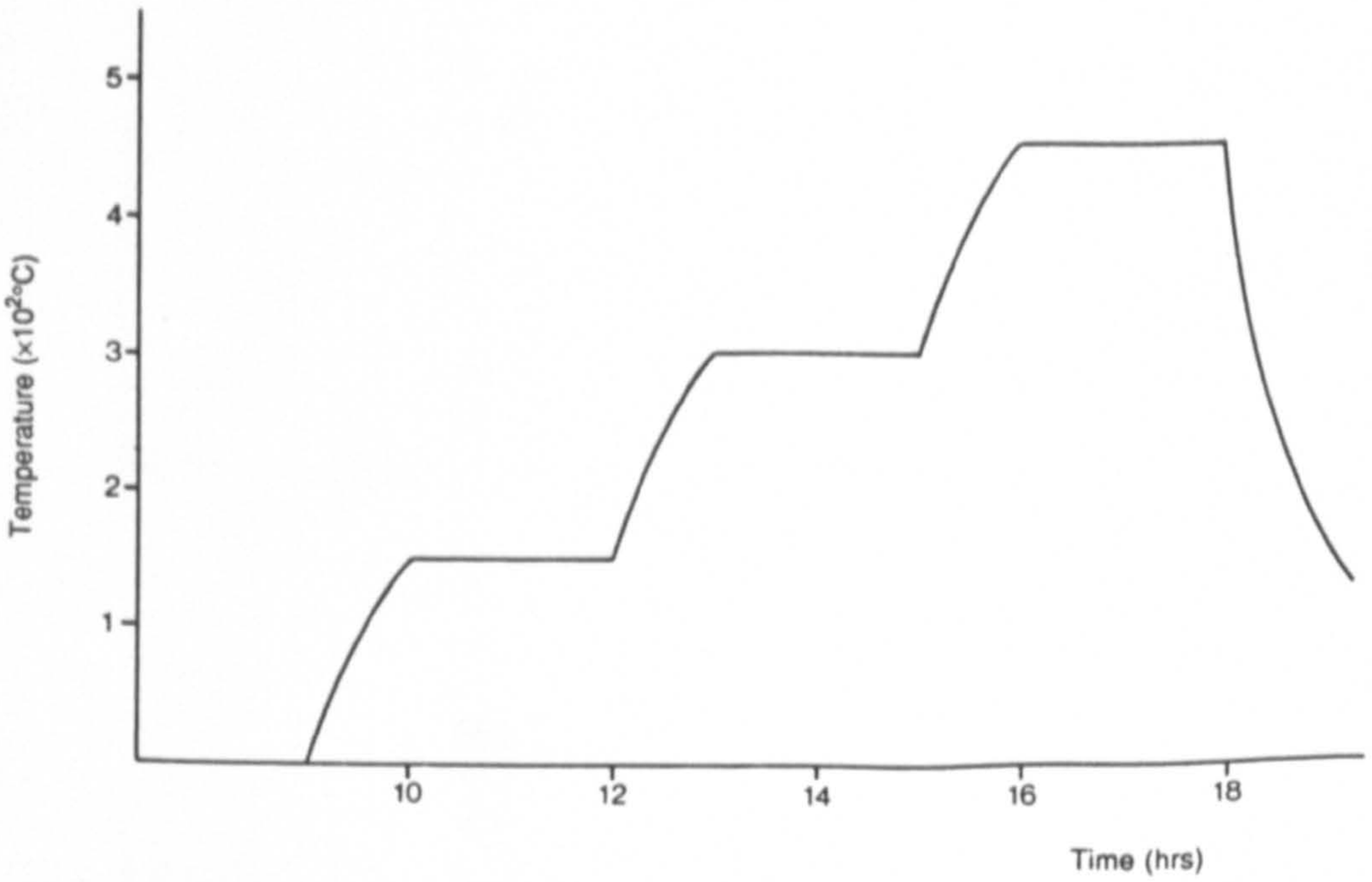

Figure 5.8 Encapsulation outgassing cycle.

a

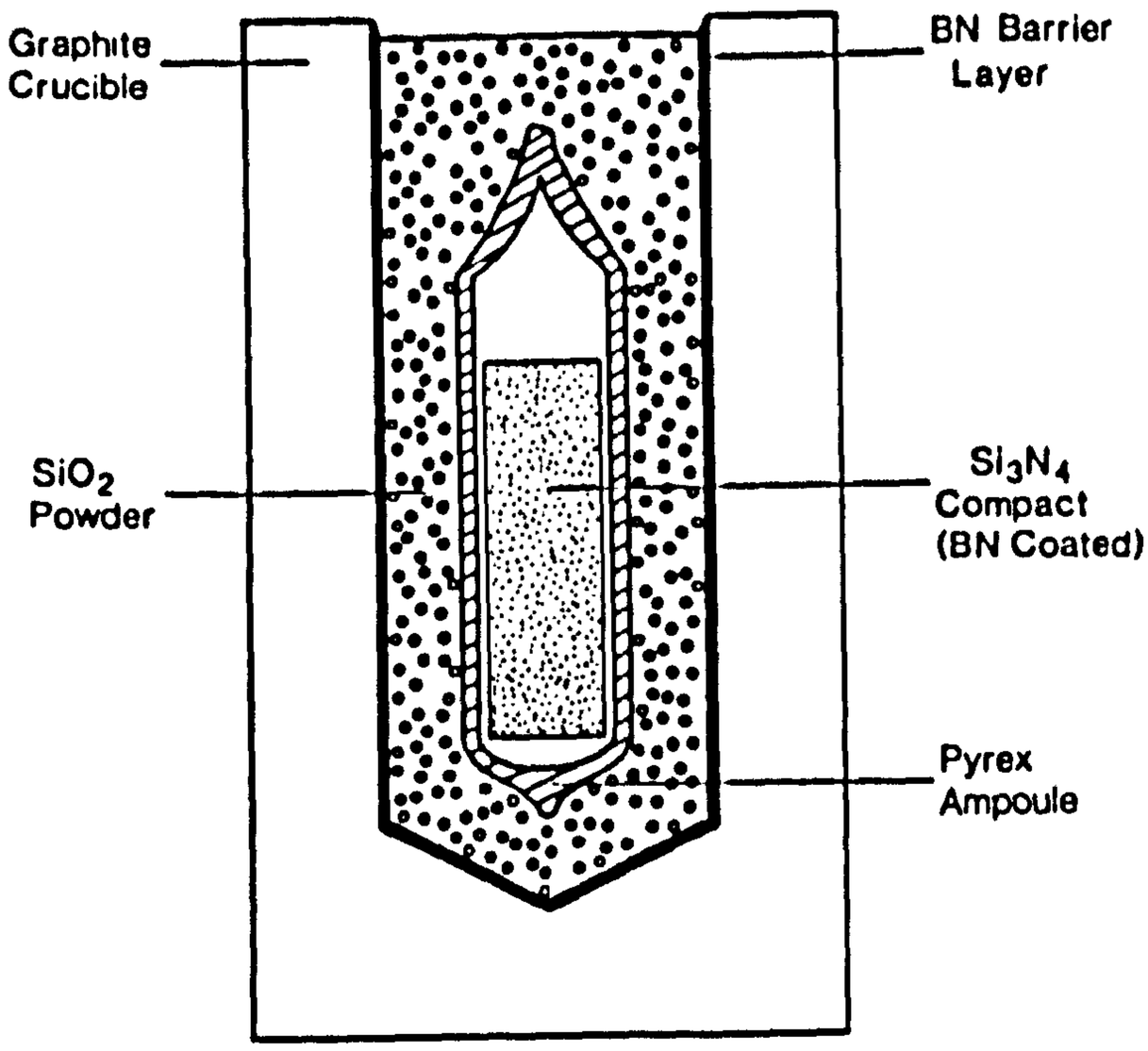

b

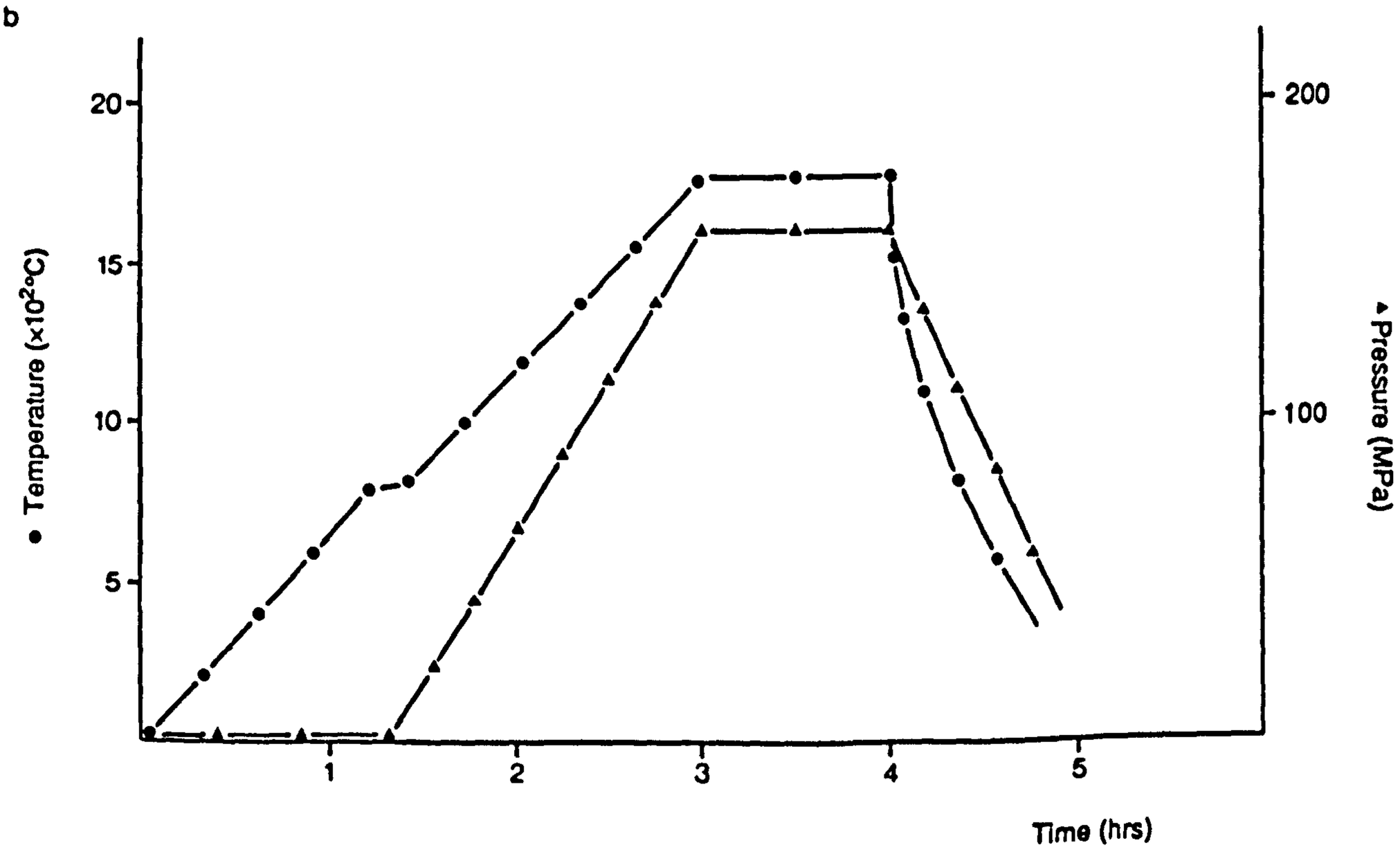

Figure 5.9 a) Schematic diagram of the specimen/crucible representation for Pyrex encapsulation, with coarse SiO_2 powder, and b) the HIP temperature/pressure cycle for this arrangement.

hours prior to use. The boron nitride layer prevents any severe reaction between the crucible and silica powder at the HIP temperature.

A revised HIP cycle was used for silica powder/Pyrex encapsulation. A 2 MPa nitrogen overpressure was applied to the specimen in the HIP system whilst the temperature was raised to the softening point of Pyrex (~ 650°C). From this point both temperature and pressure were ramped to the sintering conditions of 1750°C and 130 MPa for one hour (fig. 5.9b). After processing the specimens were rapidly cooled to prevent crystallisation of the intergranular glass phase. The graphite crucible had to be cut away from specimen A3 after HIPing and hence was not re-usable. After HIP the specimen was prepared as previously described. The post HIP bulk density of composition A3 was 3.26 gcm^{-3} (ie. >98% TD). Microstructural aspects of the HIPed A3 specimen are described in depth in section 6.4.2.

A further revision of the graphite containment method was designed to allow re-use of the graphite crucible. The crucible walls were again coated with a BN/amyl acetate/collodion mixture, although the ampoules were embedded in BN powder so that they could be removed after processing without damaging the crucible (fig. 5.10). Pyrex powder (150 mesh size) was used to cover the exposed top section of each ampoule. An identical HIP cycle to that used for sample A3 was specified, with the exception of varying the final hold pressure depending on the sample composition. A summary of the density of all compositions encapsulated with Pyrex tube and HIPed following this revised technique, together with the previous methods described in this section, is given in Table 5.1.

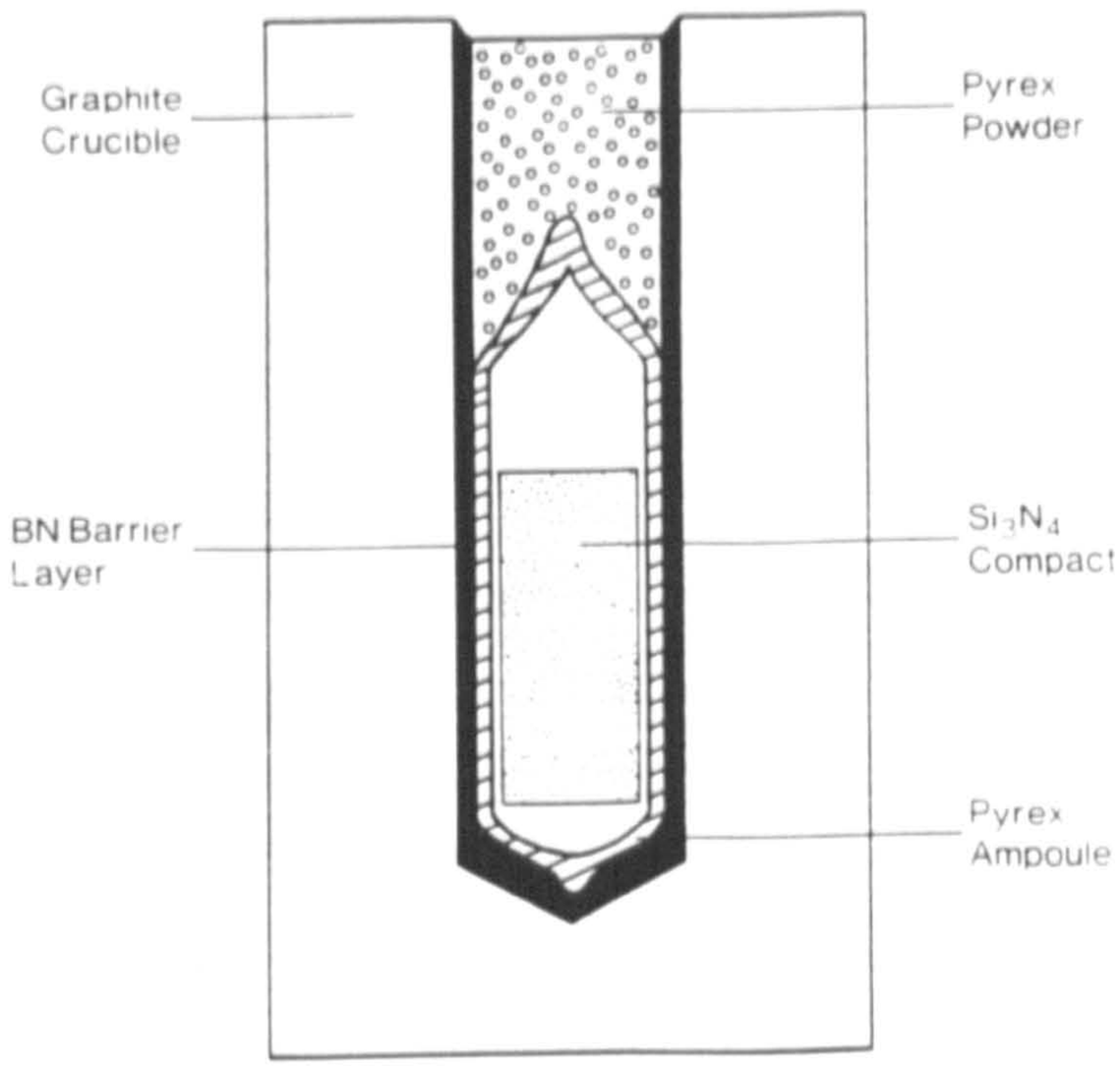

Figure 5.10 Modified specimen/crucible design, allowing crucible re-usage after processing.

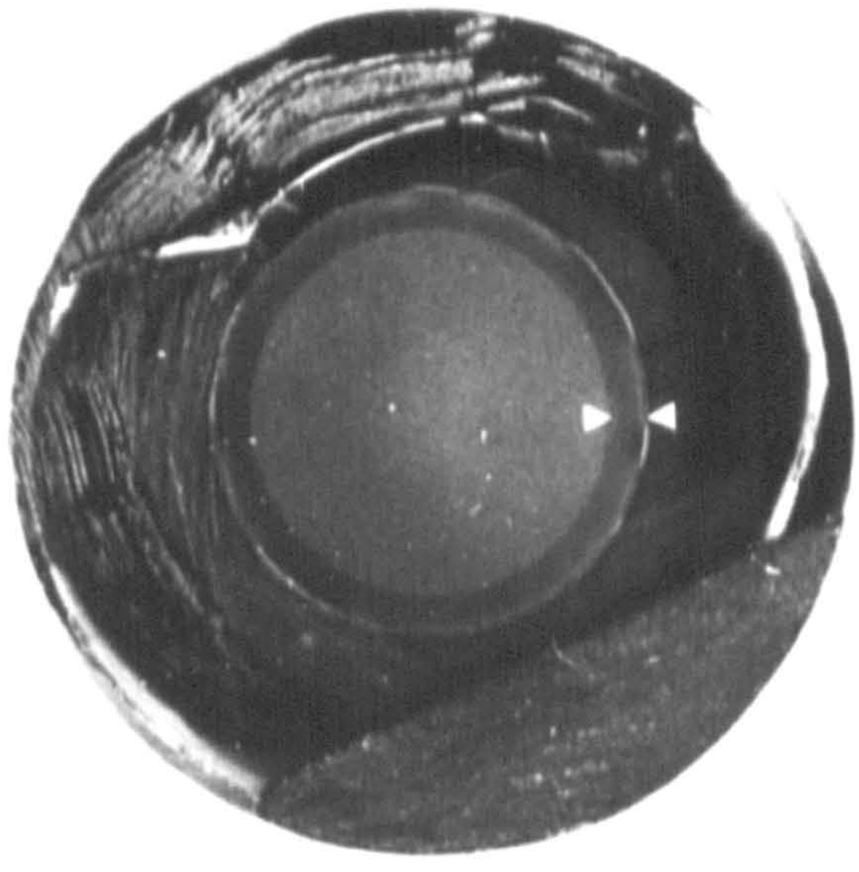

Figure 5.11 Cross-section of HIP densified ceramic, showing pore-free surface layer with low porosity bulk region (~97% TD).

Comp.	St.Powder	Additives (wt.%)	HIP Pressure (MPa)	Encap. Route	ρ ($g\,cm^{-3}$)
A1	Anzon	$10Y_2O_3/2MgO/2Cr_2O_3$	130	a	2.97
			160	b	
A2	Anzon	$10Y_2O_3/2MgO$	130	a	2.95
			160	b	
A3	Anzon	$10Y_2O_3$	130	c	3.26
B1	Ube	$5Y_2O_3$	130	a	3.19
			160	b	
B2	Ube	$5Y_2O_3/2SiO_2$	160	b	3.21
B5	Ube	$5Y_2O_3/5Si_2N_2O$	160	b	3.19
C1	Ube	$7.3\,Nd_2O_3$	130	a	3.00
C2	Ube	$4.0\,Nd_2O_3/2.25\,Y_2O_3$	130	a	2.96

Encapsulation routes:

a) Pyrex tube only; b) Pyrex tube/Pyrex powder; c) Pyrex tube/SiO_2 powder

Table 5.1 Summary of the compositions HIPed in Pyrex glass tube, with the post-HIP density attained. All specimens were processed at 1750°C for one hour, furnace outgassed and encapsulated in Pyrex tube (with Pyrex powder unless stated).

5.3.2. Macroscopic Examination of Densified HIPed Ceramics (Pyrex Tube Encapsulation)

Macroscopic examination of densified ceramic cross sections were performed via optical microscopy of polished surfaces. A pore-free sub-surface region ~1-3 mm in depth existed in all the compositions densified without capsule failure (fig. 5.11). The bulk material within the sub-surface region contained an overall porosity level of between 1-3 vol.%. There was no detectable relationship between the post-HIP bulk density, or the depth of the pore free sub-surface zone, and intergranular phase composition/volume which may be expected to occur when consolidation arises in the presence of a sharp densification front. It is proposed that full densification is inhibited by one or both of the following mechanisms:

1. The densification occurring because of the existence of a thermal gradient through the 'green' state ceramic material into the bulk. This behaviour has been experimentally documented by Ashby, examining the consolidation of powdered metals [159,160].

2. Gas pressure build up in the specimen bulk until, when a high degree of interconnecting porosity has been removed by the densification process, the internal pressure is of an equivalent order of magnitude to the externally applied (HIP) gas pressure. At this point no further densification will occur. The entrapped gas arises predominantly from volatilised B_2O_3 from the internal walls of the Pyrex crucible (under vacuum), with a possible additional contribution from residual organic species in the boron nitride layer.

Gas pressure build-up is believed to have the greatest effect upon the inhibition of full densification, with the final HIPed densities showing no relation to the matrix composition (ceramic B1 was HIPed to theoretical density). Additionally, DTA of Pyrex glass after HIP (section 5.5.2, figure 5.13) demonstrates a considerable increase in softening temperature through decomposition of the borate additive in Pyrex under vacuum.

5.4. ENCAPSULATION IN ALTERNATIVE GLASS COMPOSITIONS

An alternative to the Pyrex tube encapsulation route was devised to allow the use of a selection of different encapsulant glass compositions. Silicon nitride compacts, A3 and B1, with single Y_2O_3 additions, were used for this developmental aspect. The silicon nitride compacts were packed in each of the glass powders and then encapsulated in Pyrex tube as before. This method allows the use of differing glasses, in contact with the silicon nitride compact, to be HIPed using an identical cycle to the standard Pyrex tube encapsulated specimens. Generally, high viscosity glasses were used, silica and an Y-Si-O-N composition similar to the predicted silicon nitride matrix glass. Additionally

B_2O_3 was used, to assess any reaction between this low viscosity glass and the silicon nitride during HIP. A BN barrier layer was not used with any of these glass compositions.

5.4.1. Y-Si-O-N Encapsulant Glasses

An encapsulant glass of Y-Si-O-N composition was produced with the aim of reducing or removing any encapsulant/ceramic interaction. A glass composition of $Y_{1.524}Si_{1.851}O_{4.98}N_{0.68}$ was chosen, close to the expected ceramic intergranular phase composition. It is necessary to incorporate a small nitrogen content to retain a glassy structure after melting, as a pure Y_2O_3-SiO_2 eutectic composition will readily crystallise as $Y_2Si_2O_7$ on cooling.

The glass constituents Y_2O_3 (Ventron Alfa), Si_3N_4 (UBE SNE10) and SiO_2 (Ventron Alfa), were 'dry-milled' for 24 hours in batches of 50 grammes. Pellets of ½" diameter were produced by uniaxial pressing of 8-10 grammes of powder. A stainless steel die was used for compaction and stearic acid was applied to the die faces to aid removal of the pellets after pressing.

Melting of 15-20 gramme batches of pressed pellets was performed in an RF furnace. Melting was conducted at 1680°C under a static nitrogen atmosphere for a period of one hour. Graphite crucibles coated with a BN/acetone slurry were used for pellet containment during melting. After melting the crucible was rapidly removed from the furnace hot zone and quenched in a liquid nitrogen atmosphere by Mr. J. Fernie, Dept. of Physics. The melted glass pellet was crushed and sieved giving a maximum particle size of 250μm.

Green state silicon nitride billets (with 5 and 10 wt.% Y_2O_3 additions) were packed in the crushed glass powder within a graphite crucible. The inner crucible walls were coated with a BN/acetone slurry prior to packing. The packed crucibles were then sintered in a

vertical tube furnace, with sintering conducted at 1620°C in a flowing N_2 atmosphere for a period of one hour. The sintered glass pellets (containing a silicon nitride billet) were then hot-evacuated and sealed in heavy wall Pyrex tube as described previously in section 5.3.1.

5.4.2. Single Component Encapsulant Glasses

Pure B_2O_3 and SiO_2 composition encapsulant glasses were produced from the constituent powders. Si_3N_4 billets containing 5 and 10 wt.% Y_2O_3 were packed in each glass powder as previously described. The pure B_2O_3 powder specimens were sintered in air at 175°C for 30 minutes. SiO_2 powder specimens were sintered in flowing nitrogen at 1550°C for a period of 60 minutes. After sintering the SiO_2 glass pellets were encapsulated in Pyrex as described in section 5.3.1. The B_2O_3 pellets were vacuum outgassed in a partially sealed Pyrex tube at 150°C for a period of 5 hours prior to sealing. The Pyrex ampoules containing a B_2O_3 glass pellet were annealed at the sealed end of the ampoule only, using an oxygen-free natural gas flame to avoid melting the B_2O_3 powder.

5.4.3. Densification Behaviour Using Alternative Glass Compositions

Direct density assessment, by immersion, of ceramic specimens HIPed in glass powder (within Pyrex tube) was not possible because of the small specimen size. Consequently the degree of densification was calculated from the specimen porosity volume estimated via scanning electron microscopy. The approximate densities of compositions A3 and B1, HIPed in SiO_2 powder, are tabulated in Table 5.2. Both ceramics encapsulated in SiO_2 powder were densified to greater than 96% of theoretical. Complete densification of composition B1 would almost certainly be obtained by increasing either the nitrogen pressure or dwell period during the HIP cycle. It is improbable that internal volatilisation of the encapsulant occurs with pure SiO_2 and therefore can be discounted as a factor contributing to densification inhibition in B1. This assumption is confirmed by the full

consolidation of A3 in the same HIP cycle.

Composition	Additive (wt.%)	Density ($g\,cm^{-3}$)	% TD
A3	10 Y_2O_3	3.29	>98%
B1	5 Y_2O_3	3.16	>96%

Table 5.2 Approximate densities of ceramics A3 and B1 HIPed in SiO_2 (calculated from observed porosity levels in SEM).

The low density (<80% TD) observed in the two compositions encapsulated and HIPed in B_2O_3 was caused by a combination of capsule failure and unavoidable aborting of the HIP cycle after 10 minutes (caused by furnace power loss through contamination by gaseous B_2O_3 reacting with the graphite heating elements). Volatilisation of the sintered B_2O_3 powder, within the evacuated Pyrex ampoule, had occurred during the early stages of the HIP cycle. This behaviour lead to gas pressure build-up within the ampoule and, finally, failure when the Pyrex glass softened. No further examination of the B_2O_3 encapsulation route was conducted and it is unlikely that this route can be successfully modified.

After encapsulation and HIP in Y-Si-O-N glass powder (sealed in a Pyrex ampoule), optical and scanning electron microscopy revealed no residual porosity remaining from the 'green' state, though glass bloating was observed in the sub-surface region of this specimen. This observation was attributed to a diffusive reaction with the encapsulant glass leading to excessive incorporation of nitrogen in the ceramic intergranular phase and eventual nitrogen evolution on cooling. This phenomena is further described, from the viewpoint of microstructural modification, in section 6.7.3.

5.5. HIP OF NET SHAPE ARTICLES

5.5.1. Net Shape Encapsulation

The need to produce ceramic articles of complex shape has led to the development of a technique of net shape encapsulation. Green state billets of composition A3 were machined to produce discs of approximate dimensions 20 mm diameter × 5 mm thick. Pyrex powders of two different particle sizes were used to partially encapsulate the silicon nitride discs. The sintering temperatures of the two powders were determined by differential thermal analysis (Table 5.3). Further glass compositions were fabricated by melting precursor mixtures of Pyrex and B_2O_3 in a platinum crucible, though these were not studied as encapsulation materials.

Powder type	Particle mesh size	Sintering temp. (°C)
Fine Pyrex	150	750
Coarse Pyrex	30	810

Table 5.3 The sintering temperatures determined for two grades of Pyrex powder (via DTA)

Silicon nitride specimens were packed in the fine Pyrex powder and pre-sintered in air at 750°C for 45 minutes, and further specimens were packed in the coarse powder and pre-sintered at 775°C for 45 minutes. After sintering, the coarse Pyrex powder had been consolidated into a solid block containing the ceramic specimen at the centre. However, the Pyrex glass still contained a high degree of interconnecting porosity, thus allowing outgassing of the specimen within. The finer Pyrex powder had a tendency to crack during the sintering, due to the greater degree of shrinkage, and therefore the coarse (150 mesh) powder was used for the development of the glass powder bed encapsulation technique.

5.5.2. Powder Bed Encapsulation Cycle Development

The temperature/pressure cycle required for the hot out-gassing, encapsulation and final densification of 'green' state ceramic articles within a glass powder bed is understandably more complex than that required for HIPing simple Pyrex tube encapsulated specimens. It is necessary to vacuum out-gas the 'green' compact within the glass powder prior to melting the glass to form a pressure-transmitting fluid. The specimen/crucible arrangement is shown in figure 5.12a.

The HIP facility at HIP Ltd. allows the HIP chamber to be evacuated to a pressure of 2×10^{-3} Torr via a double rotary vacuum pump system. It is doubtful whether there is any significance in the vacuum level attainable at HIP relative to the 2×10^{-5} Torr achieved with the rotary and diffusion pump system used at Warwick for tubular encapsulation.

Initially a series of three temperature/pressure cycles were examined at HIP. Each cycle was taken to the final pressure/temperature ramp point (1050 - 1100°C) and then subjected to a slow furnace cool to prevent thermal shock of the melted glass encapsulant on solidification. The first cycle (fig. 5.12b) involved two out-gassing stages, at 450°C (for one hour) and 675°C (for 40 minutes), under vacuum. Both stages were performed at a temperature which was less than that required to sinter the glass powder. After out-gassing the temperature was ramped to ~1000°C, still under vacuum, and held for approximately 50 minutes. At this point the HIP chamber was back-flushed with nitrogen and the system pressurized to 12.8 MPa (1800 psi), temperature and pressure were then ramped to the hold conditions, 1100°C and 20.4 MPa. These conditions were held for ~ 18 minutes, after which temperature and pressure were slowly ramped down. The encapsulated sample was easily removed from the crucible after processing, although some limited cracking of the encapsulant glass was noticed due to thermal shock (fig. 5.12c). After sectioning the encapsulant was glassy and translucent and contained no detectable porosity. The encapsulation cycle was therefore physically successful, however it was later discovered that a 'bug' existed in the control computer

a

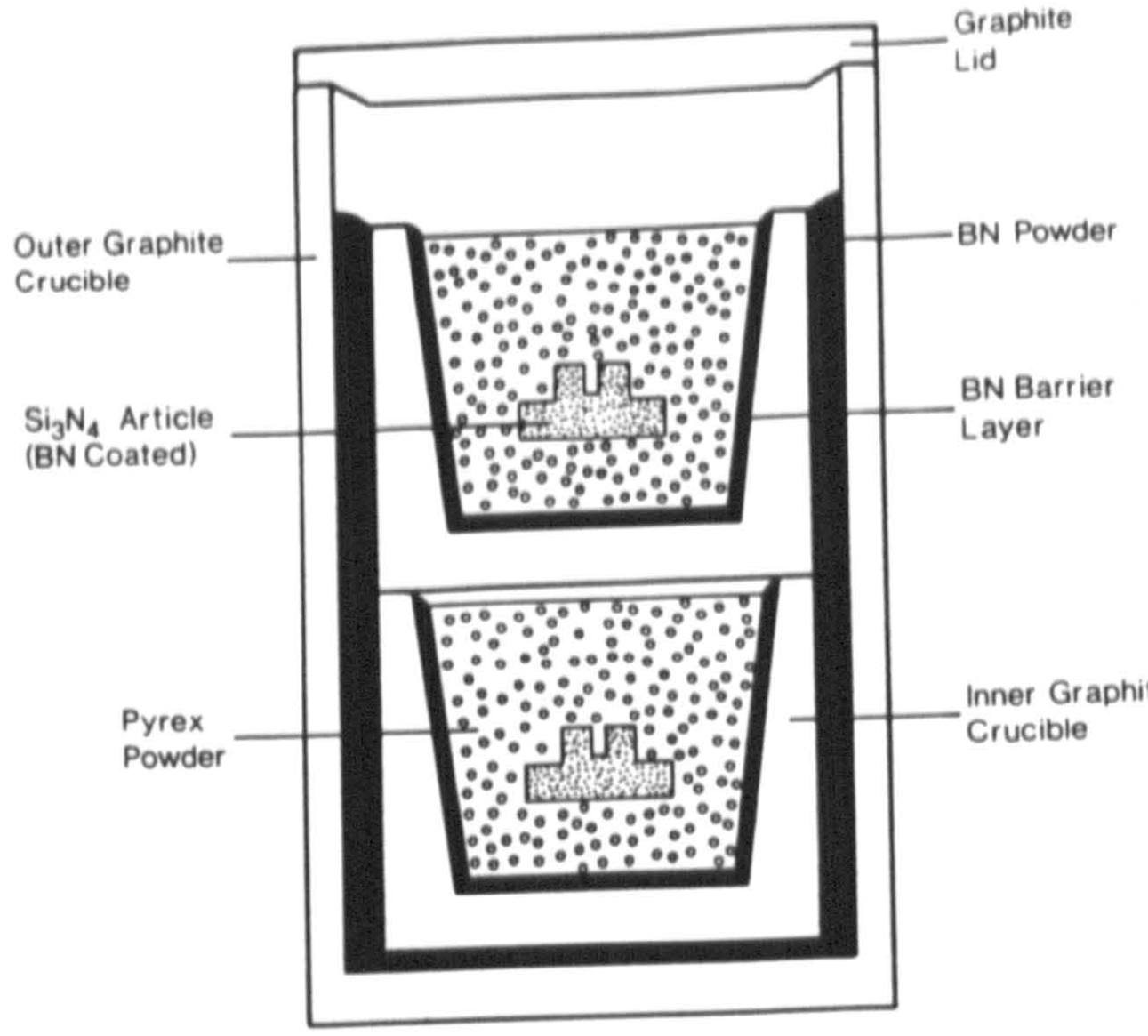

b

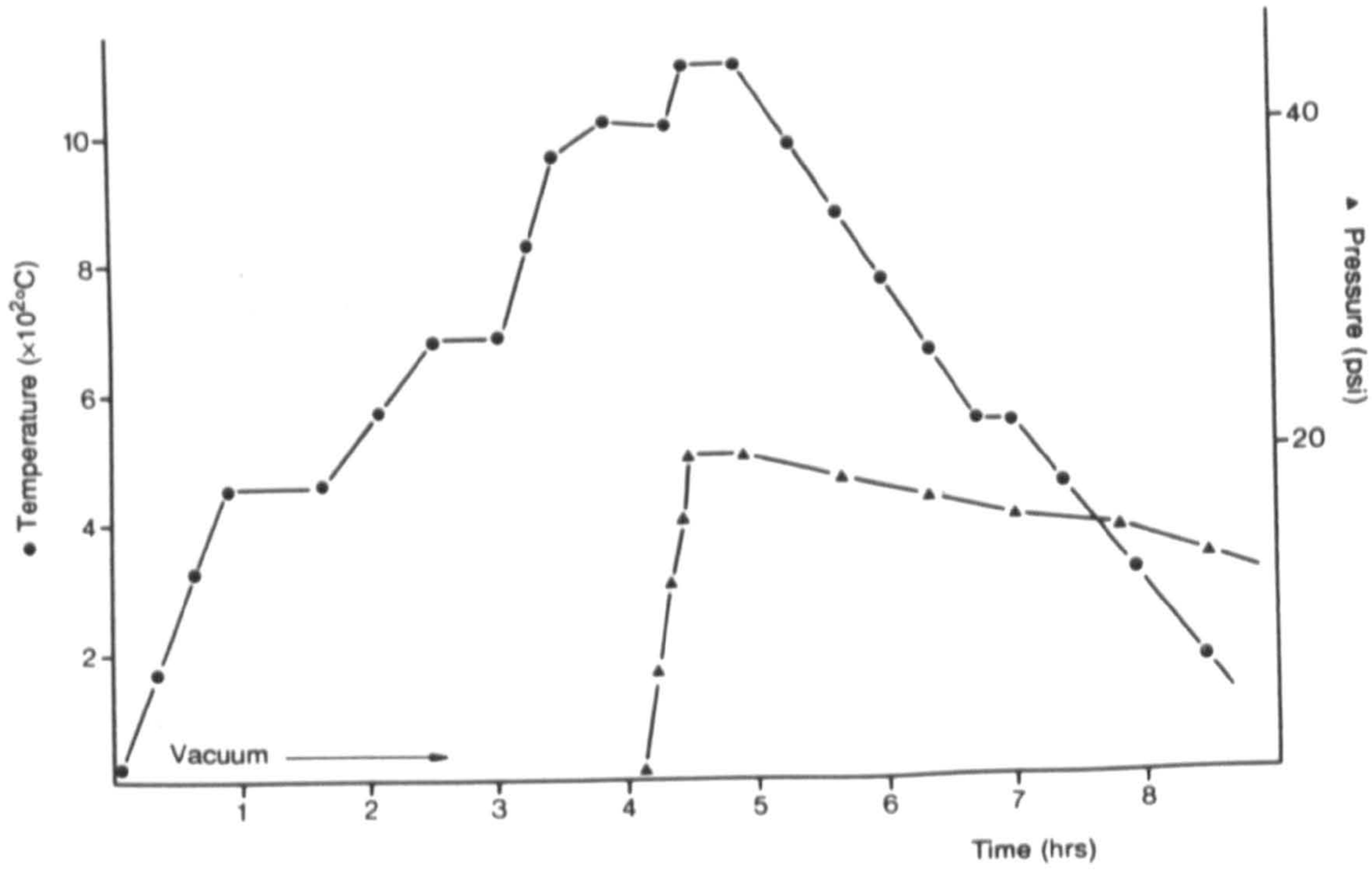

c

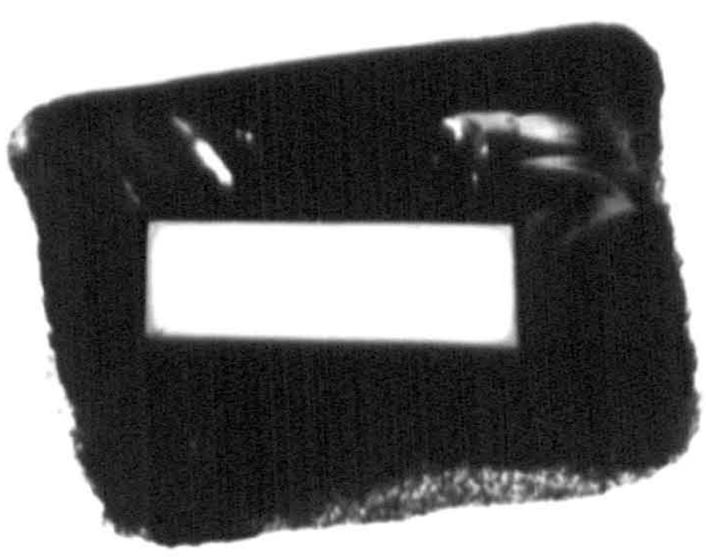

Figure 5.12 a) Schematic diagram of the specimen/crucible arrangement for glass powder bed encapsulation. b) The temperature/pressure cycle for the first HIP glass powder encapsulation trial. c) Cross-section of the encapsulated specimen after the first trial, showing a continuous pore-free encapsulant glass (NB. cracking has occurred through 'thermal shock' during the cooling cycle).

program that governs the HIP system operation. A pressure of 0 MPa had been input into the program for the out-gassing stage of the cycle, causing the closure of the valve isolating the HIP chamber from the vacuum pump system. Hence there occurred a gradual leakage of air/nitrogen into the chamber during the cycle. It is difficult to assess the actual pressure within the chamber in the HIP system during encapsulation because, at present, a low pressure transducer is not incorporated. This omission is currently under review at HIP Ltd. with the possible future inclusion of a pressure transducer for the range 0 - 50 psi. A controlled, low pressure nitrogen atmosphere could therefore be used after out-gassing, at low to medium temperature (400 - 600°C), but prior to final encapsulation. This would probably overcome the problems that occurred during the second and third encapsulation trials.

After the gradual chamber vacuum loss that occurred with a specified input pressure of 0 MPa an input of 'vacuum' was used for the second and third encapsulation trials, overcoming the previous valve closure problem and allowing complete evacuation throughout the cycle to the time of back-flushing with nitrogen and subsequent pressure application. Both of these cycles were performed using an identical silicon nitride composition to the first trial. The second encapsulation cycle was similar to the first with the obvious exception of vacuum level. The out-gassing periods were slightly shorter in duration and the final holding temperature lower at ~ 1025°C. The applied nitrogen pressure was also lower during the holding period, an average of 4 MPa. After cooling the specimen was removed from the crucible and sectioned. The Pyrex encapsulant glass had retained its powder-like texture and there was still a high degree of inter-connecting porosity between the sintered glass particles. A small portion of the encapsulant was ground to a fine powder, of similar particle size to the fine Pyrex powder, for differential thermal analysis (DTA) (fig. 5.13). The cross-sectioned sample is shown in figure 5.14.

The third cycle was similar to the second, except the final hold temperature was lower, ~ 930°C, and the hold period was extended to 150 minutes. Upon cycle completion the

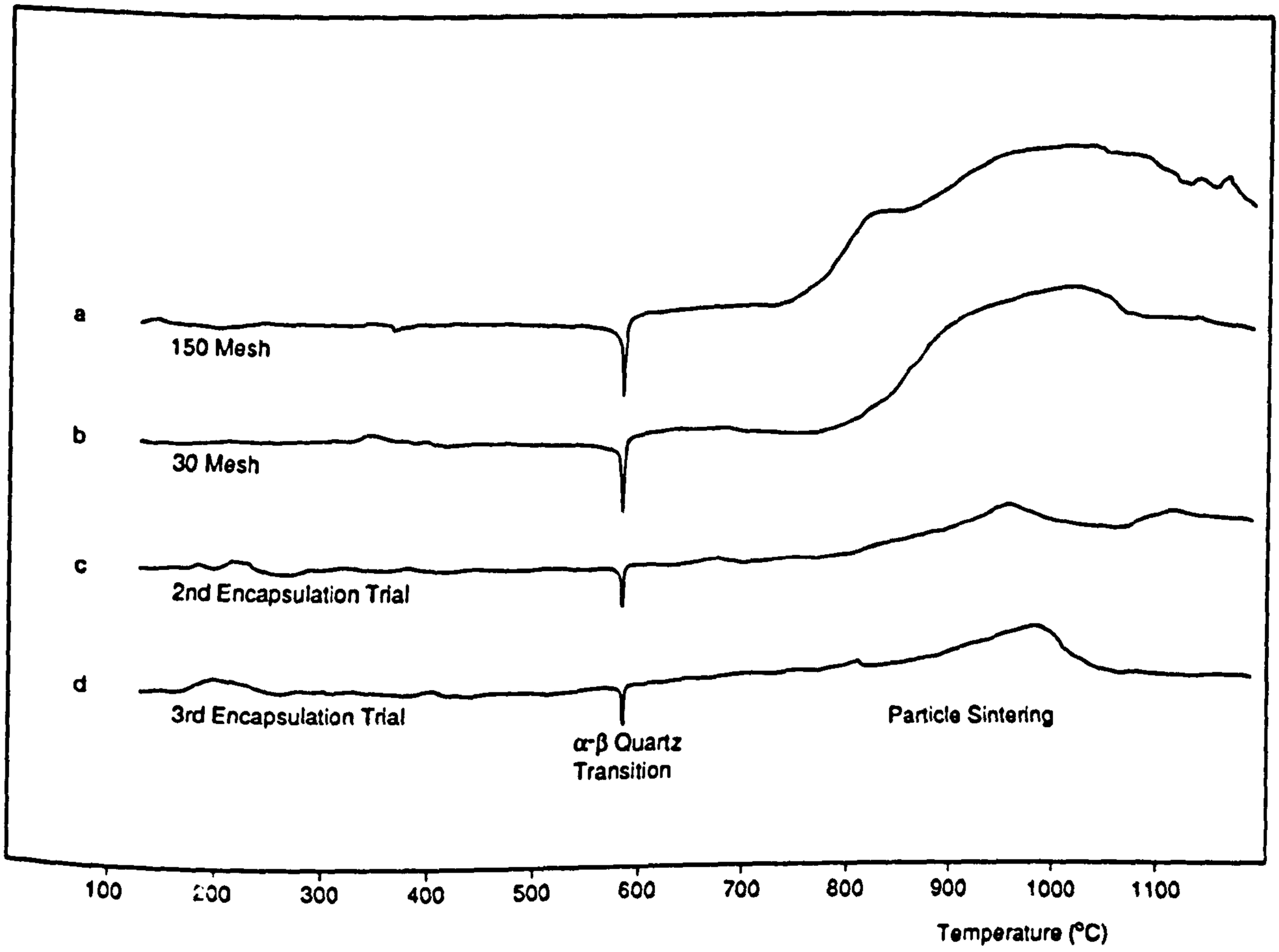

Figure 5.13 Differential thermal analysis traces for a) fine Pyrex powder (150 mesh), b) coarse Pyrex powder (30 mesh), and ground Pyrex from the c) second and d) third glass powder encapsulation trials. Isothermal lines indicate 100°C intervals.

specimen was sectioned, revealing a high degree of interconnecting porosity and relatively poor particle adhesion. There was also a region, adjacent to the central silicon nitride specimen, where severe glass bloating had occurred. A small proportion of the encapsulant glass was ground to a fine powder for DTA analysis (fig. 5.13). The particle size was similar to the fine Pyrex powder (30 mesh).

Comparison of the data obtained for DTA on glass powder from the second and third encapsulation trials and the commercial Pyrex powders (fig. 5.13) revealed an increase in the sintering temperature from ~750°C (30 mesh Pyrex powder) to 800 - 850°C for the glasses that had been taken through the HIP trials. It can also be seen that the trace deviations is not as distinct, possibly indicating a range of sintering temperatures, arising from compositional variation. It is proposed that volatilisation of the borate component in Pyrex occurs when the glass powder is heated under vacuum, and thus the overall composition is made more silicon rich. Variation of the glass composition increases the softening temperature/viscosity, thus accounting for the observation of 'non-melting' in the latter encapsulation trials.

A similar effect to that noted in the second and third trials was obtained during parallel investigation into powder bed encapsulation using a large volume vacuum furnace at T&N. Similar out-gassing/encapsulation cycles were performed with a hold temperature of 1200°C using low ramp rates of 3°C/minute, and a vacuum of 1×10^{-2} Torr. Gas bubbling was again present towards the top of the encapsulant glass, although there was little interconnecting porosity and the bubbles appeared to be discrete. Towards the bottom of the encapsulant there was still evidence of the original glass powder which had not completely melted.

5.5.3. Glass Powder Bed Encapsulation and HIP

The first complete HIP cycle utilizing a glass powder bed to produce a pressure transmitting fluid was performed using temperature and pressure conditions similar to the

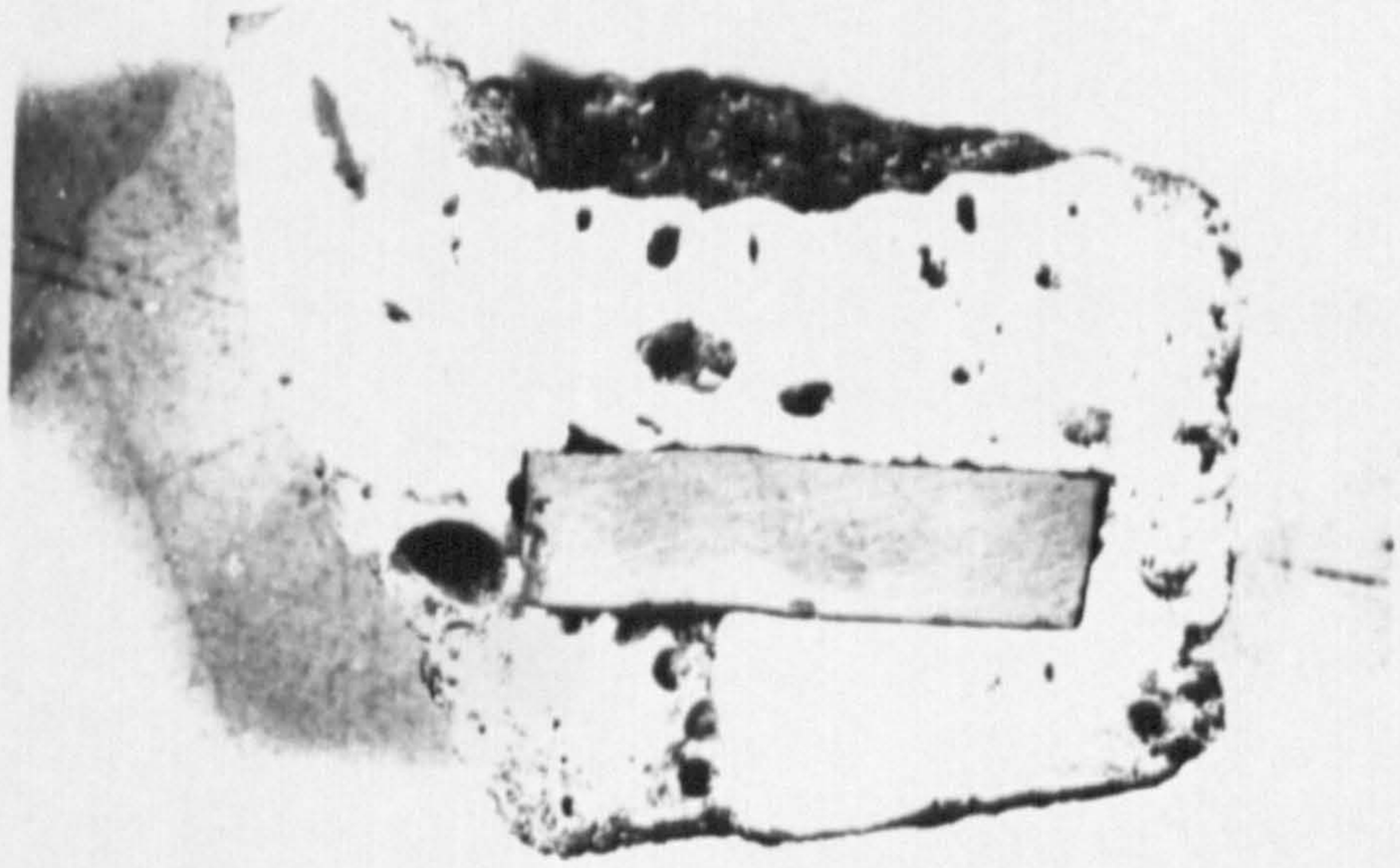

Figure 5.14 Cross-section of the second encapsulation trial.

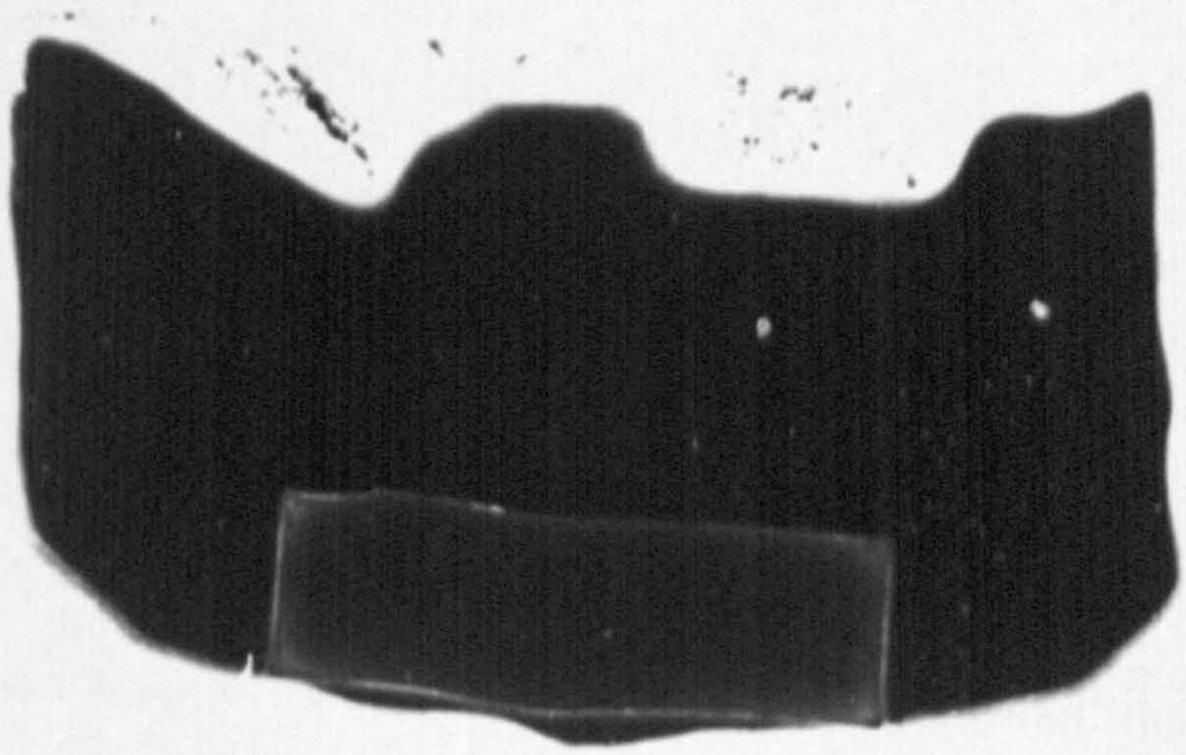

Figure 5.15 Cross-section of the glass powder bed HIP densified ceramic, composition A3.

first encapsulation trial as this had shown the most promising results. An identical Anzon Si_3N_4 based composition (A3) with a 10 wt.% Y_2O_3 addition was used as for the initial trials. The initial preparation and pre-encapsulation stage were as previously described. After the initial out-gassing and encapsulation stages, conducted under partial vacuum, the system was backflushed with nitrogen and then both temperature and pressure were ramped up to the standard hold conditions 1750°C and 160 MPa for one hour. After the initial pressurization, argon gas was added until, during the hold period, the argon to nitrogen ratio was approximately 10:1. A slow furnace cool was used after HIPing to prevent thermal shock of the encapsulated specimen.

5.5.4. Post HIP Examination: Macroscopic

The sectioned silicon nitride specimen was found to have sunk during densification, probably towards the end of the hold period and during the initial stages of the slow cool stage when the encapsulant glass is still fluid in nature (fig. 5.15). A similar effect has been noted with tubular encapsulation and HIPing of dense silicon nitride ceramics as the specimen density is greater than that of the encapsulant glass. Full densification of composition A3 was obtained with this technique and it is probable that, when using the 'lower' vacuum attainable in the laboratory HIP unit at Chesterfield, volatilisation of B_2O_3 from the Pyrex powder is inhibited and gas pressure build up in the ceramic is avoided.

5.6. COMMERCIAL HIP PROCESSING: THE ASEA PROCESS

In addition to materials prepared at HIP Ltd., Chesterfield, further full billets of compositions B1 to B7 were HIPed in a large volume system at ASEA Cerama AB, Robertsfors, Sweden. Prior to encapsulation and HIPing the individual ceramic billets were coated with a powder interlayer to inhibit/prevent any reaction occurring between the ceramic and encapsulant. The billets were vacuum encapsulated in a glass powder bed during an early stage of the HIP cycle to prevent gas ingress. The encapsulant glass

composition was not specified by ASEA. However, analysis of residual glass present on one sample after processing is described in 5.6.2. The sintering conditions were a temperature of 1725°C and pressure of 160 MPa, held for one hour. After HIPing the encapsulant glass was removed by sand blasting. No further information was provided by ASEA, although it was assumed that a slow furnace cool occurred due to the large furnace volume.

5.6.1. Densification Behaviour of ASEA HIPed Ceramics

All compositions B1 to B7 were densified to greater than 99% of theoretical (Table 5.4). Progressive replacement of nitrogen by oxygen in the starting powder mix (compositions B1 to B4 and B5 to B7) resulted in a decrease in the overall density (fig. 5.16) via α-Si_3N_4 re-precipitating as Si_2N_2O as opposed to β-Si_3N_4. This behaviour is described in further detail in section 6.7.1.

Designation	Additives (wt.%)	Density (g cm^{-3})	% TD
B1	5 Y_2O_3	3.244	99.6
B2	5 Y_2O_3 + 2 SiO_2	3.223	99.5
B3	5 Y_2O_3 + 4 SiO_2	3.193	99.3
B4	5 Y_2O_3 + 8 SiO_2	3.145	99.2
B5	5 Y_2O_3 + 5 Si_2N_2O	3.223	99.3
B6	5 Y_2O_3 + 10 Si_2N_2O	3.210	99.4
B7	5 Y_2O_3 + 25 Si_2N_2O	3.148	99.0

Table 5.4 Densities of ceramics B1 to B7 HIPed at ASEA

5.6.2. Assessment of ASEA Encapsulant Glass Composition

Two densified tensile test bars (of composition B1) were also provided for examination after HIPing at ASEA. These pieces were originally destined for high temperature mechanical testing at Rolls-Royce Plc (Leavesden). However, after HIPing, large cracks had formed in the test bars (fig. 5.17). Crack opening had arisen through penetration of the encapsulant glass into microscopic cracks present in the test pieces prior to HIPing.

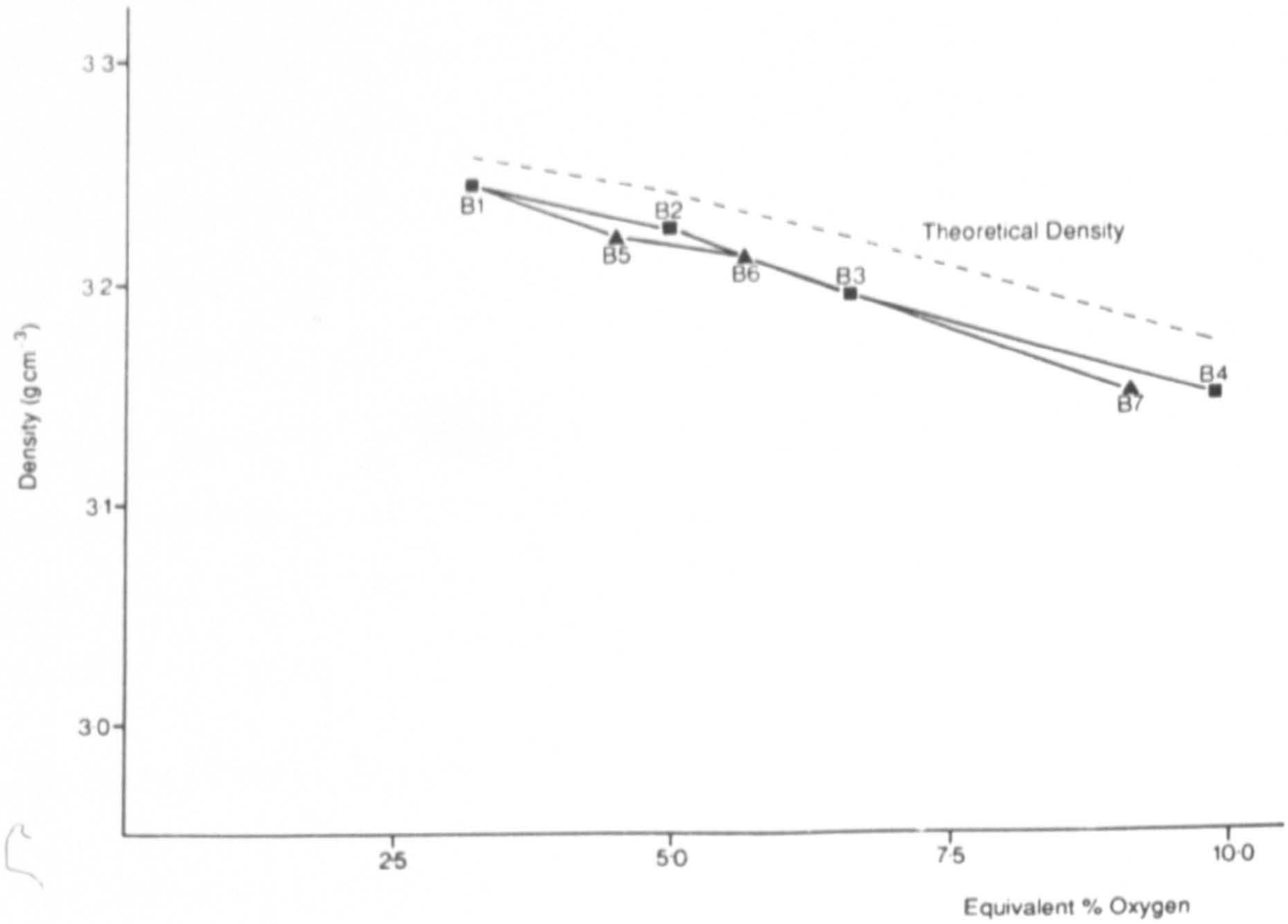

Figure 5.16 The variation of density with equivalent percentage of oxygen for ASEA HIPed compositions B1 - B7.

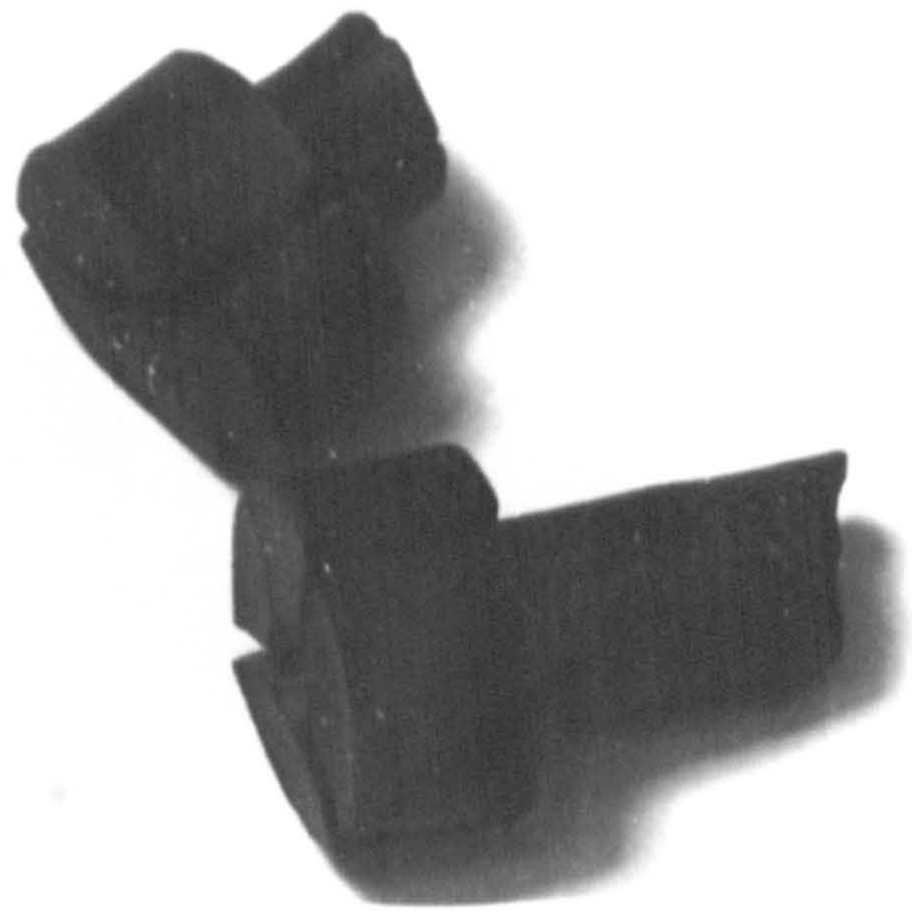

Figure 5.17 Crack formation in the HIPed tensile test piece (composition B1).

The cracks were believed to have been stress induced at the contact points of the lathe chuck during 'green' machining. Using the pre-existing cracks as a critical flaw the test pieces were fractured to allow examination of the internal face of the crack. A glassy residue was observed at the crack tip which had not been removed by sand blasting at ASEA. The residue composition was determined via microanalysis in the S.E.M. and was found to be similar to Pyrex, although the detected Al level (together with Ca) was lower. Partial crystallistation of the encapsulant glass, to an SiO_2 form, was also observed. Crystallisation occurs on cooling, after HIP, and may be be responsible for the apparent compositional difference, when compared to Pyrex. However the encapsulant glass borate content was not assessed and direct comparison of the two glasses is therefore not possible.

5.7. DISCUSSION: GLASS ENCAPSULATION

The ceramic encapsulation techniques previously described in this chapter have been developed to allow glass 'cladded' HIP of green state materials.

The applicability of silica for simple tubular encapsulation is currently questionable. This is primarily because of the HIP system limitations with the laboratory unit at HIP Ltd. Greater potential (with respect to ease of encapsulation and economics) is revealed in Pyrex tube encapsulation. The lower softening temperature of Pyrex relative to silica has allowed more flexibility in the determined HIP cycle, enabling gas pressure application at a considerably reduced temperature (~ 600°C). Near theoretical density (>97% T.D.) was obtained for a variety of silicon nitride based compositions after encapsulation and HIP in Pyrex tube. However the attainment of complete densification was not generally observed because of gaseous pressure build-up within the Pyrex capsule, arising from partial volatilisation of the internal surface of the evacuated ampoule. This behaviour can be inhibited with the use of a less efficient vacuum during outgassing of the ceramic specimen.

A similar approach was used during the outgassing and encapsulation of silicon nitride samples within Pyrex glass powder. Full densification (>99% TD) was obtained using the glass powder encapsulation technique, which allows the consolidation of complex shaped parts.

Full HIP densification of silicon nitride based ceramic was obtained using the commercial ASEA process, a method that allows the fabrication of complex shaped parts via the use of glass powder. A commercial alternative to the current ASEA glass encapsulation process, summarised in a series of European and American patents [102-104,113-120], does not currently exist. However, the use of tailored encapsulant glasses does offer a viable alternative. During the current programme a Y-Si-O-N encapsulant glass was devised to allow the encapsulation and HIPing of Si_3N_4 ceramics using Y_2O_3 additions. Furthermore, it would be relatively simple to devise a range of encapsulant glasses with compositions dependent upon the ceramic additive system chosen, and further research in this area would be of interest.

5.8. GREEN STRENGTH ENHANCEMENT BY PRE-SINTER HEAT-TREATMENT

One of the primary benefits of hot-isostatic pressing as a densification technique can be found in the production of complex near net shaped ceramic pieces [121]. The principal shaping routes that are currently used for ceramic forming prior to densification are slip-casting and injection moulding [184]. However, both suffer from certain limitations. The main disadvantages of slip-casting are:

1. Poor dimensional control; both drying and firing shrinkage must be carefully controlled [184]. Particular difficulties arise during the casting of whisker loaded ceramic composites, where whisker alignment can occur parallel to the mould surface [185]. Research conducted at Warwick University has demonstrated that anisotropic whisker distribution produces specimen warping during HIP

densification [186].

2. Low production rates, difficult to automate and high tooling costs [184].

Further drawbacks are apparent with injection moulding of ceramic powders, namely:

1. High material costs, including tooling costs and the use of high polymeric binder levels. Additionally a lengthy binder removal stage is required (typically 20 hours plus) [184].

2. Difficult to ensure complete reliability, eg. incomplete die filling, leading to non-uniform densities and uneven shrinkage during densification. The binder removal stage is critical as complete elimination of the polymer is required. If the binder removal rate is too great warping, cracking and void formation may occur [184].

3. The processing of SiC whisker-loaded Si_3N_4 composites has demonstrated that specific whisker alignment occurs during inject moulding, and hence a revision of inject moulding equipment is required [187].

A potential alternative to these forming routes is 'green machining' of cold isostatically pressed blocks of ceramic. Green state ceramic articles are inherently brittle in nature; consequently a high degree of component wastage can occur during the machining of complex shapes. It is therefore desirable to introduce a certain amount of mechanical strength to green materials prior to machining. One method of enhancing the green strength is in the use of a small volume of organic binder [188], however a binder burn-out stage is still required. An increase in green strength can also be obtained by subjecting the powder body to a suitable pre-sinter heat-treatment, a technique that has been successfully used in the production of RBSN (pre-sintering of Si prior to nitridation) [189].

This section describes the effect of pre-sinter heat-treatment on the toughness, density and composition of three 'green' state silicon nitride compositions. Heat-treatment was

performed in nitrogen for a period of two hours (the procedure is described in section 3.2.3). A summary of the pre-sintering conditions used and compositions studied is presented in Table 5.5.

Designation	Si_3N_4 powder	Sintering additives (wt.%)	Sintering temperatures (°C)	Powder bed composition (wt.%)
A1	Anzon	$10Y_2O_3/2MgO/2Cr_2O_3$	1250-1450	$50BN/45Si_3N_4/5MgO$
A3	Anzon	$10Y_2O_3$	1550-1700	$50BN/50Si_3N_4$
B1	UBE SNE10	$5Y_2O_3$	1550-1700	$50BN/50Si_3N_4$

Table 5.5 Pre-sintering conditions for green strength enhancement of silicon nitride

Assessment of potential toughness increase was made by the single edge notched beam (SENB) fracture toughness technique.

5.8.1. Effects of Pre-Sinter Processing on Green State Si_3N_4

The variation of specimen fracture toughness with pre-sintering temperature is shown graphically, for compositions A1, A3 and B1, in figure 5.18a. The densities of these specimens, after heat-treatment, is presented in figure 5.18b. It is apparent that a 400 to 500% increase in fracture toughness can be obtained when using higher pre-sinter temperatures, with simultaneous density increases of ~5% for the single additive specimens and ~15% for composition A1.

K_{IC} enhancement at the higher temperatures is accompanied by a near complete transformation of α- to β-Si_3N_4 for the single additive compositions. The high liquid viscosity at the pre-sinter temperatures keeps the material transport rate low and thus only minimal densification occurs. Only partial transformation had occurred for composition A1 after pre-sinter treatment at 1450°C, although the densification level was greater than A3 and B1, and a more rapid material transport process is apparent for the mixed additive system. XRD revealed that the α-β transformation begins at ~1600°C for

a

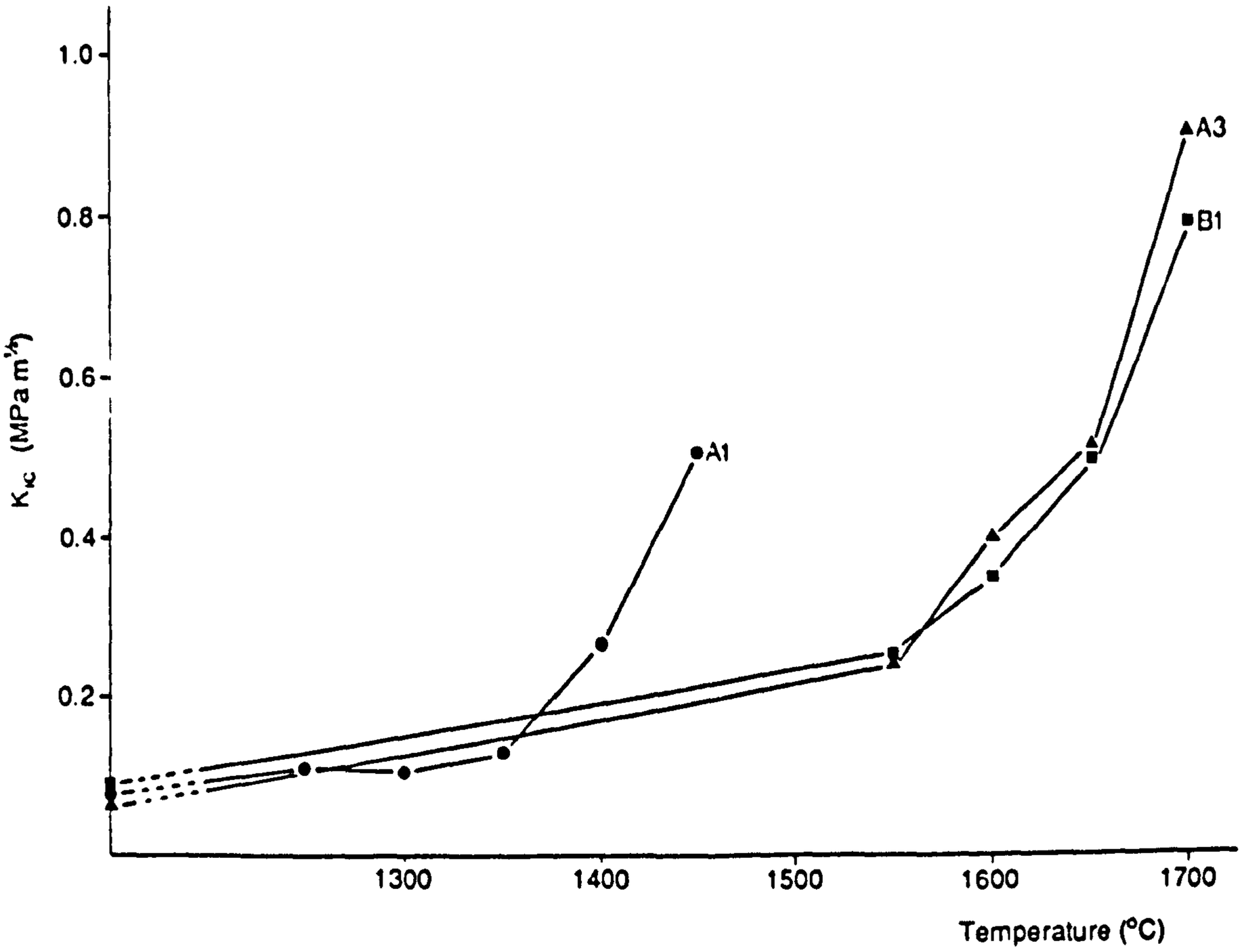

b

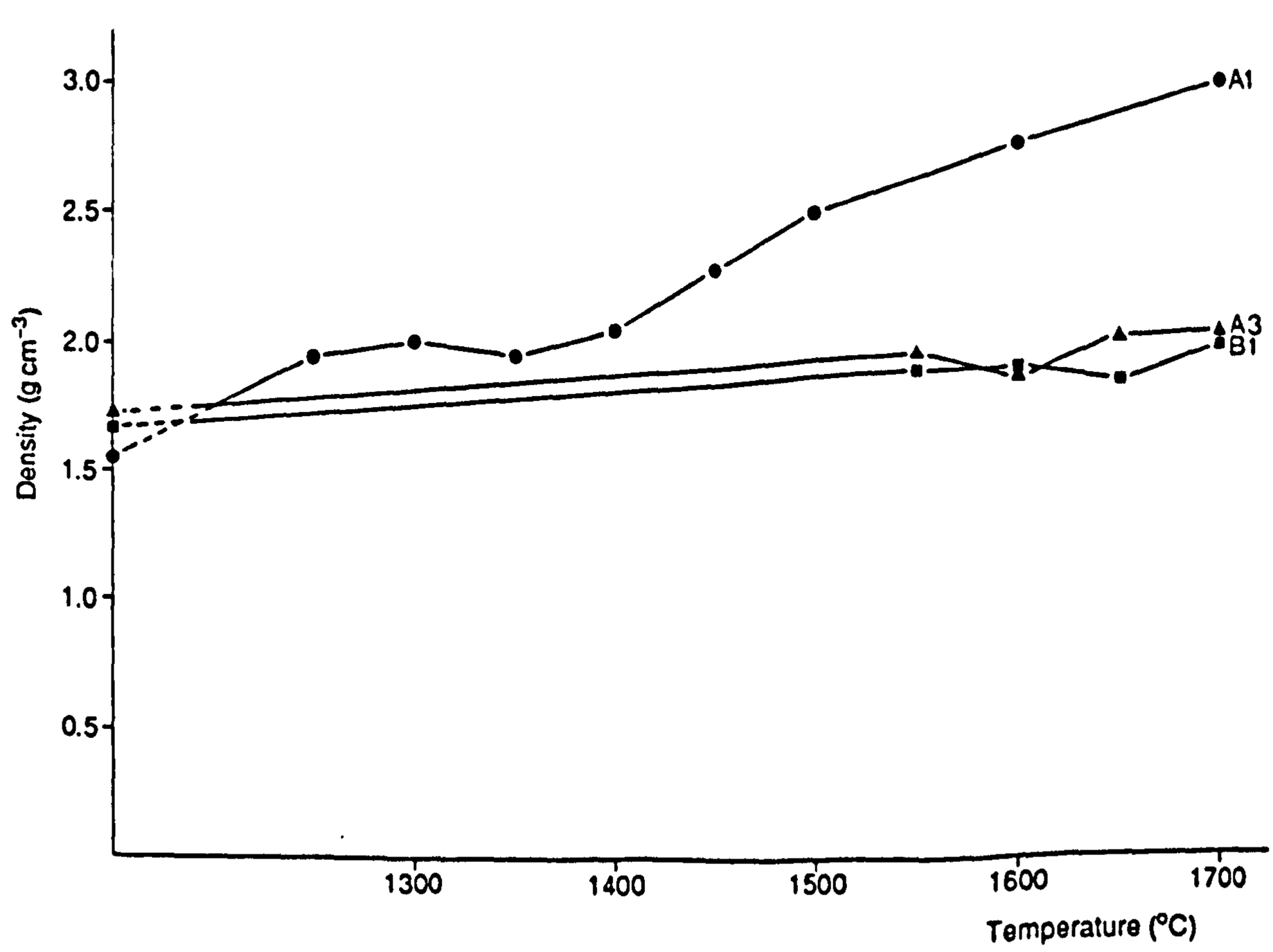

Figure 5.18 The variation of a) fracture toughness, and b) density, for ceramics A1, A3 and B1, as a function of pre-sinter temperature.

A3, approximately 60°C below the Y_2O_3-SiO_2 eutectic, and ~1650°C for B1. The lowering of the transformation temperature can be attributed to a combination of

1. An increase in the secondary phase liquid volume.

2. A lowering of the liquid viscosity, arising from an increased impurity concentration with Anzon Si_3N_4 relative to Ube SNE10.

The mechanism of K_{IC} enhancement after heat treatment is predominately dependent upon oxide additive (and surface SiO_2) melting to produce 'bridging' between individual silicon nitride particles (shown schematically in figure 5.19). Crack propagation therefore requires the fracture of these interparticle glass bridge regions. Additionally microscopic porosity is believed to increase K_{IC} levels via the dissipation of energy and the formation of microcracks. This behaviour will be exaggerated at higher pre-sinter processing temperatures, where, as the glass phase becomes more fluid, a greater rounding of the glass morphology will occur as the wetting and flow characteristics are altered (fig. 5.19).

The application of green machining to the shaping of silicon nitride shows a high degree of promise. However, prior to its successful implementation as a commercial process, further investigation is required in the following areas:

1. The effect of a high β-Si_3N_4 content on the densification behaviour. This is particularly relevant for HIP processing, when compositions similar to B1 would be used, as it has been demonstrated that, in the absence of pressure, shrinkage is directly related to the proportion of α-Si_3N_4 already transformed to β-Si_3N_4 [190].

2. Demonstration that consistent shrinkage can be obtained during densification. Butler *et al* [188] have already shown that a high dimensional stability is obtained when HIPing green machined silicon nitride turbine blades (machined with binder). To maintain a uniform and reproducible shrinkage in machined components it is

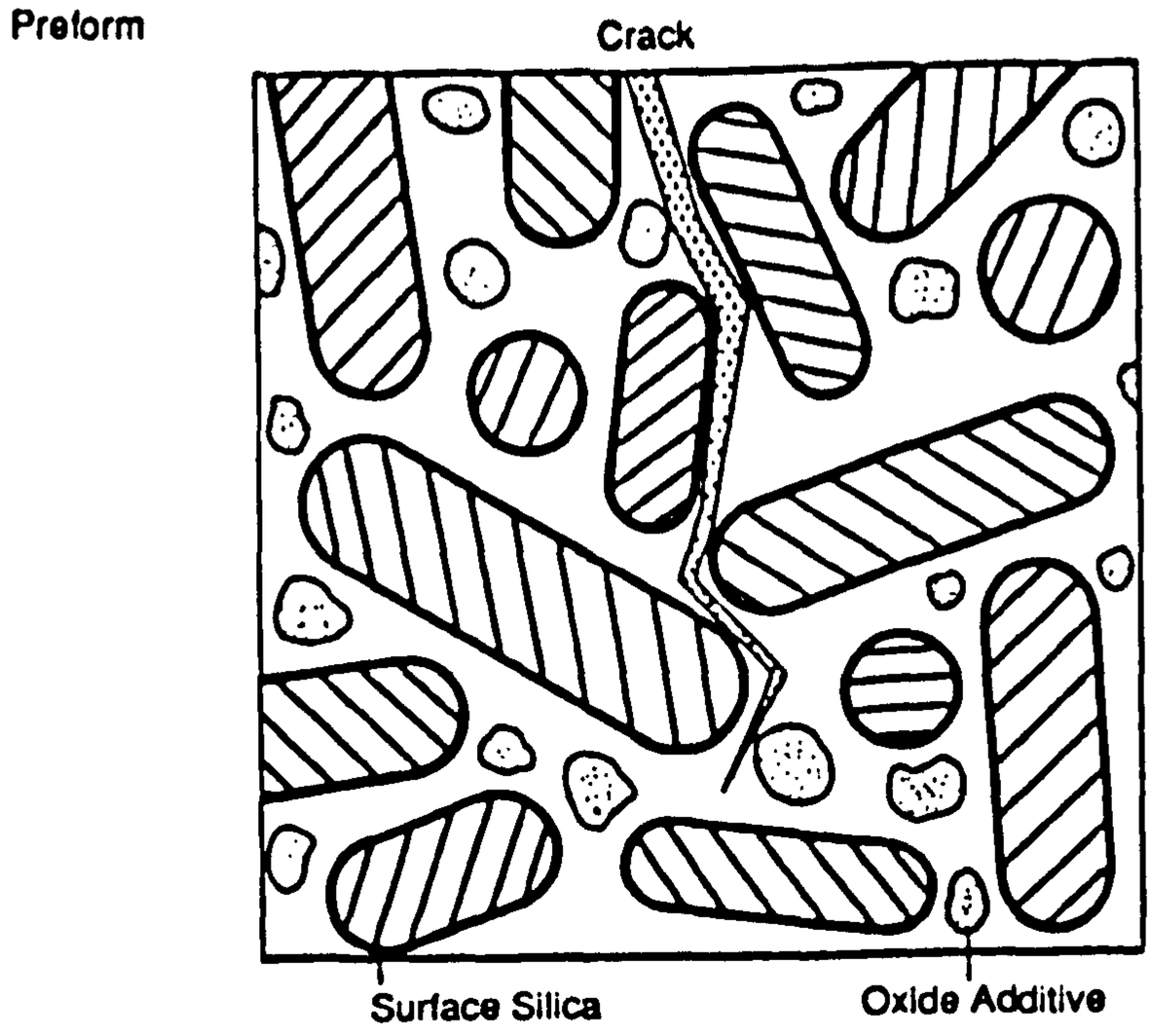

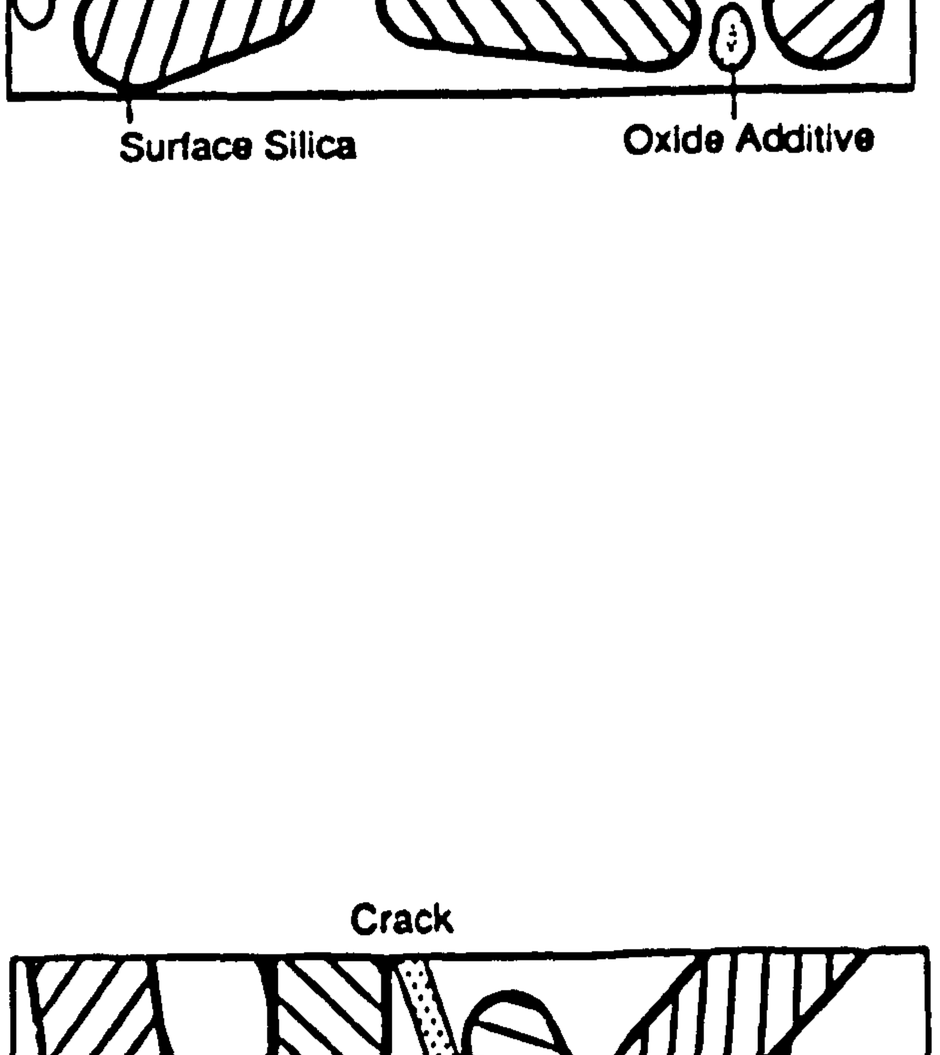

Figure 5.19 Schematic representation of the mechanism of toughness enhancement occurring at the lower pre-sinter temperatures (prior to β-Si_3N_4 re-precipitation).

necessary to use a consistent quality powder source and to optimise the mixing/milling process to produce homogeneous green state billets.

necessary to use a consistent quality powder source and to optimise the mixing/milling process to produce homogeneous green state billets.

CHAPTER SIX

THE EFFECT OF GLASS ENCAPSULATED HOT-ISOSTATIC PRESSING UPON THE MICROSTRUCTURE OF SILICON NITRIDE

6.1. INTRODUCTION

This chapter summarises the microstructural evaluation of a variety of Si_3N_4 based ceramics, fabricated by glass encapsulated hot-isostatic pressing. The encapsulation techniques and HIP processing details have been described in the previous chapter, together with an assessment of the densification of these Si_3N_4 ceramics.

The microstructure of HIPed materials, using predominately Y_2O_3 sintering additives and encapsulated in a selection of differing glass tubing and powders, is examined. Particular attention has been paid to any interaction occurring at the ceramic/encapsulant interface during HIPing.

The initial stages of the encapsulation development/interaction assessment programme (using SiO_2 and Pyrex tube) were conducted using typical 'pressureless-sintered' type ceramics with a high volume, low viscosity matrix phase (compositions A1, using additions of 10 wt.% Y_2O_3, 2 wt.% MgO and 2 wt.% Cr_2O_3, and A2, identical except for the lack of a Cr_2O_3 addition). After the development of a reliable encapsulation/HIP technique (using Pyrex tube) a range of single additive ceramics were processed. Initially ceramic A3 (10 wt.% Y_2O_3) was HIP densified to assess the processing conditions required for full transformation/consolidation of a high matrix volume/viscosity material. Later in the programme a range of Y_2O_3 and Nd_2O_3 based silicon nitride ceramics (B1 to B7 and C1, C2 respectively, summarised in Chapter 3) were used for both the Pyrex tube encapsulation/HIP investigation and for a parallel microstructure/interaction examination of the commercial ASEA encapsulation process.

These single-additive ceramics utilise a low volume, high viscosity matrix phase. Assessment of the effect of glass encapsulated HIP processing upon the microstructure of densified silicon nitride was performed with the LCS Type 201 ceramic.

6.2. SILICA TUBE ENCAPSULATION

6.2.1. Composition A1

Full densification of samples of Si_3N_4 composition A1 did not occur after encapsulation and HIP in SiO_2 tube, primarily because of capsule failure arising during an early stage of the HIP cycle, with recorded densities of 83-84% TD.

Complete transformation of α- to β-Si_3N_4 had occurred in all specimens, indicating a diffusion-controlled densification and transformation mechanism. It is therefore clear that ingress of the pressurising N_2 gas within the interconnecting porosity acts as a driving force to counteract densification, though the transformation of α-β is not inhibited. It is likely that N_2 dissolution within the intergranular matrix occurs with pressurised gas ingress. This behaviour does not change the matrix glass viscosity sufficiently to alter the degree of β-Si_3N_4 re-precipitation.

SEM examination of the ceramic cross-section revealed a high percentage (up to 14%) of porosity in the bulk material, decreasing near to the surface (fig. 6.1a,b). This densification behaviour is consistent with the presence of a thermal gradient through the specimen during HIPing. A predominately monomodal β-Si_3N_4 grain size distribution was apparent, with fine high aspect ratio grains. It is believed that the finer grain size in the HIPed A1 ceramic arises from a variation in the temperature ramp rate during the initial stages of the HIP cycle, coupled with a shorter processing duration such that grain coarsening does not occur. The influence of sintering ramp rates upon the β-grain morphology is not currently fully understood.

a

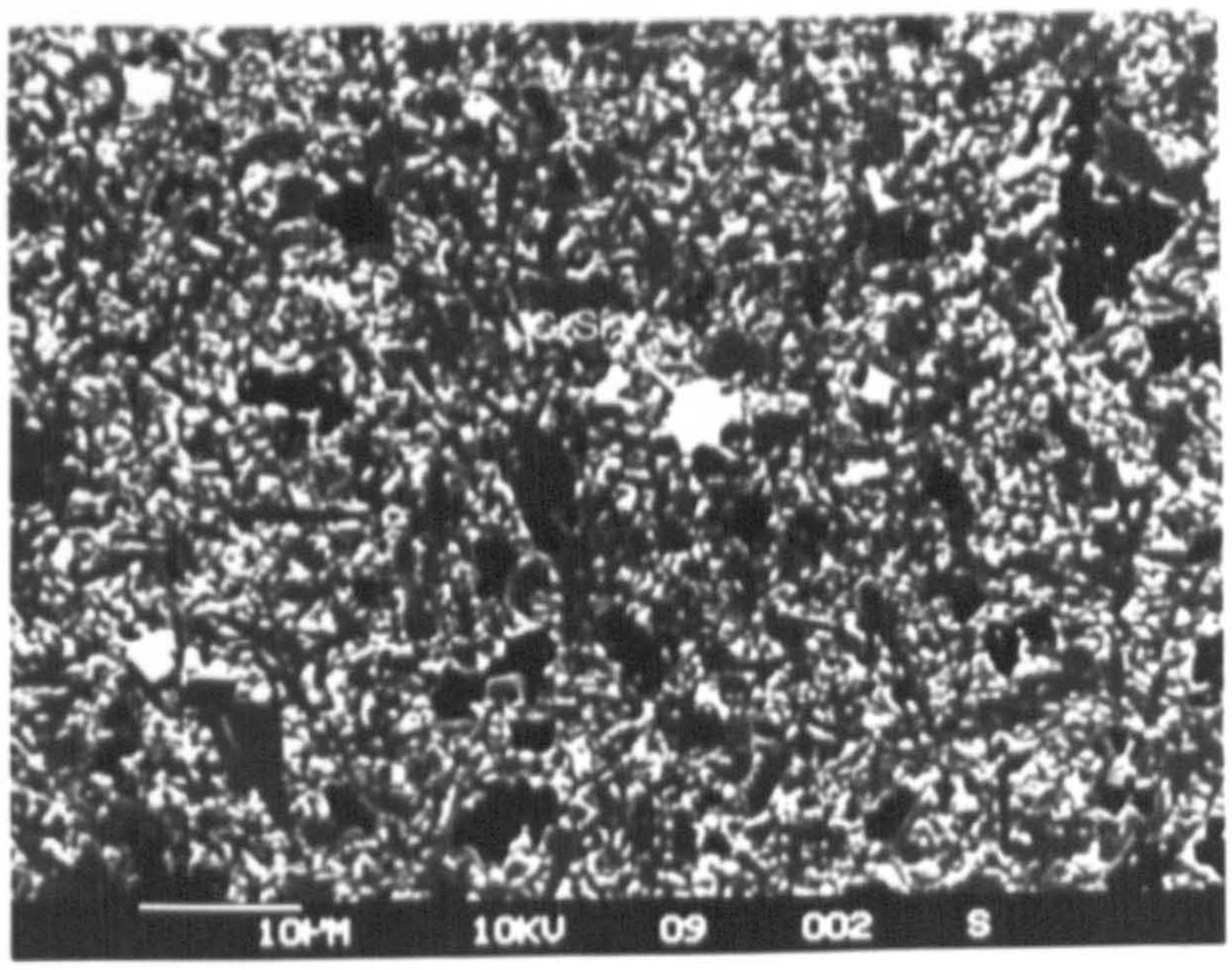

b

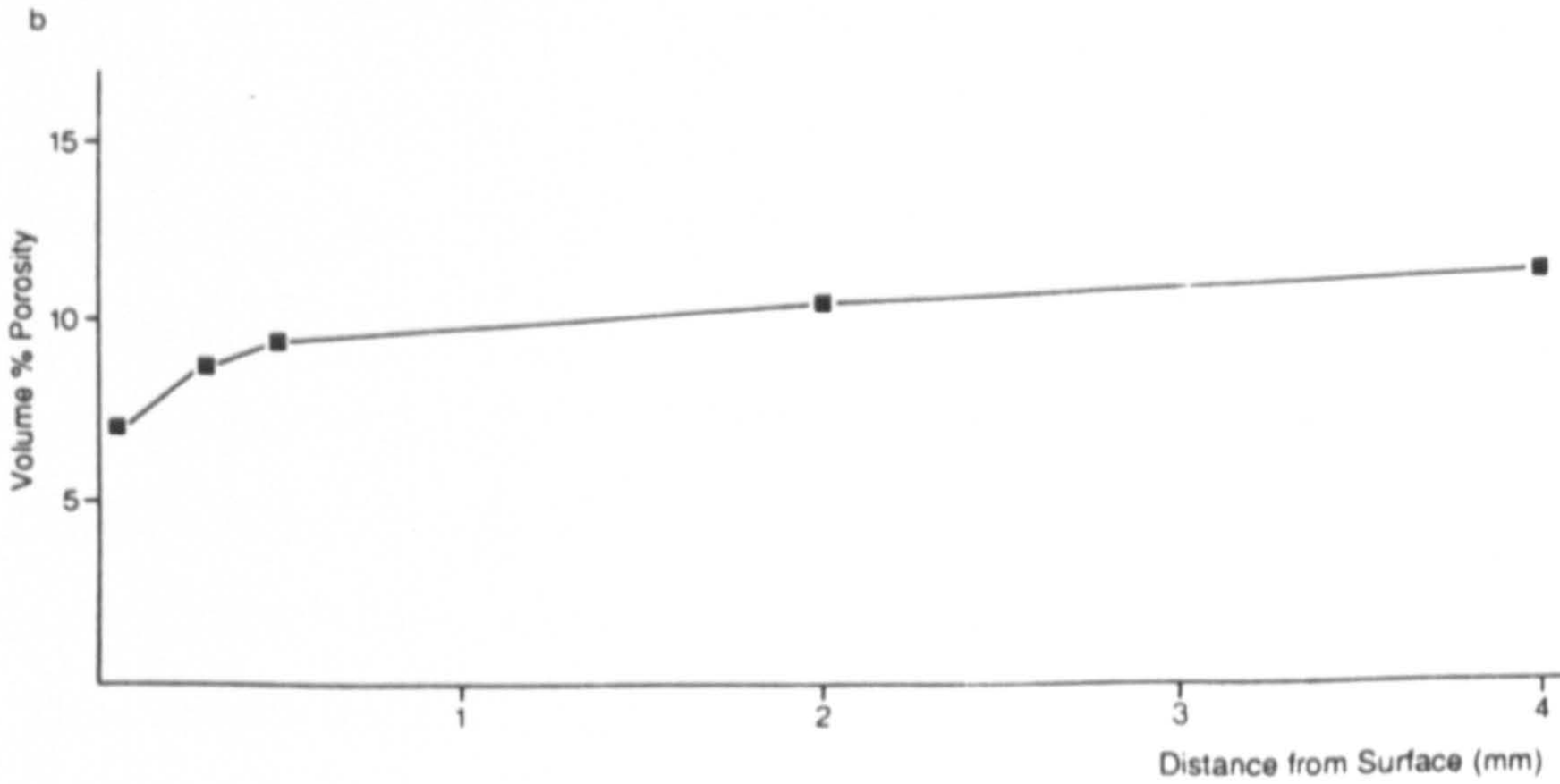

Figure 6.1 a) SEM micrograph of the bulk region of ceramic A1, HIPed in SiO_2 glass capsule, showing relative porosity level. b) The variation of porosity volume as a function of depth from the specimen surface.

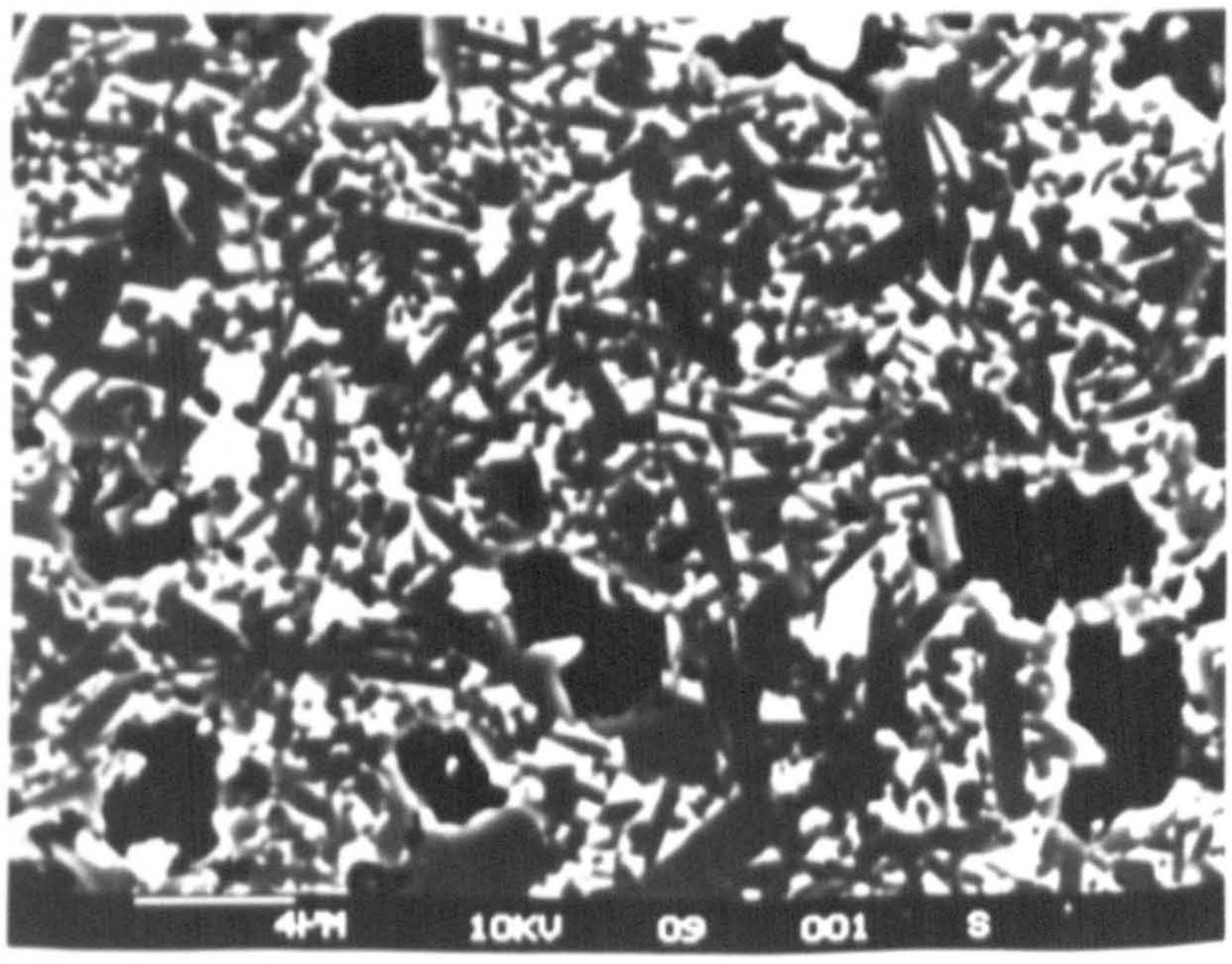

Figure 6.2 Isolated regions of chromium silicide in SiO_2 encapsulated, HIPed ceramic A1.

The secondary phase composition, of HIPed A1, was identical to the pressureless sintered variant of the same composition. Isolated chromium silicide regions were present in a semi-granular form similar to the pressureless sintered material (fig. 6.2), although they were not mixed with the Y/Mg-silicate glass as for the pressureless sintered material.

Surface examination, via XRD, revealed only β-Si_3N_4 to be present. There was no detectable enhancement of the matrix glass volume in the subsurface region of composition A1, and no ceramic/encapsulant reaction was observed.

6.2.2. LCS 201

The SiO_2 encapsulated HIPed 201 microstructure exhibited an almost unchanged hexagonal prism morphology of substituted β′-Si-Al-O-N grains (Z = 0.45) within a secondary phase of between 7-9 vol.% (fig. 6.3a). The crystallised YAG second phase had reverted to glass at the HIP processing temperature and had remained in this state upon cooling (fig. 6.3b). Heath demonstrated that, in an inert atmosphere, the crystalline YAG phase reverted to glass at a temperature in excess of 1525°C [44]. The impurity iron silicide regions, present in the as-received material, were retained after HIP processing and the α′-Si_3N_4 content and composition in the bulk ceramic remained unchanged after HIP (~ 5 vol.%).

A glass depleted region (~ 10-20μm in thickness) existed at the surface of the SiO_2 encapsulated 201 samples. Increasing the level of atomic number contrast in the SEM, for back-scattered electrons, revealed a glass denuded layer principally consisting of rounded β′-Si-Al-O-N grains (Z = 0.36) and the Al substituted form of silicon oxynitride (O′-Si_2N_2O) with small intergranular regions of impurity iron silicide which is stable with respect to the two other phases (fig. 6.4a).

The lower substitution levels for β′ (and O′) relative to the bulk concentration arise from

a

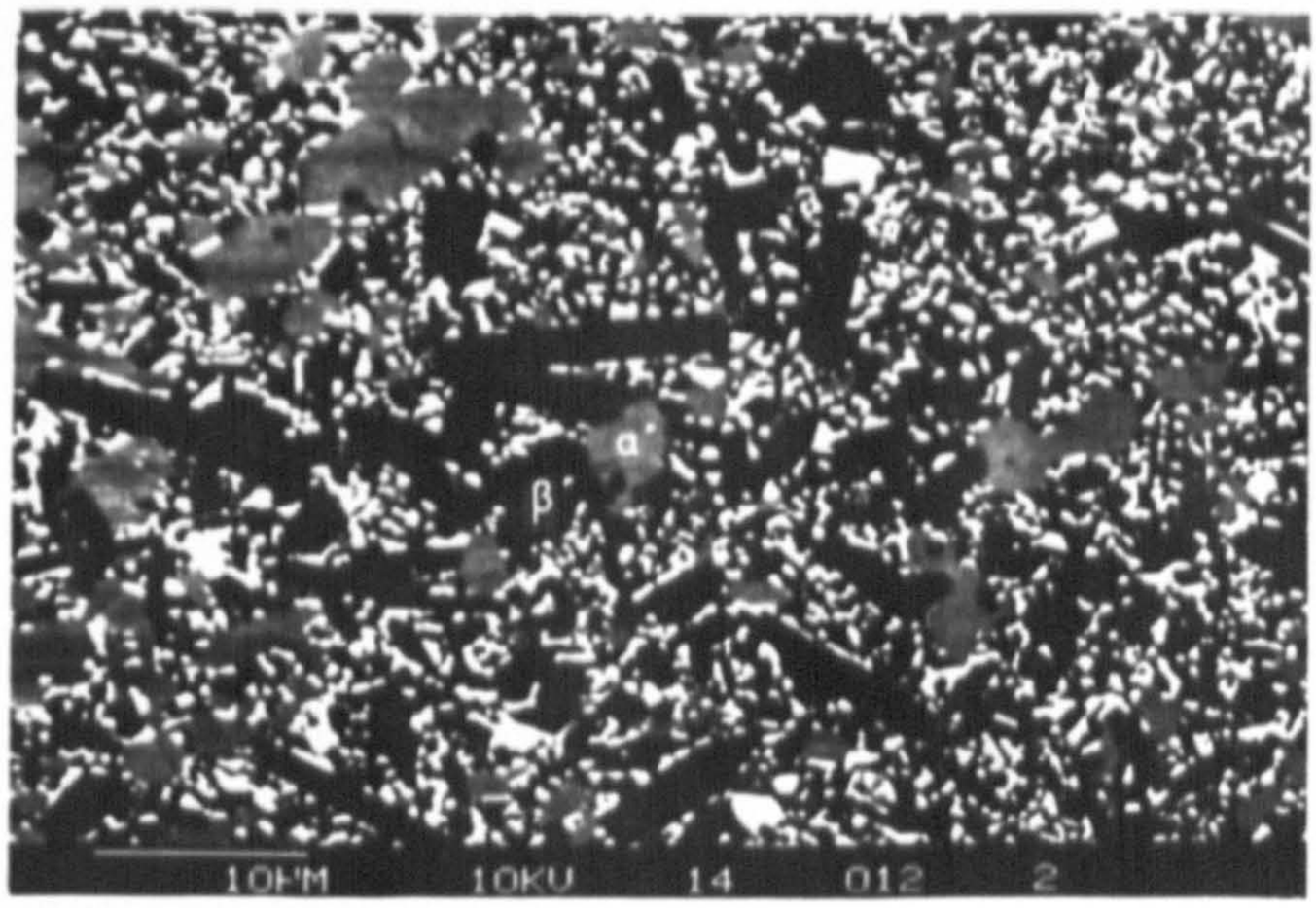

b

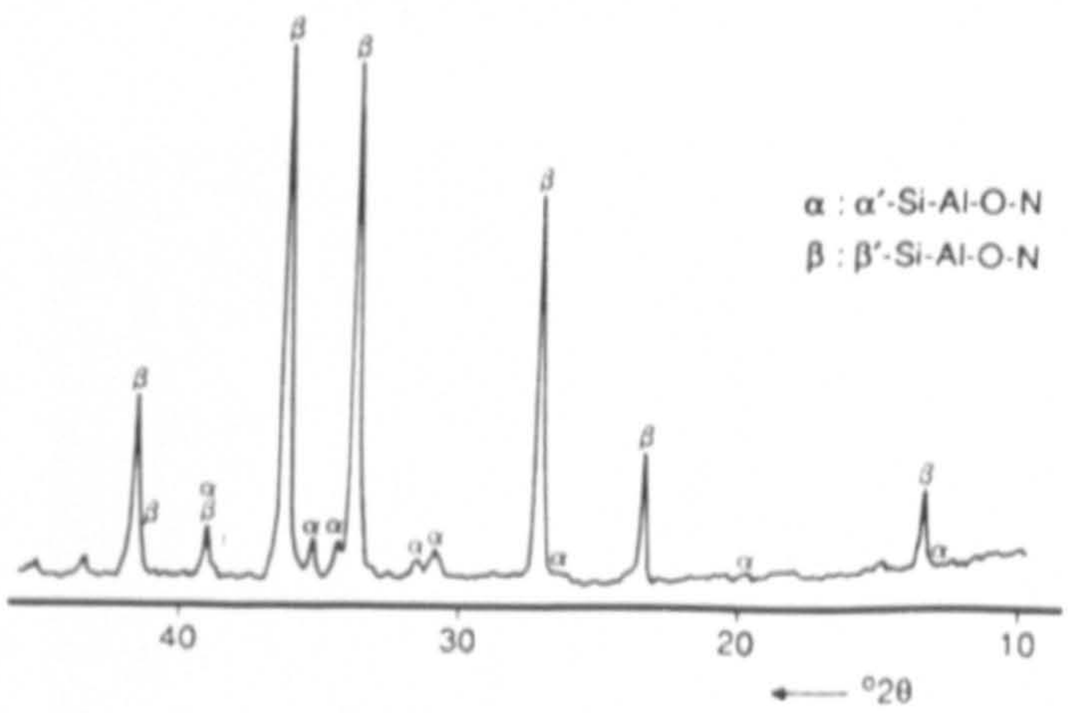

Figure 6.3 a) SEM micrograph of the bulk ceramic of HIPed Lucas 201, encapsulated in SiO_2 tube, revealing the retention of α'-Si_3N_4 and impurity iron silicide after HIP processing. b) XRD reveals the reversion of the primarily YAG matrix to glass.

a

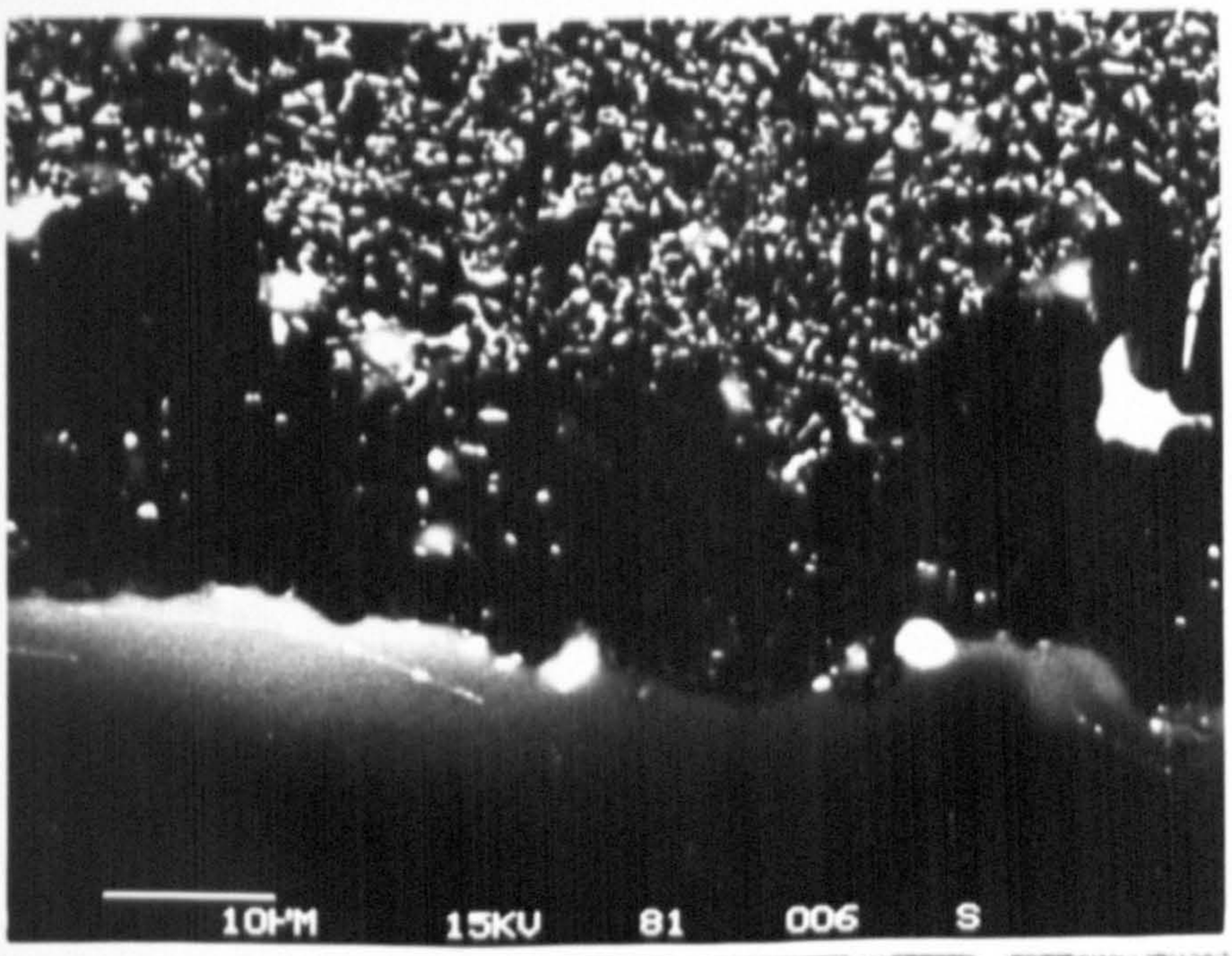

β′-Si-Al-O-N
+
O′-Si_2N_2O

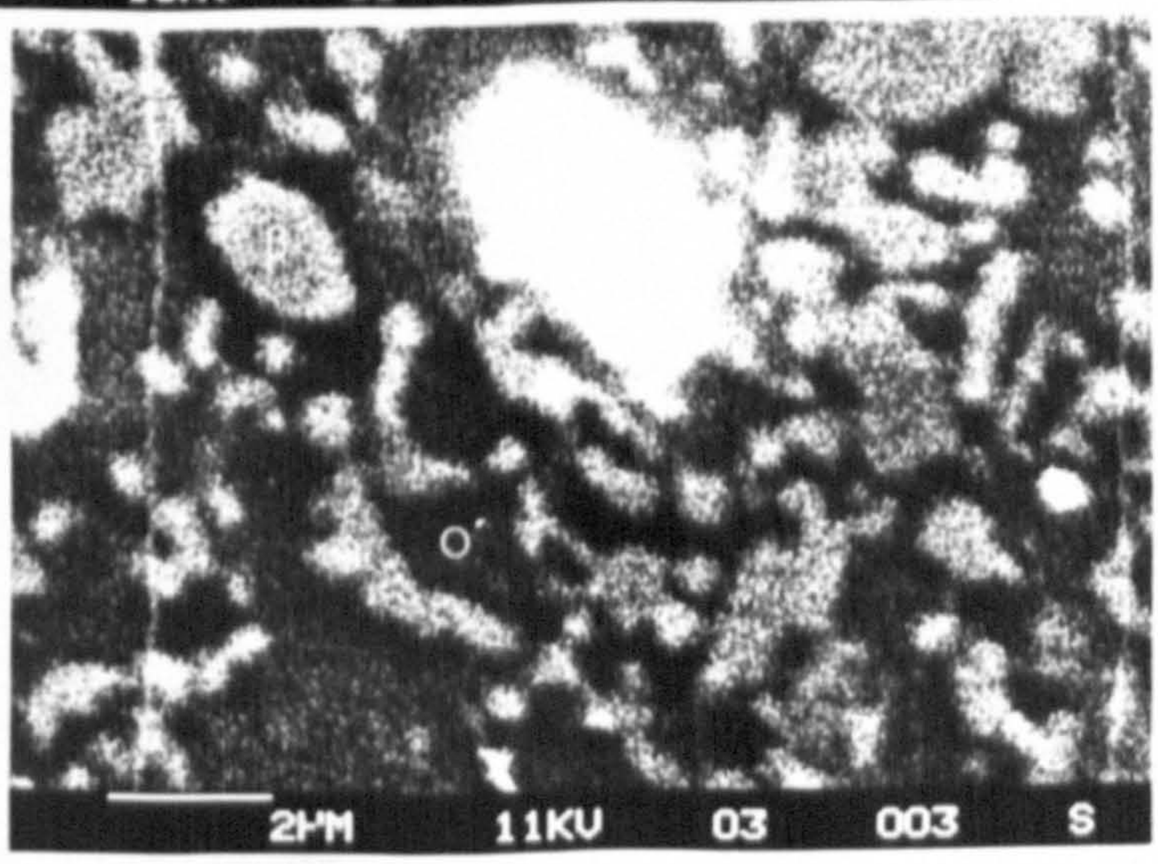

b

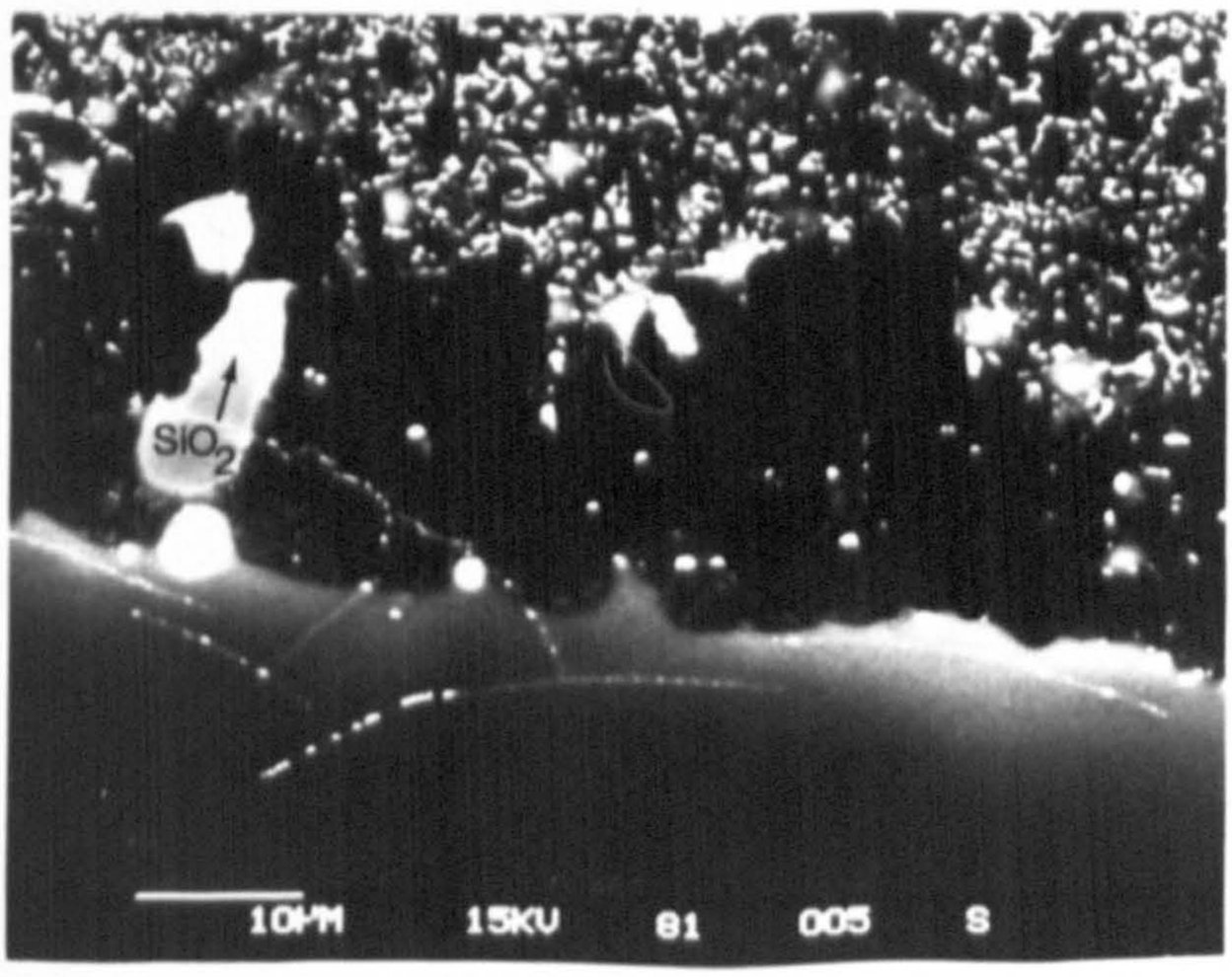

Figure 6.4 a) SEM micrograph of the HIPed Lucas 201 surface reaction layer formed from interaction between the densified ceramic and SiO_2 encapsulant. The surface layer is comprised of β′-Si-Al-O-N and O′-Si_2N_2O, with residual areas of iron silicide. b) Isolated 'fingers' of the SiO_2 encapsulant are apparent penetrating into the surface connected porosity.

loss of Al^{3+} cations to the pure SiO_2 glass layer.

In regions where the surface connecting porosity was relatively large scale (> 5μm wide pores), 'fingers' of encapsulant SiO_2 were observed penetrating into the densified ceramic (fig. 6.4b). The O′/β′ interaction layer thickness generally increased at the tip of the SiO_2 'fingers'.

Depletion of the intergranular glass phase (having reverted from YAG above 1525°C) occurs as the constituent cations, primarily Y^{3+} and Al^{3+}, out-diffuse into the SiO_2 encapsulant glass. In-diffusion of O^{2-} from the encapsulant occurs simultaneously. This behaviour is analogous to the formation of O′ during the oxidation of Y-Si-Al-O-N ceramics [44], with O′ growth arising from β′ solution and O′ precipitation within a small volume of liquid phase. However the silicate film formed during passive oxidation of Y-Si-Al-O-N ceramics is relatively thin (typically 10 - 40μm in thickness, depending on temperature and time) and out-diffusion of Al^{3+} and Y^{3+} cations significantly modifies the silicate glass composition and viscosity (as described in section 1.5.1). Conversely the viscosity and composition of the SiO_2 encapsulant layer will not be significantly altered as the SiO_2 is effectively an 'infinite' volume cation sink, being 1-2mm thick.

Two mechanisms are proposed for O′ formation during HIP of densified silicon nitride:

1. Direct 'oxidation' of β′ by the SiO_2 layer. Oxidation effectively occurs in a low oxygen potential with the liquid SiO_2 layer following

$$Si_3N_{4(s)} + SiO_{2(l)} \longrightarrow 2Si_2N_2O_{(s)}$$

The production of solid Si_2N_2O, or more accurately O′-Si_2N_2O, is preferred under HIP conditions where the high isostatic gas pressure inhibits the formation of SiO and N_2 gaseous species, which form during 'active' oxidation via the reaction

$$Si_3N_{4(s)} + 3SiO_{2(s)} \longrightarrow 6SiO_{(g)} + 2N_{2(g)}$$

The formation of O′ is believed to occur via a liquid phase.

2. The solid state transformation of β′ to O′ following the loss of Al^{3+} from β′ to the glassy silicate surface layer. The curved β′/O′ grain boundaries, evident in figure 6.4a, indicate the occurrence of a solid state transformation mechanism and the attainment of a surface energy equilibrium state.

The kinetics of these two reactions will be considerably enhanced at the HIP processing temperature of 1750°C, with the volume of O′ formed after HIP being comparable to the oxidation of Y-Si-Al-O-N ceramics at 1320°C for 100 hours [44].

The subsurface microstructure, below the β′/O′ composite layer, was generally similar to the bulk ceramic. However, a lower level of α′ was apparent in this region, typically ~ 2 vol.%, and the Al substitution level for both α′ and β′ was lower than in the bulk ceramic. It is proposed that O^{2-} in-diffusion to the subsurface region occurs during the early stages of the hold period of the HIP cycle and this behaviour has the effect of lowering the localised N/O ratio. As previously described (section 5.2.6) a high N/O ratio plays an important role in the determination of sintering re-precipitation products, with α′ formation favoured in high N conditions. Therefore during HIP sintering dissolution of the low volume of α′ grains occurs, which is followed by re-precipitation as β′. Enhancement of the O^{2-} content in the sub-surface region (to a depth of ~ 20μm) occurs with a simultaneous loss of Al^{3+} from the β′ grains resulting in the lower β′ substitution level, previously described.

6.3. PYREX TUBE ENCAPSULATION: ASSESSMENT OF CERAMIC BULK MICROSTRUCTURES

6.3.1. Ceramics with a High Volume, Low Viscosity Matrix Phase (A1,A2)

Initially sections of the 'green' state ceramics A1 and A2 were HIPed to 88-90% TD, with capsule failure allowing N_2 gas ingress. A complete α-β transformation had

occurred in both specimens although a large porosity residue was apparent in the bulk regions of the HIPed ceramics. The bulk microstructures and compositions were essentially identical to ceramic A1 HIPed in an SiO_2 tube (section 6.2.1), although no chromium silicide deposits were present in ceramic A2. The intergranular glass composition of ceramic A2 was similar to ceramic A1, which contradicts the observation made in section 5.2.5 where a maximum MgO concentration of ~ 0.5% was analysed. The inhomogeneity of MgO and Y_2O_3 additive dispersion in composition A2 was emphasised with the above observations and it was assumed to be a 'rogue' material batch which was insufficiently mixed during the milling process.

The bulk microstructure of HIP densified ceramics A1 and A2 (> 98% TD) was of a finer scale than the equivalent pressureless sintered ceramic A1 (fig. 6.5a,b,c), with β-Si_3N_4 grains in the size range 0.25 - 5μm with aspect ratios varying between ~ 2:1 and 6:1. A complete α-β transformation had occurred for both ceramics. It was apparent that these ceramics had a slightly less 'needle-like' β-Si_3N_4 structure than the pressureless sintered materials (A1). The tendency towards a more equiaxed β-grain morphology arises because HIP processing increases the effective densification contribution from particle rearrangement (stage I) as the average interparticle distance is reduced under the influence of pressure. The β-grain nucleation and growth are therefore increased, leading to an overall reduction in grain aspect ratio.

The intergranular glass compositions for the densified ceramics A1 and A2 were essentially identical to those analysed for the partially densified materials.

A variation in chromium silicide morphology was again observed in HIPed A1 when compared to the pressureless sintered material. The silicide regions, of analysed composition $CrSi_2$, were generally globular in appearance and of a finer scale (typically 1 to 2μm in diameter) as opposed to the more granular form arising in pressureless-sintered A1. The rounding of $CrSi_2$ regions is indicative of a state of minimisation of surface free

a

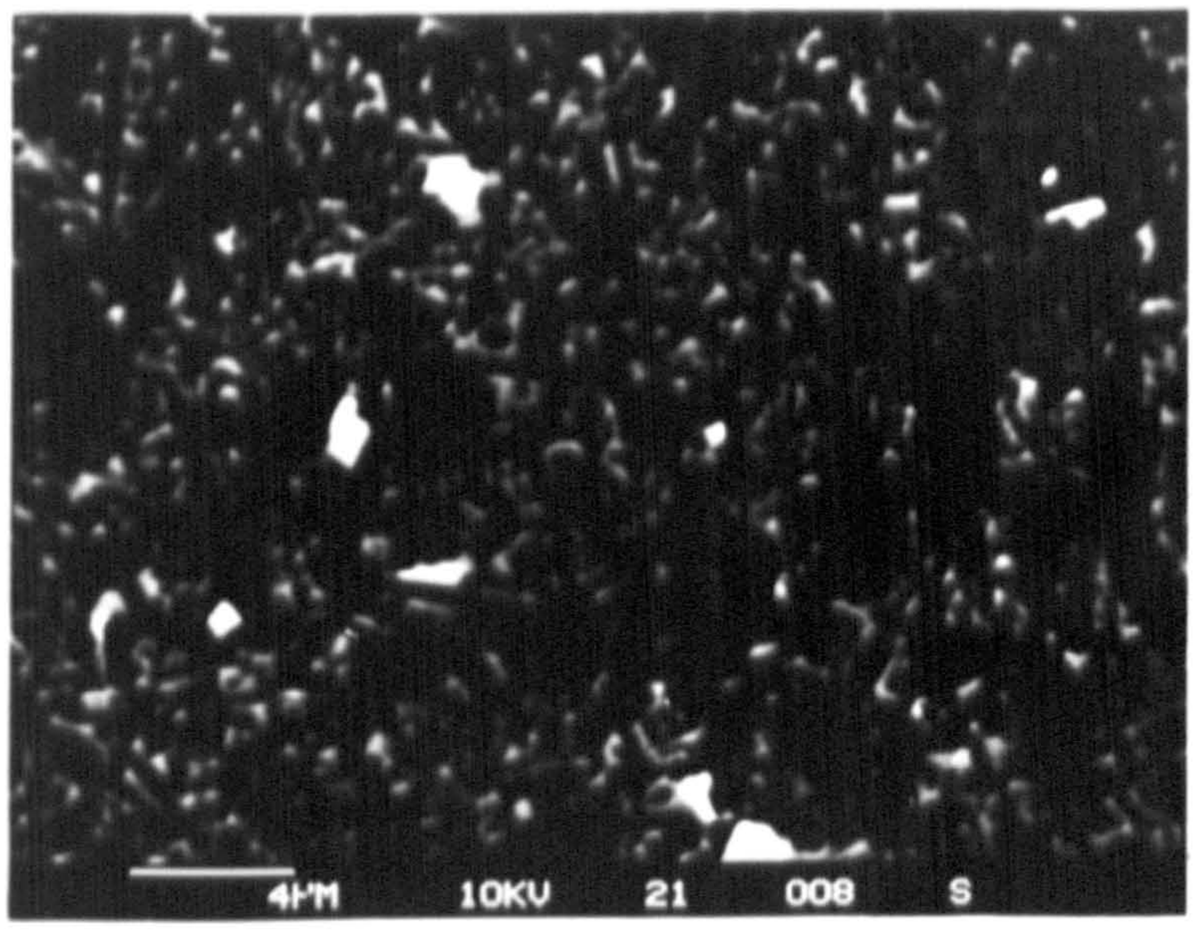

b

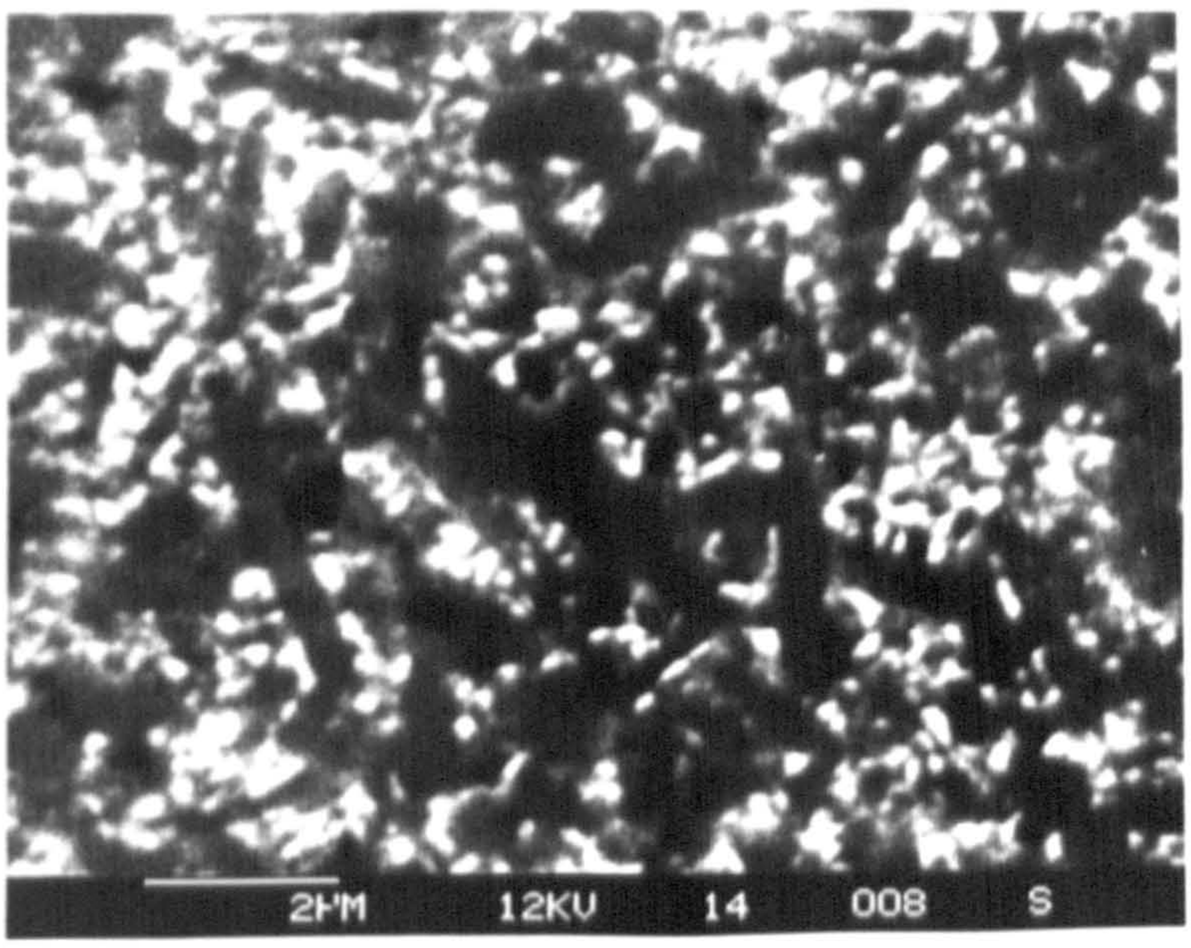

c

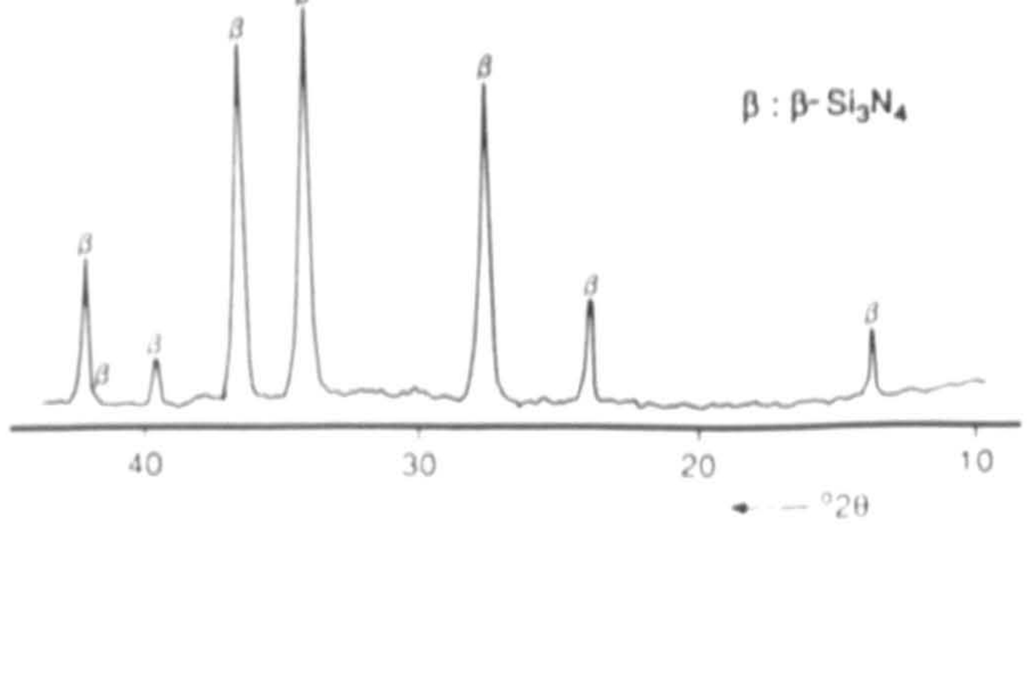

Figure 6.5 a) SEM micrograph of bulk microstructure of a) ceramic A1 and b) ceramic A2, both HIPed to > 98% TD. c) XRD demonstrates complete α-β transformation.

energy. A similar effect was apparent in impurity regions of iron silicide present in composition A2 (and A1).

6.3.2. Ceramic with a High Volume/High Viscosity Matrix Phase (A3)

The bulk microstructure of the HIPed A3 silicon nitride specimen consisted of hexagonal β-Si_3N_4 crystals within an intergranular glass phase of ~ 15-16 vol% (fig. 6.6a).

It was discovered that this glass volume was not identical throughout the bulk ceramic and rose to 18-19 vol% in isolated areas. The variation in glass volume is a possible explanation for the macroscopic inhomogeneity noted during SEM preparation. Certain isolated areas of the specimen, ~ 0.5 - 1mm in size, proved to be more susceptible to grain pullout and hence it was difficult to obtain a totally smooth surface finish.

By energy dispersive X-ray analysis, the intergranular glass phase was analysed as being close to that of the Y_2O_3-SiO_2 binary eutectic comprising 35 mol.% Y_2O_3 and 65 mol.% SiO_2 (fig. 6.6b) [191]. This composition is SiO_2 rich when compared to the starting mix and it must therefore be assumed that a finite nitrogen level is incorporated into the matrix phase, arising from solution of α-Si_3N_4 within the glass. The binary eutectic composition for the Y_2O_3-SiO_2 system is ~ 28 mol.% Y_2O_3 and 72 mol.% SiO_2 ie. $Y_2Si_{2.57}O_{8.14}$ (fig. 6.6b).

The β-Si_3N_4 crystals typically exhibited an aspect ratio in the range 4:3 to 2:1 although this increased to 5:1 in a small number of crystals. A high percentage of the β-Si_3N_4 crystals were sub-micron in size (½ to 1 μm), however some larger crystals were present up to 4 μm in length, which were of the high aspect ratio type. Energy dispersive X-ray microanalysis revealed that there was no detectable interstitial yttrium accommodation in the major phase. XRD revealed only β-Si_3N_4 in the bulk ceramic and hence a full α- to β-Si_3N_4 transformation has occurred during HIP (fig. 6.6c).

a

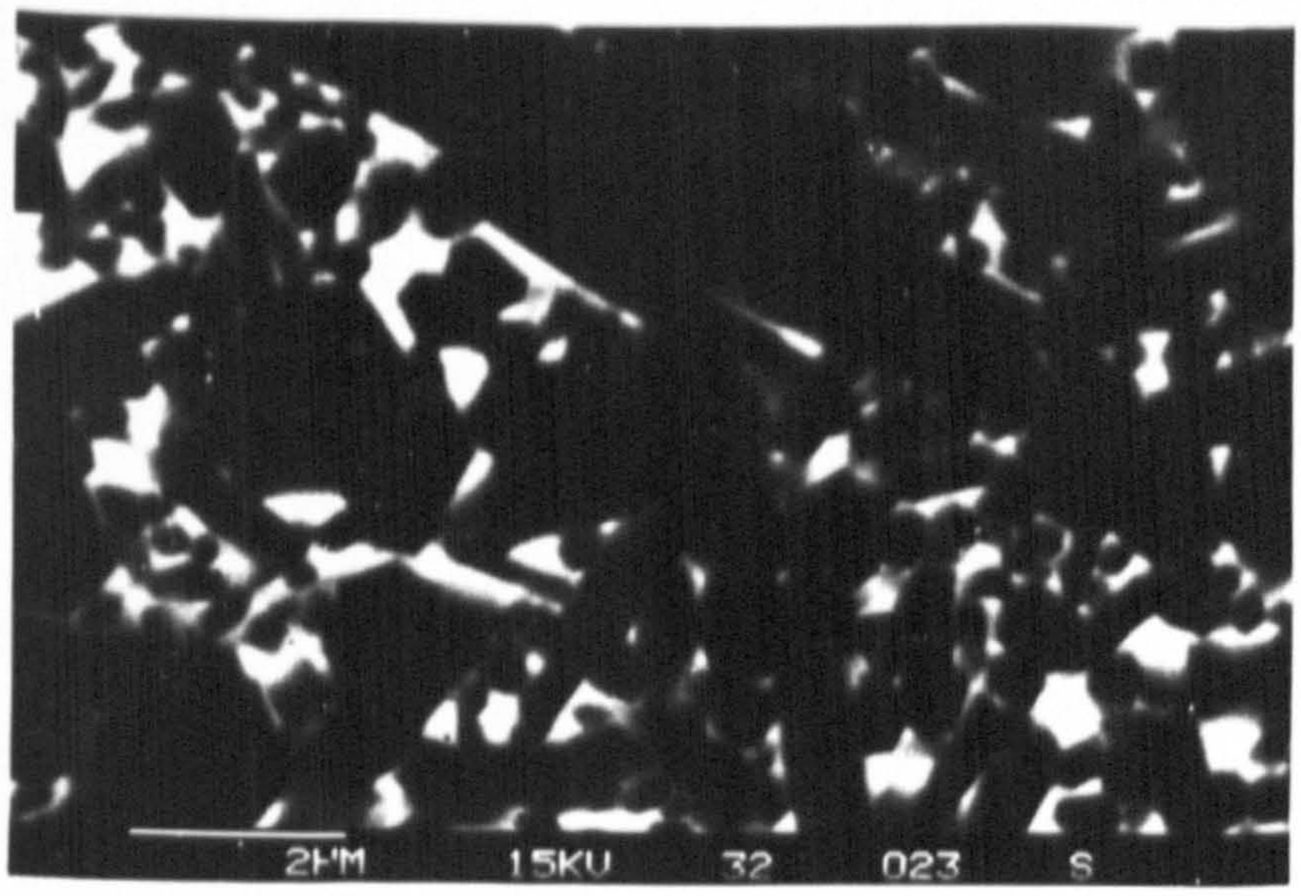

b

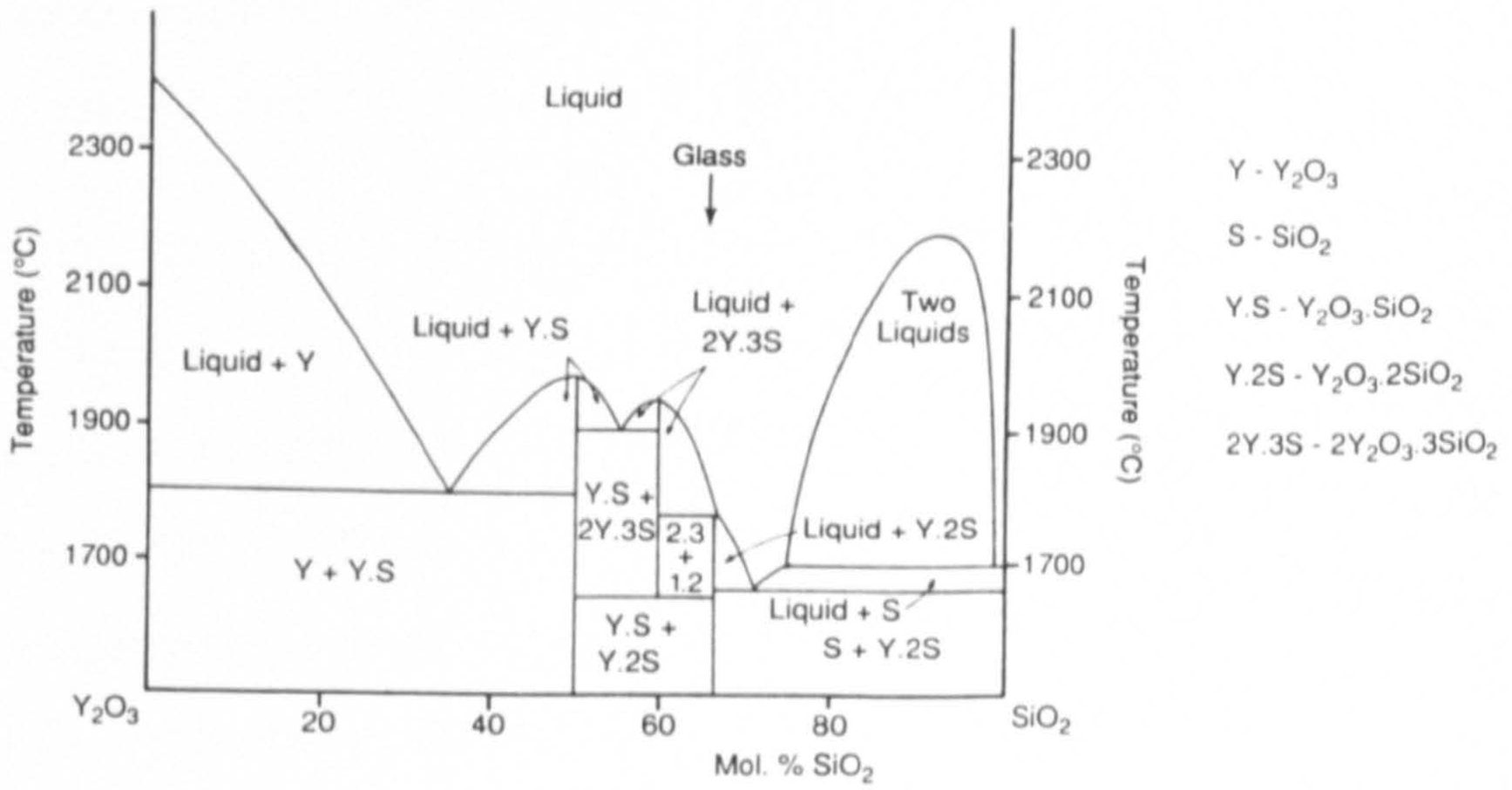

c

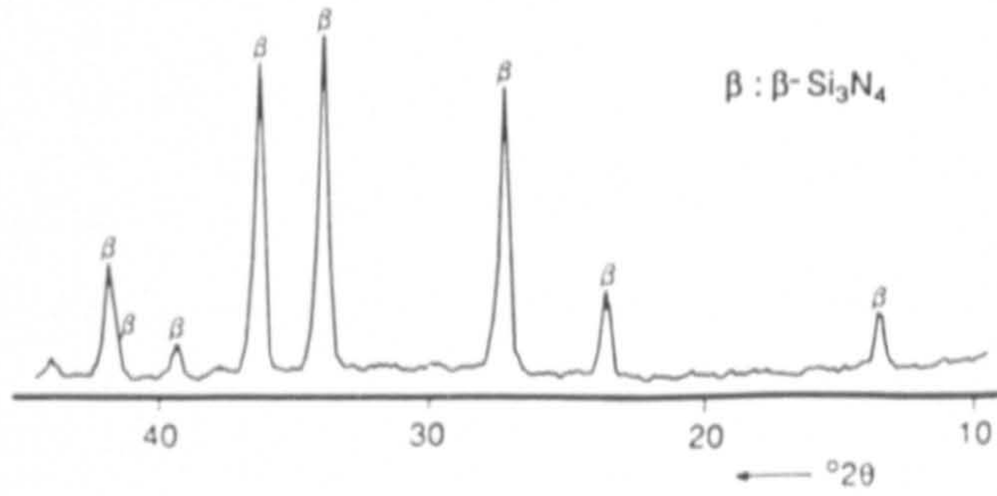

Figure 6.6 a) SEM micrograph of bulk microstructure of ceramic A3, HIPed to ~ 98% TD with b) the intergranular phase composition plotted on the Y_2O_3-SiO_2 binary phase diagram. c) XRD reveals only β-Si_3N_4 present in the bulk ceramic.

6.3.3. Ceramics with a Low Volume, High Viscosity Matrix Phase (B1,B2,B5,C1,C2)

XRD analysis of the bulk of ceramic composition C1 revealed the presence of three crystalline phases, which were identified as α-Si_3N_4, β-Si_3N_4 and Nd-N-apatite ($Nd_5(SiO_4)_3N$) (fig. 6.7a), with an α- to β-Si_3N_4 ratio of 15:85. Microstructural examination revealed the presence (mainly) of fine β-Si_3N_4 grains 0.25 - 2μm in length, with aspect ratios between 2:1 and 3:1, within a semicontinuous, crystalline apatite matrix (fig. 6.7b). Transmission electron microscopy of ceramic C1, conducted by Dr. G. Leng-Ward, revealed complete crystallisation of the intergranular phase to Nd-N-apatite with negligible residual glass (fig. 6.7c) [192].

The crystallisation of the quaternary apatite phase occurs because the residual glass composition lies within the Si_3N_4-$Y_2Si_2O_7$-$Y_5(SiO_4)_3N$ phase field.

XRD of the bulk of ceramic C2 demonstrated the presence of three crystalline phases: α-Si_3N_4, β-Si_3N_4 and a mixed Y-Nd-apatite phase (identified by Dr. G. Leng-Ward from selected area diffraction, or SAD, studies in the TEM [192]), with a measured α-β-Si_3N_4 ratio of 23:77. The bulk microstructure was essentially similar to ceramic C1 with a relatively high volume of porosity present. TEM examination revealed the matrix phase to be a glass/apatite mixture [192].

It is apparent that the ingress of nitrogen gas into the bulk of ceramics C1 and C2, with a high viscosity matrix phase, inhibits not only densification but also the α-β-Si_3N_4 transformation. A complete transformation occurred in similar compositions HIPed at ASEA under comparable processing conditions. Transformation is believed to be impaired in these lower matrix volume ceramics, with nitrogen dissolution increasing the glass viscosity such that the material transport rate (α-solution followed by β-precipitation) is slower than in comparable, fully densified, HIPed ceramics. Nitrogen dissolution in the matrix glass occurred after capsule failure, early in the HIP cycle, and will affect the whole of the silicon nitride body, which has a high level of interconnecting

a

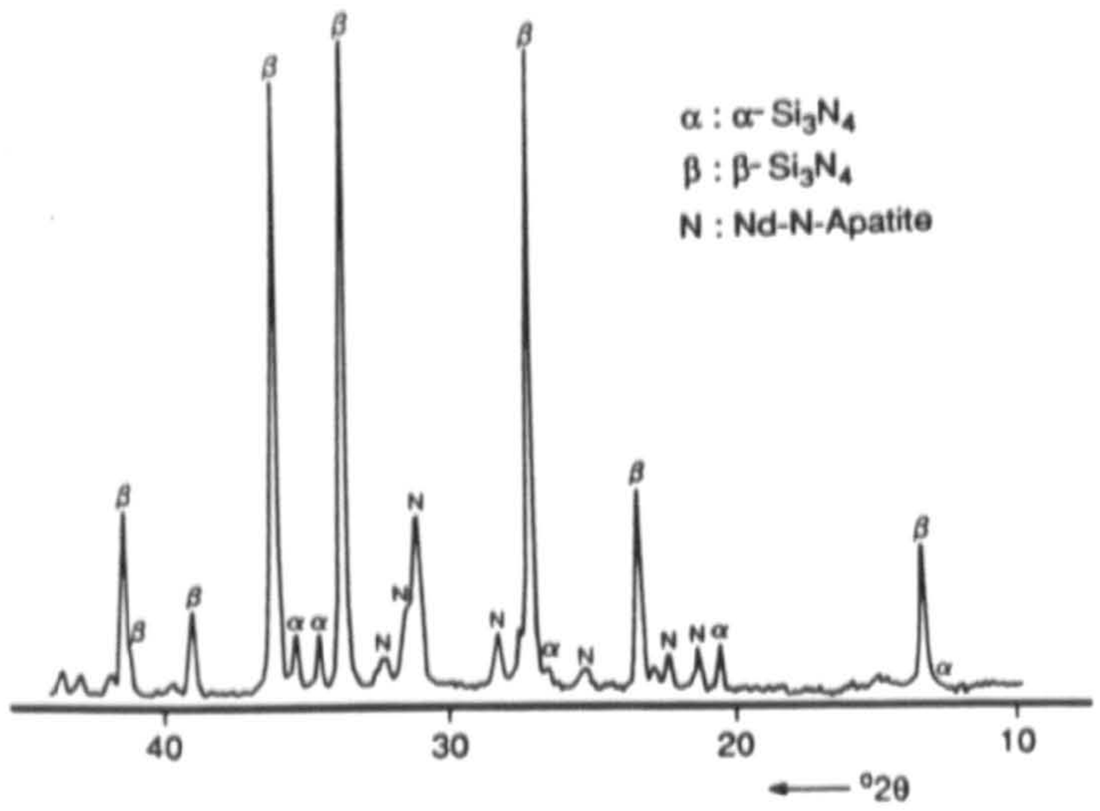

b

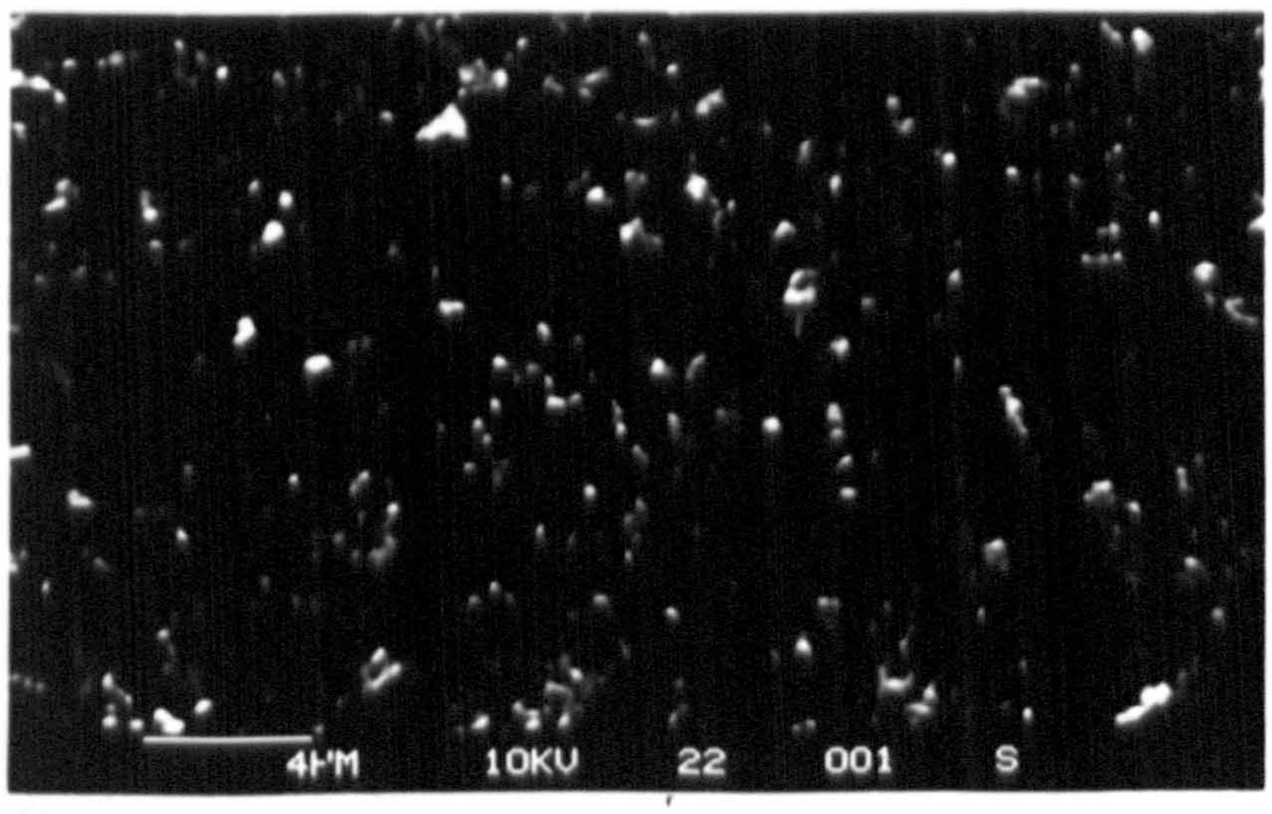

c

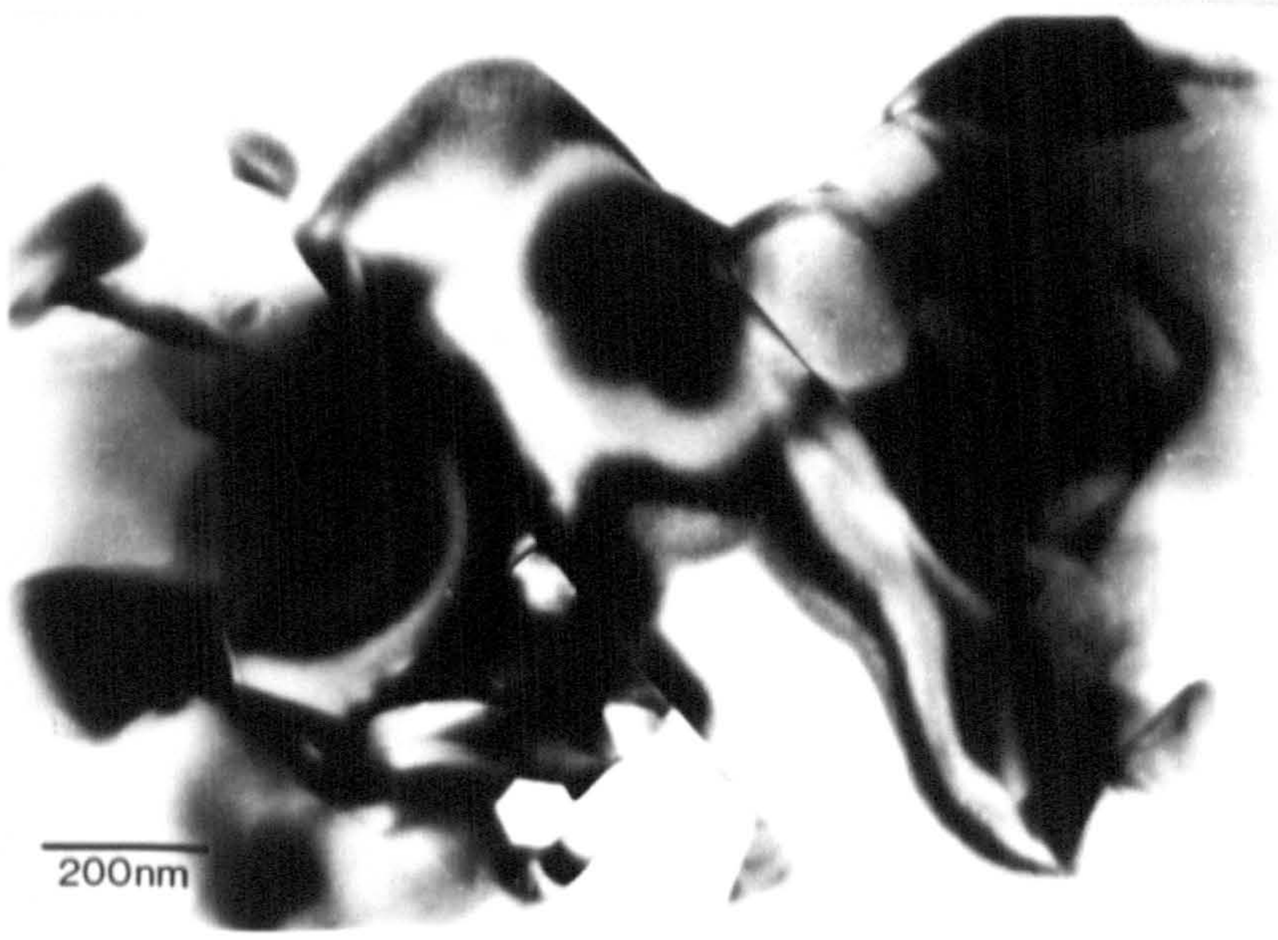

Figure 6.7 a) XRD of the bulk of ceramic C1, with Nd_2O_3 addition, reveals incomplete reprecipitation of β-Si_3N_4 and crystallisation of the matrix phase as Nd-N-apatite. b) SEM micrograph of the bulk microstructure of ceramic C1 revealing a fine, mainly, β-Si_3N_4 grain structure with ~ 10 vol.% porosity. c) TEM micrograph of bulk microstructure of ceramic C1, with fully crystalline Nd-N-apatite matrix. Small β-Si_3N_4 grains, present in the intergranular phase, are believed to have precipitated from the high nitrogen glass on cooling, with the glass crystallising as the neodymium apatite phase. (Courtesy of Dr G. Leng-Ward).

porosity in the early stage of the HIP cycle. Nitrogen incorporation in the glass structure has been shown to increase the viscosity, hardness and glass transition temperature in oxynitride glass systems [193].

The microstructure of composition B1, HIPed to ~ 88% TD, exhibited a high degree of bulk porosity. A partial α- to β-Si_3N_4 transformation had occurred during HIP and an approximate α-β ratio of 33:67 was measured via XRD. A fine β-Si_3N_4 grain structure had formed after HIP, with predominately needle like grains precipitated to a maximum size of ~ 2μm.

It is believed that the high HIP gas pressure partially inhibits transformation, as for ceramics C1 and C2, although it is thought that a full α-β transformation could be obtained by increasing the process time to two hours (composition B1 was pressureless sintered at 1700°C for two hours, giving a complete transformation (section 5.10)).

Crystallisation of the secondary phase did not occur upon cooling, as a rapid cooling rate was employed after HIP, and a Y-Si-O-N glass remained. A 48 hour post-HIP heat treatment in nitrogen (at ~ 1250°C), conducted by Dr. G. Leng-Ward, produced complete crystallisation of the intergranular glass, principally to yttrium-nitrogen-apatite ($Y_5(SiO_4)_3N$), although an unidentified XRD peak was observed at d = 3.03Å [192]. This individual peak corresponded to the strongest peak of an unidentified phase reported by Yeheskel [144].

The microstructures of HIP densified ceramics B1, B2 and B5 were essentially very similar, with a dispersion of β-Si_3N_4 grains within a low-volume, semi-continuous glassy matrix (fig. 6.8a,b). Low levels of bulk porosity were apparent in both B2 and B5 (~ 2-3 vol.%) although ceramic B1 appeared to be free of porosity. All three compositions exhibited bimodal β-Si_3N_4 grain size distribution, with aspect ratios between 2:1 and 4:1. The grain size ranged from 0.25 to 4 μm.

XRD revealed β-Si_3N_4 as the only crystalline phase present in composition B1, however compositions B2 and B5 contained small volumes of silicon oxynitride, Si_2N_2O (approximately 5 vol.%) (fig. 6.8c). The observation of Si_2N_2O formation is consistent with the initial batch compositions of B2 and B5, with 4.96 and 4.99 eq.% oxygen respectively. Increasing the percentage of oxygen in the starting powder mixture has the effect of pushing the overall composition into the Si_3N_4-Si_2N_2O-$Y_2Si_2O_7$ compatibility triangle. Consequently Si_2N_2O becomes more favourable as a reprecipitation product. HIP processing therefore offers the potential of fabricating a dense ceramic with a purely Si_2N_2O major phase (by balancing the overall composition on the Si_2N_2O-$Y_2Si_2O_7$ tie line), overcoming the problem of Si_2N_2O decomposition at temperatures greater than 1600°C.

6.4. PYREX TUBE ENCAPSULATION: ASSESSMENT OF SURFACE CERAMIC/ENCAPSULANT INTERACTION

The variation of ceramic/encapsulant interaction with Pyrex encapsulated specimens was generally assessed in two circumstances for each of the compositions previously discussed. The comments made regarding boron nitride (BN) coating thickness refer to measurement of the layer *after* HIP processing. Typically the layer thickness appears to be reduced, from the original painted coating, by a factor of between five and ten (eg. 0.5mm painted coating reduced to 60 - 100μm).

Generally a coating ~ 250 - 500μm thick was applied to the green state billets prior to encapsulation. To compare the reaction level some regions were given a very thin coating, <100μm thick. After HIP the thickest coated regions were ~ 80μm, whilst the thinnest areas were ~ 5 - 10μm. A few isolated regions of coating 'break-down' were apparent in some specimens, and it was in these areas that the most severe interactions occurred.

a

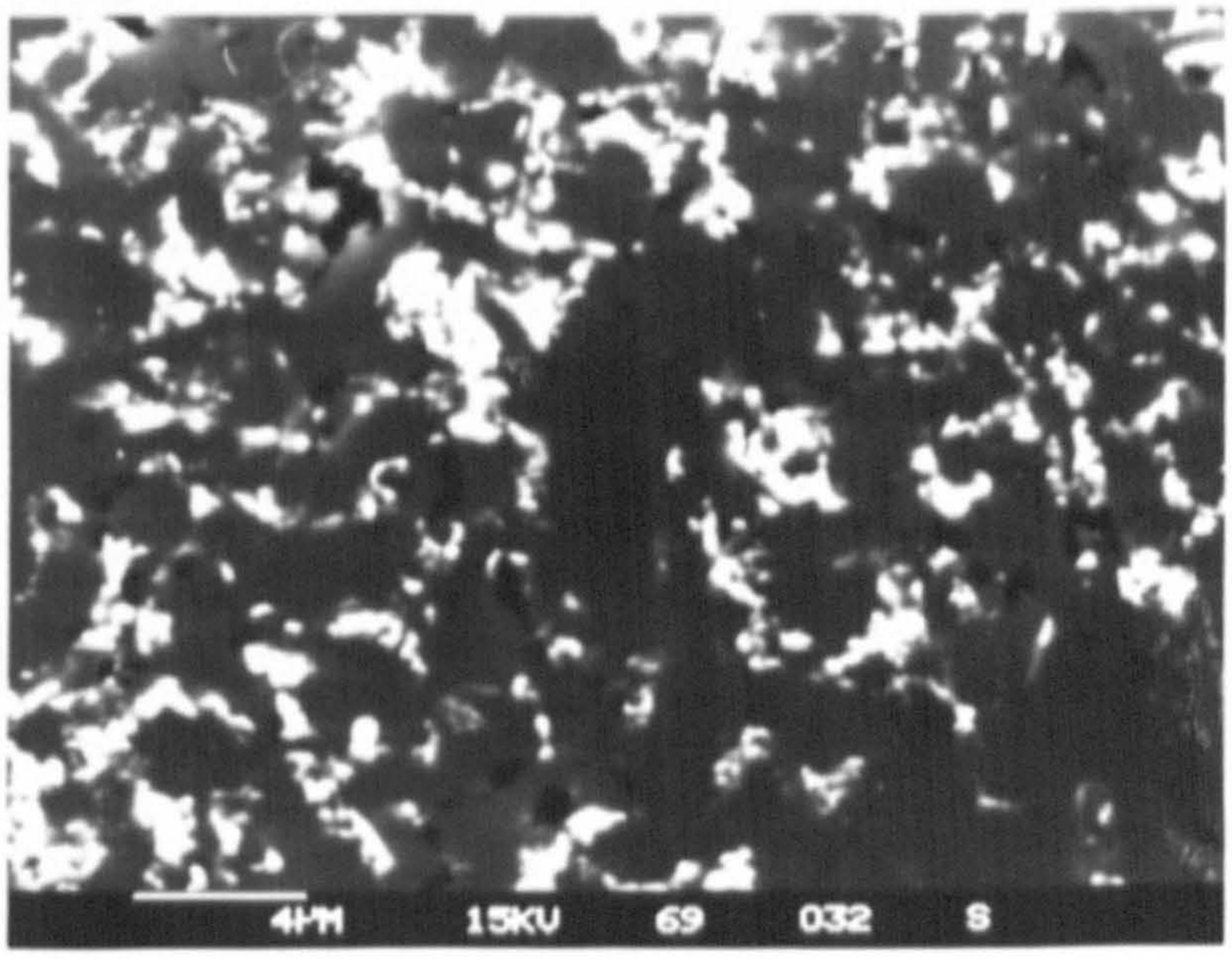

b

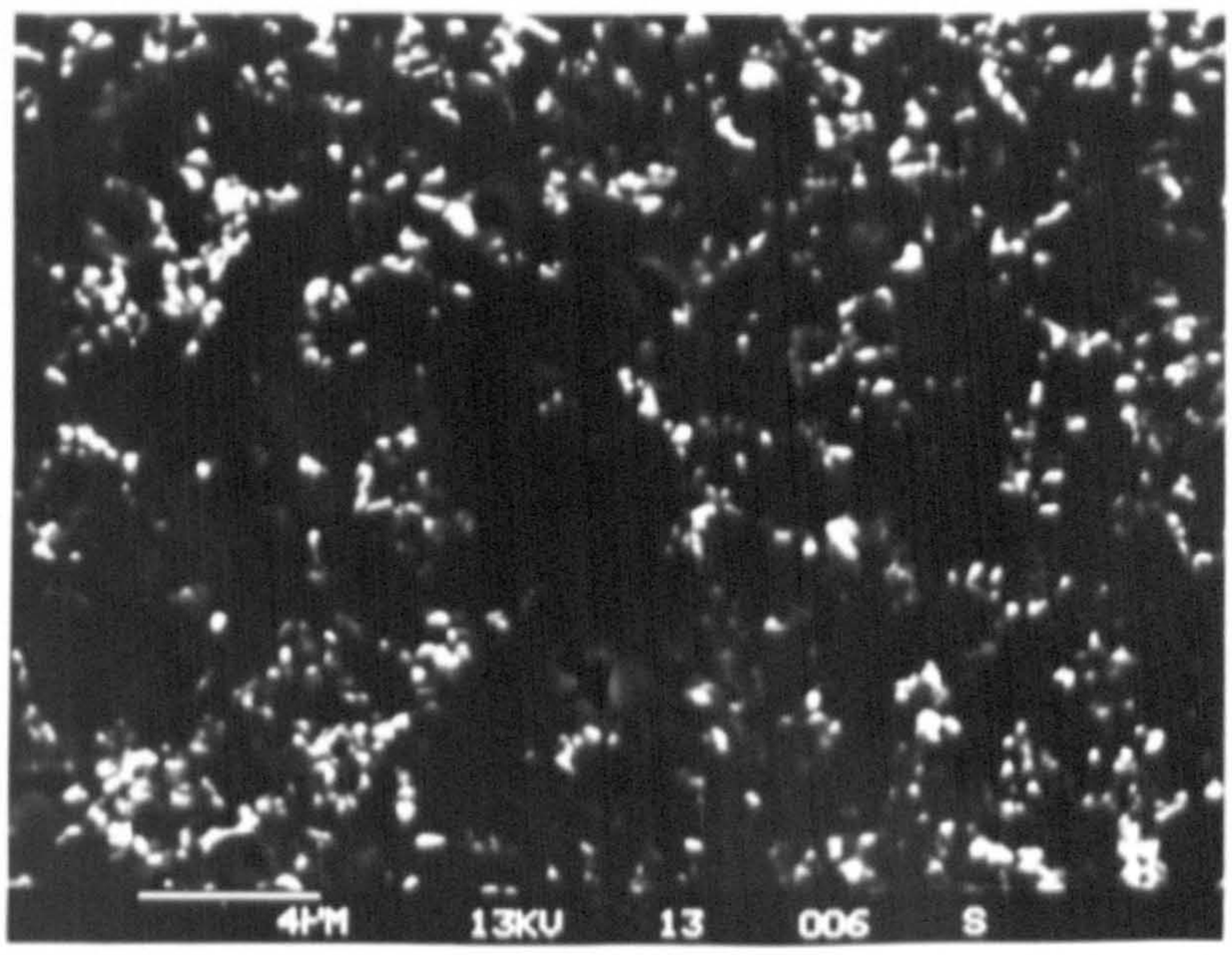

c

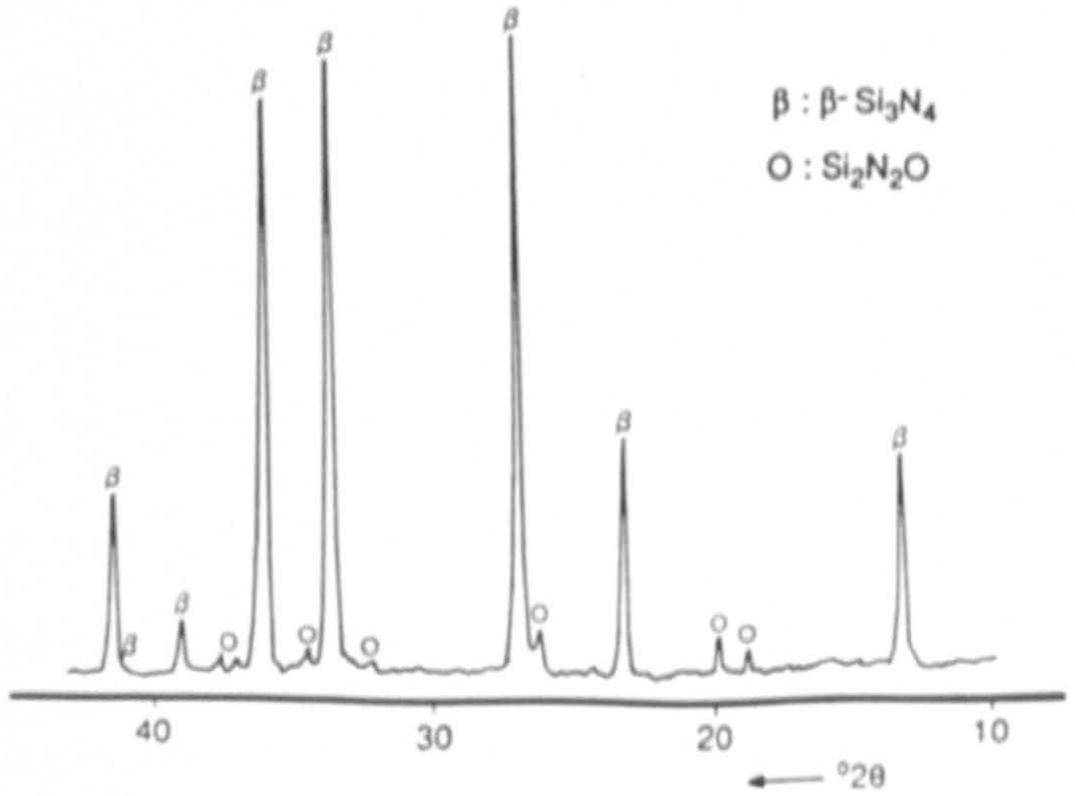

Figure 6.8 SEM micrograph of dense HIPed ceramics, a) B1 and b) B2, illustrating the emergence of Si_2N_2O as an additional reprecipitation product with increasing oxygen content. c) XRD demonstrates the formation of Si_2N_2O at higher oxygen levels (B2).

6.4.1. Ceramics with a High Volume, Low Viscosity Matrix Phase (A1,A2)

No surface interaction region was observed for either of the low-viscosity glass phase ceramics when a post-HIP BN layer thickness of greater than 50μm was retained after densification (fig. 6.9a). The surface microstructure of ceramics processed under these conditions was similar to the bulk material, with a typical β-Si_3N_4/glass morphology. The intergranular glass volume at the extreme surface of these regions was noticeably lower than the bulk material and, within ~ 1μm of the ceramic, levels of Mg (and Y) were detected in the BN layer. Despite the BN layer thickness it is apparent that a chemical couple arises between the ceramic and encapsulant, with the material transportation of the ceramic intergranular glass-forming cations towards the encapsulant and species from Pyrex towards the ceramic, although the transport rate through the porous BN layer is slow. The driving force for interdiffusion is the desired formation of an equilibrium composition glass.

Where a thin BN layer existed, ie. less than 10μm, a relatively severe interaction had occurred. A glass depleted monophase layer (up to 80μm thick) was formed at the surface of the ceramic (fig. 6.9b). The surface reaction layer was totally devoid of any glass phase, however the chromium silicide regions were retained in this layer after HIP. Light element EDX analysis revealed the surface layer to be predominately silicon oxynitride (Si_2N_2O). Isolated regions of a high average atomic number glass phase were present at the extreme surface of the monophase layer. The composition of these regions was generally based upon the elements Y, Mg and Si, with low levels of Al, K, Ca and Na, however the composition of individual glass pockets varied considerably. This behaviour appeared to be a general function of the BN barrier layer thickness, with negligible Al, K, Ca and Na present when the layer thickness is increased (~ 20μm). These 'impurity' elements are not initially present in either the ceramic or the BN powder, and therefore only originate from the Pyrex encapsulant glass. This assumption is confirmed by EDX analysis of the BN layer close to the encapsulant, with the detection

a

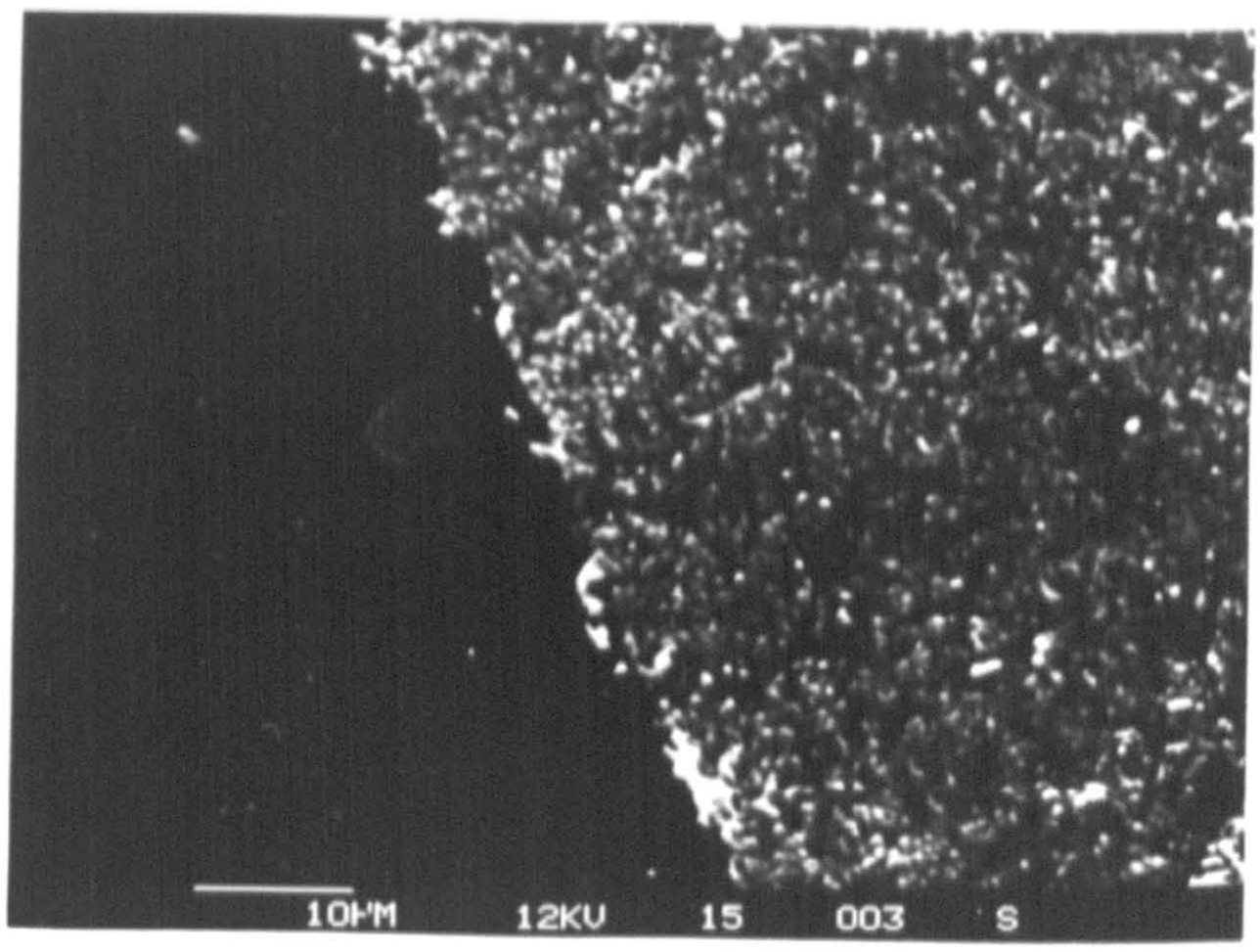

b

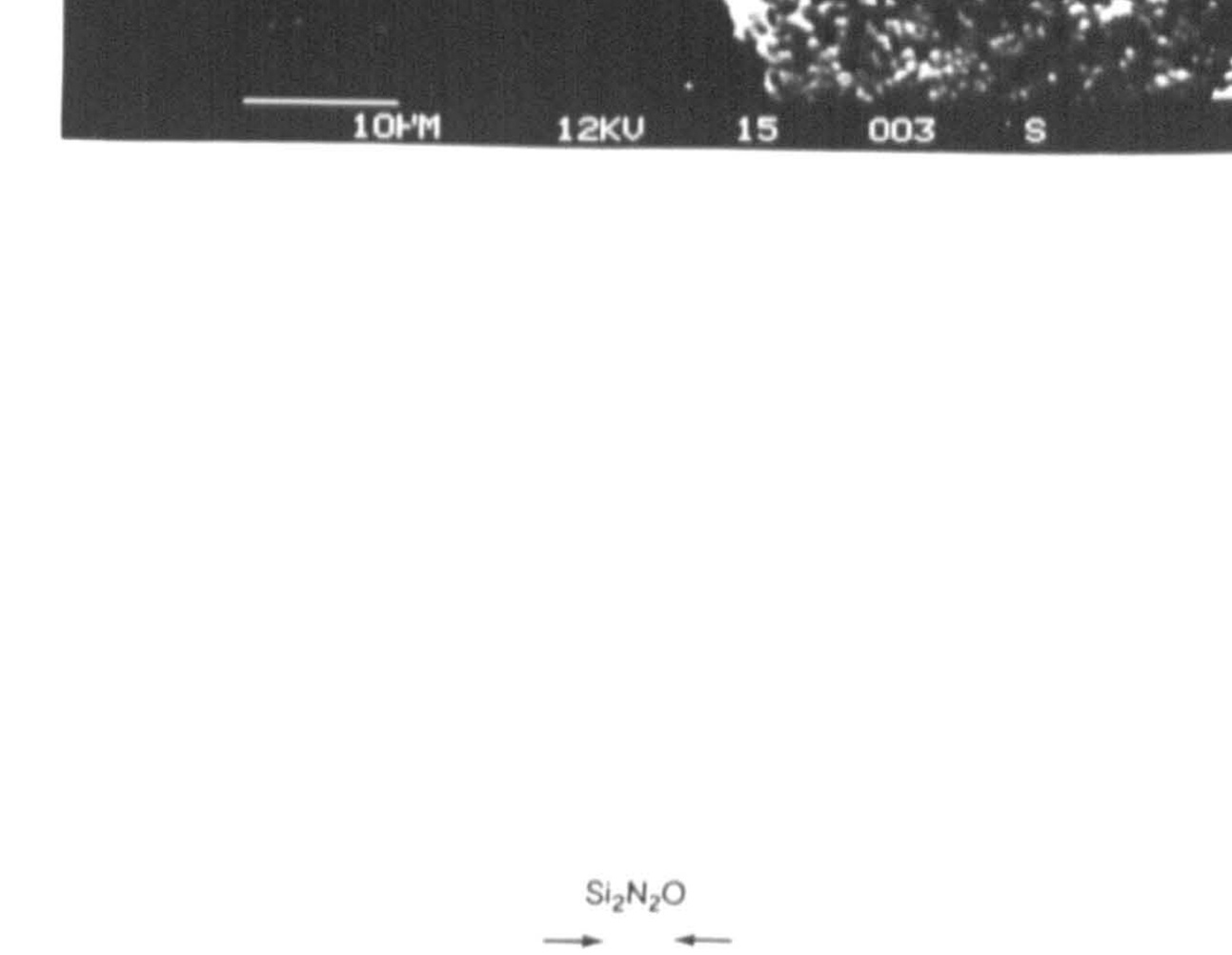

Figure 6.9 a) SEM micrographs of the surface microstructure of ceramic composition A1, densified by HIP, demonstrating the absence of any surface interaction layer and the retention of a β-Si_3N_4/glass surface structure. b) SEM micrograph of the reaction layer formed at the surface of HIPed ceramic A1 (and similarly for A2), showing the formation of a Si_2N_2O mono-phase layer.

of Si, K and Ca, together with trace amounts of Na and Al.

The composition of the monophase surface was actually found to vary slightly nearer to the ceramic substrate. At the surface of the layer only Si_2N_2O was present (fig. 6.9a) and this was the case most of the way into the layer. However, a composite β-Si_3N_4/Si_2N_2O region was present between the Si_2N_2O layer and the bulk ceramic, and a few isolated Si_2N_2O grains were present in the bulk ceramic which was otherwise microstructurally identical to that described in section 6.3.1. The mechanism of Si_2N_2O formation is discussed in section 6.5.

6.4.2. Ceramic with a High Volume, High Viscosity Matrix Phase (A3)

Optical microscope examination of a cross-section of the 10 wt.% Y_2O_3 specimen through the encapsulating glass and ceramic, revealed a complex surface transformation. There existed a surface reaction layer which extended ~ 1.5mm into the material from the ceramic/BN/Pyrex interface.

Scanning electron microscopy of the specimen interface disclosed an essentially monophase layer at the ceramic surface (Fig. 6.10a), which was found to be silicon oxynitride by X-ray microanalysis. The layer thickness was constant at ~ 20 μm and extended over the whole ceramic surface.

X-ray diffraction of the 10% Y_2O_3 surface revealed the presence of three crystalline phases (Fig. 6.10b). Two of the phases present were identified as β-Si_3N_4 and silicon oxynitride (Si_2N_2O). No α-Si_3N_4 was detected, indicating a full α- to β- transformation. Initially it was difficult to identify the third phase because, after identification of the β-Si_3N_4 and Si_2N_2O there existed only one unidentified peak. However this phase was later identified as hexagonal boron nitride, present on the specimen surface, after comparison with a powder X-ray diffraction trace of the same material.

a

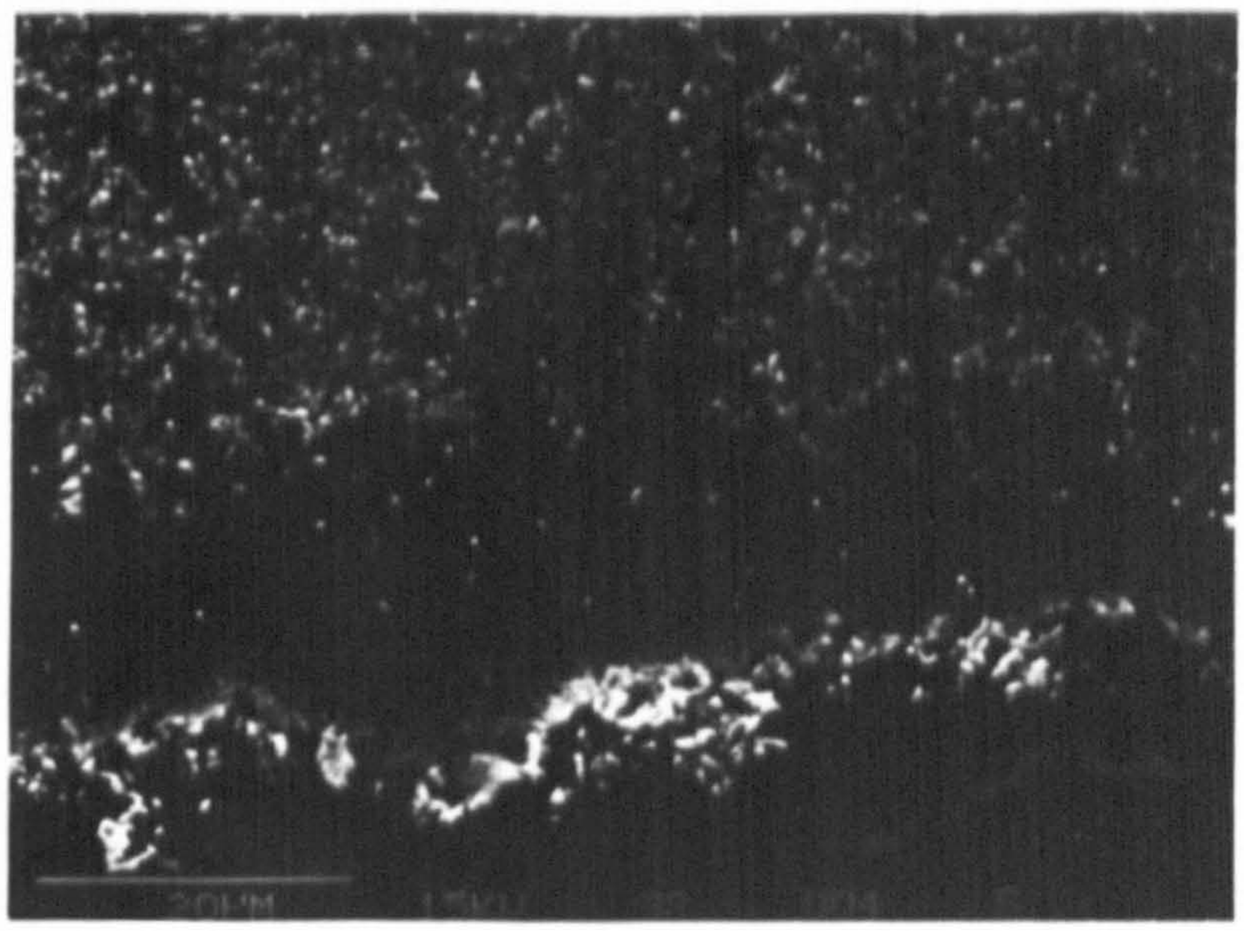

b

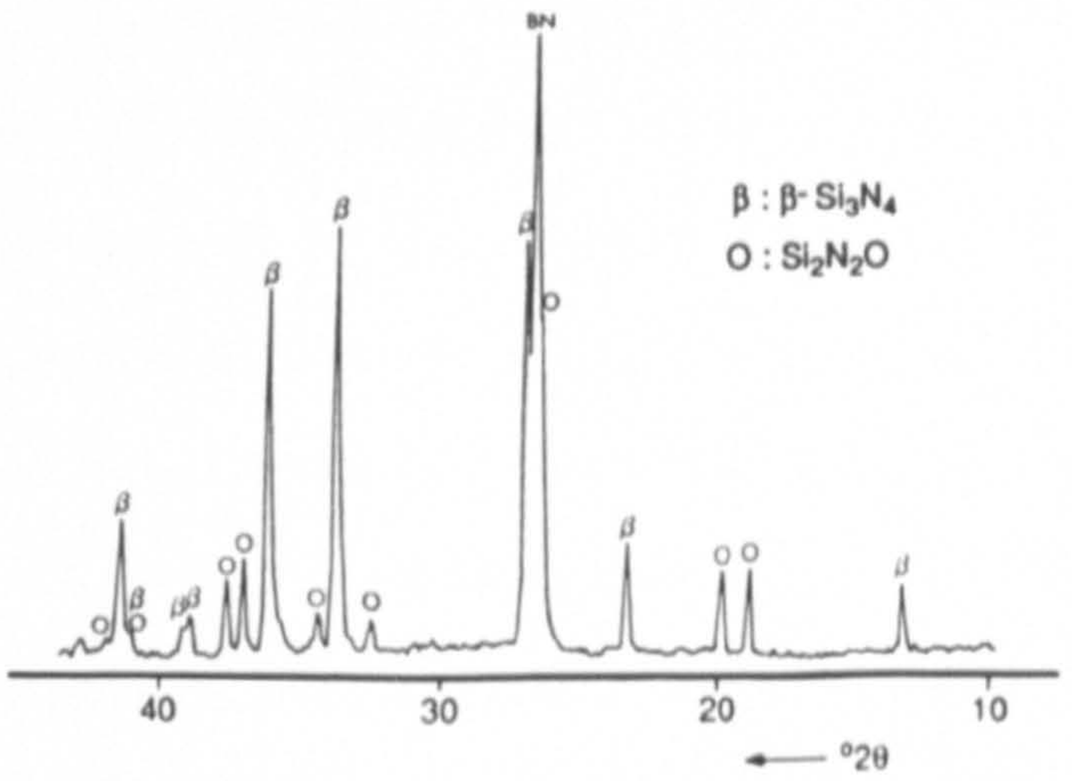

c

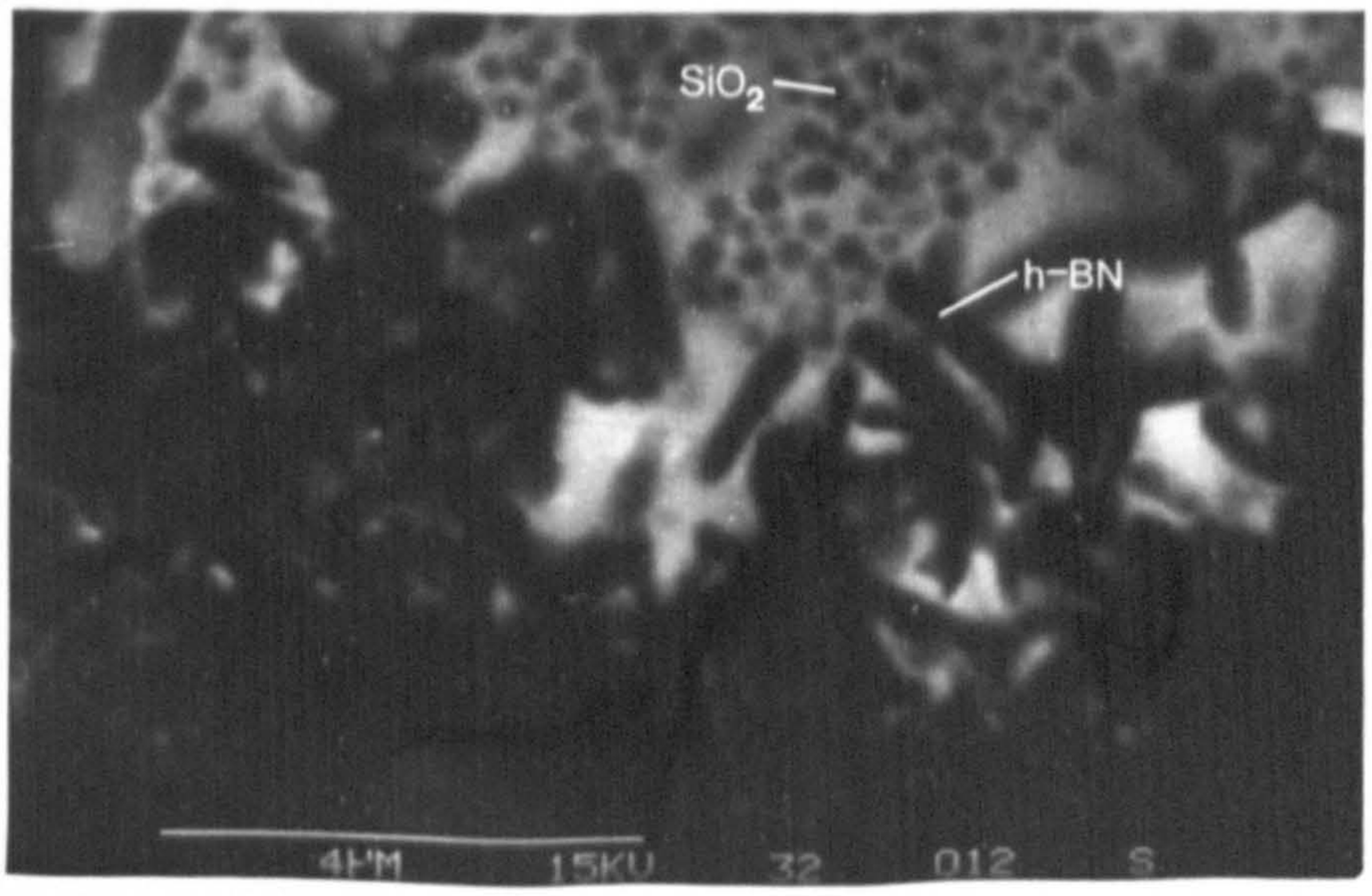

Figure 6.10 a) SEM micrograph of HIPed ceramic A3 demonstrating the formation of a Si_2N_2O surface layer, also observed via XRD b). c) SEM micrograph of isolated yttrium silicate pockets at the surface of the Si_2N_2O layer of composition A3, showing phase-separated SiO_2 droplets (dark contrast), formed via a nucleation and growth mechanism during cooling. The dark contrast needle-like crystals present in the lower portion of the micrograph are believed to be hexagonal boron nitride (h-BN), enveloped by the silicate liquid, and could not be detected by EDX analysis.

Yttrium out-diffusion was also noted by the presence of yttrium silicate based glass pockets (up to ~8μm in diameter) outside the Si_2N_2O layer (fig. 6.10c). These pockets are in direct contact with the BN powder layer. Regions of globular phase separated SiO_2 was apparent in many of these yttrium silicate pockets, particularly in areas where the BN layer was thinnest. It is interesting to note that the transportation of yttrium across the BN layer appears to be very slow, because only small traces of yttrium are found within the layer at a distance of ~2μm from the ceramic and no yttrium was present further from the ceramic.

Dark contrast, needle like, crystals are present within the yttrium silicate glass pockets. They are believed to be hexagonal boron nitride enveloped by the glassy silicate regions.

A region of modified composition intergranular glass extends ~20μm into the 10 wt.% Y_2O_3 specimen from the Si_2N_2O layer. This is due to the continued Si and O in-diffusion past the growing Si_2N_2O until the layer has grown to such an extent that it forms a barrier, inhibiting further in-diffusion. The continued Si and O in-diffusion leads to a modification of the intergranular glass phase composition and a slight increase in the glass volume (~18 vol.%). The β-Si_3N_4grains within the modified surface reaction layer are more needle-like than those present within the bulk ceramic. Growth of these crystals, typically 1/2-2μm in length with an aspect ratio between 4:1 and 8:1, is due to sintering in the presence of an increased volume glass.

6.4.3. Ceramics with a Low Volume, High Viscosity Matrix Phase (B1,B2,B5,C1,C2)

XRD and SEM examination of ceramics C1 and C2 did not reveal any detectable surface interaction with the Pyrex encapsulant, with a purely β-Si_3N_4 (α-Si_3N_4)/glass (apatite) surface microstructure. A lower porosity level was apparent at the ceramic surface. Additionally the α- to β-Si_3N_4 ratio was markedly different at the surface, with a complete transformation observed for ceramic C1 and a lower α-β ratio for C2 (7:93),

relative to the bulk material (section 6.3.3). It is clear that the presence of a thermal gradient through each of the ceramics during HIP increases both the densification and transformation at the surface.

A β-Si_3N_4/glass surface microstructure (with some Si_2N_2O in compositions B2 and B5) was present at the surface of densified ceramics B1, B2 and B5 (>98% TD) when a BN barrier layer of greater than 20μm thickness was retained after HIP. The sub-surface microstructure was relatively unchanged from the bulk material, although a few isolated β-Si_3N_4 grains (up to ~ 10μm in length) were present close to the surface (fig. 6.11a).

When a thin BN layer was present after HIP (<10μm), a thin Si_2N_2O layer was apparent (~4μm in thickness) and below this a thin mixed Si_2N_2O/β-Si_3N_4 layer was formed. The Si_2N_2O/β-Si_3N_4 layer was generally less than 5μm thick and an approximately 50/50 composite mixture of the two crystalline phases (fig. 6.11b). A thin β-Si_3N_4, Si_2N_2O and glass subsurface region, ~ 10μm in depth, was present below the glass free composite layer. The microstructure appeared identical to the bulk ceramic below the surface reacted layer. The out-diffusion of Y^{3+} ions from the glassy intergranular phase, coupled with in-diffusion of Si, Al, Ca, K and Na, had again led to the formation of a silicate glass phase at the very ceramic surface.

Fine dark-contrast crystals were again detected in the surface yttrium silicate layer (fig. 6.11c). These crystals are believed to be boron nitride, and have a hexagonal morphology. A slight increase in the observed level of Si_2N_2O formation was apparent below regions of barrier layer breakdown (fig. 6.11c).

6.5. THE FORMATION OF Si_2N_2O AND Si_2N_2O/β-Si_3N_4 COMPOSITE LAYERS DURING DENSIFICATION

During HIP densification, ionic species, present in the Pyrex encapsulant glass, follow a diffusion path into the ceramic via the BN layer. Concentration gradients of elements

a

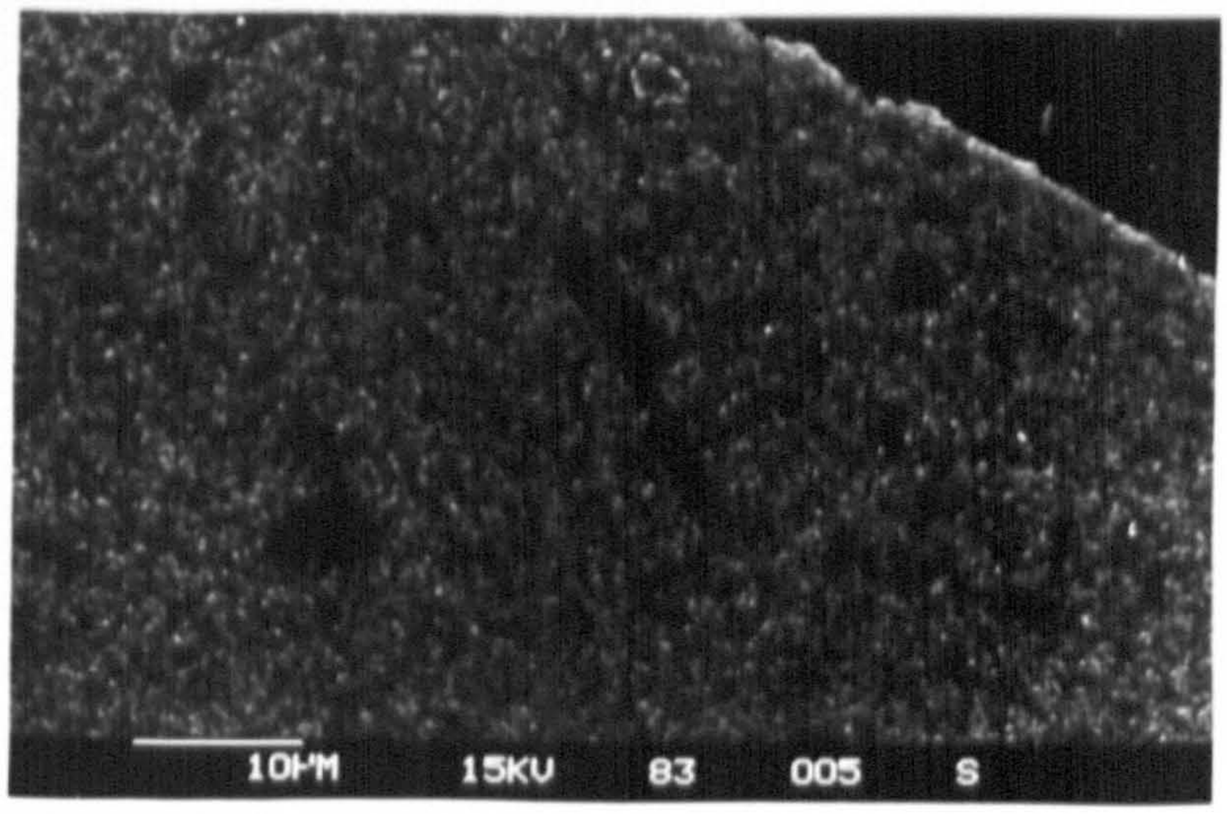

b

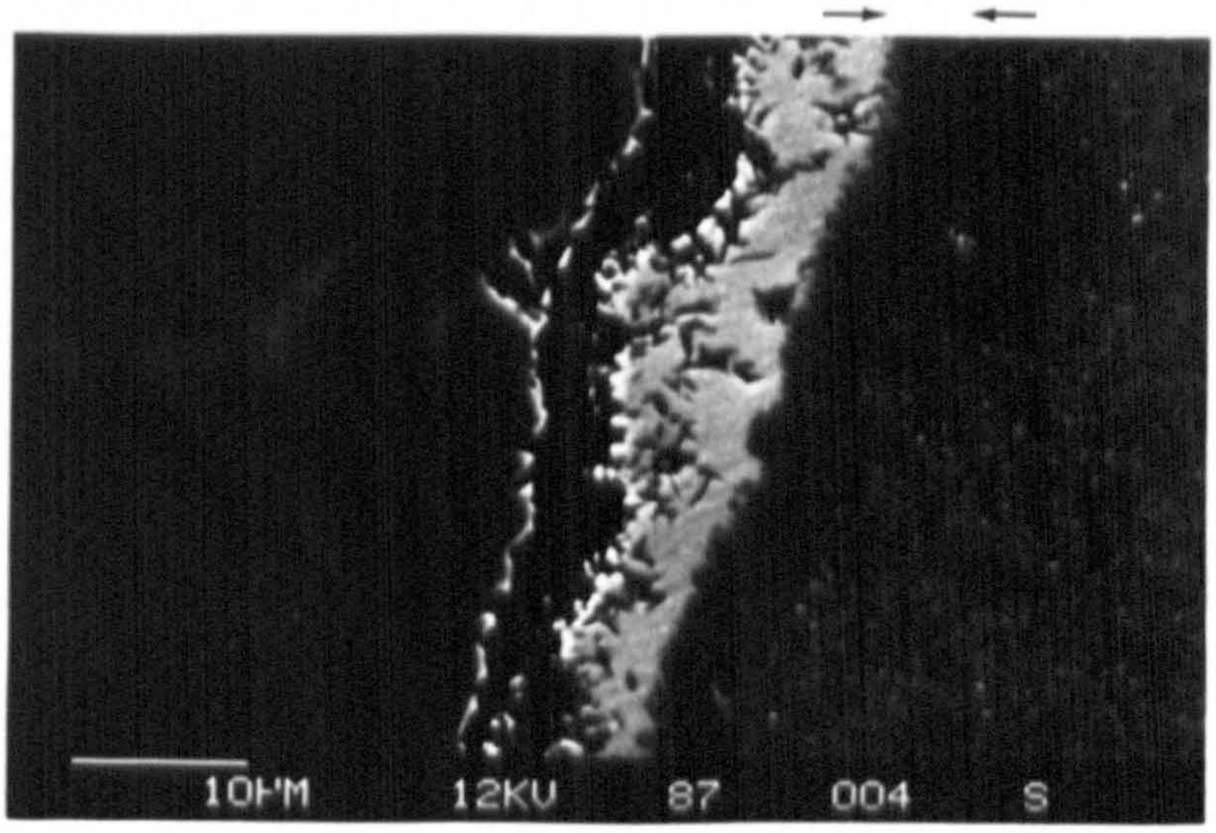

c

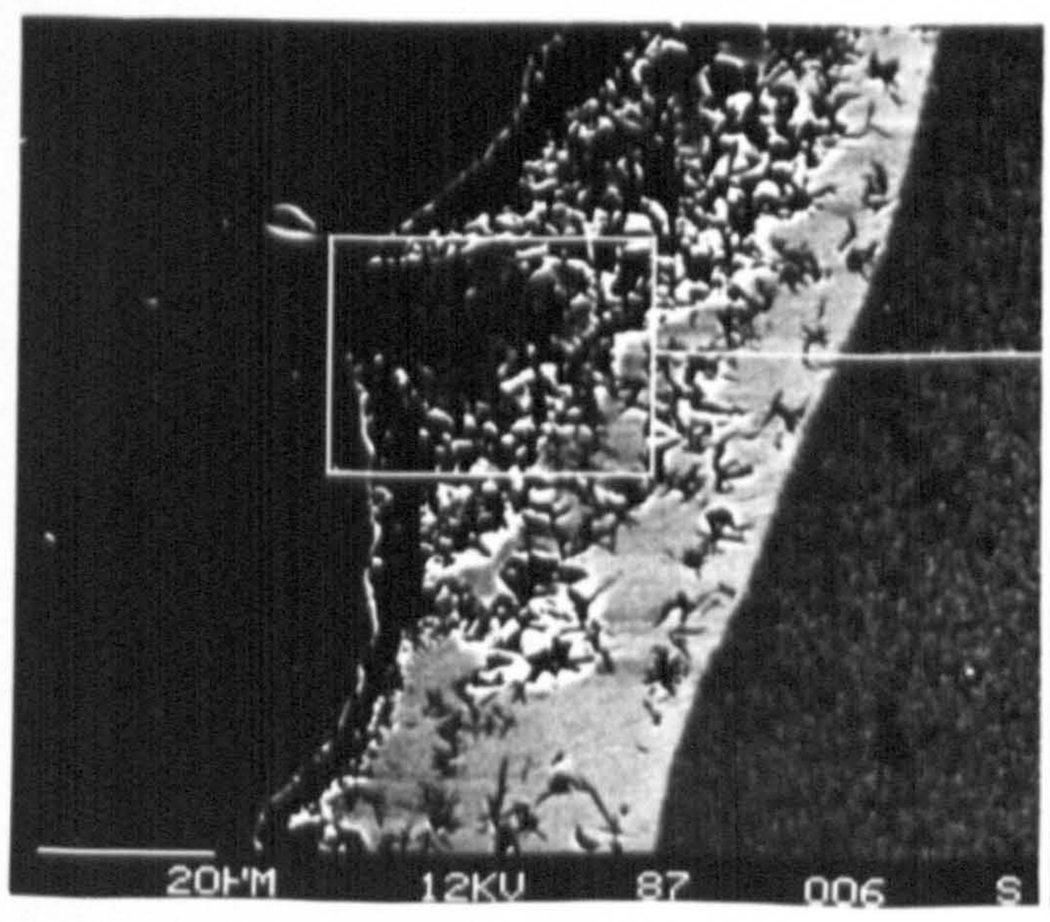

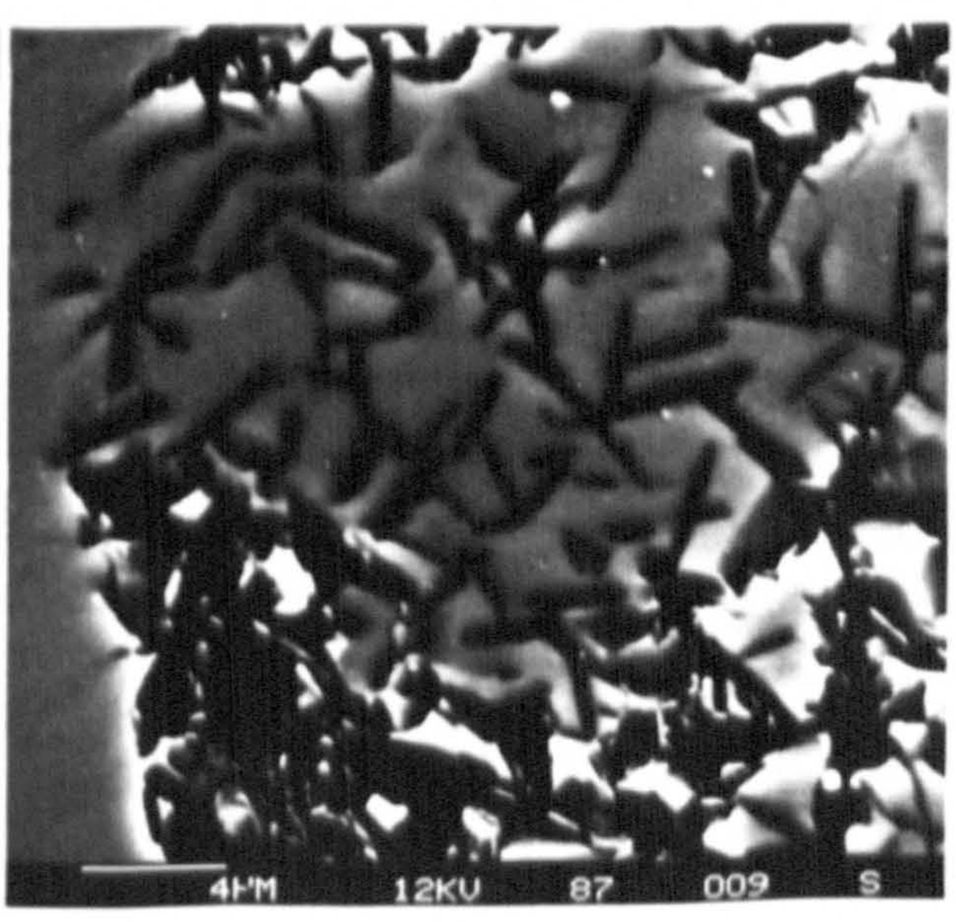

Figure 6.11 a) SEM micrograph of β-Si_3N_4/glass surface structure formed when a BN layer greater than 50μm thick is retained after HIP. The presence of large, heterogeneously nucleated β-Si_3N_4 grains can also be seen, arising from local fluctuations in the glass composition/viscosity. b) Surface reaction layer formed with thin BN layer (<10μm thick). c) Fine h-BN crystals were observed enveloped by the surface silicate liquid, which are particularly prominent in regions where the barrier layer coating had 'broken-down'.

present in both the ceramic and encapsulant glass were measured through the BN layer using EDX analysis. Gradients observed for compositions A3 and B2 are presented in figure 6.12a,b. The transport of ionic species through the BN layer arises because of a chemical couple between the encapsulant and the ceramic glasses, with flow of the Pyrex glass through the semi-porous, sub-micron BN particle interlayer. The driving force for interdiffusion is the formation of an equilibrium composition glass, with an equal ionic concentration in both the encapsulant and the intergranular phase. Obviously this ultimate equilibrium state will not be reached in reality.

The exact mechanism of material transport through the porous BN layer is not known. Transport is believed to occur by one (or a combination) of two routes:

1. Penetration of the borosilicate glass through the porous BN layer due to capillary action.

2. Surface diffusion through the BN barrier layer.

Direct evidence for the transport mechanism was difficult to obtain via electron microscopy. However, the (relatively) high cation content detected within the BN layer, together with occasional isolated high atomic number contrast regions (via back-scattered electron imaging) indicated that the first transport mechanism was predominant. Attempts were made to produce thin foil T.E.M. sections of the BN layer but were unsuccessful due to the brittleness of the layer and the adherence of the BN to both the ceramic and the encapsulant glass.

Densification during HIPing occurs through a combination of processes summarised in section 2.1. However, the liquid phase sintering process is the controlling factor in crystalline phase determination. Three densification stages have been outlined for the liquid phase sintering process [24] and the first two of these stages are of the greatest importance during the consolidation of silicon nitride, described in section 1.3.2. In the bulk ceramic the re-precipitation of β-Si_3N_4 occurs after solution of the α phase within

a

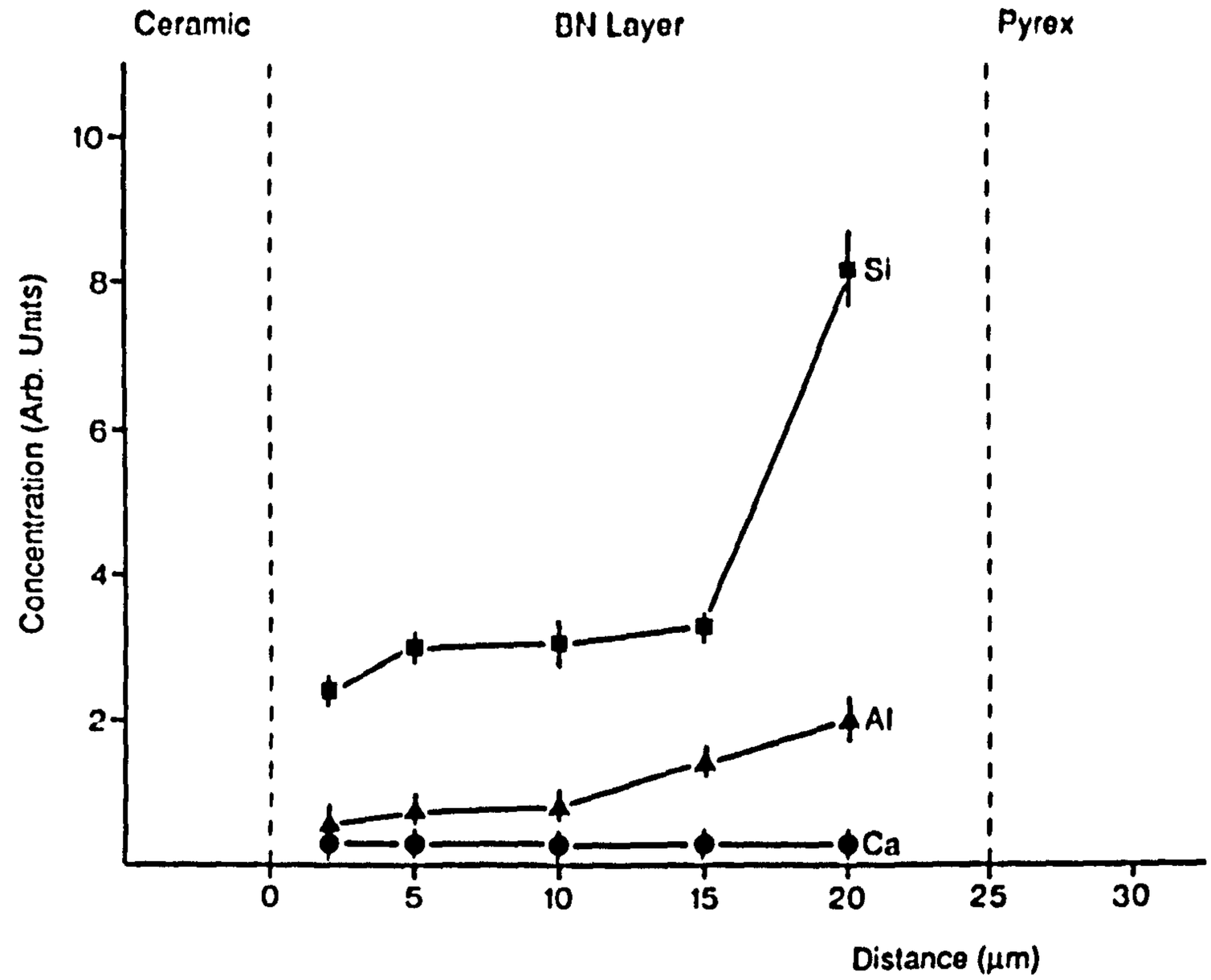

b

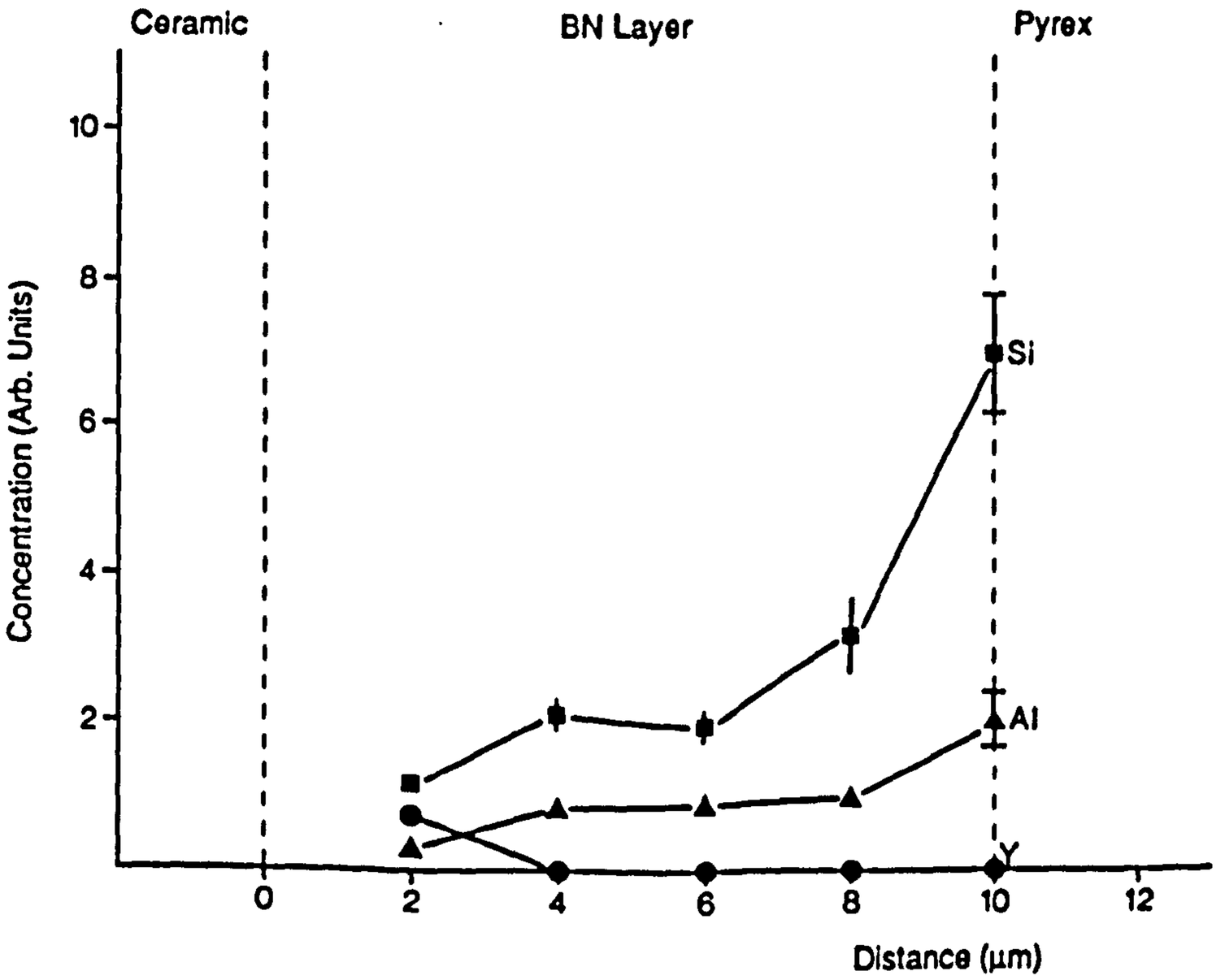

Figure 6.12 Concentration gradients for various cations detected within the BN barrier layer of ceramics a) A3 and b) B2 (each point averaged over a minimum of ten EDX analyses).

the silicate liquid sintering medium. It has been demonstrated that alteration of the silicate liquid composition, for example by adding SiO_2 to the initial mixture (section 6.3.3), can change the major precipitation product from β-Si_3N_4 to Si_2N_2O. This behaviour can be predicted when considering the Y_2O_3-SiO_2-Si_3N_4-YN system, with increasing oxygen content moving the overall composition into the $Y_2Si_2O_7$-Si_2N_2O-Si_3N_4 compatibility triangle (fig. 6.13a). The tetragonal Si_2N_2O crystal structure differs from the hexagonal β-Si_3N_4 structure by the incorporation of one oxygen atom in the SiN_4 tetrahedra such that the SiN_3 units are linked by Si-O-Si bonds. A comparable variation in the re-precipitation product has been observed when a high nitrogen content is incorporated into the glassy silicate liquid during sintering of Si-Al-O-N ceramics, with the subsequent formation of α'- in preference to β'-Si-Al-O-N [180,181].

During HIP processing in-diffusion of various ionic species occurs from the encapsulant and among these are found Si^{4+} (and O^{2-}), undergoing migration in an effort to form a high silicate content glass within the ceramic. The in-diffusion of Si and O, and the concurrent out-diffusion of Y^{3+} from the ceramic intergranular phase, increases the effective equivalent oxygen percentage in the localised subsurface region of the ceramic (fig. 6.13b). Increasing the relative Si^{4+} and O^{2-} concentration in this subsurface zone alters the overall compositional balance in a manner such that Si_2N_2O becomes the favoured crystallisation product upon dissolution of α-Si_3N_4 in the matrix liquid phase (fig. 6.13b). As growth of the Si_2N_2O layer continues so will in-diffusion of Si^{4+} and O^{2+} (plus other cations) towards the substrate ceramic. Eventually, but within the duration of the HIP cycle, a coherent, glass depleted layer is formed and the interdiffusion path then becomes more tortuous, with the absence of any appreciable volume of grain boundary glass phase.

The growth rate of Si_2N_2O, and the penetration depth of Si^{4+} and O^{2-}, demonstrates a dependency upon two main factors:

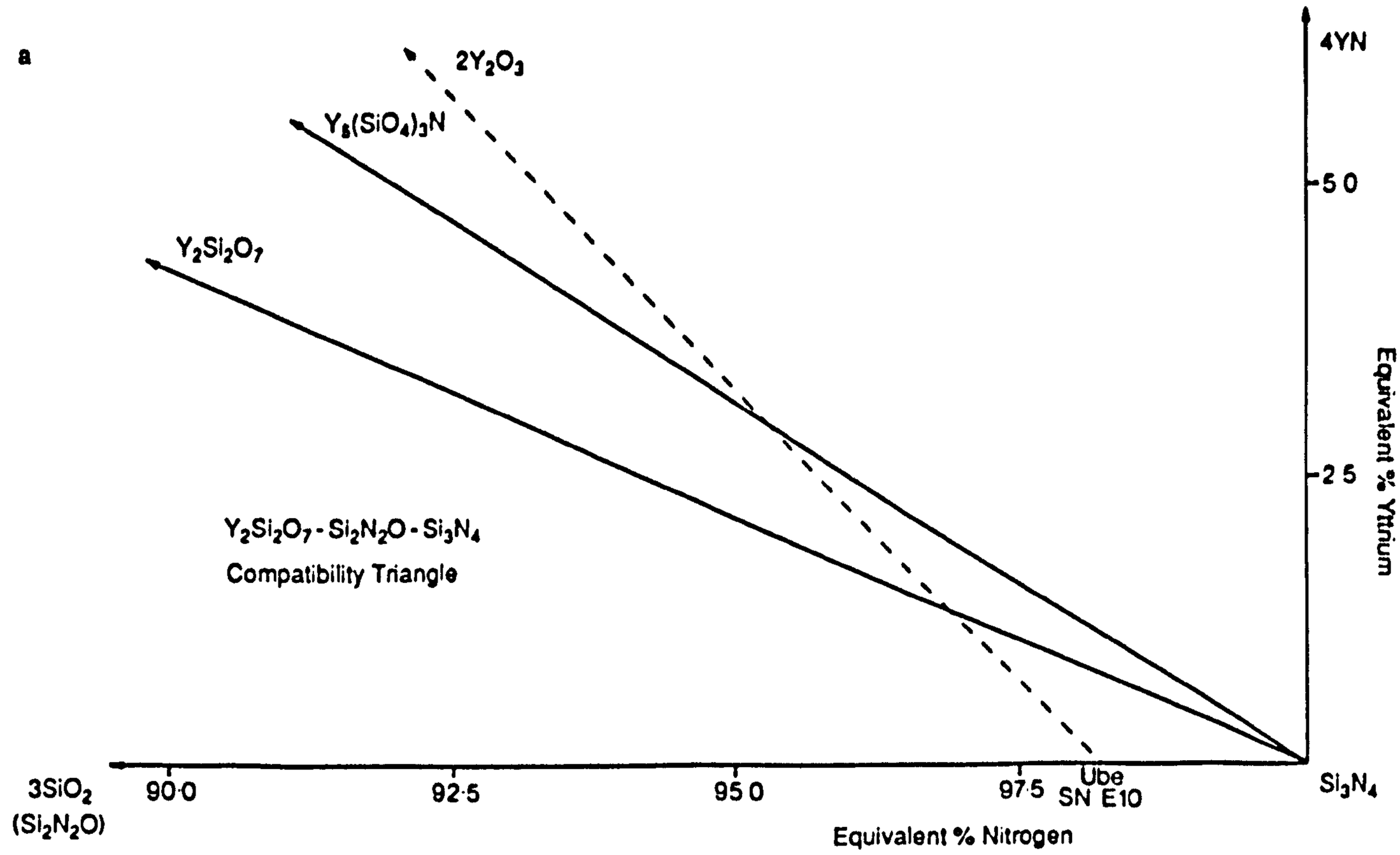

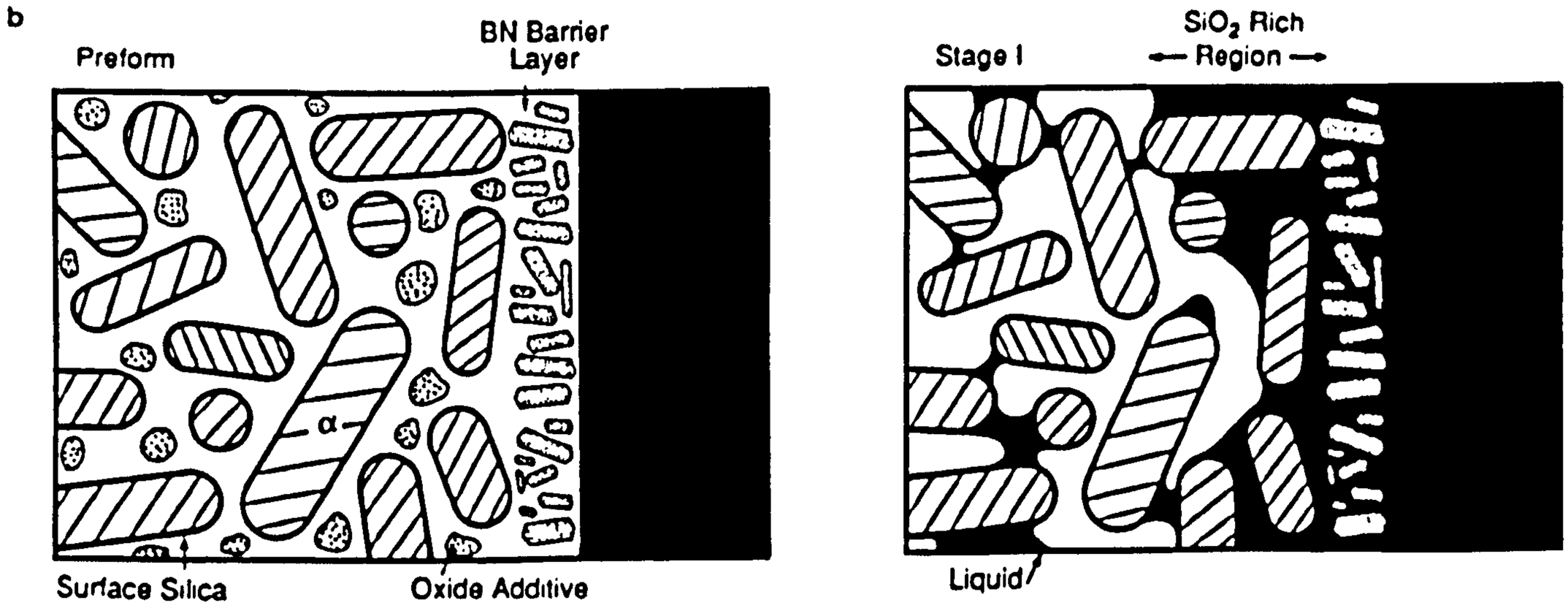

Figure 6.13 a) Representation of the effect of in-diffusion of Si^{4+} and O^{2-} (in the form of SiO_2) upon the sintering precipitation product in the Si_3N_4-SiO_2-Y_2O_3-YN system. b) Schematic representation of the mechanism of Si_2N_2O formation at the surface (and β-Si_3N_4/O–Si_2N_2O in the subsurface) of HIPed ceramics with a thin barrier layer. c) The volume percentages of Si_2N_2O and β-Si_3N_4 as a function of depth from the ceramic surface, for compositions A1, A3 and B1.

c

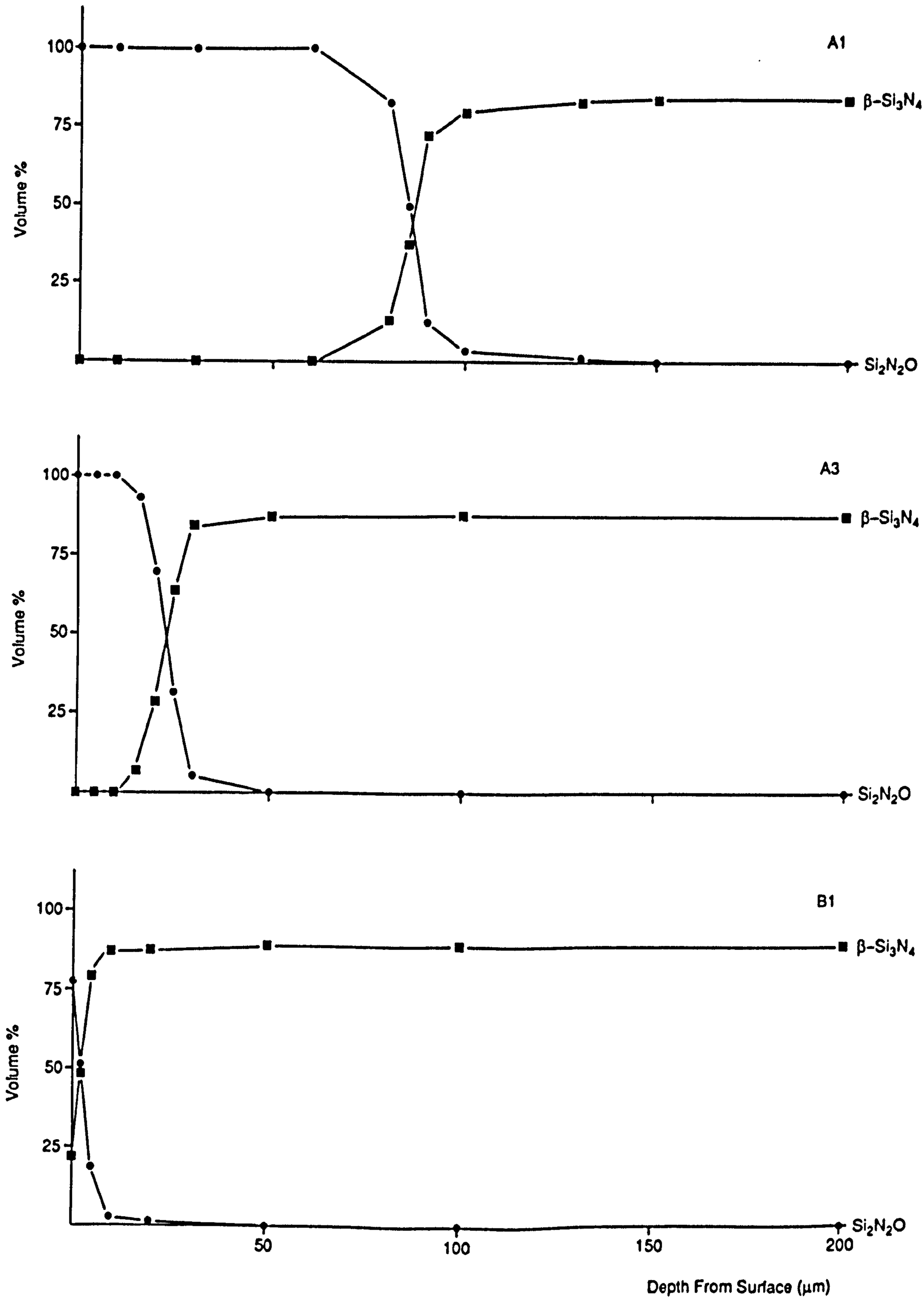
A1
β-Si3N4
Si2N2O
A3
β-Si3N4
Si2N2O
B1
β-Si3N4
Si2N2O
100
75
50
25
Volume %
50
100
150
200
Depth From Surface (μm)

1. The thickness of the BN barrier layer is a controlling factor in determining whether a Si_2N_2O surface layer is formed. However, the efficiency of the barrier layer thickness did not appear to be specifically dependent upon the ceramic intergranular glass composition, with interaction occurring for all ceramic compositions with a barrier layer thickness below ~20μm and no detectable reaction when a layer greater than ~50μm remained after HIP.

2. The volume and viscosity of the ceramic intergranular glass phase is of particular importance in determining the degree of sub-surface reaction. Figure 6.13c reveals the relative volume percentages of selected phases at the surface of the three ceramic types studied, together with the variation in phase percentages with measured depth into the ceramic, for approximately equivalent BN barrier layer thicknesses.

A narrow layer of Si_2N_2O (~ 5μm thick) formed under the most extreme reaction conditions (barrier layer 4 - 10μm), at the surface of the low volume, high viscosity glass phase ceramics (B1, B2 and B5). In comparison, an approximate layer thickness of 80μm was formed in the high volume, low viscosity intergranular phase ceramics under similar conditions. A Si_2N_2O layer, at the lower end of the size range (~ 10-15μm thick), was formed in the high volume, high viscosity ceramic (A3) and it should be remembered that the glass viscosity for ceramic A3 will be lower than ceramics B1, B2 and B5 at the HIP processing temperature because of the higher impurity content of the Anzon α-Si_3N_4 silicon nitride powder.

The formation of a composite β-Si_3N_4/Si_2N_2O region below the purely Si_2N_2O surface layer arises when the enhanced Si^{4+} and O^{2-} concentration in the ceramic sub-surface region is sufficiently low that complete re-precipitation of α-Si_3N_4 as Si_2N_2O cannot occur. In this instance partial re-precipitation of β-Si_3N_4 as the major phase arises. Further into the ceramic the Si^{4+} and O^{2-} concentration will be almost identical to the

a

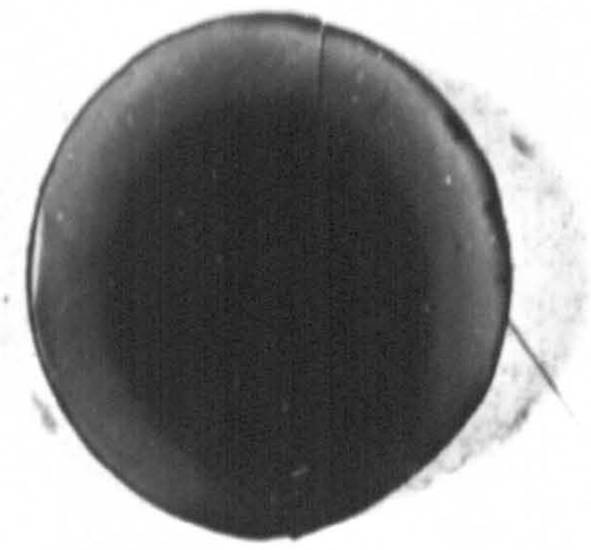

B1

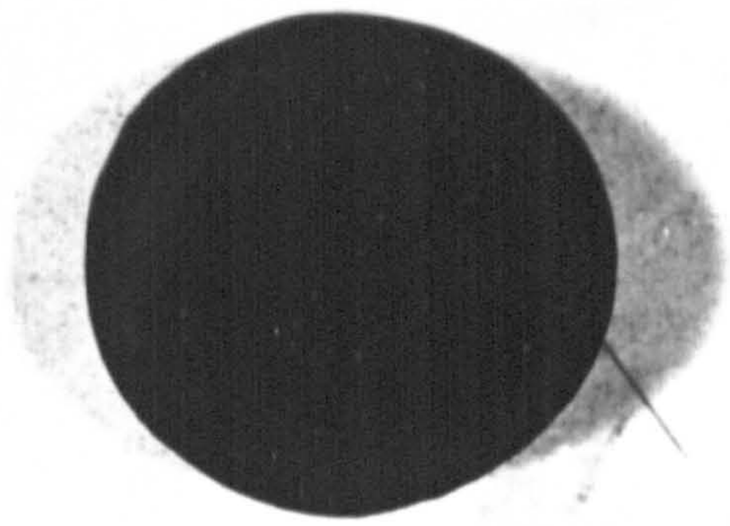

B2

b

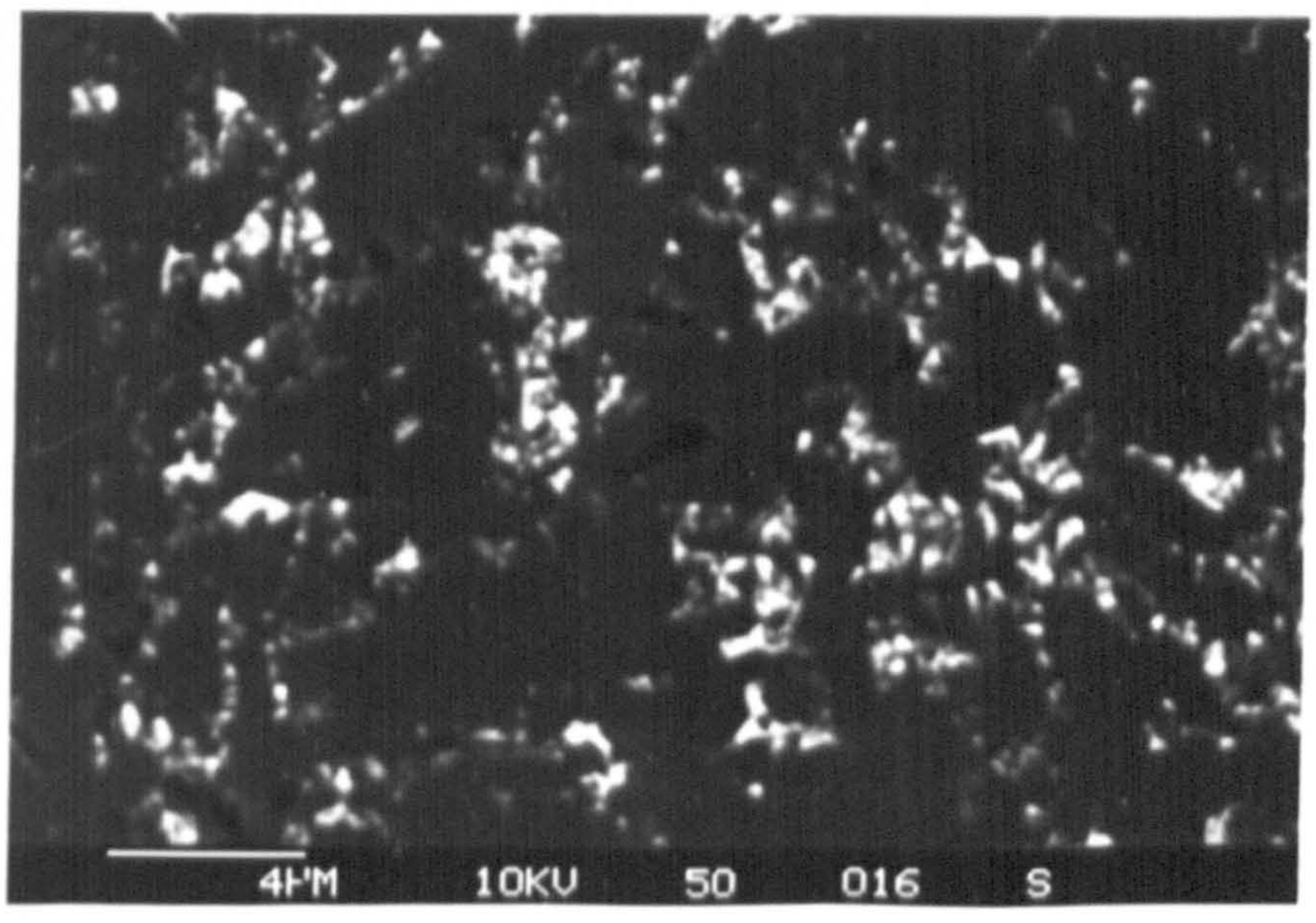

Figure 6.14 a) Reflected light optical image of a cross-section of the surface reaction zone in ASEA HIPed ceramic B1, with a similar cross-section for B2 showing the absence of any reaction zone. b) SEM micrograph of the bulk microstructure of ASEA HIPed B1, showing typical bimodal grain size distribution. c) TEM micrograph of the bulk microstructure of ASEA HIPed B1 and B4. d) XRD demonstrates the crystallisation of α-$Y_2Si_2O_7$ as the matrix phase in ceramic B1 (and all the other materials in the series B2 to B7 except B6, where β-$Y_2Si_2O_7$ was observed).

c

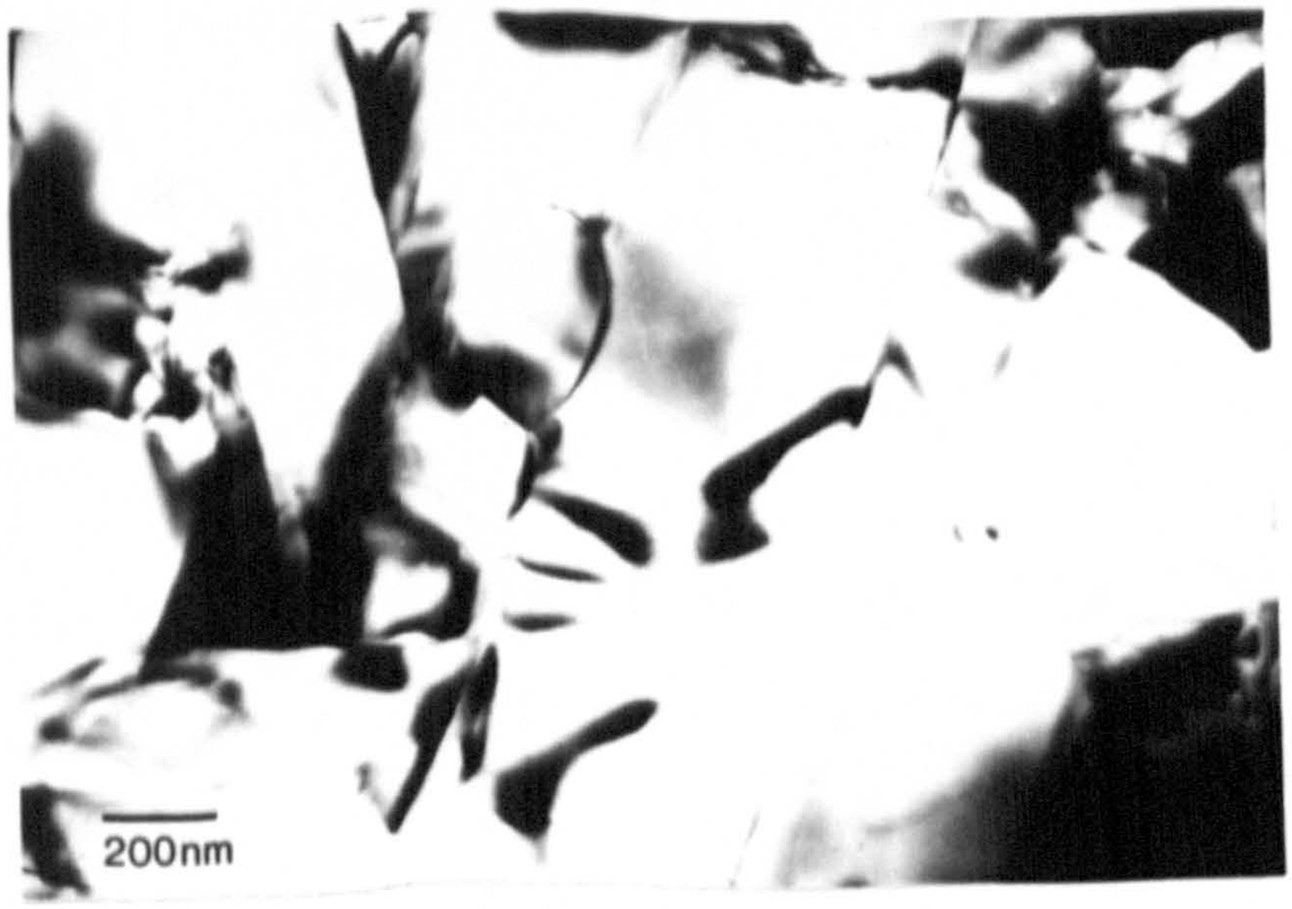
200nm

B1


400nm

B4

d

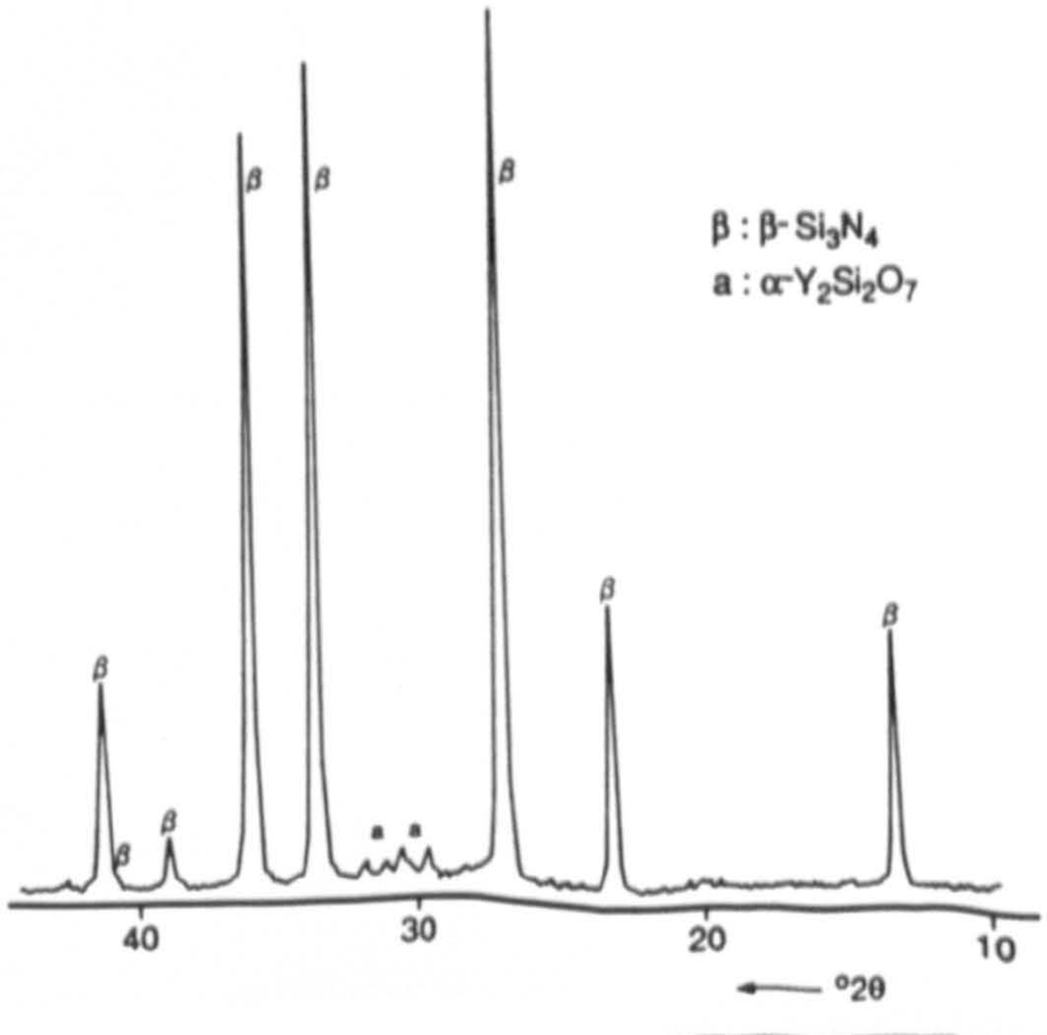
β : β- Si3N4
a : α-Y2Si2O7
40
30
20
10
°2θ

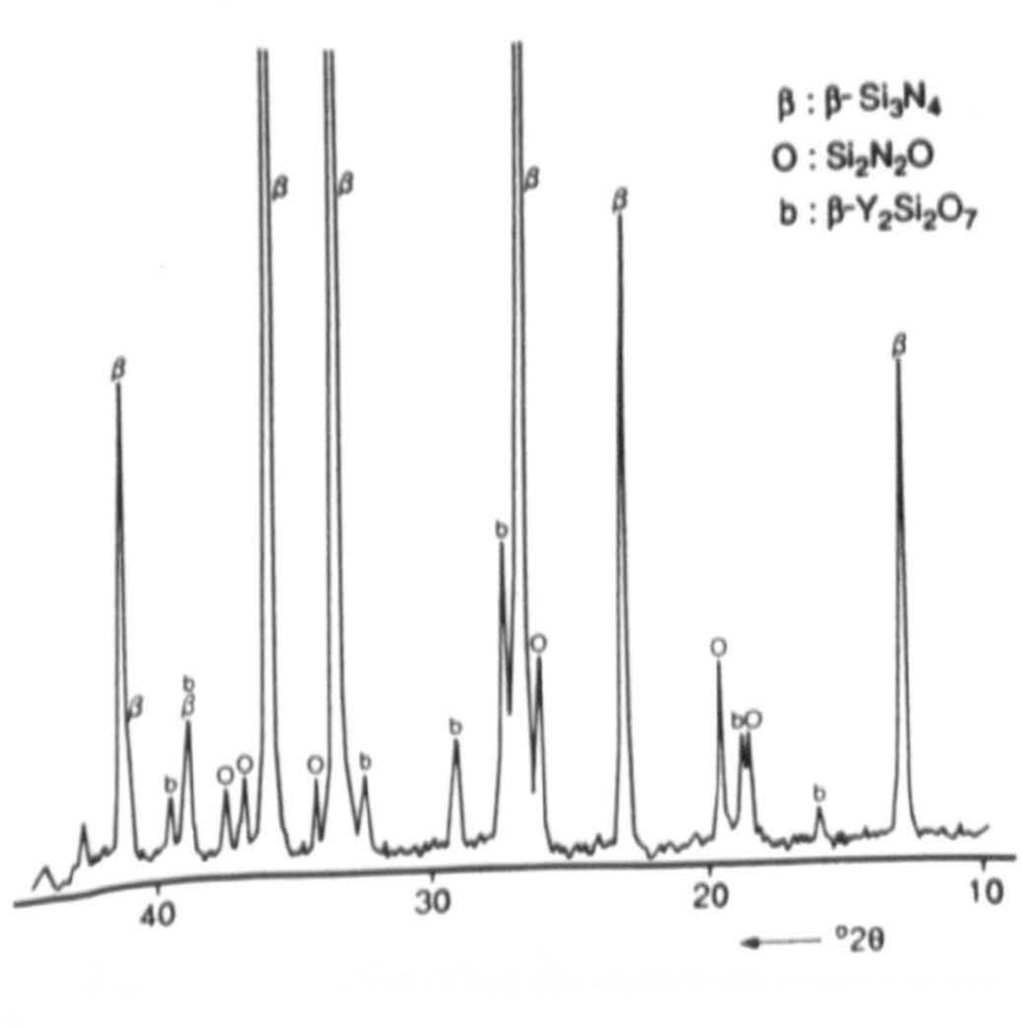
β : β- Si3N4
O : Si2N2O
b : β-Y2Si2O7
40
30
20
10
°2θ

bulk ceramic, and only a few isolated Si_2N_2O grains will be formed. A similar feature is observed in the bulk of compositions B2 and B5 where a slight increase in the equivalent percentage of oxygen in the starting mixture produces homogeneous nucleation of Si_2N_2O throughout the ceramic.

6.6. ASSESSMENT OF THE ASEA HIP PROCESS

6.6.1. Bulk Microstructure

Optical microscope examination of ceramics HIPed at ASEA revealed that increasing the oxygen content in the starting powders, B2 - B4 and B5 - B7, was found to lighten the grey shade of the bulk material. This effect was most apparent when comparing ceramic B1 with the higher oxygen content materials (fig. 6.14a).

The bulk microstructure of each of the seven compositions, B1 - B7, exhibited a typical hexagonal β-Si_3N_4 grain morphology (fig. 6.14b). A bimodal grain size distribution was observed for all of the ASEA HIPed materials, which is typical of silicon nitride ceramics possessing a low volume, high viscosity intergranular phase. The bimodal effect in the ASEA HIPed material was more distinct than that exhibited by a typical low intergranular volume Si-Al-ON ceramic such as LCS 201. The grain size varied between 0.1-0.5 μm and 2-4 μm. The aspect ratios of the majority of β-Si_3N_4 grains were in the range 1:3 to 1:5, although a few high aspect ratio grains (~ 1:8) were apparent (fig. 6.14b,c).

X-ray diffraction disclosed that a complete α-β transformation occurred in the pure 5 wt% Y_2O_3 specimen (fig. 6.14d). Increasing the overall oxygen content relative to nitrogen (B2 - B7) however, gave a partial preferred reprecipitation of the major phase as silicon oxynitride (Si_2N_2O) (fig. 6.15a,b). The level of Si_2N_2O present in the bulk material increased approximately proportionally with increasing oxygen content (Table 6.1). The intergranular phase in all specimens was found to be crystallised to α-$Y_2Si_2O_7$

a

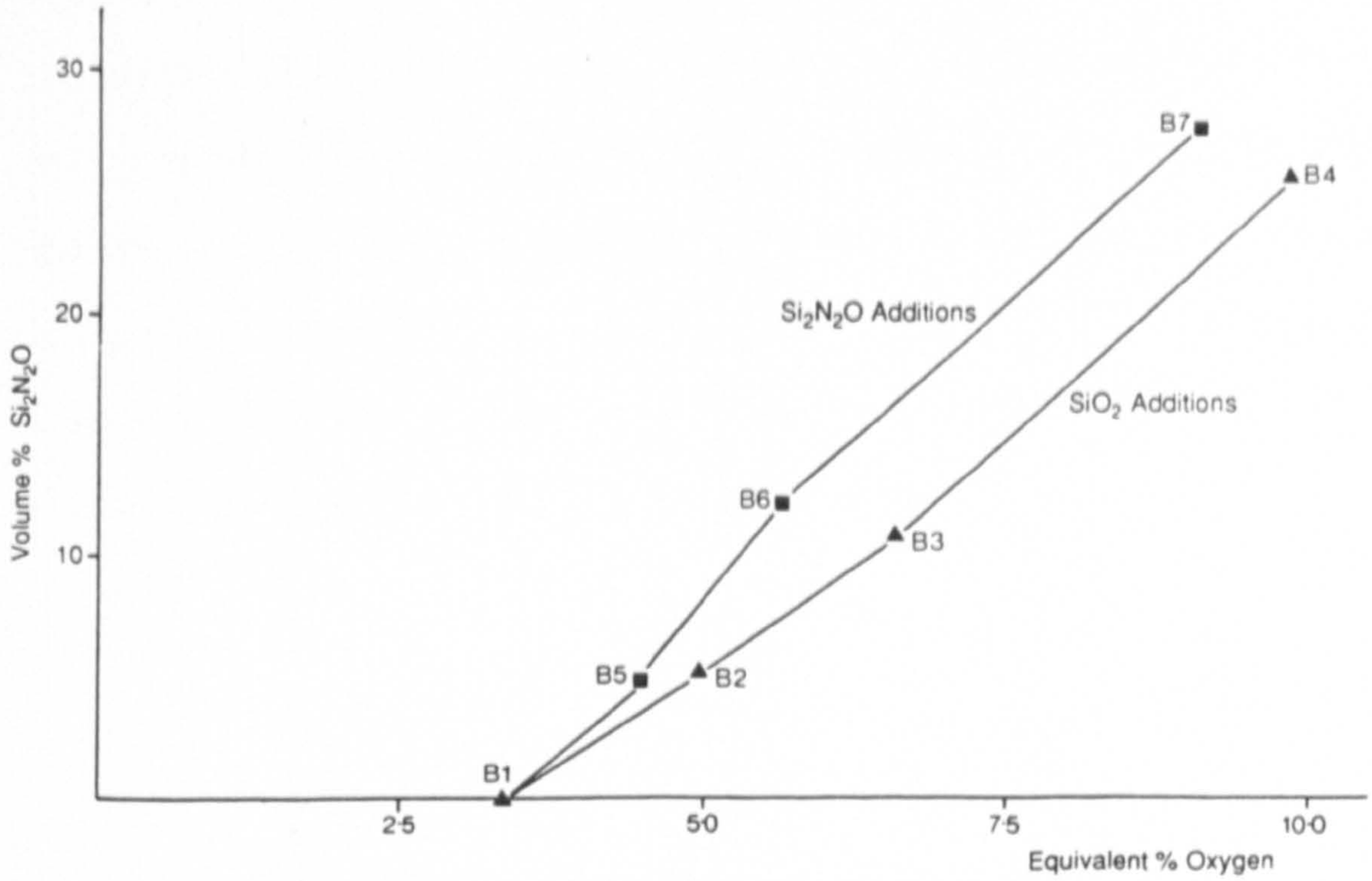

b

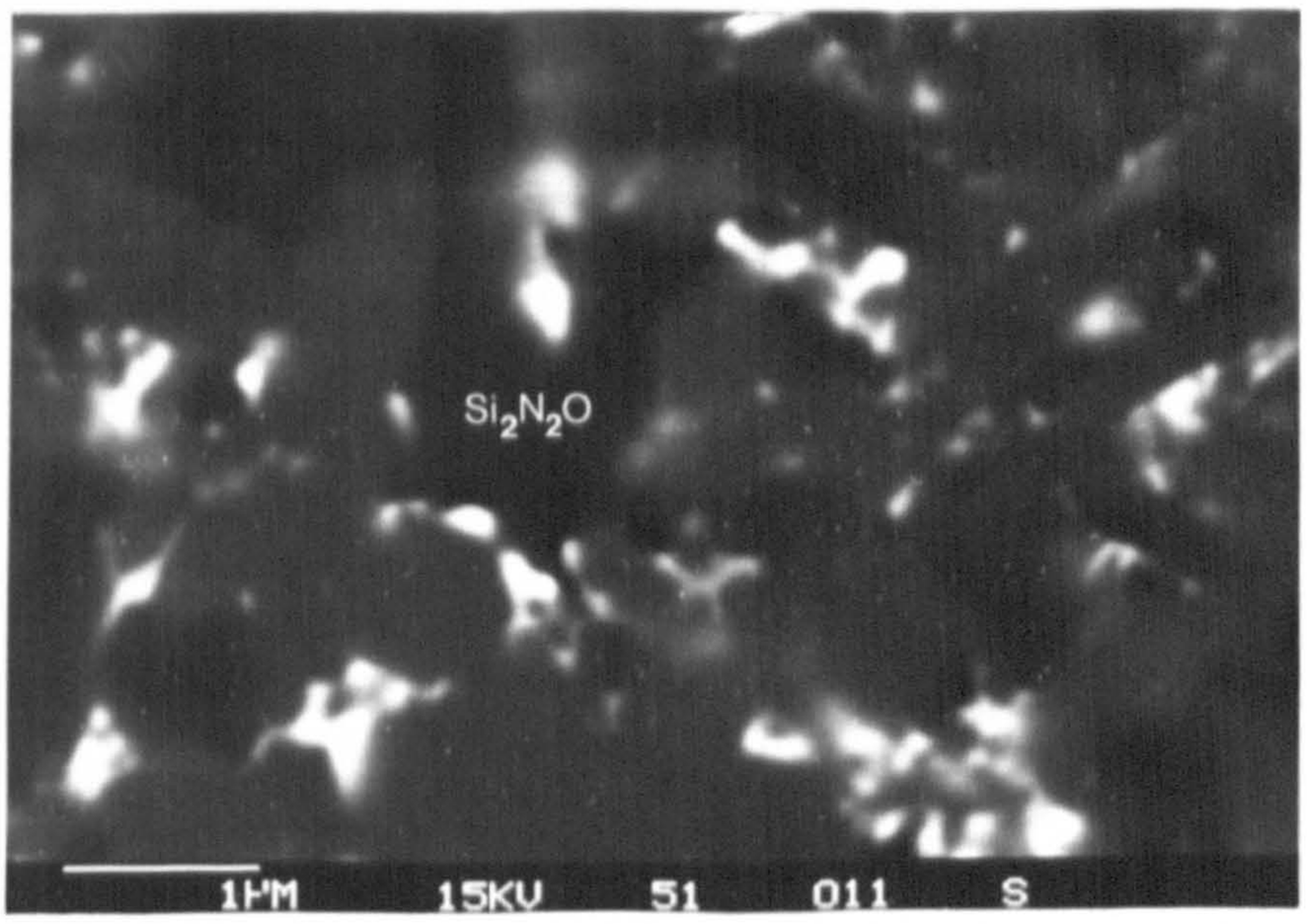

c

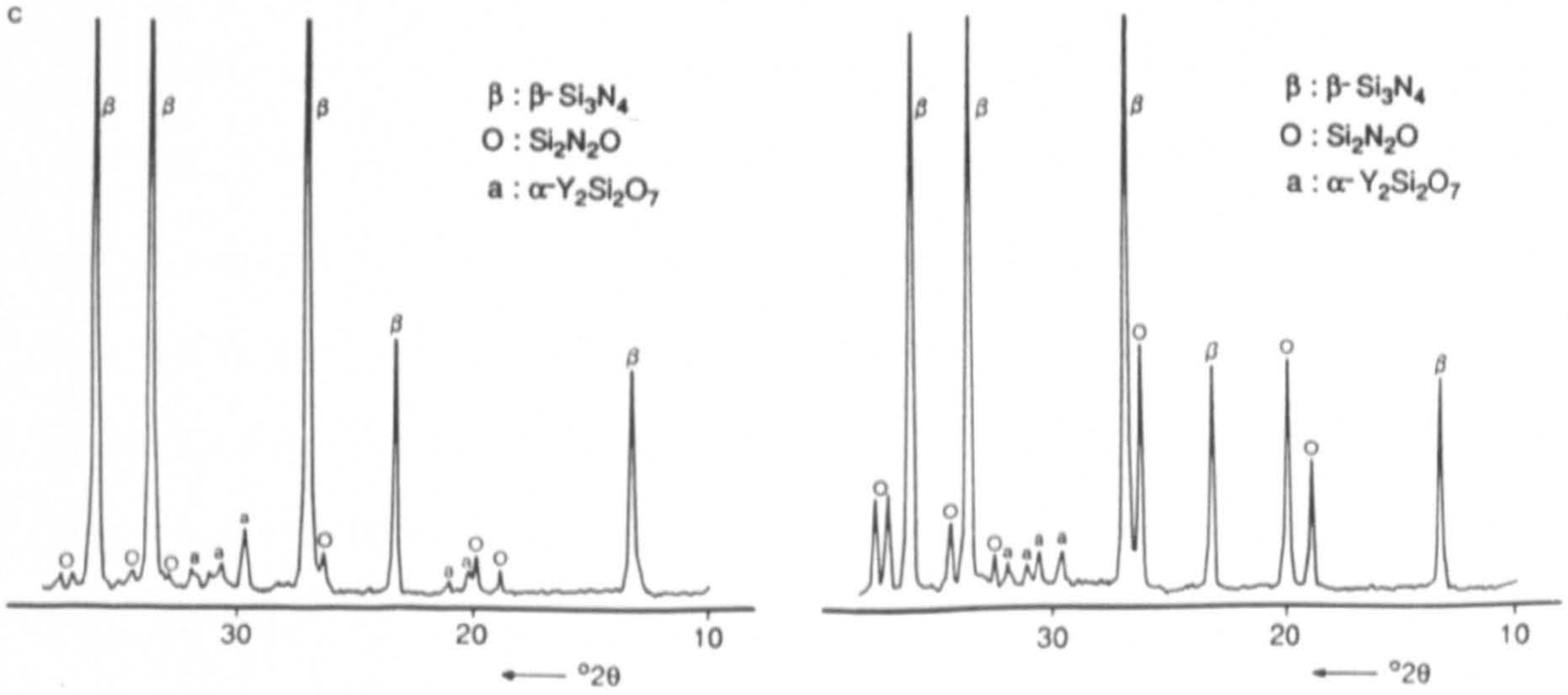

Figure 6.15 a) The variation of precipitated Si_2N_2O content as a function of equivalent % oxygen addition to the starting powder mix. b) SEM micrograph and XRD illustrating the preferred reprecipitation of Si_2N_2O as the major phase with increasing oxygen content (B1 to B4).

except B6 (5 wt% Y_2O_3 + 10 wt% Si_2N_2O) which crystallised as the high temperature polymorph β-$Y_2Si_2O_7$ (fig. 6.14d). The α-$Y_2Si_2O_7$ level was found to decrease slightly with increasing SiO_2 additions, most notably in specimens B1 - B4, although this trend was less evident with Si_2N_2O additions. It is believed that thermal gradients, occurring in the large volume furnace on cooling, produce subtle variations in the minor phase nucleation temperature leading to the formation of different polymorphs of $Y_2Si_2O_7$. This behaviour is unique to the $Y_2Si_2O_7$ system [194].

	B1		B2		B3		B4	
	B	S	B	S	B	S	B	S
Si_3N_4	100	83.9	93.9	75.9	85.7	57.6	72.4	56.2
Si_2N_2O	–	16.1	6.1	24.1	14.3	42.4	27.6	43.8

	B5		B6		B7	
	B	S	B	S	B	S
Si_3N_4	94.7	90.5	86.8	76.9	70.4	68.4
Si_2N_2O	5.3	9.5	13.2	23.1	29.6	31.6

Key: (B) bulk ceramic, (S) extreme surface

Table 6.1 Crystalline major phase content in as-received HIPed ceramics

6.6.2. Post-HIP Surface Transformation

A region of surface interaction had occurred in all specimens B1 - B7. The interaction was most prominent in the pure 5 wt% Y_2O_3 (B1) containing material, where a light grey region was evident that extended ~3 mm into the specimen (fig. 6.15a). The interface area between the surface reaction layer and the very dark grey bulk region of the B1 specimen was fairly sharp in comparison with other compositions. Only two crystalline phases were present in the lighter grey sub-surface reaction layer, β-Si_3N_4 and α-$Y_2Si_2O_7$. The volume of crystalline α-$Y_2Si_2O_7$ in this layer (determined by XRD) was

slightly less than that present in the bulk.

X-ray diffraction examination of the post-HIP surface of specimens (B1 - B7) revealed three crystalline phases present in each of the seven compositions, β-Si_3N_4, Si_2N_2O and α-$Y_2Si_2O_7$ (β-$Y_2Si_2O_7$ in billet B6) (fig. 6.16a). As with the bulk material the Si_2N_2O level, relative to β-Si_3N_4, increases with increasing oxygen content in the starting powders. The level of Si_2N_2O at the surface of each billet was higher than the respective bulk regions, typically by a factor of two or more. The ratio of surface Si_2N_2O to bulk Si_2N_2O was discovered to decrease with increasing oxygen content. This trend was particularly noticeable in the specimen B7 (5 wt.% Y_2O_3 + 25 wt.% Si_2N_2O) where the ratio was approximately 1:1. Examination of cross sections of each composition revealed regions of the surface layer, up to 4 μm in thickness that were largely free of the $Y_2Si_2O_7$ intergranular phase (fig. 6.16b). X-ray microanalysis of the surface layer disclosed a noticeable aluminium content particularly at the very surface and it is likely that a substitution reaction has occurred at the extreme surface leading to reprecipitation of β′-Sialon and O′-silicon oxynitride during HIPing. The average Al level in the surface reaction layer relative to the depth from the specimen surface is plotted in figure 6.16c for composition B2 (5 wt.% Y_2O_3 and 2 wt.% SiO_2). The mechanism of Si_2N_2O formation (and O′-Si_2N_2O with Al in-diffusion) is essentially identical to the Pyrex encapsulant samples (described in section 6.5).

A general microstructural variation between the bulk ceramic and near surface region was observed for all specimens in the series B1 to B7. The bulk microstructure, as previously described, has a distinct bimodal β grain distribution with isolated $Y_2Si_2O_7$ regions. However, the near surface microstructure of all specimens was far more homogeneous, with the β-Si_3N_4 grain size being generally finer than the bulk material, between 0.2 and 2 μm and with an aspect ratio of 1:2 to 1:4. The size distribution of β grains was also less bimodal than the bulk region. The intergranular α-$Y_2Si_2O_7$ (or β)

phase was observed to be more continuous in the sub-surface microstructure, most notably for composition B1. The subtlety of the variation between the surface and bulk microstructure is revealed in figure 6.17.

6.6.3. Methods of Trace Boron Determination

It is reasonable to assume that, with in-diffusion of various cationic species (Si^{4+}, Ca^{2+}, Al^{3+}, K^{+} and Na^{+}), boron diffusion into the ASEA HIPed ceramics will also occur. B^{3+} is a highly mobile ionic species, however detection of this element is not possible via conventional electron microscopy analytical techniques.

In an attempt to detect and possibly quantify the level of boron within ceramic compositions B1 to B7 after HIP, two analytical techniques were examined:

1. Inductively coupled plasma mass spectrometry (ICP/MS)

ICP/MS is a relatively new analytical method, and is typically used for the rapid identification and measurement of multiple trace elements [195]. The technique is particularly suited to the analysis of glasses, ceramics and refractory materials as it is a high temperature ablation process which involves the atomisation and/or ionisation of small sample regions by the ICP source [196]. Detection of the plasma constituents can then be made by either atomic emission or fluorescence spectrometry or by mass spectrometry [196].

The ICP/MS data obtained on a selection of ASEA HIPed ceramics was acquired by Dr. J.G. Williams of the Department of Chemistry, University of Surrey. The instrument at Surrey utilizes a pulsed ruby laser to ablate the specimen surface [197]. The sample is situated within a borosilicate glass cell whilst Ar gas, at atmospheric pressure, flows over the sample surface towards the outflow take-off point, which transfers the ablated material to the plasma torch. Ionic detection was then performed by mass spectrometry.

a

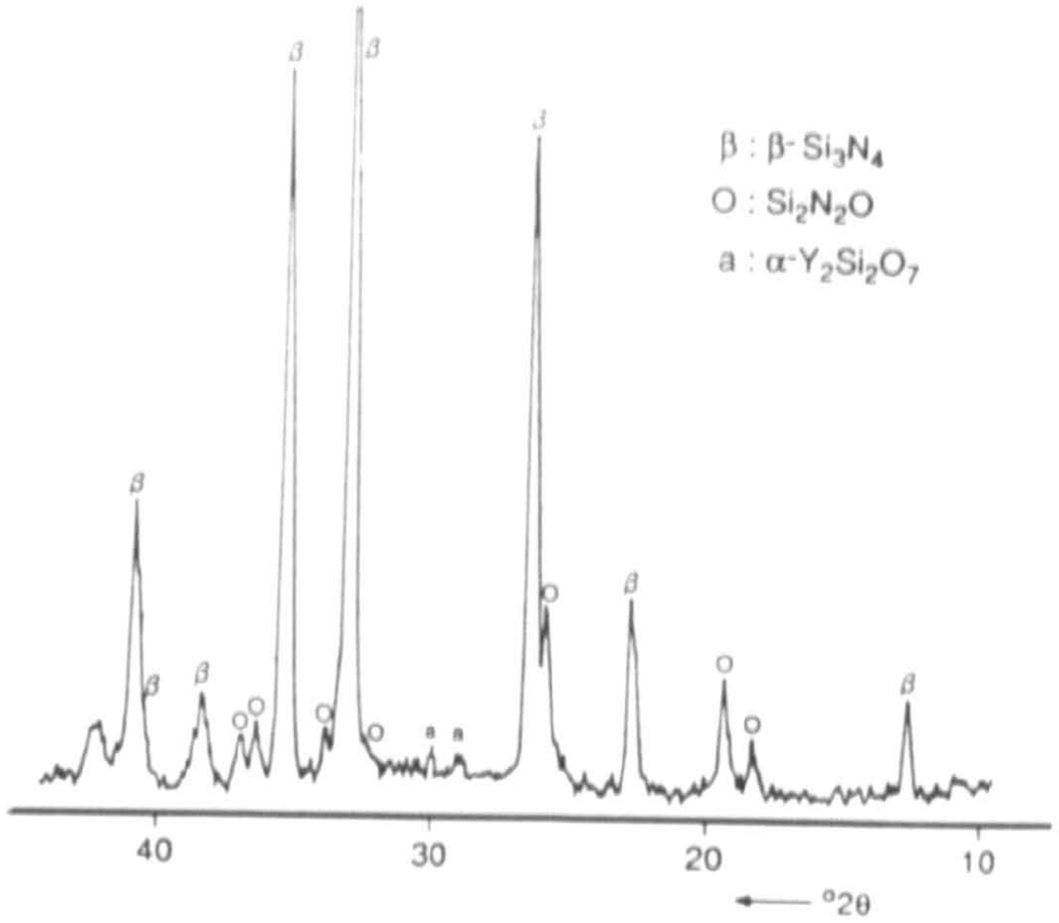

b

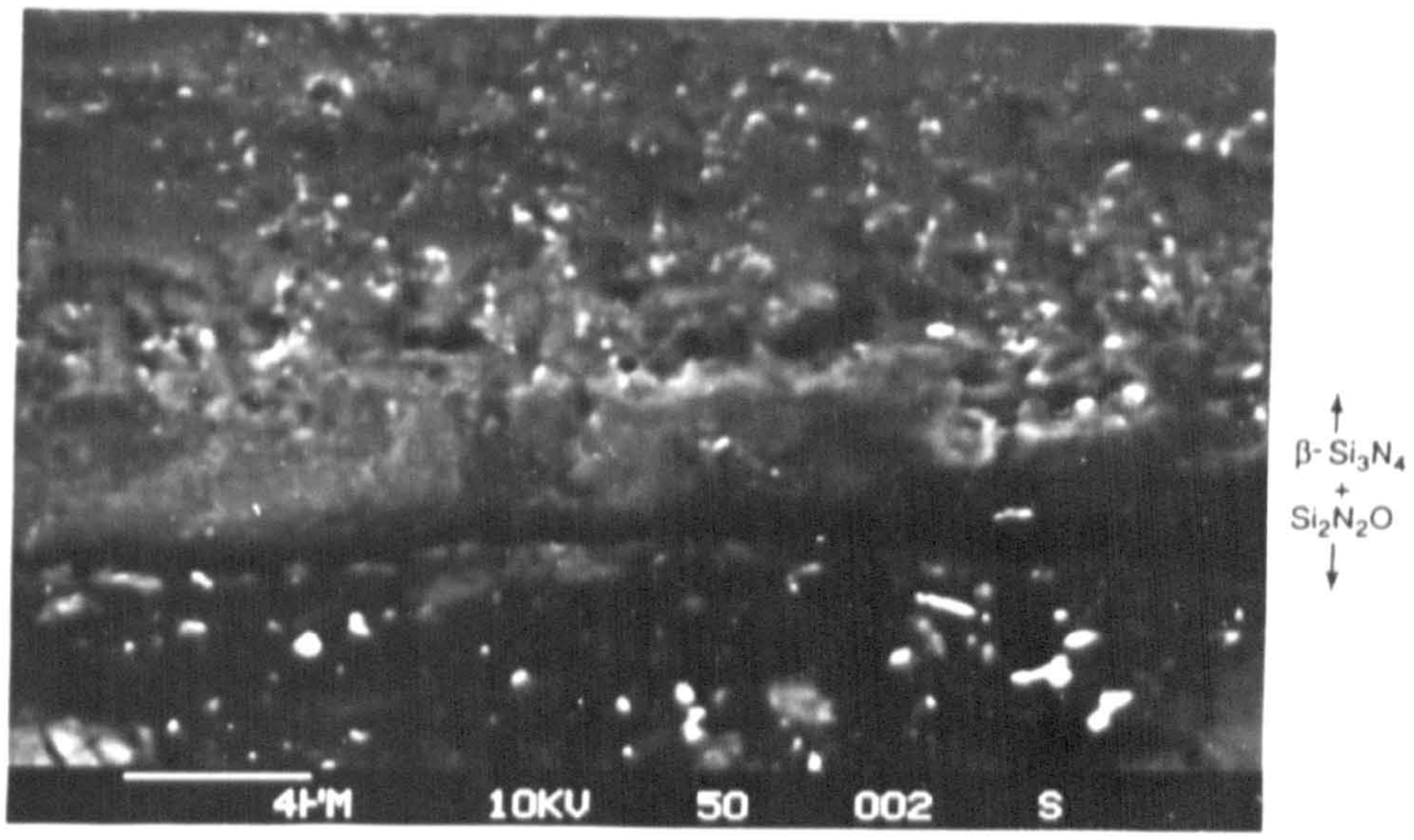

c

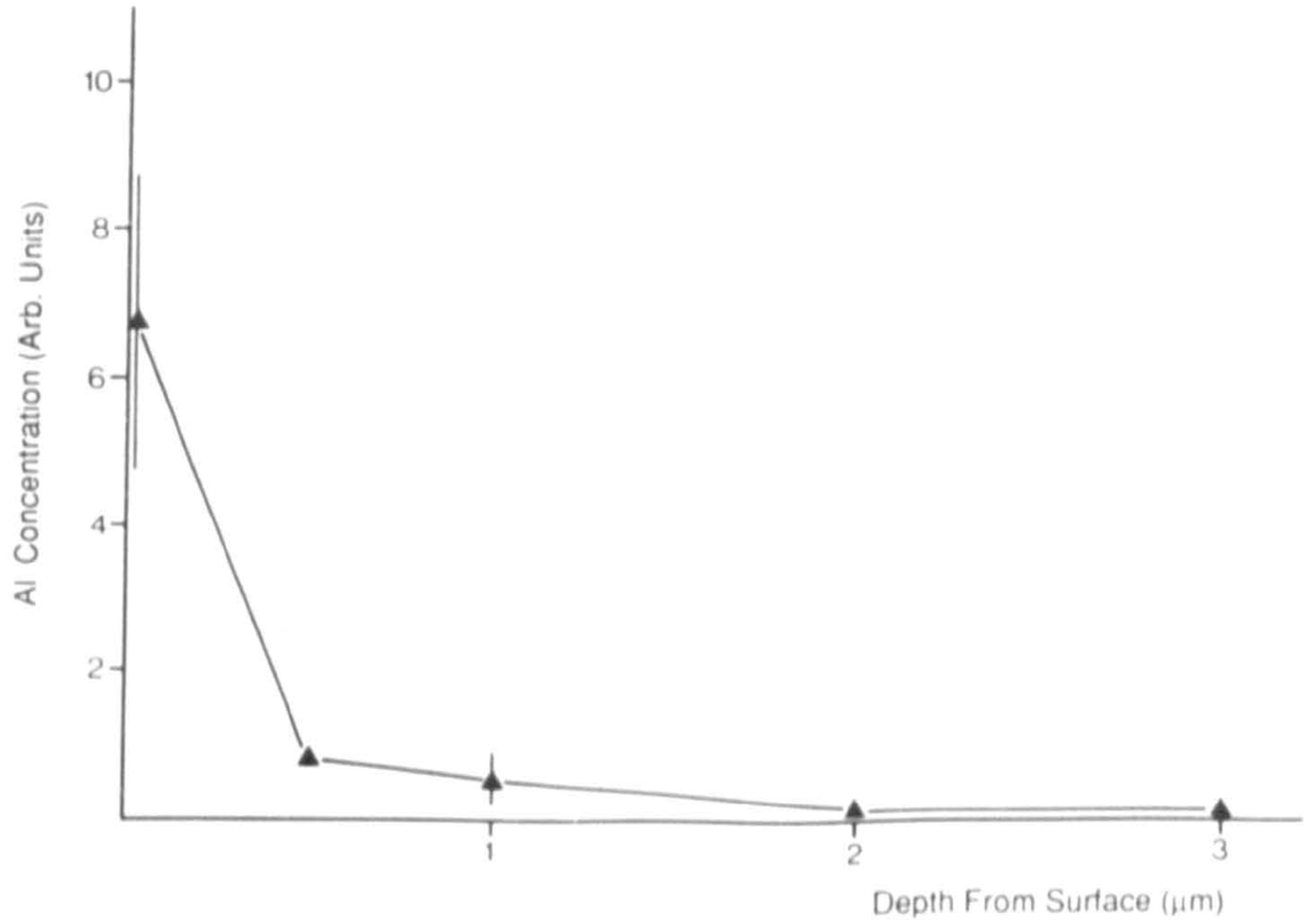

Figure 6.16 a) XRD demonstrates the increased Si_2N_2O content at the surface of composition B1; a similar trend was generally observed for all ceramics HIPed at ASEA (B1 to B7). b) SEM micrograph of the Si_2N_2O/β-Si_3N_4 (and O'/β') reaction layer formed at the surface of ASEA HIPed ceramic B1. c) The variation in aluminium concentration, within the surface layer, as a function of depth into the specimen, for composition B2.

2. Secondary Ion Mass Spectrometry (SIMS)

The SIMS technique involves the generation of secondary ions at the specimen surface by the penetration of a primary ion into the material, which results in a series of atomic collisions. Atoms within a few Angstroms of the surface can thus be ejected, either as neutral atoms or in various positive or negative ionic states. The SIMS analysis was conducted on a sample of composition B1, HIPed at ASEA, by Mr. G. Gregory of the Department of Metals and Materials Engineering, City of Sheffield Polytechnic. Analysis is performed under UHV conditions (10^{-10} Torr) using an argon primary ion source.

6.6.4. Boron Level Determination

The first series of ICP/MS analyses were conducted upon a silicon nitride based ceramic utilizing an equivalent mole percentage of Nd_2O_3 (replacing Y_2O_3) sintering aid as composition B1. HIPing of this composition was performed in the same ASEA cycles as B1 - B7. The ceramic, identical to C1, had a lightened surface reaction layer similar to the ASEA HIPed B1 ceramic. Laser ablation was performed on the bulk ceramic, subsurface reaction layer and the as-received surface.

The 'raw' data obtained for this sample is presented in figure 6.18a. After computer processing of the data at Surrey only four element concentrations were observed to be considerably different between the bulk and surface regions. The processed data for these and other selected elements are presented in Table 6.2.

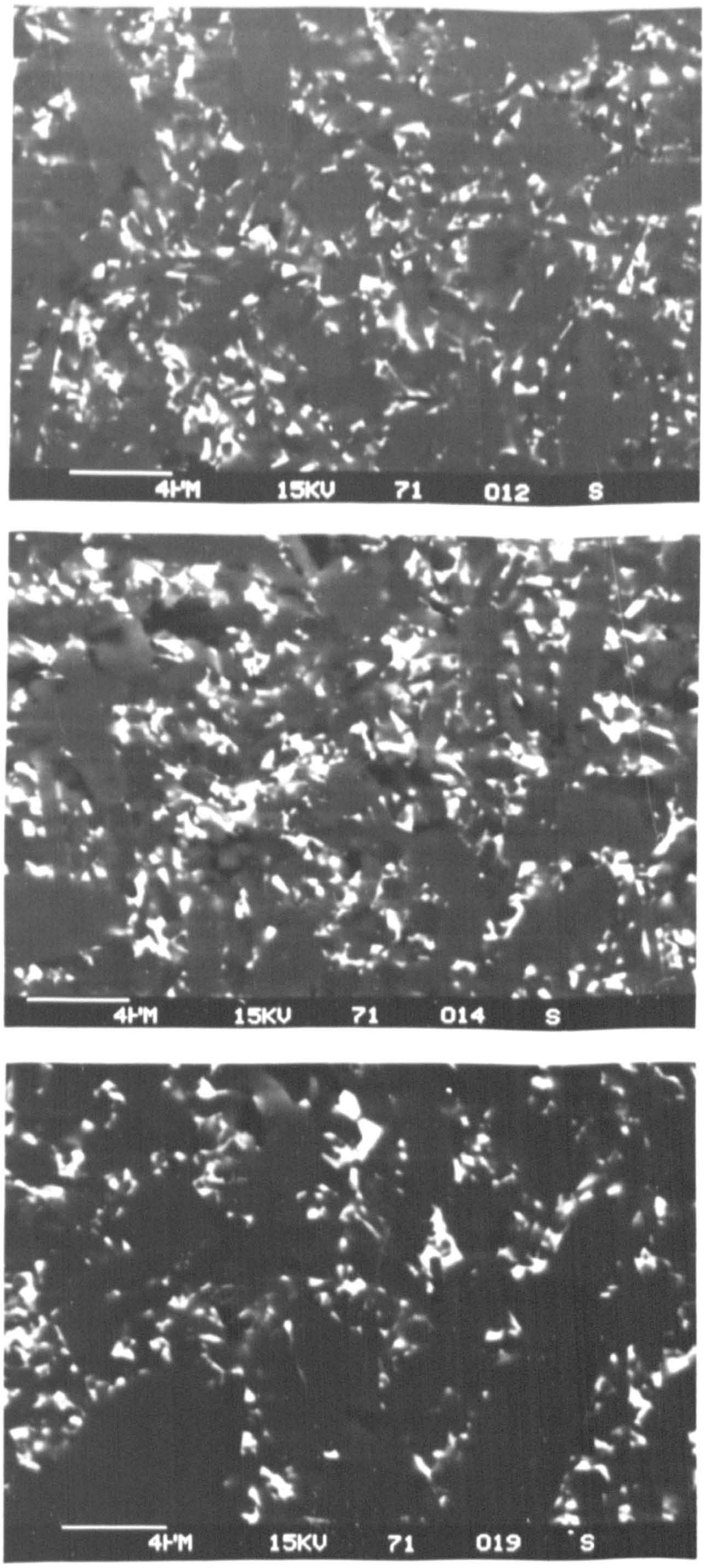

50μm from surface

200μm

Bulk

Figure 6.17 SEM micrographs demonstrating the variation in β–Si_3N_4 morphology with depth from the surface, for composition B1.

a

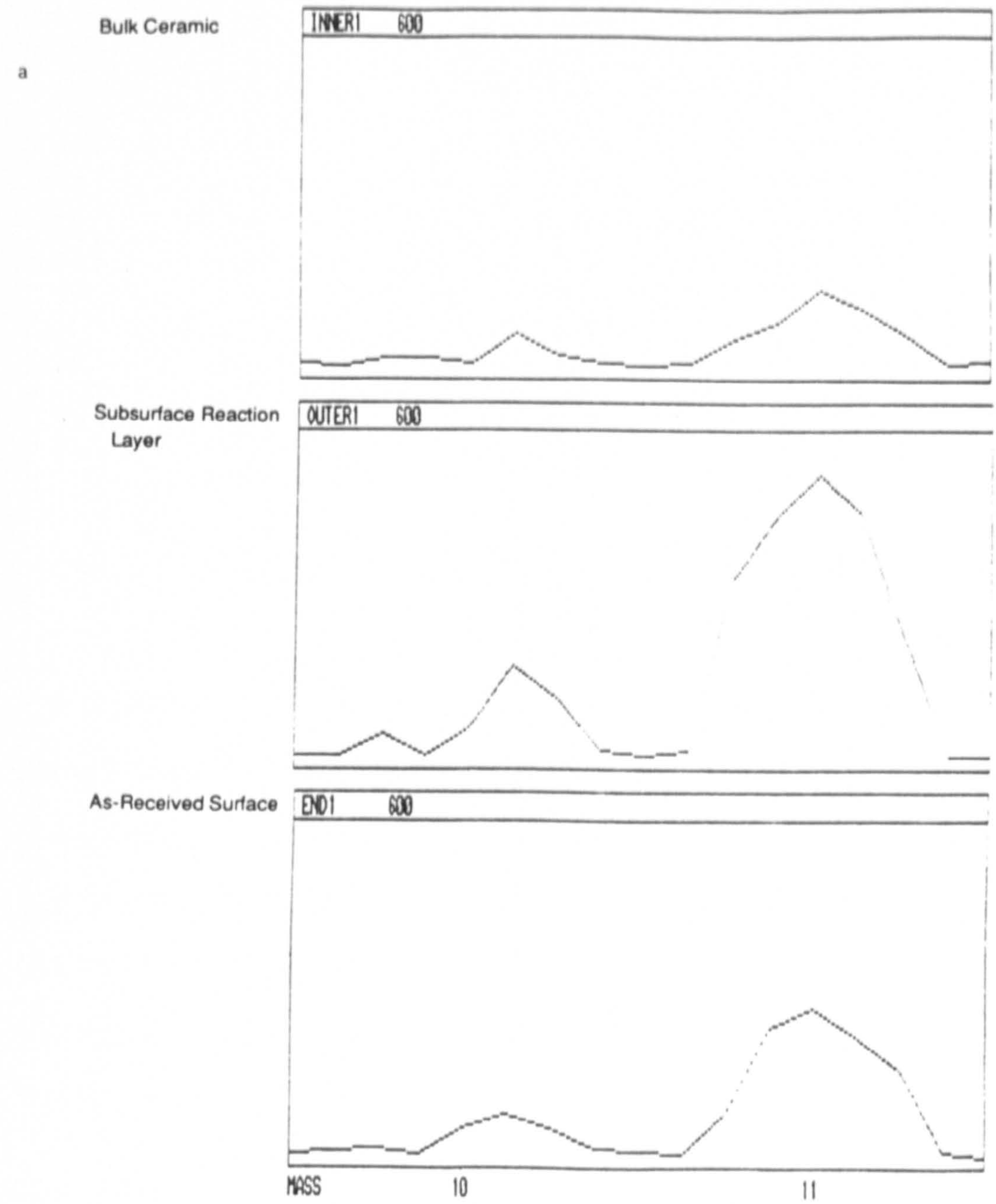

b

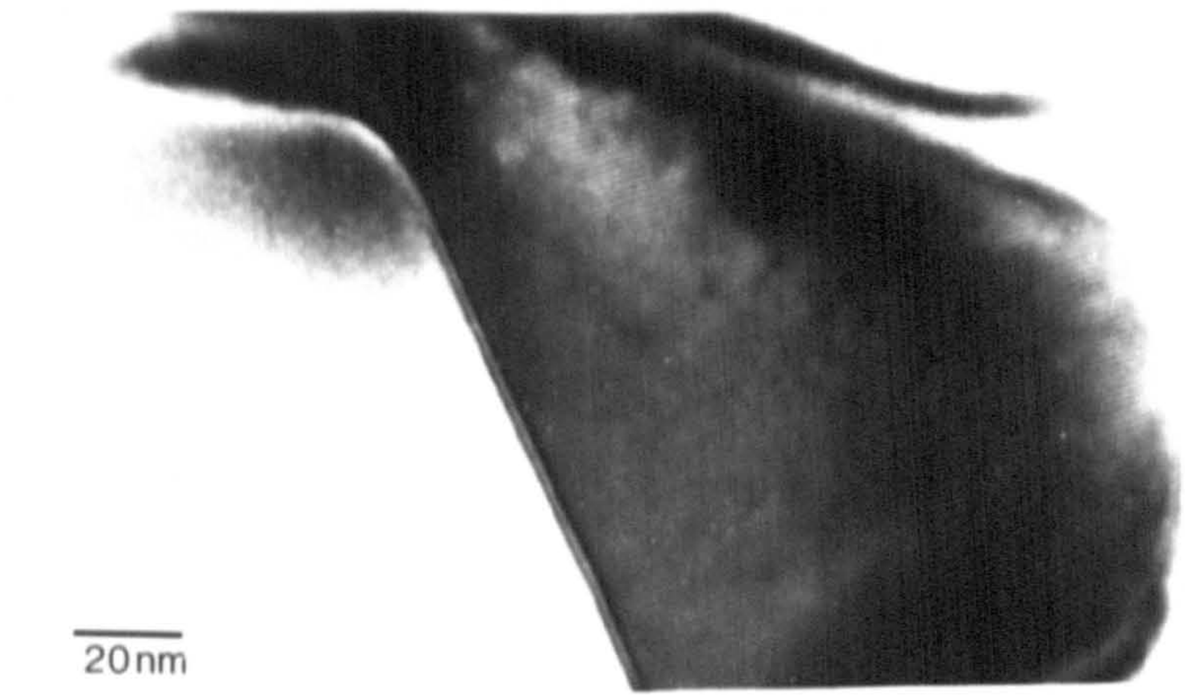

Figure 6.18 a) Data obtained from the laser ablation ICP/MS technique conducted at Surrey University, demonstrating the variation in boron concentration between the bulk ceramic and surface reaction layer (obtained for ASEA HIPed ceramic C1, 7.3 wt.% Nd_2O_3, which demonstrated a similar reaction zone to B1, shown in figure 6.14a). b) TEM micrograph of the microstructure in the 3mm thick lighter grey surface reaction layer of ASEA HIPed ceramic B1, showing a thin amorphous intergranular residue. (Courtesy Dr. G. Leng-Ward).

Element	Atomic mass	No. counts Bulk	Sub-surface	Surface	Sub-surface/bulk % variation
Li	7	12	12	1	0
B	11	31	1194	521	3752
Na	23	15331	13722	14919	- 10
Mg	24	404	683	458	69
Al	27	1958	2392	2651	22
Si	29	154682	158441	181123	2
Ba	137	22	146	39	564
Nd	145	388876	402204	405474	3
Bi	209	37	121	16	227
U	238	9	76	5	744

Table 6.2 Processed data for ICP/MS analyses of HIPed Nd_2O_3 additive Si_3N_4.

It is necessary to note that individual elements are not calibrated with respect to one another and direct compositional information cannot be obtained. The variation in bismuth and uranium level are not believed to be important, however the detection of Ba may be representative, as isolated pockets of barium silicate were present on the surface of the HIPed ASEA ceramics. The variation at the surface may be accounted for by the ablation of a barium silicate-'free' region. As Table 6.2 reveals, a considerable increase in boron concentration was apparent in the subsurface region.

In a further attempt to quantify the level of boron in HIPed ceramics, a glass of composition $Y_{0.9}Si_{1.4}Al_{1.23}O_{6.27}B_{0.18}$, was produced by Dr. G. Leng-Ward. Modifications to the ICP/MS system and variations in the operating procedure meant that the data obtained for the neodymia-containing specimen could not be calibrated against the boron containing glass. The additional HIPed silicon nitride ceramics studied by ICP/MS are given in Table 6.3. The variation of boron concentration within the HIPed samples, calculated by comparison with the glass of known boron content, is also presented in Table 6.3.

		No. counts (boron) *		% B inc. at	Relative B conc. †	
		Surf.	Bulk	surface	Surf.	Bulk
Nd	¶ §	75	3	3650	–	–
5Y	§	1246	616	102	0.060	0.030
3.5Y	‡	18	12	50	0.0009	0.0006
5Y	‡	24	15	60	0.0011	0.0007
7.5Y	‡	28	11	154	0.0014	0.0005
Glass		–	2665	–	–	0.129

Notes

* Normalised to 10 000 counts for Si.

† Number of boron atoms per silicon atom.

§ Densified in 1st ASEA HIP cycle; the same cycle as B1 to B7.

‡ Densified in 2nd ASEA HIP cycle, under the same conditions as the first cycle. The microstructure of these ceramics was not analysed during the current programme, but is described in [76].

¶ Studied in first ICP/MS run.

Table 6.3 Data obtained for various HIPed Si_3N_4 ceramics from the ICP/MS ablation technique.

It can be seen that the two largest boron levels are recorded in the ceramics processed in the first ASEA HIP cycle, with both of these materials exhibiting the highest level of surface interaction (from optical microscopy – section 6.4.2). The relative boron concentration for composition B1 is calculated at approximately one boron atom for 17 silicon atoms, by comparison with the glass standard. This result must be regarded with a certain degree of caution. The observed levels of other elements, particularly yttrium (which should be consistent for each specimen – and varying by a maximum of ~100% in real terms, 3.5 to 7.0 wt.% Y_2O_3), were found to vary by up to 1000% from one specimen to another (when normalised with respect to silicon).

It should also be noted that preparation of boron containing glasses is difficult, due to the tendency of B_2O_3 to vaporise, and further study is required to assess whether the glass produced by Dr. G. Leng-Ward retained its starting composition after melting.

Examination of the complete set of data obtained by ICP/MS has revealed a relatively high reproducibility of results during a single set of ablation runs on one specimen. ICP/MS can not, however, currently be regarded as a quantitative technique for this type of analysis, as comparison between separate specimens has demonstrated.

The direct analysis of boron levels in ceramic B1 via the SIMS technique was not possible, with negligible boron detected and specific problems occurring with the resolution of the boron region of the SIMS spectra (arising from 'matrix' effects, namely interaction of the primary ion bean with silicon nitride).

High resolution transmission electron microscopy (HRTEM) conducted by Dr. G. Leng-Ward did not reveal any detectable increase in the amorphous residue volume at the β-Si_3N_4/α-$Y_2Si_2O_7$ grain boundary. It is not believed that boron resides in the amorphous grain boundary phase (fig. 6.18b).

Although the presence of boron at the specimen surface has been detected, further investigation is required to assess and quantify the behaviour of boron during HIPing. The potential effects of boron contamination upon high temperature material properties are discussed in the next chapter.

6.6.5. Post-HIP Surface Condition

The surface state of the ASEA produced ceramics was examined and analysed via scanning electron microscopy. The smoothness of the post-HIP specimen surface was found to vary considerably from specimen to specimen, although there was no compositional relation (fig. 6.19a). The surface state generally was consistent over the whole billet surface, on both a micro- and macroscopic scale. Rubber bag cold-isostatic

a

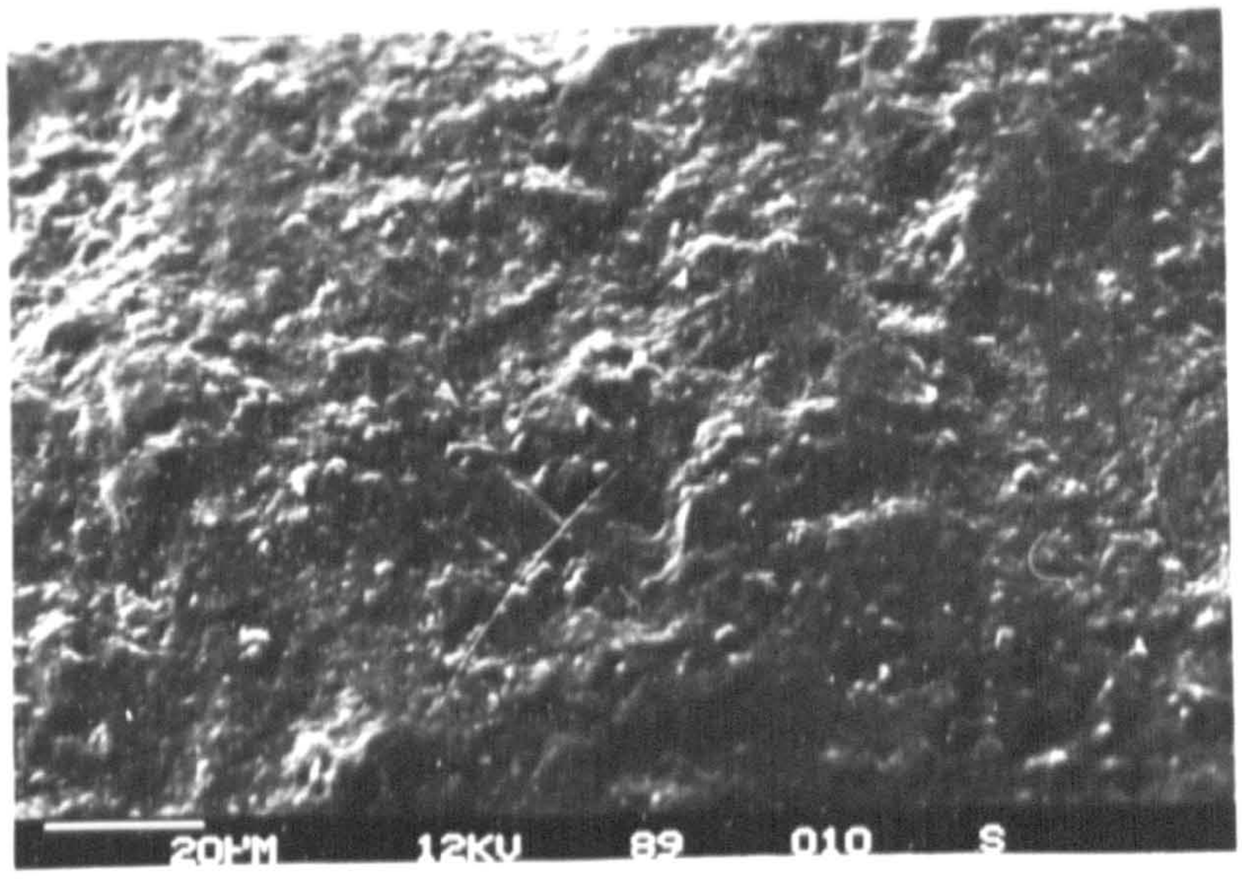

B3

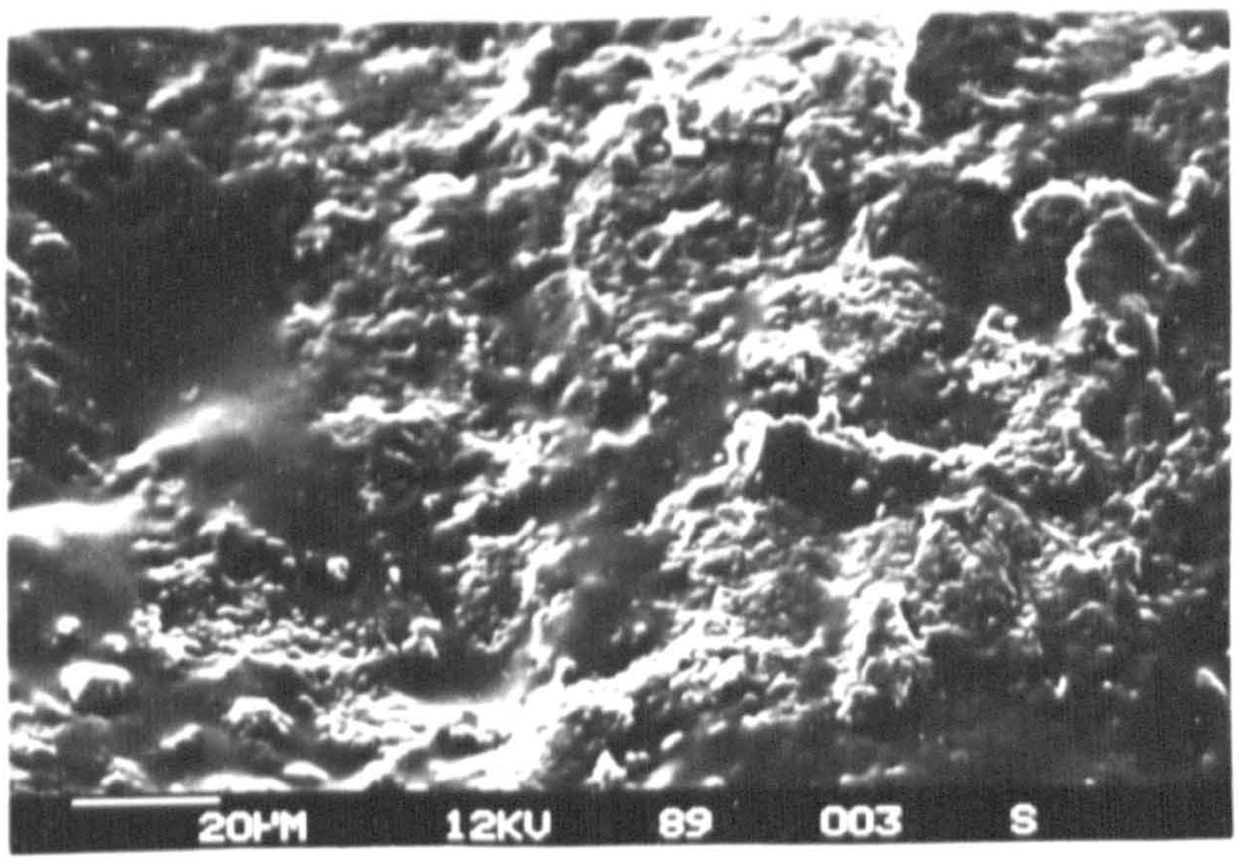

B4

b

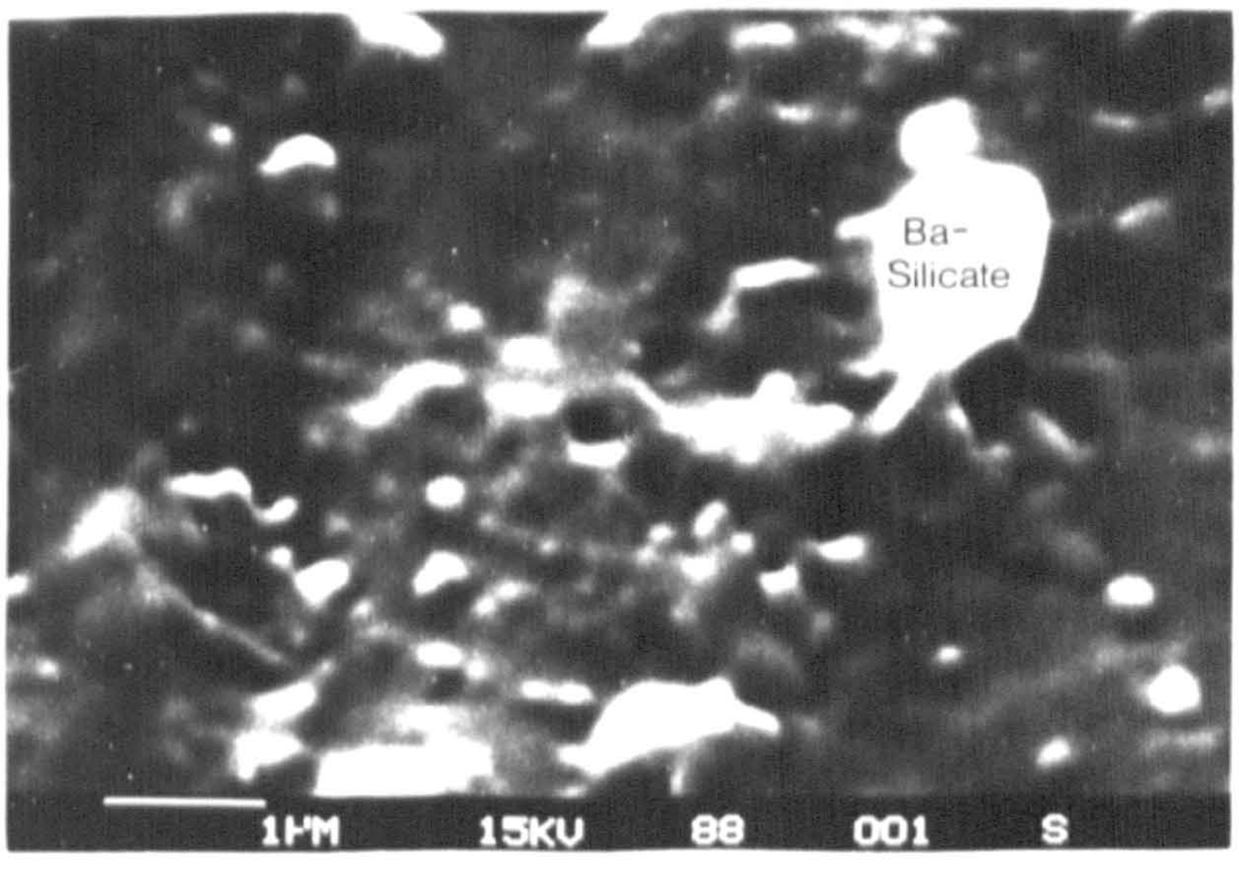

Figure 6.19 a) Secondary electron SEM micrographs of the as-received surface condition of ASEA HIPed ceramics B3 and B4. The surface state can be seen to vary considerably and some post-HIP diamond machining is likely to be required for finished components. b) Region of barium (aluminium) silicate contamination on the surface of composition B1; additionally regions of cerium and lanthanum impurity silicates were detected on the as-received surface.

pressing of each billet, prior to HIP, probably accounts for the variation in smoothness and it is likely that, after HIPing, a limited amount of diamond machining would be necessary to produce a consistent, flaw free surface finish on components. Back-scattered electron imaging of the HIPed billet surfaces, to reveal average atomic number contrast, indicated a constant composition across the whole of the surface, namely β-Si_3N_4 and Si_2N_2O, or more probably the substituted equivalent forms. A noticeable Al level was detected over the whole surface of each specimen and it is most probably contained in the substituted forms of both β-Si_3N_4 and Si_2N_2O as no further crystalline Al containing phase was detected by X-ray diffraction. Substitution values z were calculated for specimens B1 to B4 using the formula [39]:

$$Si_{6-z}Al_zO_zN_{8-z}$$

and are presented in Table 6.4.

The values are calculated assuming that all, or nearly all, the in-diffusing Al is taken into the major crystalline phase β-Si_3N_4 (giving rise to β-Si-Al-O-N formation) as the solid solution limit of Al in silicon oxynitride is low by comparison.

Specimen	B1	B2	B3	B4
Additives wt.%	$5Y_2O_3$	$5Y_2O_3/2SiO_2$	$5Y_2O_3/4SiO_2$	$5Y_2O_3/8SiO_2$
Approx. substitution level (z)	0.58	0.43	0.84	0.52

Table 6.4 Approximate Al substitution level at the surface of ASEA HIPed ceramics B1 to B4

A few isolated light contrast areas were present on selected compositions (B1 - B4) (fig. 6.19b). Analysis of these regions identified the presence of several impurity elements including barium, calcium and potassium. A few of the isolated regions in specimen B1 were found to be amorphous areas containing the rare earth elements cerium and

lanthanum with an approximate composition

$$Si\ Al_{0.075}\ Ba_{0.02}\ Ce_{1.75}\ La_{0.84}\ Ca_{0.06}\ K_{0.01}\ O_{6.93}\ .$$

The rare-earth impurities most probably arise from contamination by other specimens in the HIP chamber contacting the 5 wt.% Y_2O_3 additive billet surface. The barium containing phase, present in all four analysed billets was of the approximate composition

$$Si\ Al_{0.09}\ Ba_{0.03}\ Ca_{0.016}\ K_{0.02}\ O_{2.2}\ ,$$

with the oxygen level estimated from the standard elemental valencies. It is expected that both types of amorphous impurity phase present will have softening temperatures considerably lower than the intergranular $Y_2Si_2O_7$ regions.

6.7. ENCAPSULATION IN GLASS POWDER WITHIN PYREX TUBE: MICROSTRUCTURE AND CERAMIC/ENCAPSULANT INTERACTION

Certain drawbacks are present with the Pyrex tube/powder type encapsulation process. These include the apparent fluidity of Pyrex at HIP processing temperatures, with failure to densify occasionally arising because the encapsulant glass tends to 'run-off' the ceramic sample, and the interaction of boron with the silicon nitride sample during HIP.

An alternative encapsulation route was devised to allow the use of different encapsulant glasses (in powder form) within a Pyrex capsule, such that the standard Pyrex tube HIP cycle can be used. Two encapsulant glass powder compositions were examined using this technique: SiO_2, with a considerably higher softening temperature than Pyrex, and a Y-Si-O-N glass, tailored to have a composition close to the matrix phase. The effect of each encapsulant upon the microstructure of HIPed was primarily examined for composition A3, with a high volume, high viscosity matrix phase.

6.7.1. SiO_2 Powder Encapsulation (A3)

The bulk microstructure of ceramic A3, HIPed to full density in SiO_2 powder, was

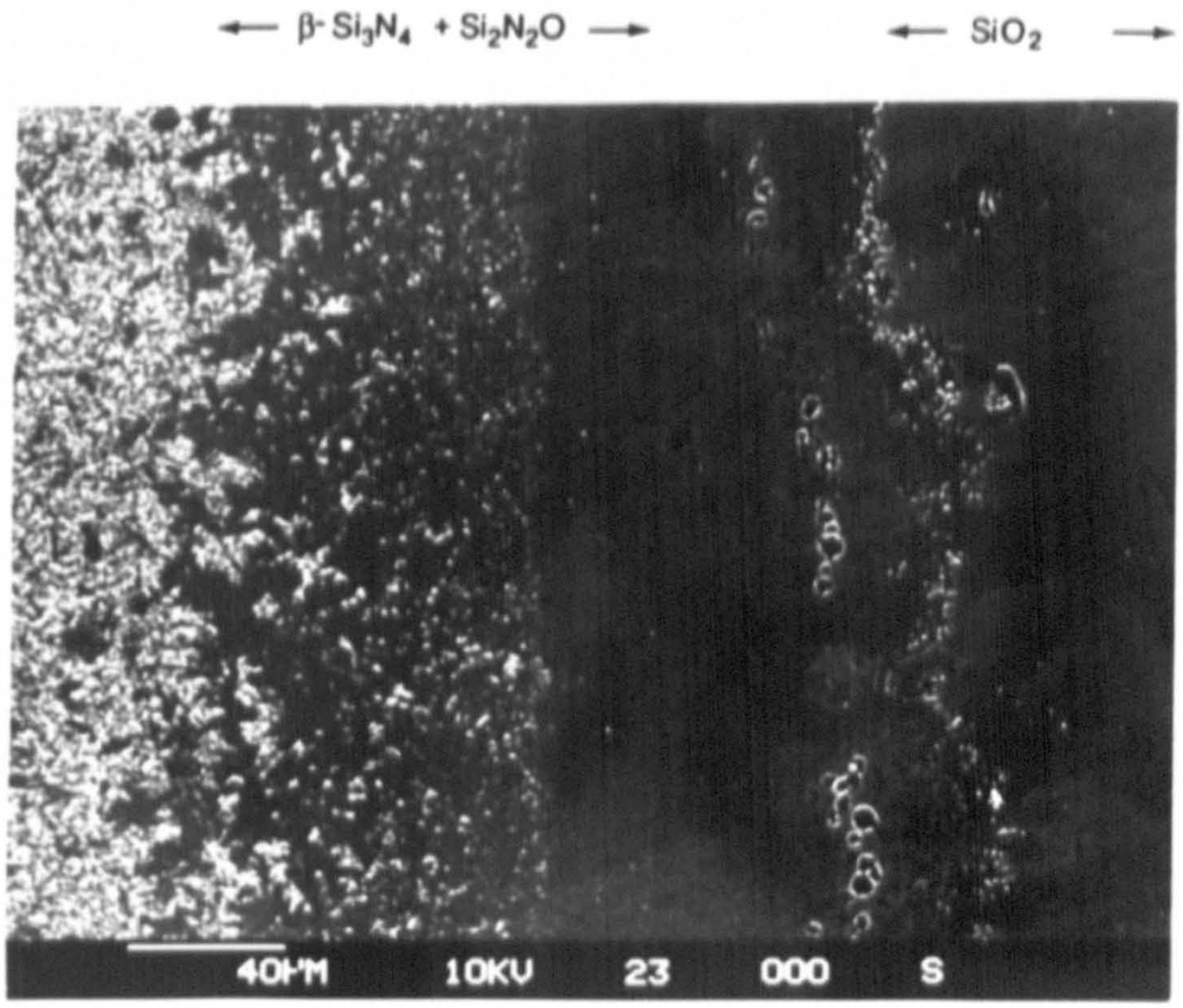

b

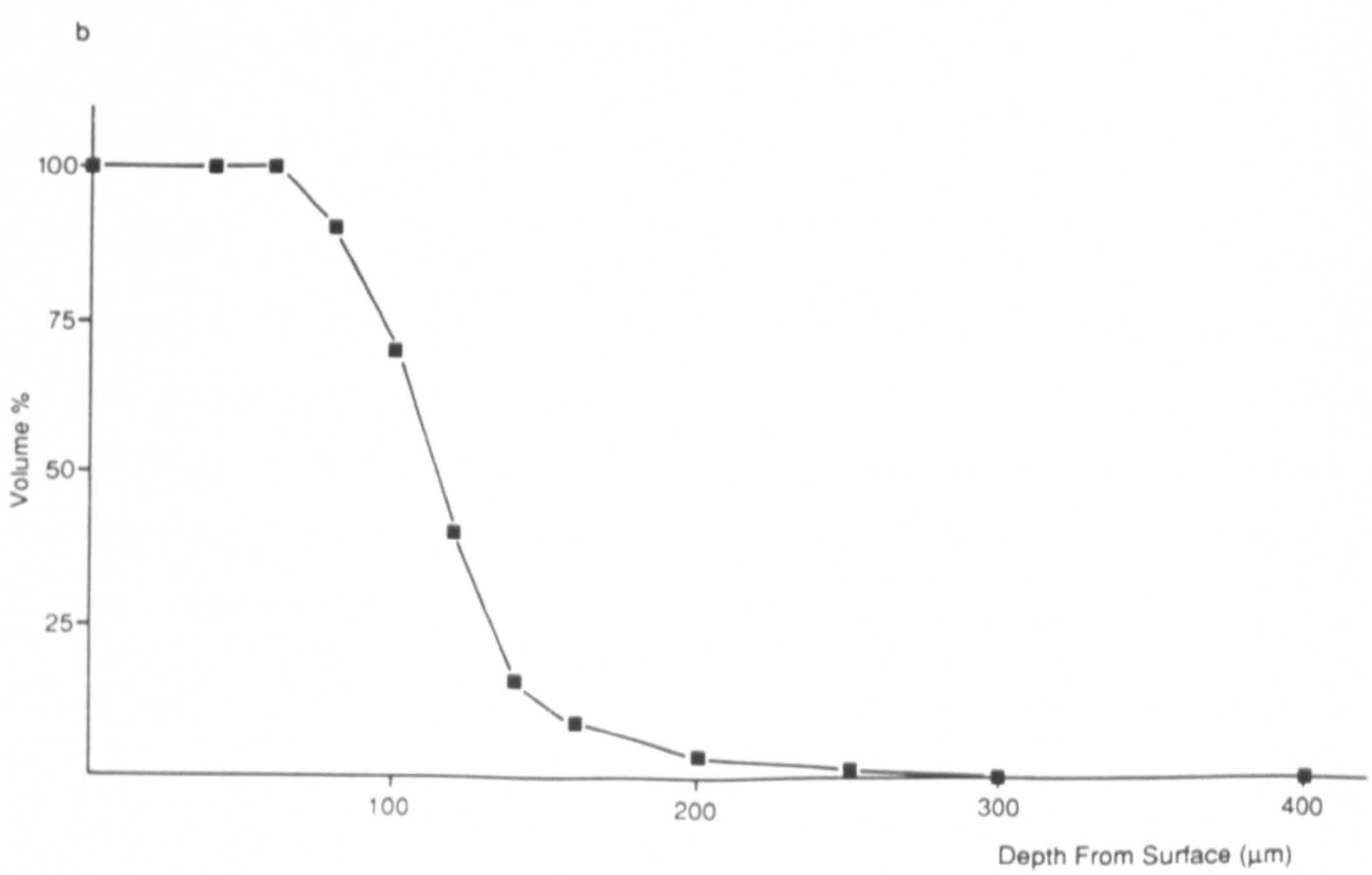

Figure 6.20 a) SEM micrograph of the surface reaction layer of ceramic A3 HIPed in SiO_2 glass, showing the formation of a uniform thickness, large grained Si_2N_2O layer (no BN layer was used for SiO_2 encapsulation). b) Variation of precipitated Si_2N_2O volume as a function of depth from the ceramic surface.

essentially identical to the same composition HIPed in Pyrex tubing with complete transformation of α- to β-Si_3N_4 grains.

Examination of the surface ceramic/encapsulant reaction zone of ceramic A3 (prepared without a BN coating) revealed the formation of a thin, uniform Si_2N_2O layer (fig. 6.20a). The Si_2N_2O layer formed at the ceramic surface was of considerably greater uniformity, with regard to depth, than those observed for Pyrex encapsulated ceramics – where a variable thickness BN layer was present. The Si_2N_2O layer appeared to be of a larger grain size than occurs when a BN barrier is present and large Si_2N_2O grains were observed below the glass free surface region (to a depth of ~ 400μm). Isolated Si_2N_2O grains were apparent below the monophase layer, forming through Si^{4+} and O^{2-} penetration deeper into the ceramic than the Si_2N_2O layer. Some isolated high contrast regions were apparent in the bulk region of A3, and EDX analysis revealed these to be of a Si:Y ratio 3:2, indicating the presence of Y-N-melilite ($Y_2Si_3O_3N_4$).

The variation of Si_2N_2O volume with depth into the ceramic is shown in figure 6.20b.

6.7.2. Y-Si-O-N Encapsulation: Ceramic A3

The bulk region of ceramic A3, HIPed in a Y-Si-O-N glass powder, did not show any detectable sign of porosity from optical microscopy, however a severe degree of gas bloating had occurred near the specimen surface, with the scale of voids (up to ~ 15μm diameter) considerably larger than typical residual pores (fig. 6.21a). The densified ceramic (A3) was a very light shade of grey, almost white, and was notably different in appearance from the other HIP consolidated materials.

SEM microstructural evaluation of the bulk regions of this ceramic revealed a substantial enhancement of the intergranular matrix volume (fig. 6.21b). A uniform, monomodal β-Si_3N_4 grain size distribution was observed in the ceramic bulk, with grains ranging from 1 - 4μm in length and aspect ratios from 2:1 to 4:1. High aspect Si_2N_2O grains

a

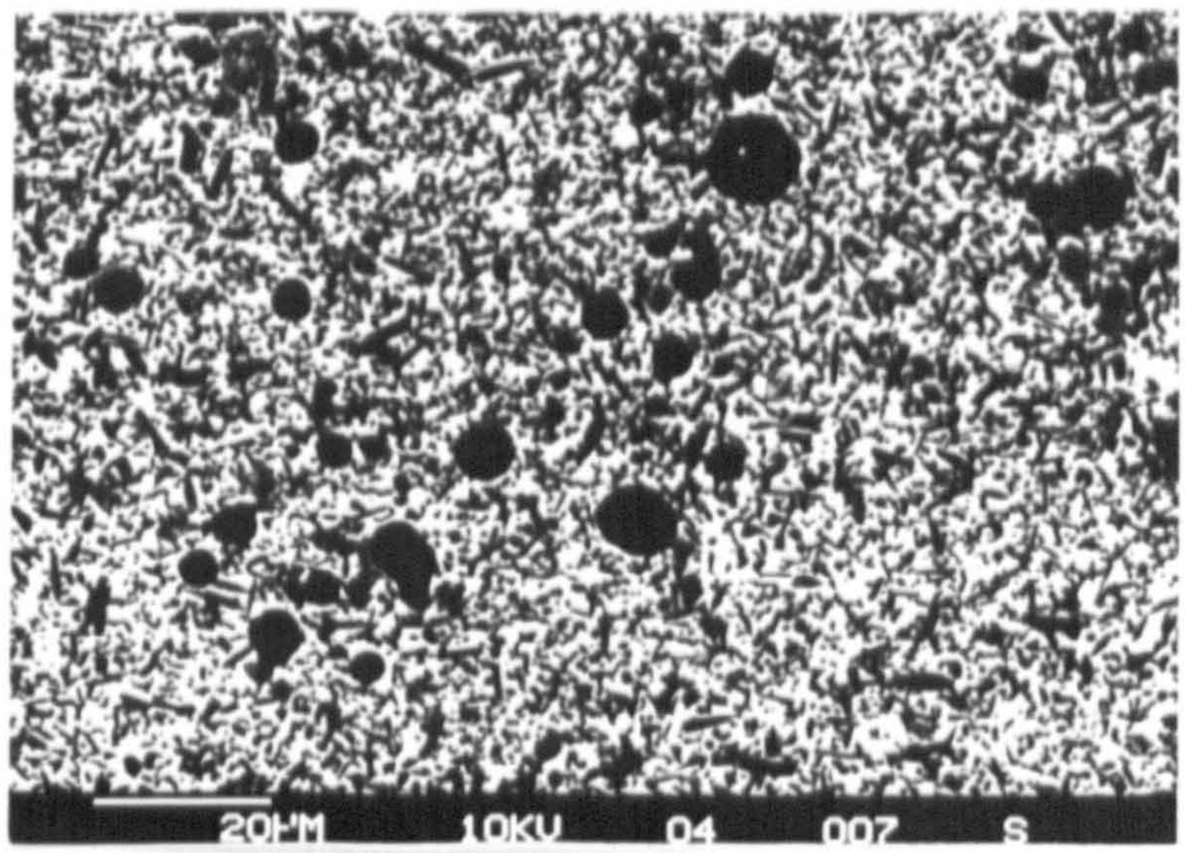

b

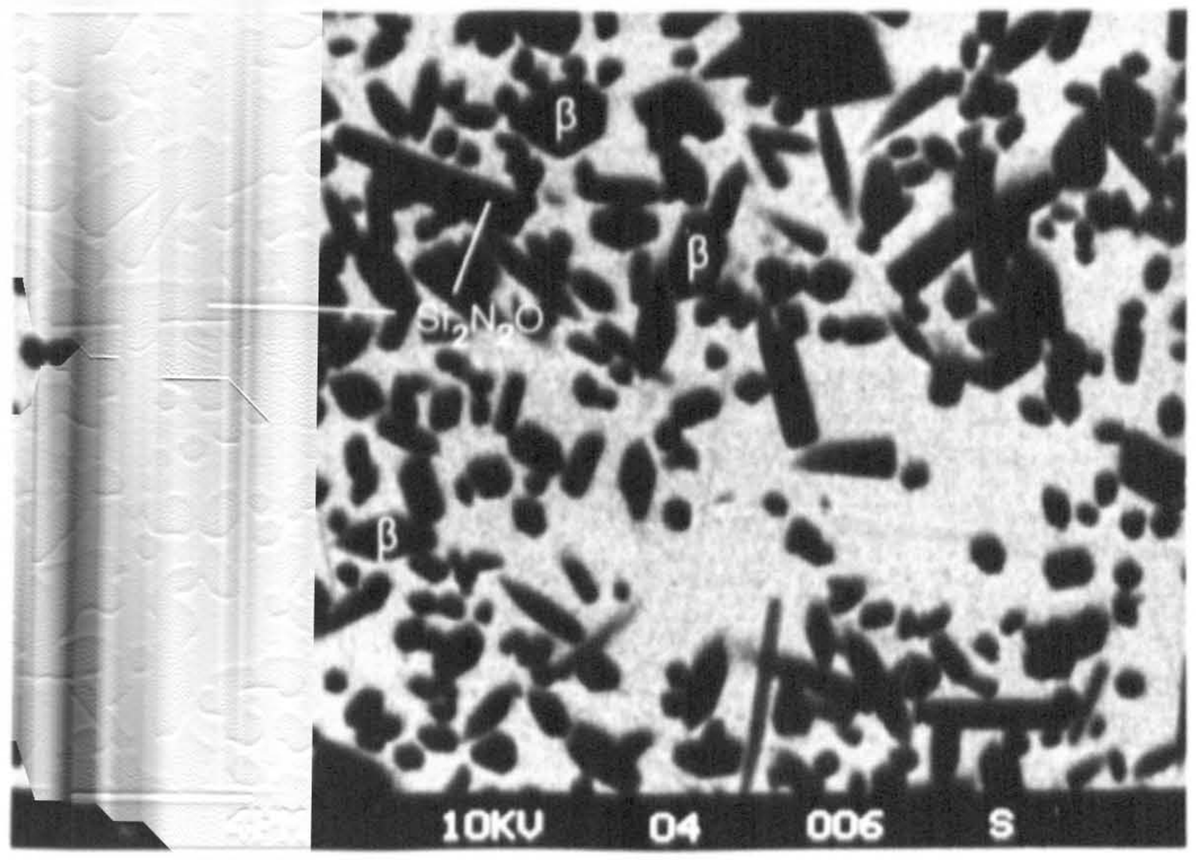

c

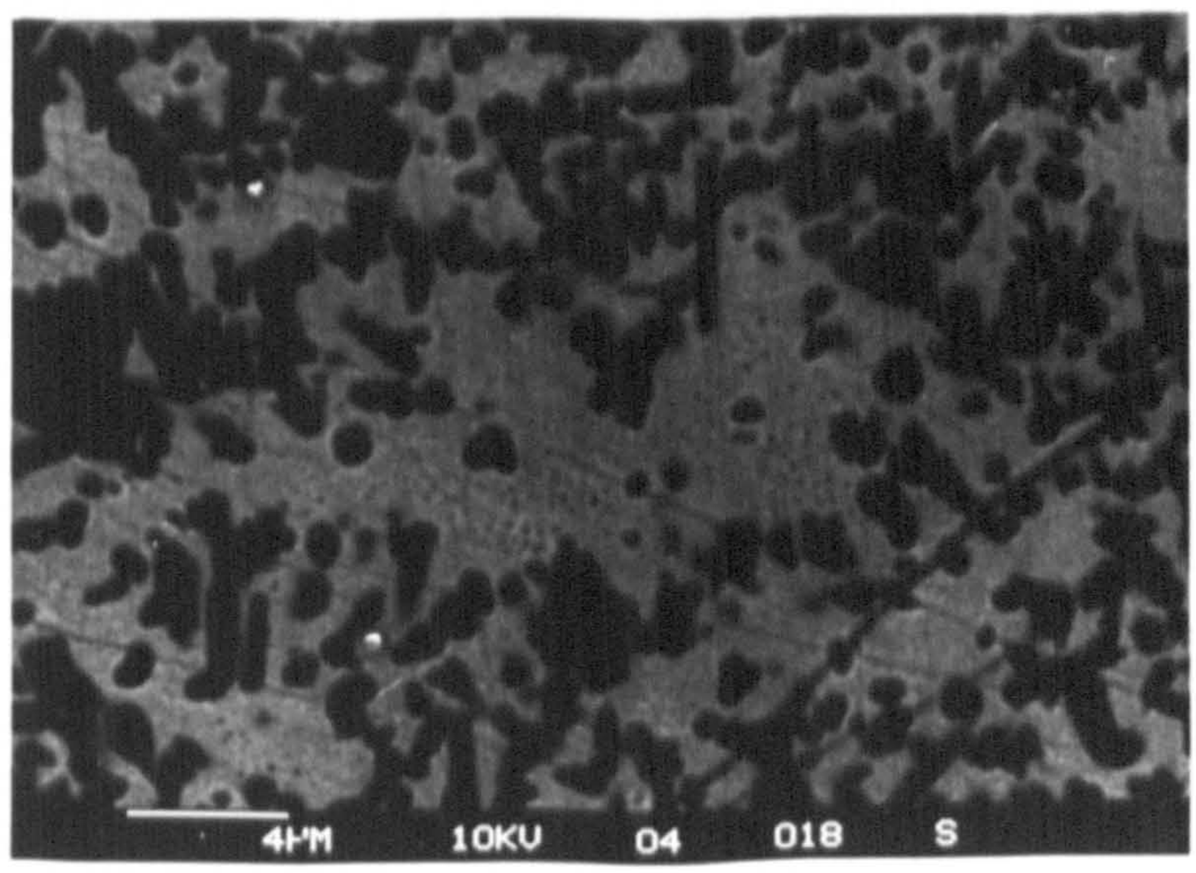

Figure 6.21 SEM micrographs of composition A3 HIPed in Y-Si-O-N glass: a) Gaseous void formation in the near surface region (~ 100μm from surface). b) Bulk microstructure showing the considerable matrix volume enhancement, with a similar effect noted at the surface c), where the glass composition is SiO_2 rich.

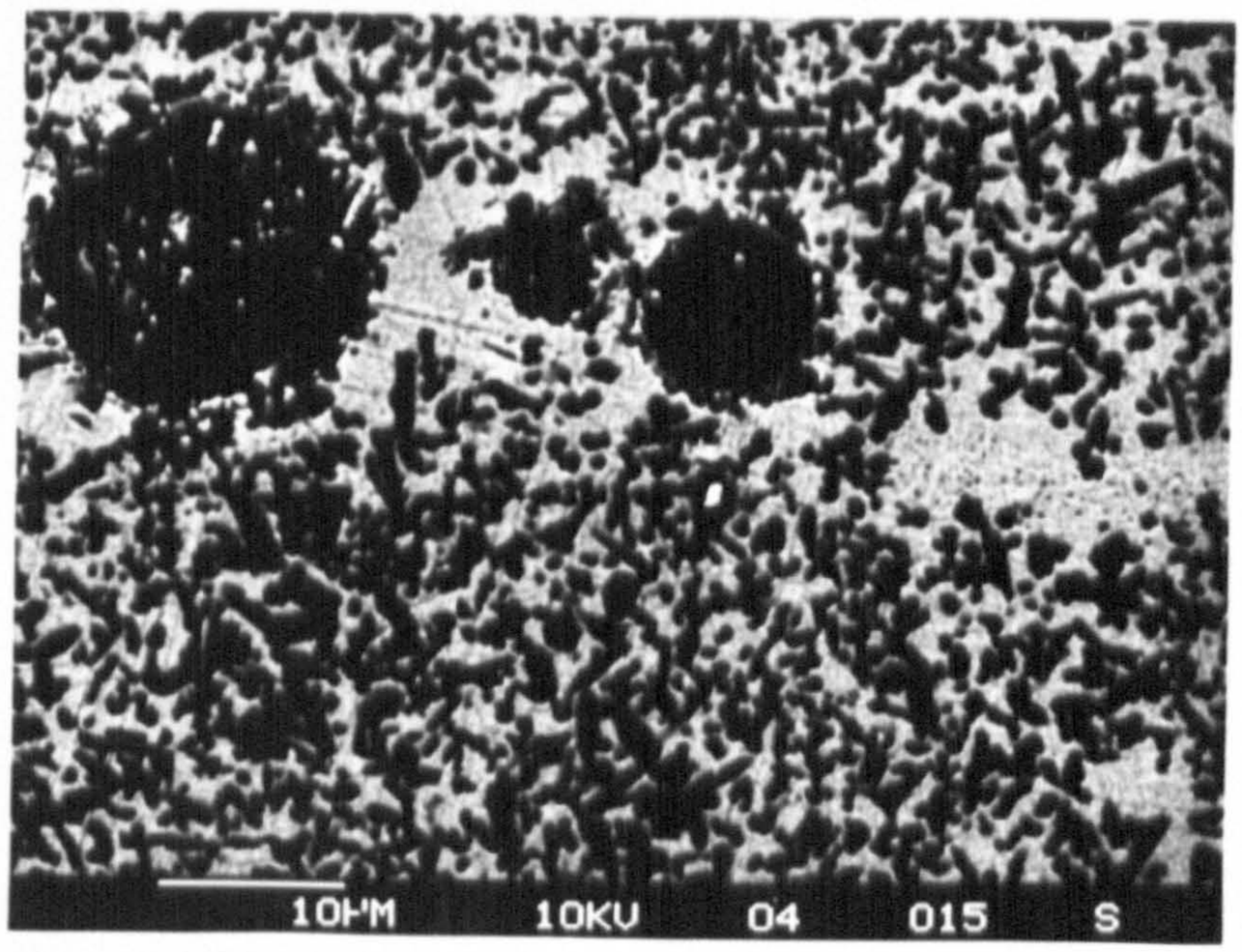

Figure 6.22 SEM micrograph of glass volume enhancement at pore tip in the sub-surface of the ceramic A3 (in Y-Si-O-N glass).

were also apparent in the bulk ceramic (fig. 6.21c). The bulk intergranular glass composition was $Si\,Y_{1.2}\,O_{3.8}\,N_x$. Determination of the glass nitrogen content cannot be accurately made, however it is probable that a moderate level of nitrogen has been incorporated in the enhanced volume matrix phase, via dissolution of α-Si_3N_4 in the glass followed by incomplete reprecipitation of β-Si_3N_4. This behaviour is similar to the fabrication of high nitrogen glass ceramics where the nitrogen is incorporated via the addition of α-Si_3N_4 to the other glass constituents.

A similar matrix volume enhancement was observed at the surface of HIPed Y-Si-O-N encapsulated ceramic A3 (fig. 6.21c). The β-Si_3N_4 structure appeared to be generally identical to the bulk material, although the presence of some higher aspect ratio grains was apparent. A silica rich Y-Si-O-N glass composition was determined near the ceramic surface, of an approximate composition of $Si\,Y_{0.44}\,O_{2.66}\,N_x$. Some isolated β-Si_3N_4/Si_2N_2O-free areas were apparent in the ceramic subsurface region with the analysed composition being closer to the Y-Si-O-N encapsulant glass (fig. 6.22).

6.7.3. Glass Powder Encapsulation in Pyrex Tube: Discussion

The use of ground glass powder within a Pyrex tube has been shown to be a successful technique for encapsulation and HIPing to full density (the densification is described in section 5.4.3). The interaction mechanism with the substrate ceramic is essentially identical to that described in section 6.5, however the severity of reaction is increased in the absence of any BN barrier layer. Penetration of both encapsulant glasses is observed deep into bulk ceramic, via Si_2N_2O formation in the SiO_2 encapsulated example, and considerable matrix volume (measured in the SEM using the Link AN10000 system) enhancement using the Y-Si-O-N glass. The variation of matrix volume and composition as a function of depth from the ceramic surface is shown in figure 6.23a,b. The higher silica concentration near the surface may be attributed to SiO_2 diffusion (from the outer Pyrex capsule) through the Y-Si-O-N encapsulant glass to the ceramic. This interaction

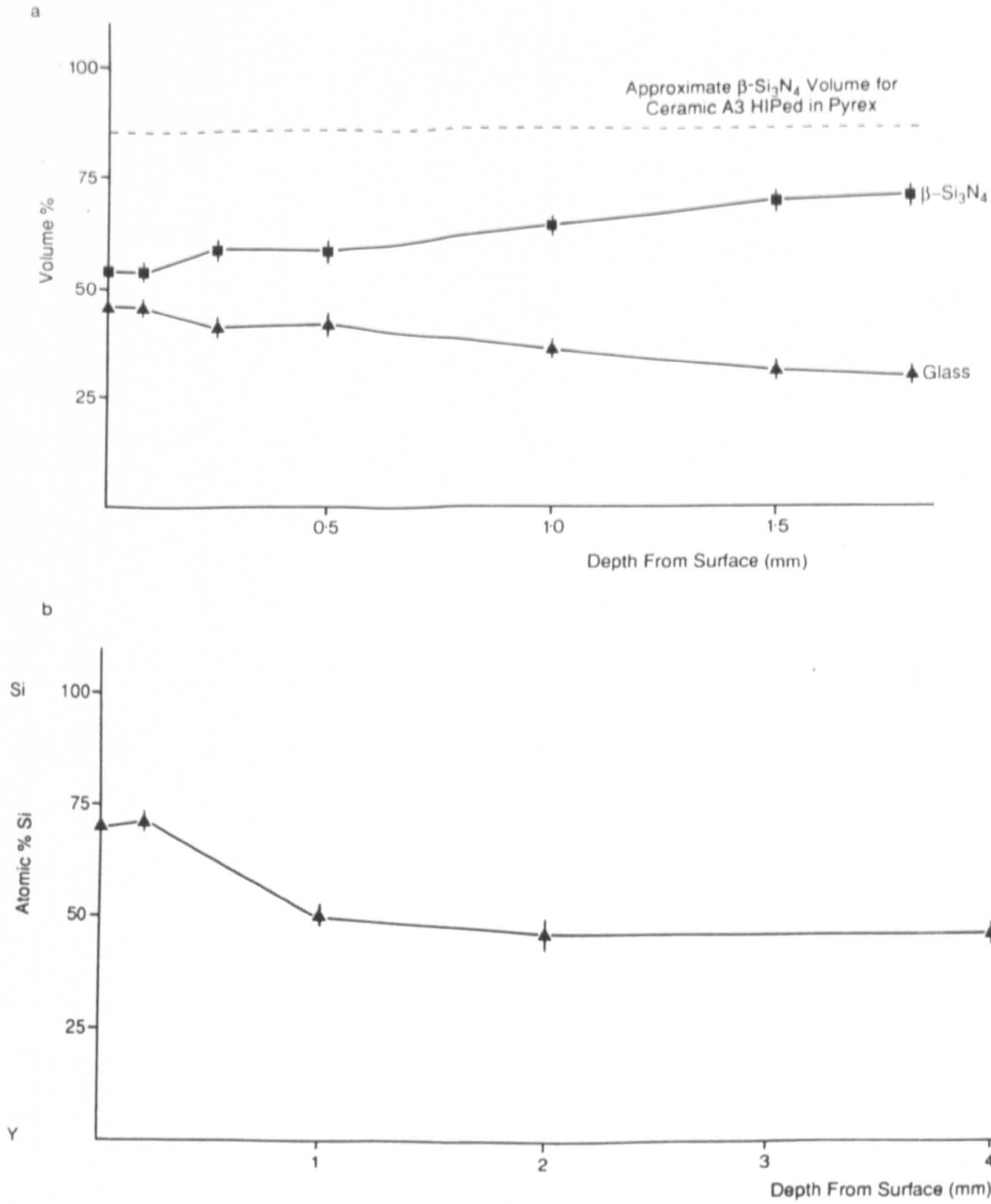

Figure 6.23 Variation of a) intergranular matrix volume, and b) intergranular matrix composition with depth from the ceramic surface for Y-Si-O-N encapsulation.

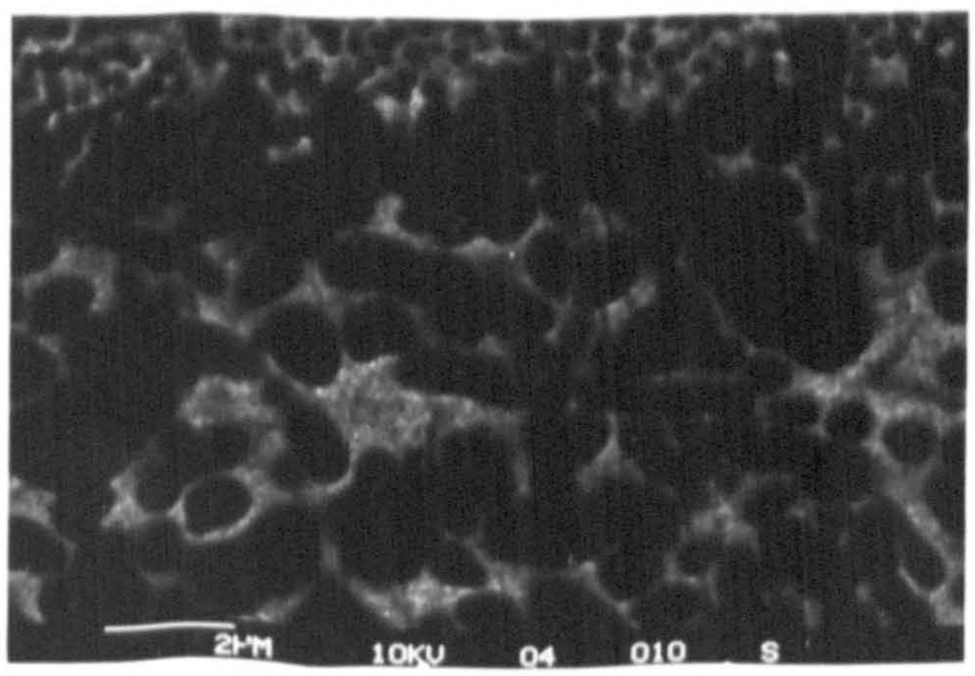

Figure 6.24 The nucleation of phase-separated SiO_2 upon β-Si_3N_4 grains.

occurs during the latter stages of the HIP cycle, as shown by the nucleation of SiO_2 upon β-Si_3N_4 grains at the extreme ceramic surface (fig. 6.24). Understandably, surface interaction using these encapsulant glasses could be avoided with the use of a BN layer as used for Pyrex tube encapsulation.

6.8. GLASS ENCAPSULANT HIP PROCESSING: SUMMARY

A range of silicon nitride ceramic compositions has been HIPed to near theoretical density following the glass encapsulation route. Several techniques for encapsulation were developed and these are documented in the previous chapter.

Several authors have described the microstructure and properties of HIP densified silicon nitride, and these are summarised in chapter 2, however little attention has been paid to the characterisation of any potential ceramic/encapsulation interaction.

The majority of silicon nitride ceramics fabricated within the constraints of the current program possess a fine β-Si_3N_4 grain microstructure with relatively low levels of intergranular matrix phase, when compared with pressureless-sintered materials. Investigation of the post-HIP ceramic/encapsulant interaction for the various encapsulation routes has led to the formulation of several related reaction mechanisms that are dependent upon specific processing variables. The major factors that control and prevent reaction between the ceramic and encapsulant can be summarised as follows:

- Any reaction is reduced or removed by the use of an inert, intermediate barrier layer to isolate the ceramic and encapsulant, eg. hexagonal boron nitride. Typically the retention of a BN interlayer greater than 50μm after HIP inhibits the formation of any interaction layer, leaving a β-Si_3N_4/glass surface structure visually identical to the bulk ceramic.

- The pre-HIP ceramic state determines the type of interaction that can occur. For dense Si_3N_4 HIPed without an inert barrier layer the reaction mechanism is

analogous to the 'active' oxidation of the ceramic. With the HIP densification of 'green' state silicon nitride a diffusive interaction can occur that alters the surface reprecipitation product, formed during liquid phase sintering, from β-Si_3N_4 to Si_2N_2O because of a localised increase in oxygen content of the sintering medium.

- When a diffusive interaction does occur, the degree of surface reaction is dependent upon the ceramic intergranular phase composition/viscosity (ie. the ionic diffusion transport rate), in a similar manner to silicon nitride oxidation. Additionally the level of interaction is controlled by the encapsulant composition. The role of the encapsulant glass is of particular importance, especially when using borosilicate type glasses. The interaction of the Si^{4+} and O^{2-} ionic species, present in borosilicate glass, with the ceramic substrate can be easily observed. However, the possible presence of the highly mobile B^{3+} cation within the HIPed ceramic cannot be detected with any ease, particularly when only trace concentrations arise. An assessment of the potential boron contamination level has been conducted during the current research program. Semiquantization of the boron concentrations throughout a selection of silicon nitride ceramics, HIPed in a Pyrex-type borosilicate glass at ASEA, have been made using a relatively new mass-spectrometry technique (described in 6.6). Large increases in boron levels were detected near to the ceramic surface in some samples, and the potential effect of this interaction on high temperature material properties will be discussed in the following chapter.

6.9. CERAMIC JOINING BY HIP IN SILICA TUBE: LCS 201

The requirement for fabricating dense, complex-shaped silicon nitride parts often includes the need for joining separate components via the formation of a ceramic-ceramic bond. The use of both high temperature and pressure during HIP allows the possibility of mating individual components to one another. HIP bonding was briefly

examined during the current programme, using densified silicon nitride samples. The ceramic pieces (LCS 201 type ceramic) were surface finished to ~ 6μm and encapsulated in SiO_2 as described in section 5.2.1.

The two sections of LCS 201 Si_3N_4, encapsulated in SiO_2 tube, were successfully bonded together by HIP. The post-HIP bulk microstructure was identical to the HIPed 201 described in section 6.2.2. The bond region of the two pieces was distinct from the bulk material as it consisted of a mainly α'-Si_3N_4/glass microstructure (fig. 6.25a,b) of an approximately consistent thickness of 10μm. There was no observable β'-Si_3N_4 present within the bond layer, however some isolated porous regions were apparent and the glass volume was considerably lower than the bulk material (fig. 6.25c).

It is proposed that capsule failure occurred during the hold segment of the HIP cycle (ie. during bond formation) and N_2 gas ingress occurred.

The formation of α' crystals at the bond interface arises because of the high gaseous nitrogen potential at the ceramic surface, after capsule failure. This behaviour has previously been described in section 4.2.6 and is comparable to the formation of α' at the surface of as-received LCS 201 (formation mechanism described by Mason [183]).

The higher porosity level remaining in the bond region after HIP is presumably caused by entrapped N_2 gas between α' crystals and possibly from loss of gaseous SiO from β', as reported by Mason [183], although this is likely to be inhibited under the high nitrogen pressure used.

a

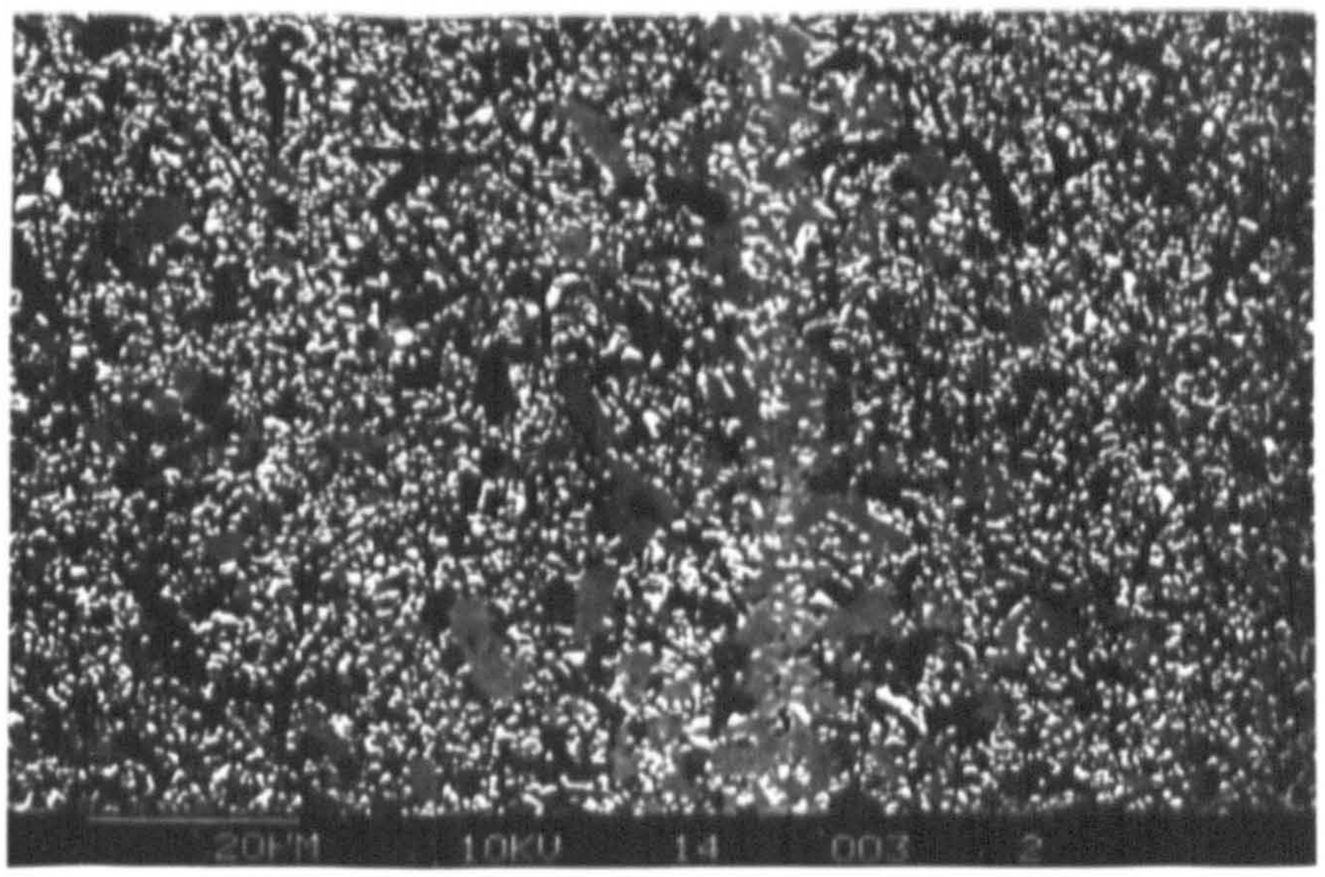

b

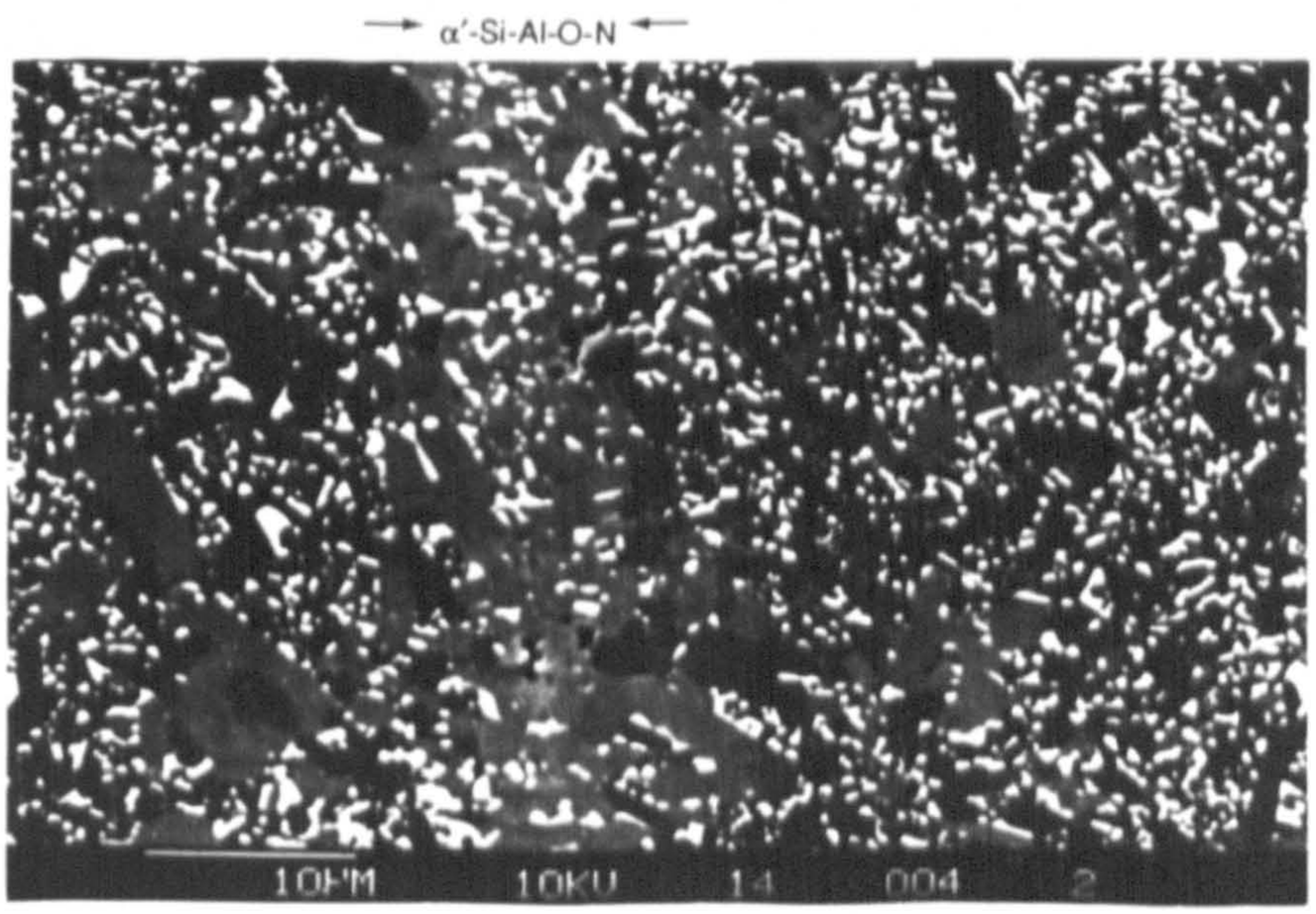

c

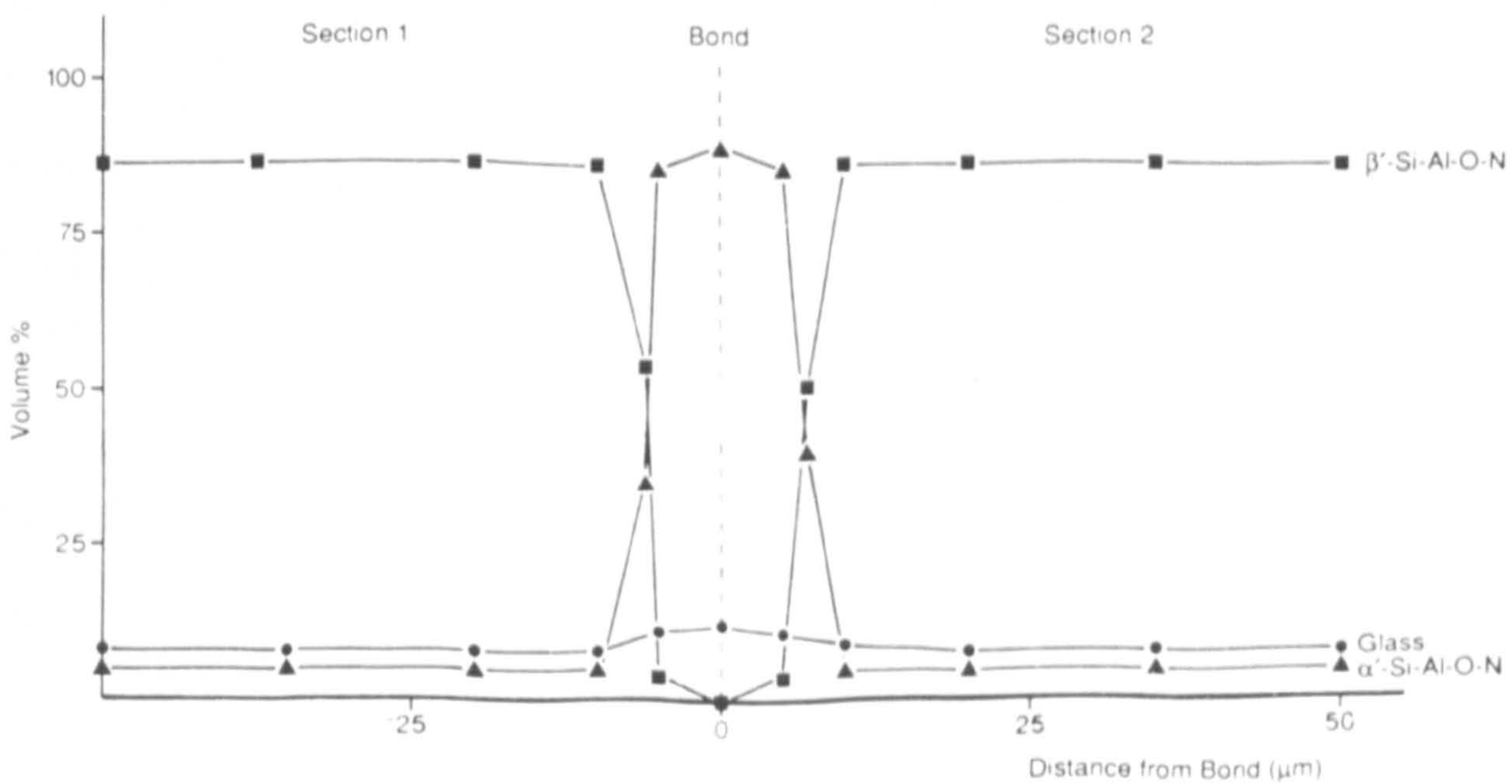

Figure 6.25 a) SEM micrograph of HIP-bond formation in HIPed Lucas 201, showing b) predominately α'-Si-Al-O-N formation in the bond region. c) Schematic representation of phase composition across the HIP-bond.

CHAPTER SEVEN

THE MICROSTRUCTURAL STABILITY OF β-Si_3N_4/$Y_2Si_2O_7$ CERAMICS IN AN OXIDISING ATMOSPHERE

7.1. INTRODUCTION

This chapter describes the mechanism and kinetics of oxidation of a range of fully crystalline β-Si_3N_4/$Y_2Si_2O_7$ ceramics, with a varying level of Si_2N_2O, densified via the technique of hot isostatic pressing (HIP) at ASEA Cerama. The materials used have previously been described in section 6.6. Passive oxidation was performed over the temperature range 1200°C - 1450°C. The microstructure of the oxidised ceramics is described in detail, with relation to both the surface oxide structure and the sub-oxide stability. Particular attention has been paid to the variation in oxidation behaviour of the cut bulk and as-received HIPed surface of the densified ceramics, with a view to assessment of the surface behaviour of net-shaped components after HIP. The aim has been to correlate any variation with the surface ceramic/encapsulant interaction, described in the previous chapter.

7.2. OXIDATION MEASUREMENT

The resistance of the ASEA HIPed materials to passive oxidation was examined by heat treatment in a high volume, low thermal mass furnace (Lenton). Circular sections (1.5 - 2 mm in thickness) were cut from the as received HIPed billets B1-B7 using a diamond slitting wheel (1 mm thick) on a Jones and Shipman surface grinder. Each section was surface finished to ~6 μm. After polishing, the circular discs were halved using an annular diamond saw. During oxidation each specimen was placed on two SiC knife edge supports, which, in turn, were held in an inverted, notched section of mullite tubing.

Oxidation testing was conducted at temperatures between 1200 and 1450°C.

Measurement of oxidation kinetics was made for each composition over the temperature range 1350-1450°C, by heat treatment for periods of 12, 24, 48 and 100 hours followed by subsequent examination of the oxide scale thickness. Examination of scale thickness was conducted for both the original specimen surface and the cut and polished bulk surface.

7.3. OXIDATION BEHAVIOUR

7.3.1. Bulk Cut Surface

Oxidative heat treatment of sections of compositions B1 to B7 produced no detectable oxide scale at the bulk cut surface after oxidation at 1200°C for 100 hours.

The cut bulk oxide scale formation for ceramics B1 to B7 was generally similar for each of the studied temperatures in the range 1350°C - 1450°C. The variation in oxide scale thickness with temperature is shown in section 7.4, describing the cut-bulk and surface oxidation kinetics.

Due to the similarity in observed oxidation behaviour of ceramics B1 - B7 over the temperature range 1350°C - 1450°C a summary of the principle structural developments will made.

The oxide scale thickness, for all compositions B1 to B7, was relatively consistent over the whole exposed cut bulk surface for each exposure time and temperature, with a maximum scale thickness of 6-7μm formed after 100 hours at 1450°C.

After a short term exposure at 1350°C for 12 hours a thin oxide scale was formed, 1-2μm in thickness, consisting almost entirely of de-vitrified SiO_2 (the low temperature α-cristobalite form, from XRD after oxidation) with small isolated regions of $Y_2Si_2O_7$ growing at the oxide scale surface (fig. 7.1a). The oxide scale formed after extended heat treatment (>24 hours) revealed an increase in the volume of $Y_2Si_2O_7$ relative to SiO_2,

a

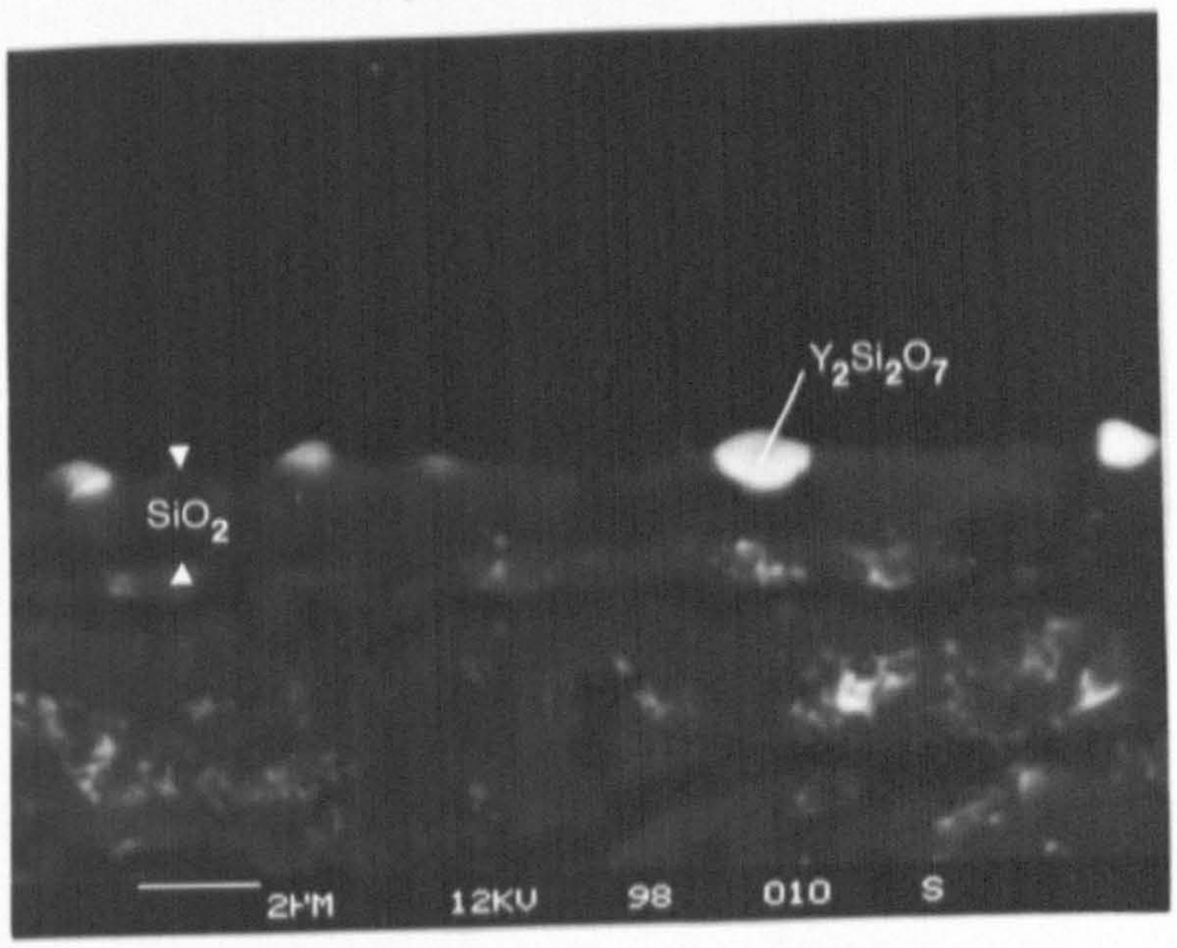

b

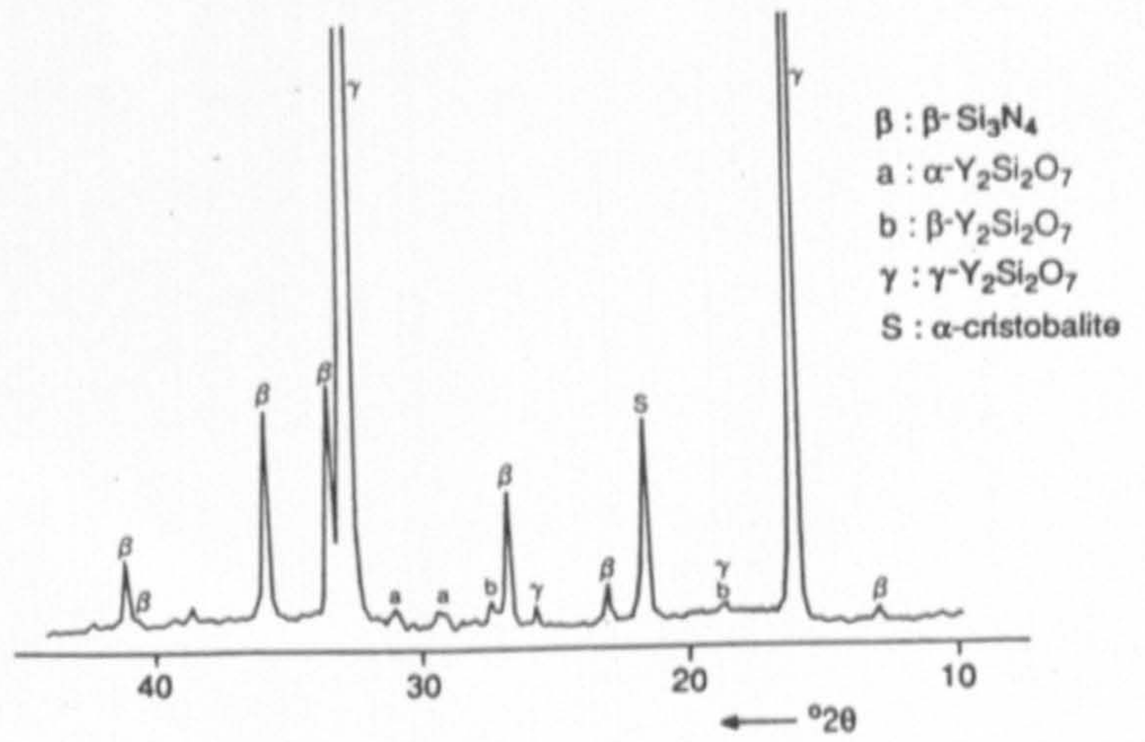

c

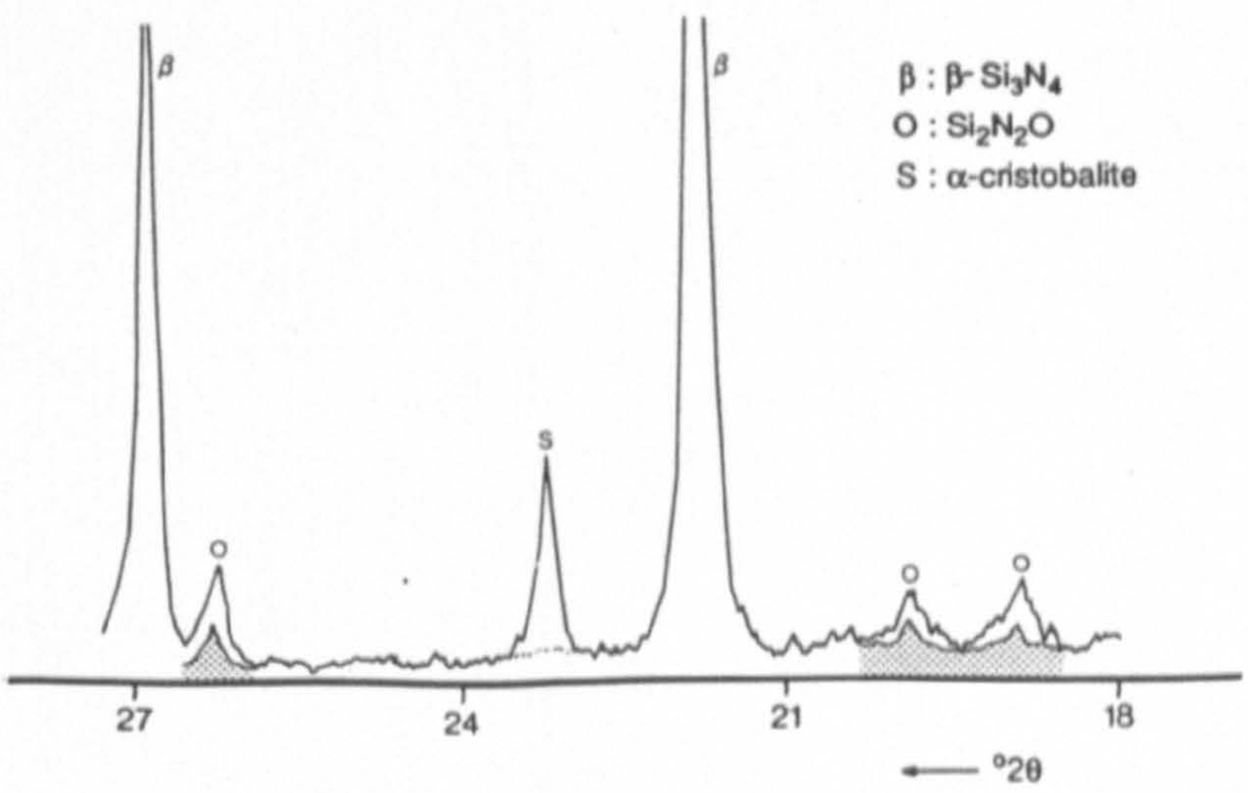

Figure 7.1 a) SEM micrograph of the cut-bulk oxide scale formed on ceramic B1, demonstrating the formation of SiO_2 (dark phase) and $Y_2Si_2O_7$ (light phase) after exposure at 1350°C for 12 hours. b) XRD demonstrates the extreme degree of preferred growth alignment of γ-$Y_2Si_2O_7$ (ceramic B1 heat-treated at 1450°C for 100 hours). c) XRD of ceramic B2, exposed at 1450°C for 100 hours, reveals the formation of Si_2N_2O in the sub-surface region (overlayed is the bulk XRD trace of the as-received ceramic, showing a lower Si_2N_2O level).

which appears to saturate after 48 hours. Further increases in the duration of oxidation produces only minimal variation in the oxide scale microstructure. A general view of the oxidation behaviour, for all exposure times at 1350°C, revealed that the SiO_2 to $Y_2Si_2O_7$ ratio increased with increasing oxygen content in the starting powders, most notably in the oxide scale of specimens B3, B4 and B7.

Oxidation at 1400°C and 1450°C produced generally similar results to those observed in the lower temperature regime. The SiO_2:$Y_2Si_2O_7$ ratio in the bulk oxide scale again increased with increasing ceramic oxygen content from B1 (~1:1) to B4 (~2:1), although the trend was less apparent for B5 to B7.

Analysis of XRD data obtained for compositions B1 - B7 after oxidation at temperatures between 1350°C and 1450°C showed a general trend relating the $Y_2Si_2O_7$ polymorph type, crystallising in the oxide scale, to both the oxidation temperature and initial ceramic oxygen content. A summary of the $Y_2Si_2O_7$ polymorphs formed at different oxidation temperatures for compositions B1 to B7 is presented in Table 7.1. It is apparent that increasing the starting powder oxygen content leads to the preferred formation of higher temperature $Y_2Si_2O_7$ polymorphs. Increasing the oxidation temperature to 1400°C leads to crystallisation of γ-$Y_2Si_2O_7$ in the oxide scale of all ceramics (except B1), with the percentage of γ-$Y_2Si_2O_7$ increasing with increasing ceramic oxygen content. Negligible α- or β-$Y_2Si_2O_7$ was formed at 1450°C, with only γ-$Y_2Si_2O_7$ detected for all types B1 to B7 (fig. 7.1b). A strong degree of growth alignment was observed for the γ-$Y_2Si_2O_7$ polymorph, with principle reflections from the (020), (040) and (060) planes. It is presumed that growth of the γ-$Y_2Si_2O_7$ occurs perpendicular to these planes, with growth into the oxide scale towards the ceramic.

The formation of y-$Y_2Si_2O_7$ in the oxide scale of ceramic B1 (at 1350°C) may be indicative of the presence of boron in the subsurface ceramic. The y-$Y_2Si_2O_7$ phase is not polymorphic with the other $Y_2Si_2O_7$ forms observed during oxidation, and is believed

to be an impurity stabilised yttrium silicate form, with a general formula $RY_5Si_6O_{21}$ (where R is a stabilising cation) [198]. This impurity containing yttrium silicate has been reported to form during the low temperature oxidation of silicon nitride densified with Y_2O_3 [198,199]. It is possible that the y-$Y_2Si_2O_7$ oxidation product formed, additionally to α-$Y_2Si_2O_7$, is stabilised by impurity boron present in composition B1 (described in section 6.6). The y-$Y_2Si_2O_7$ yttrium silicate form was also identified as a matrix phase in some additional billets of composition B1 HIPed at ASEA and examined by Dr. G. Leng-Ward [167].

Analysis of the XRD data obtained for compositions B1 to B7 after oxidative heat treatment at 1450°C for 100 hours revealed an increase in silicon oxynitride (Si_2N_2O) content in the sub-surface ceramic (fig. 7.1c). This behaviour was most apparent in composition B1, with no Si_2N_2O originally detected in the bulk ceramic using XRD.

Oxidation	Composition						
temp. (°C)	B1	B2	B3	B4	B5	B6	B7
1350	y,α	α,(β)	α,(β)	α,β	α,(β)	α,(β)	α,β
1400	α,(β)	α,(γ)	β,(γ)	β,γ	β,(γ)	β,γ	(β),γ
1450	(β),γ	(β),γ	(β),γ	(β),γ	(β),γ	(β),γ	(β),γ

Table 7.1 Summary of $Y_2Si_2O_7$ polymorph crystallising at surface

7.3.2. Oxide Scale Development at the HIPed Ceramic Surface: Dependence on Encapsulant Material

Oxidative heat treatment of all ceramics B1 to B7, at 1200°C for 100 hours did not produce an observable oxide scale at the as received surface when examined in cross section.

Generally the surface oxide scale was thicker than that of the bulk cut surface, after oxidation at 1350° for between 12 and 100 hours, typically by a factor of two or more. The composition of the surface scale of all ASEA processed specimens was found to

vary more obviously than that of the bulk. After oxidation for 12 hours the oxide scale was mainly amorphous with fine $Y_2Si_2O_7$ platelets growing within it (fig. 7.2a). The scale composition was dominated by surface impurities present prior to heat treatment. As previously described (section 6.6.5), the surface impurities predominantly arise from contamination of the ceramics by the encapsulant glass during HIPing. The amorphous content of the oxide scale varied in composition and thickness considerably from one area to another for each composition.

Isolated regions of increased scale thickness, to a maximum of 20 to 30 μm, were analysed to be of the approximate average composition:

$$Si_2Ba_{1.0}Al_{0.1}Ca_{0.1}K_{0.08}Y_{0.2}O_{5.4}$$

for B1, with the elements Ba, Al, Ca and K probably arising from the encapsulant. Higher and lower barium levels were present in the regions of oxide scale build up in all ceramics B1 to B7 and the overall concentration is dependent upon the size and frequency of occurrence of the barium silicate regions present on the surface of the as received ceramics, described in section 6.6.5. Certain areas of the amorphous regions of the oxide scale were found to be relatively free from barium contamination, with the average composition being:

$$Si_2Al_{0.08}Ca_{0.04}K_{0.08}Ba_{0.02}O_{4.2}$$

(fig. 7.2b). The lack of barium in these regions of scale is simply ascribed to an absence of barium silicate from the corresponding surface region of the as-received ceramic.

After oxidation for 24 hours a high proportion of the amorphous phase had crystallised to the low temperature SiO_2 form, α-cristobalite, which nucleated at the ceramic surface with subsequent growth into the oxide scale. The crystallised SiO_2 was globular in appearance (fig. 7.2b). With prolonged oxidation the $Y_2Si_2O_7$ level in the oxide scale had increased and the thin platelets were evenly distributed throughout the scale. The composition of the amorphous barium silicate-based phase was close to that analysed for

a

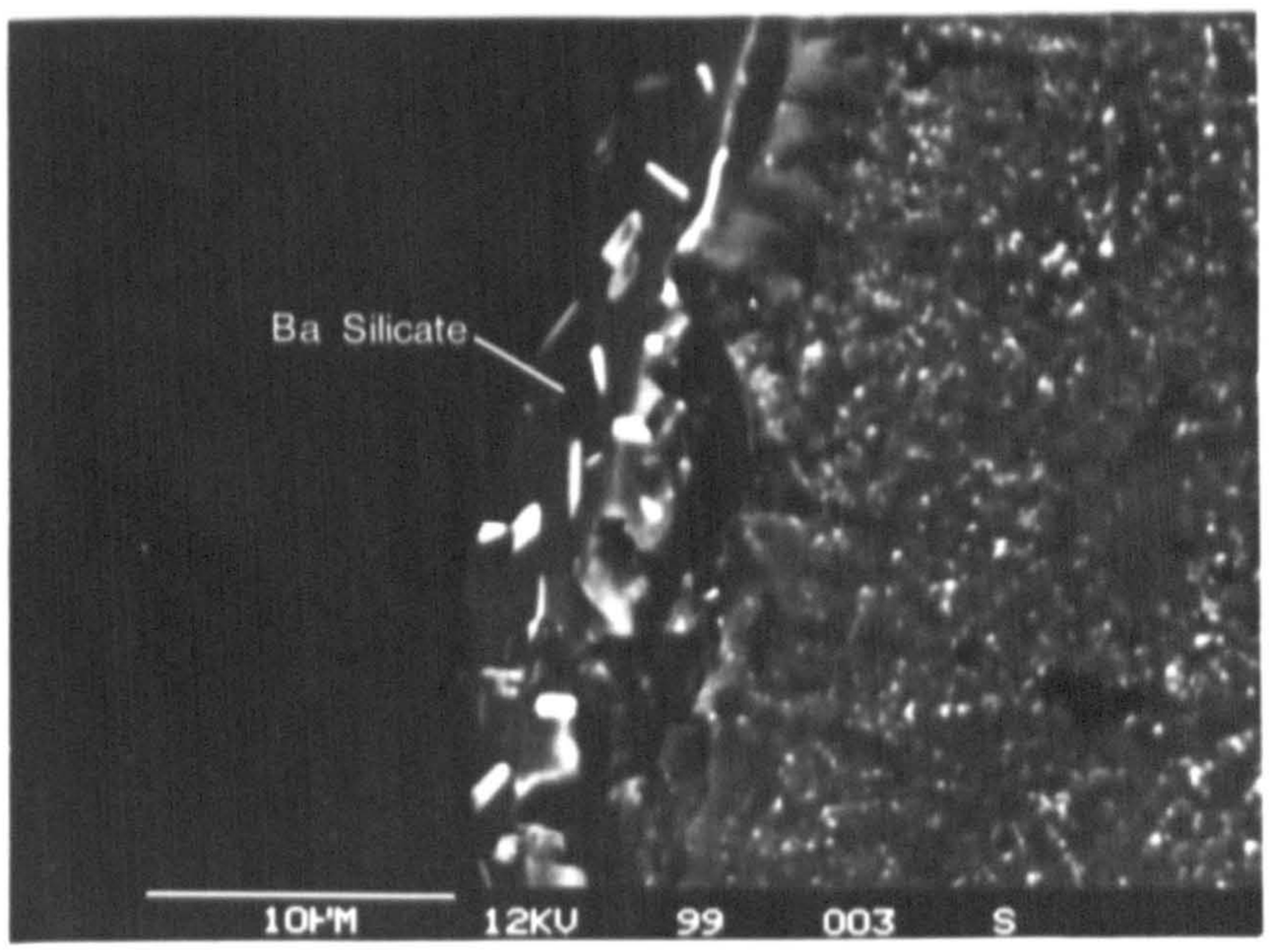

b

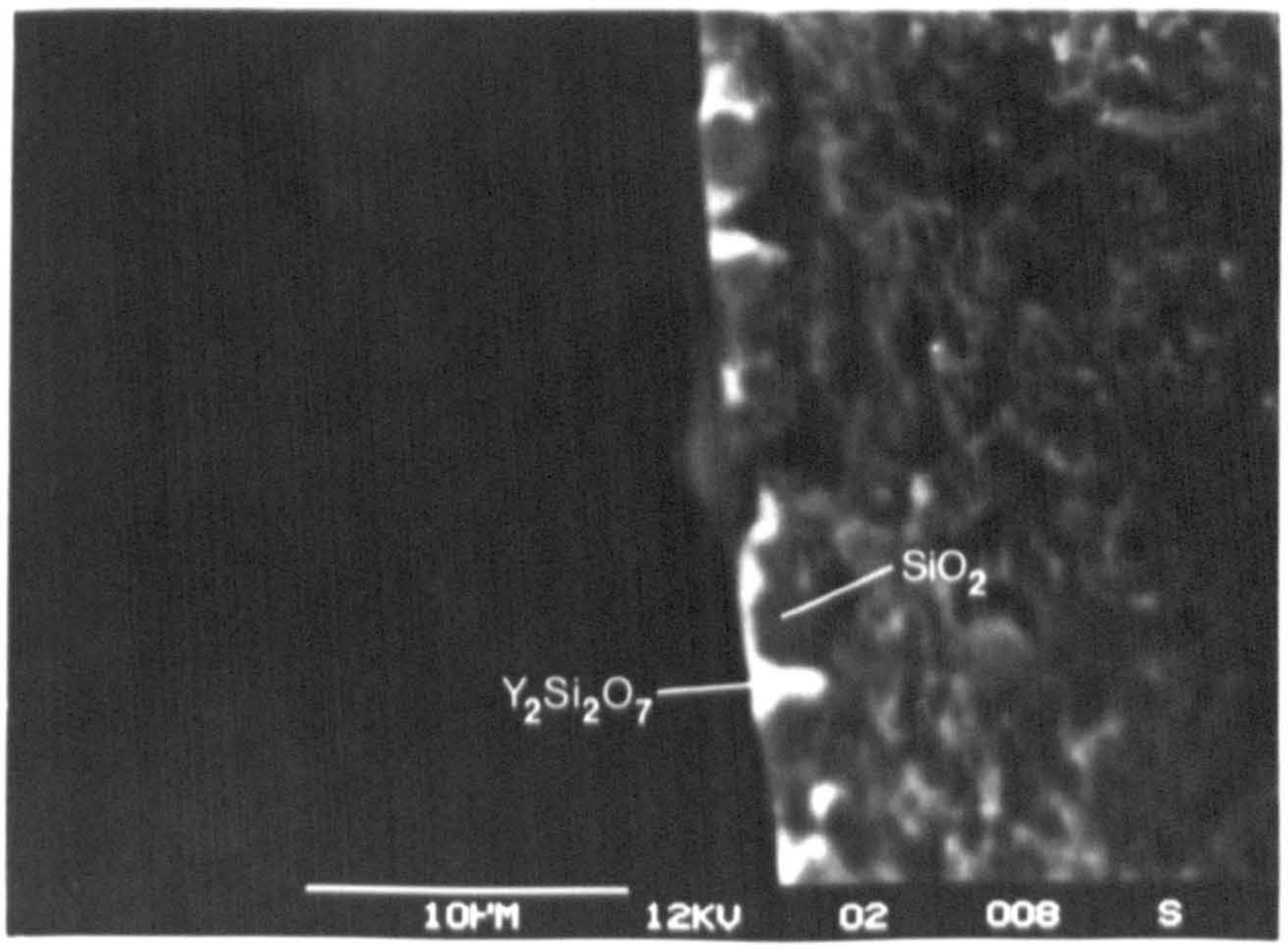

Figure 7.2 a) SEM micrograph of the surface oxide scale formed after oxidation at 1350°C for 12 hours (B4). b) SEM micrograph of 'Ba-free' region of surface scale (B4).

the short term oxidation (12 hours).

Oxide scale formation at the specimen surface (for B1 to B7) after heat treatment at 1400°C was similar in structure to that formed at the lower temperature (1350°C). After the initial period of oxidation (12 hours) a largely amorphous scale was observed, with an average composition of:

$$Si_2Al_{0.08}Ca_{0.06}Y_{0.01}Ba_{0.5}O_{4.8}$$

for specimen B1. It must be noted that the average barium content varied slightly for each composition, depending on the level of contamination on the surface of the as-received materials. Certain areas of the continuous amorphous oxide scale were totally devoid of barium contamination, with an average composition:

$$Si_2Al_{0.16}Ca_{0.02}K_{0.12}O_{4.4}$$

Small levels of magnesium were occasionally detected, however these were considerably lower than the noted calcium level. Small, fibre-like $Y_2Si_2O_7$ crystals were present within the amorphous scale. After prolonged oxidation (24 hours) a globular SiO_2 layer had nucleated at the ceramic surface and $Y_2Si_2O_7$ had generally formed at the oxide scale surface, a large amorphous residue remained in barium rich regions. Near complete crystallisation of the oxide scale occurred in regions where the barium level was low, leaving an impurity (Ca, K, Al) enriched residue (fig. 7.3a). Continued growth of SiO_2 was apparent for further extension of the oxidation duration such that, after oxidation for 100 hours at 1400°C, a semi-continuous SiO_2 layer was present (fig. 7.3b). Small globular regions of $Y_2Si_2O_7$ stoichiometry, analysed by microanalysis, were observed to have formed beneath the impermeable SiO_2 layer isolating this layer from the ceramic. Where a discontinuity arose in the SiO_2 layer the $Y_2Si_2O_7$ 'build up' was not present, however, excessive $Y_2Si_2O_7$ growth at the oxide surface was generally apparent, directly aligned with the void within the cristobalite layer.

The surface oxide scale development, during oxidation at 1450° for short time periods (<48 hours), was essentially identical to the behaviour at 1400°C. Extending the oxidation period resulted in the formation of a coherent SiO_2 layer, growing into the oxide scale, over the whole specimen surface. A continuous layer, of analysed composition $Y_2Si_2O_7$, had formed below the SiO_2 layer after oxidative heat treatment for 100 hours. The $Y_2Si_2O_7$ layer, which was more uniform than that formed after oxidation at 1400°C for 100 hours, was observed to have penetrated through the SiO_2 in isolated regions (fig. 7.4).

7.4. OXIDATION KINETICS OF ASEA HIP'ED CERAMICS

The extent of oxidation for all seven ceramic compositions were measured over temperatures between 1350°C and 1450°C. There appeared to be an approximately linear increase in oxide scale thickness with increasing oxidation temperature for equivalent exposure periods. No trend was apparent with respect to oxide thickness and compositional variation, with a reasonably consistent oxide scale thickness occurring after identical oxidation conditions for all specimens. The oxidation kinetics of the cut bulk and surface of all ceramics B1 to B7, determined by measurement of oxide scale thickness, are presented in figures 7.5 and 7.6 respectively. Oxidation rate exponents, n, were calculated for all the specimen temperature variations using the formula:

$$d^n = kt \qquad (7.1)$$

where d is the scale thickness, t the oxidation time and k is the oxidation rate constant. Generally kinetics approximating to parabolic were obtained for ceramics B1 to B7, with oxidation exponents calculated in the range 1.4 to 3.0 and rate constants in the range 0.1 to 2.5 $\mu m^2 h^{-1}$. The observation of parabolic kinetics implies a steady state cross-diffusion of ionic species during oxidation, with negligible rate variation. Non-parabolic oxidation kinetics were apparent for some areas of the surface oxide scale, where the relative barium concentration was highest. The observation of non-parabolic kinetics is

a

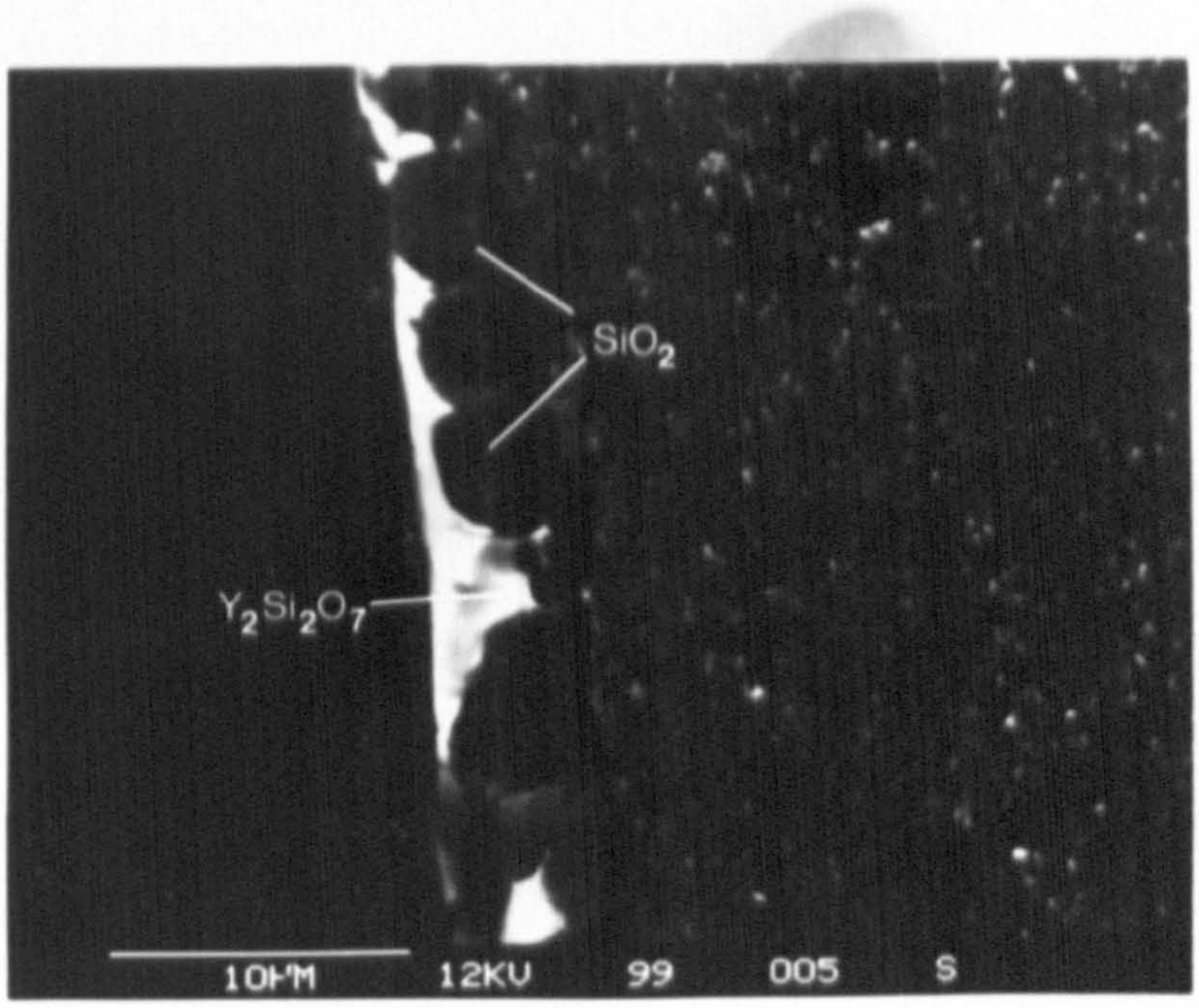

b

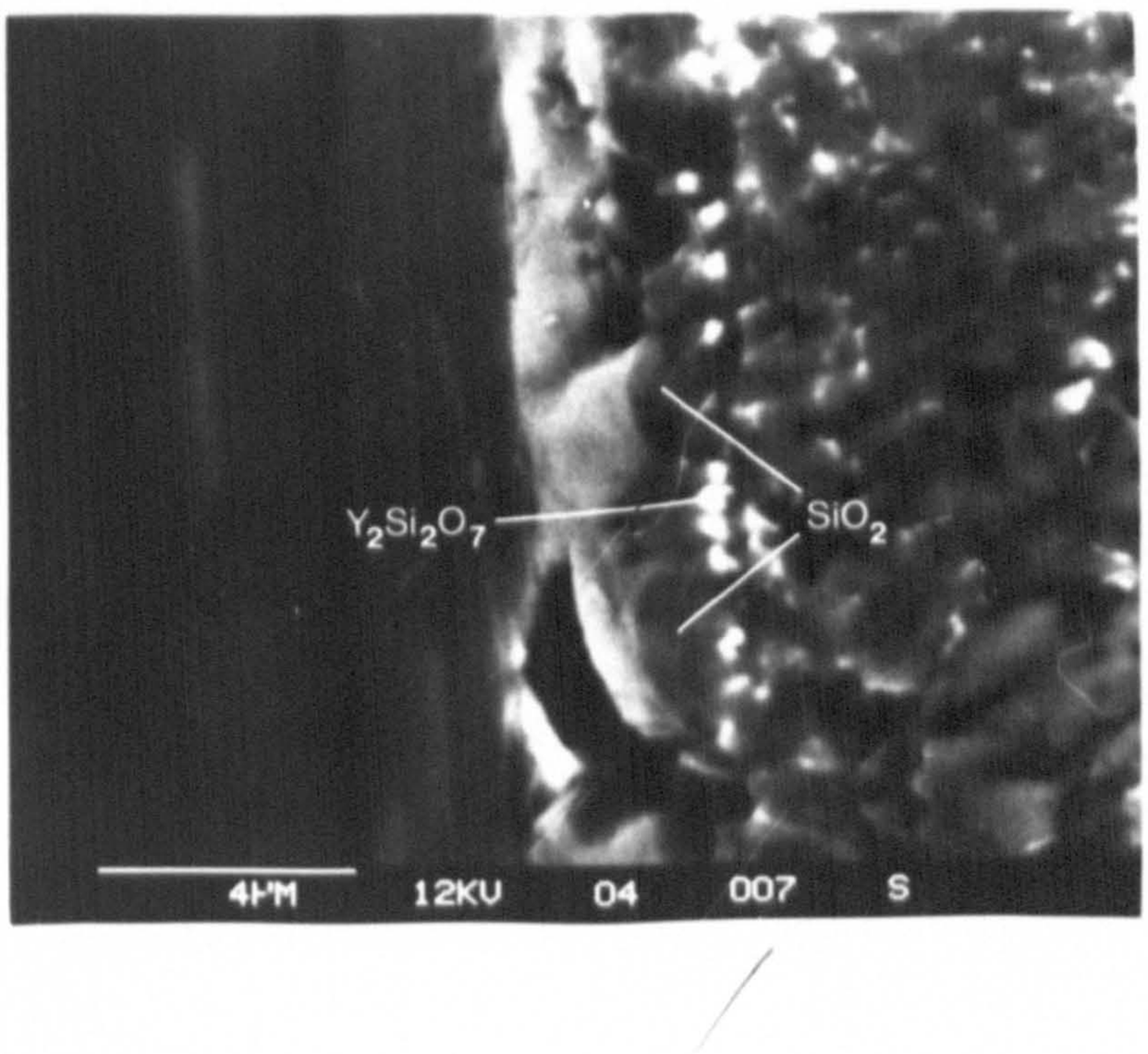

Figure 7.3 a) SEM micrograph demonstrating near-complete crystallisation of the surface oxide scale in regions of low impurity content (B1 heat-treated at 1400°C for 48 hours). b) SEM micrograph of SiO_2 layer formation at ceramic surface, with underlying $Y_2Si_2O_7$ regions (B1).

a

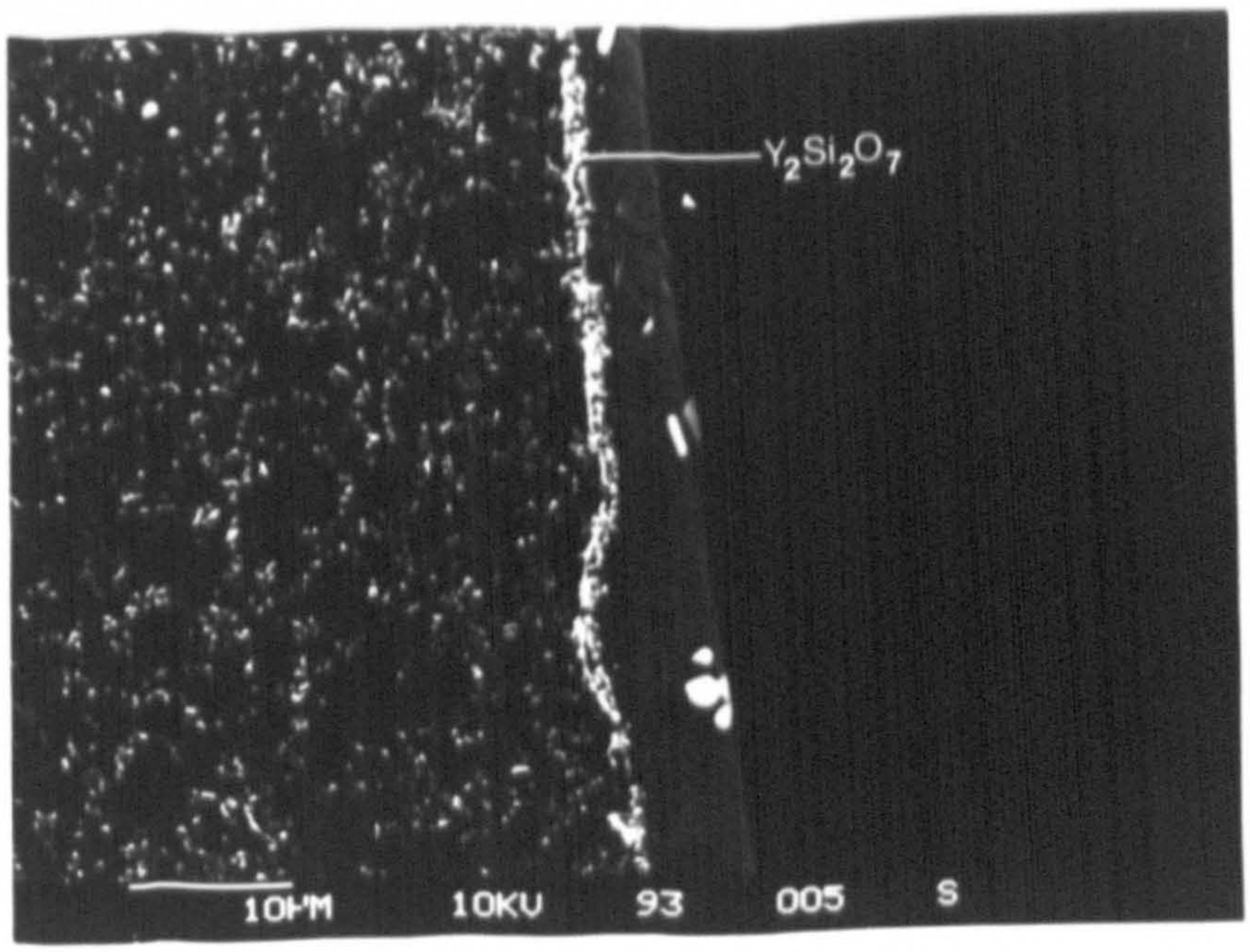

b

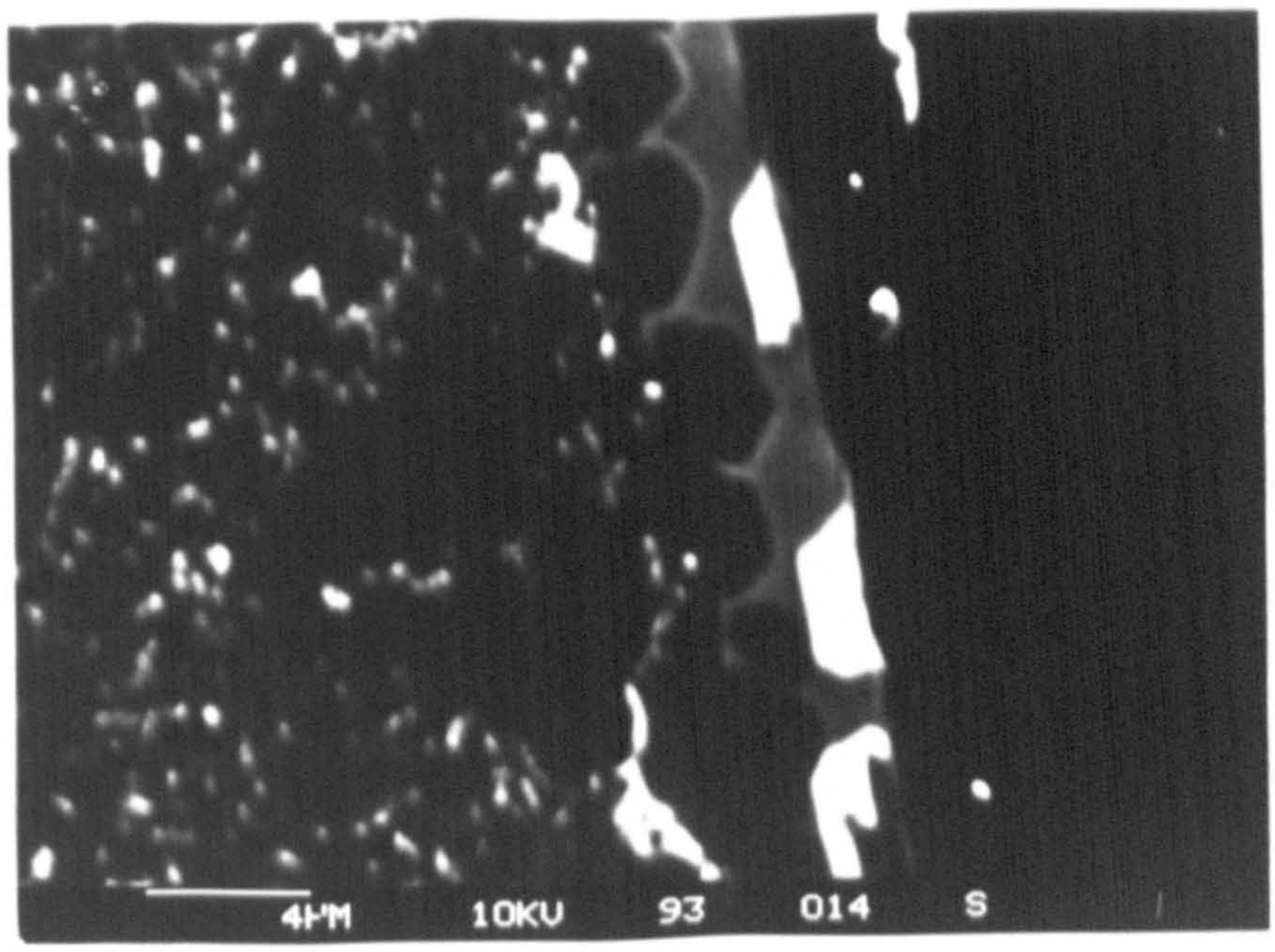

Figure 7.4 a) SEM micrograph showing the formation of a continuous $Y_2Si_2O_7$ layer below the SiO_2 layer previously nucleated at the ceramic surface (B2 heat-treated at 1450°C for 100 hours). b) SEM micrograph showing penetration of $Y_2Si_2O_7$ through discontinuity in SiO_2 layer (B2 heat-treated at 1450°C for 100 hours).

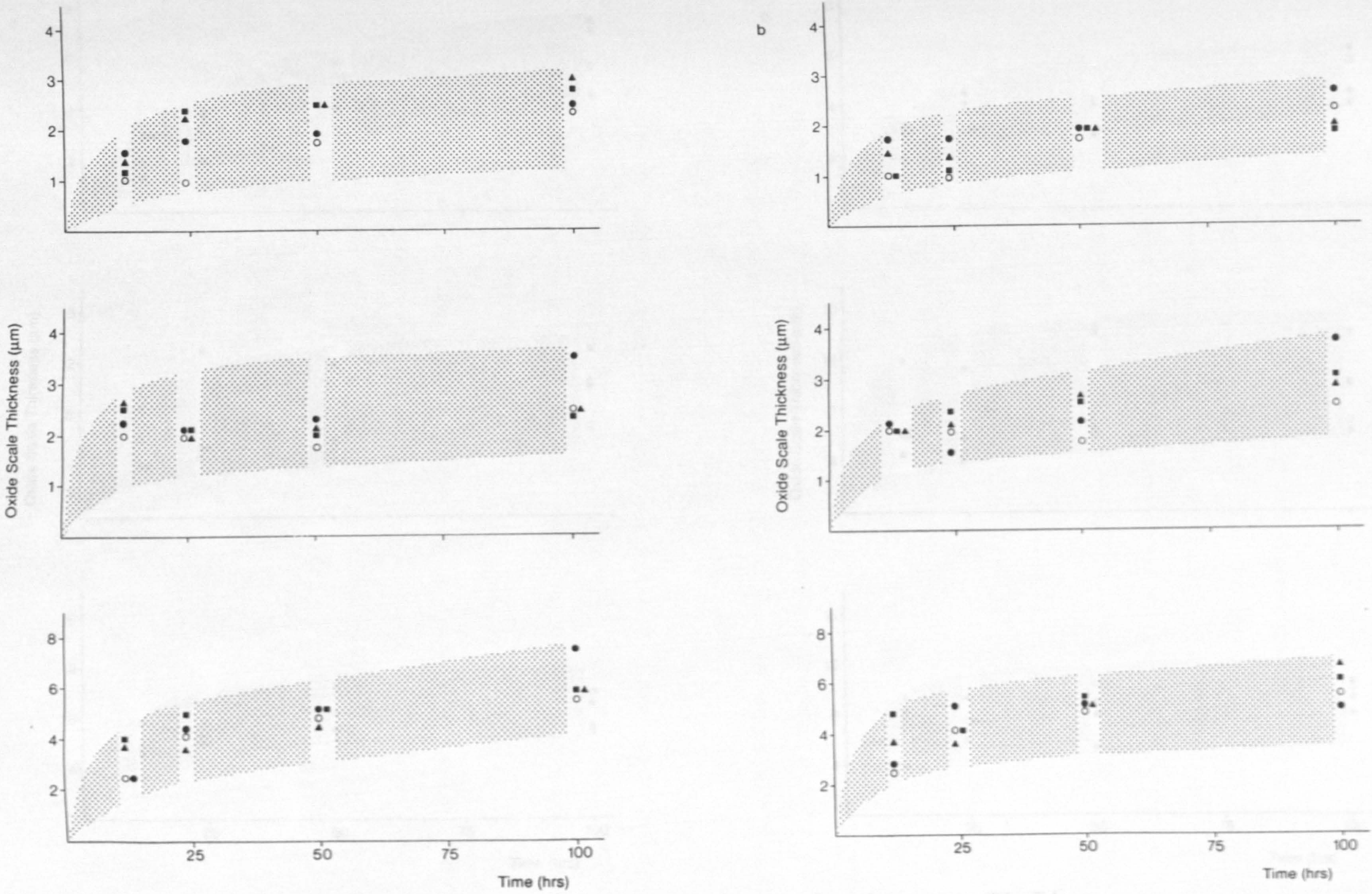

Figure 7.5 Oxide scale thickness measurements for the cut-bulk of a) ceramics B1 - B4, and b) ceramics B5 - B7 (with B1 for reference). Composition key: B1 - ○, B2 - ●, B3 - ■, B4 - ▲, B5 - ● B6 - ■ and B7 - ▲

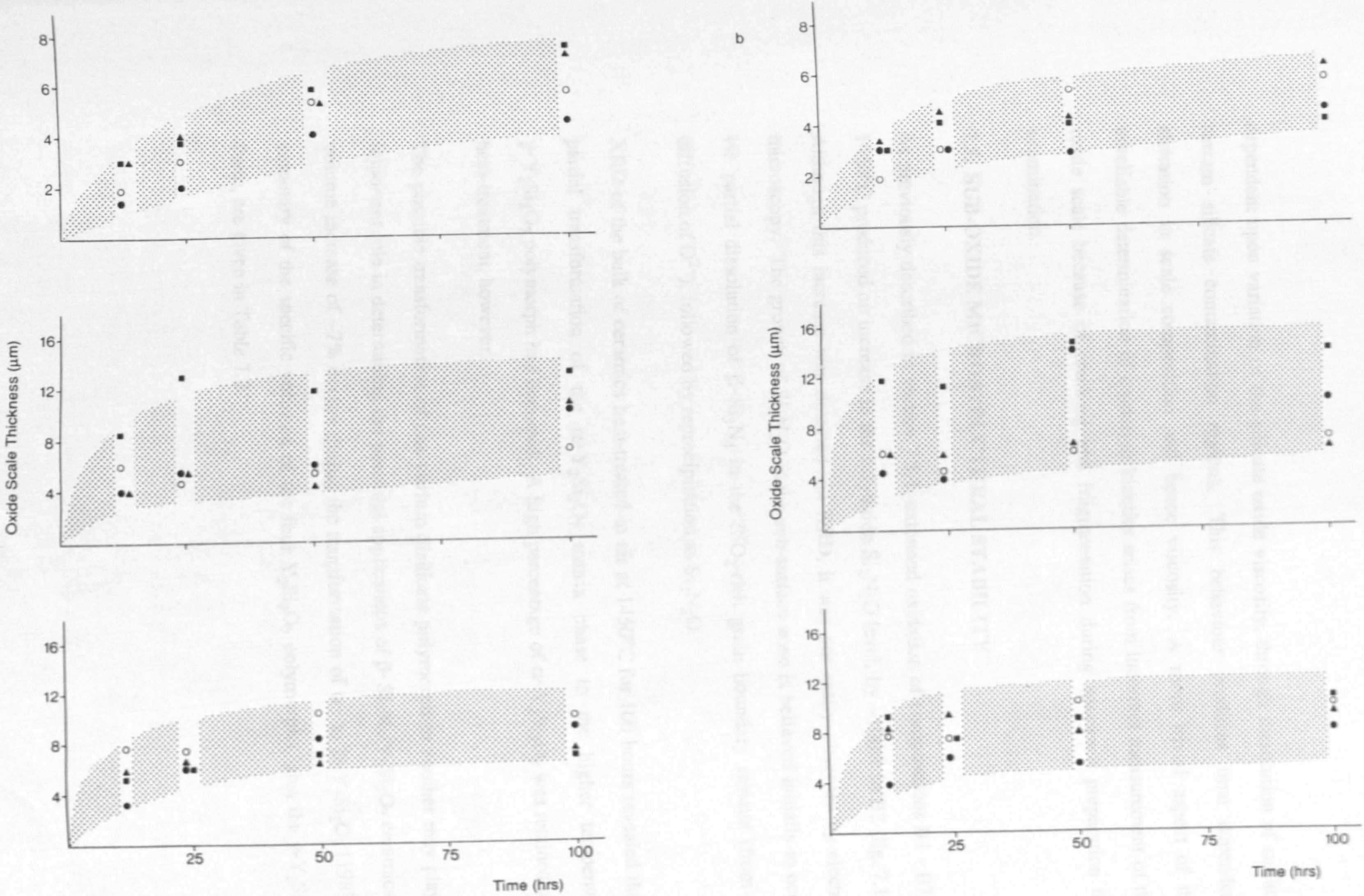

Figure 7.6 Oxide scale thickness measurements for the surface of a) ceramics B1 - B4, and b) ceramics B5 - B7 (with B1 for reference). Composition key: B1 - ○, B2 - ●, B3 - ■, B4 - ▲, B5 - ●, B6 - ■, and B7 - ▲.

dependent upon variation of the silicate oxide viscosity, through dissolution of surface barium silicate contamination regions. This behaviour produces time dependent alteration in scale composition and hence viscosity. A more trivial aspect of the unreliable determination of oxidation kinetics arises from incorrect measurement of the oxide scale because of cracking and fragmentation during specimen preparation for examination.

7.5. SUB-OXIDE MICROSTRUCTURAL STABILITY

As previously described in section 7.3.1, extended oxidation of compositions B1 - B7 at 1450°C produced an increase in the sub-oxide Si_2N_2O level, by ~100% in B2 (fig. 7.1c). Although this increase was detected via XRD, it was not easily observed by electron microscopy. The growth of Si_2N_2O in the sub-surface zone is believed initially to occur via partial dissolution of β-Si_3N_4 in the SiO_2-rich grain boundary residue (from in-diffusion of O^{2-}), followed by reprecipitation as Si_2N_2O.

XRD of the bulk of ceramics heat-treated in air at 1450°C for 100 hours revealed that a partial transformation of the α-$Y_2Si_2O_7$ matrix phase to the higher temperature γ-$Y_2Si_2O_7$ polymorph had occurred. A high percentage of α-$Y_2Si_2O_7$ was retained after heat-treatment, however.

The possible transformation of one yttrium disilicate polymorph to another may play an important role in determining the potential applications of β-Si_3N_4/$Y_2Si_2O_7$ ceramics. A volume increase of ~7% occurs during the transformation of α- to β-$Y_2Si_2O_7$ [198]. A summary of the specific volumes of the four $Y_2Si_2O_7$ polymorphs, plus the y-$Y_2Si_2O_7$ form, are given in Table 7.2.

Polymorph form	Structure	Specific vol. (Å)³
α	Triclinic	133.6
β	Monoclinic	142.5
γ	Monoclinic	142.2
δ	Orthorhombic	139.8
y	Monoclinic	140.7

Table 7.2 The specific unit cell volumes for the $Y_2Si_2O_7$ polymorphs (after reference [198])

Volume changes are also observed during the low temperature oxidation (~ 1000°C) of certain crystalline Y-Si-O-N quaternary phases (discussed in section 1.5.1, table 1.6), although they are generally greater (up to 30 vol.%). The increase in volume of these phases, which crystallise either during fabrication of subsequent oxidative heat-treatment, has been shown to lead to specimen disintegration [60]. Further study is therefore required to assess the stability of different $Y_2Si_2O_7$ polymorphs during extended heat-treatment.

7.6. OXIDATION MECHANISM: DISCUSSION

The initial stage of passive oxidation of β-Si_3N_4 ceramics involves the direct oxidation of β-Si_3N_4 present at the ceramic surface and proceeds via the well known reaction:

$$Si_3N_{4(s)} + 3O_{2(g)} \longrightarrow 3SiO_{2(s)} + 2N_{2(g)}$$

Evidence of initial silica formation has been readily observed in the range of β-Si_3N_4 (and Si_2N_2O)/$Y_2Si_2O_7$ ceramics currently under examination. A thin SiO_2 based film (1-3 μm in thickness) had formed at the cut bulk surface of all ceramics after short term oxidation (12 hours) at temperatures between 1350 and 1450°C.

The formation of a SiO_2 layer creates a chemical couple between the surface SiO_2 and the glassy grain boundary residue. The chemical diffusion couple occurs because of the relative instability of the two phases at the oxidation temperature arising from the

tendency to form a single equilibrium composition. As the oxidation period progresses the outdiffusing cations (in this instance predominantly Y^{3+} ions) crystallise at the surface of the oxide scale as $Y_2Si_2O_7$ via reaction with Si^{4+} and O^{2-} ions. The formation of crystalline $Y_2Si_2O_7$ and the continued oxidation of Si_3N_4 by O^{2-} indiffusing species maintain a chemical imbalance between the grain boundary and oxide scale glasses during Y^{3+} out-diffusion.

In the case of the β-$Si_3N_4/Y_2Si_2O_7$ ceramics HIPed at ASEA, the SiO_2 layer formed at the cut-bulk surface rapidly crystallises to an α-cristobalite/$Y_2Si_2O_7$ mixture because of the relatively low impurity content of the silicate oxide scale.

The continued oxidation of the surface Si_3N_4 of these ceramics involves the (slow) transport of O^{2-} in-diffusing through the cristobalite layer and at SiO_2 grain boundaries. This is coupled with out-diffusion of Y^{3+} cations. The rate of Y^{3+} out-diffusion will be slow and material transportation through the cristobalite crystals is likely to be extremely slow (if at all) because of relatively large cation size compared to the interstitial volume in the cristobalite structure.

This behaviour is observed experimentally after 100 hour oxidation at higher temperatures (1400°C, 1450°C). The formation of crystalline $Y_2Si_2O_7$ occurs below the SiO_2 crystalline layer, as out-diffusion of the Y^{3+} ions past the SiO_2 is inhibited. Continued transport of O^{2-} ions through the SiO_2 produces further direct oxidation of the sub-scale β-Si_3N_4 and the proposed ensuing reaction leads to the formation of $Y_2Si_2O_7$;

$$2Y^{3+} + 2SiO_2 + 3O^{2-} \longrightarrow Y_2Si_2O_7$$

where SiO_2 arises from oxidation of Si_3N_4.

Gaseous nitrogen formation observed via SEM was minimal at both the cut bulk and surface of oxidised ceramics, which was generally consistent with the low volume oxide scale formed. The out-diffusion rate of nitrogen N^{3-} through the silicate oxide scale is

lower than the rate of in-diffusion of oxygen. Consequently a gradual increase in nitrogen concentration within the scale will occur during continued oxidation. The nitrogen concentration will be dependent upon oxide scale thickness, with gas N_2 evolution eventually occurring when a thick oxide scale is formed (observed when the silicate nitrogen concentration becomes too great to be stably contained within the silicate scale).

An alternative $Y_2Si_2O_7$ formation mechanism involves the interaction of diffusing Y^{3+} and O^{2-} species with the surface oxide SiO_2, in which case the $Y_2Si_2O_7$ layer may act in a protective manner with respect to the Si_3N_4 substrate, and nitrogen evolution will be inhibited.

The surface oxide formation mechanism is generally similar to the cut bulk, although the high surface impurity concentration increases the rate of oxide scale formation. Additionally the growth of a coherent SiO_2 layer, nucleating at the ceramic surface, does not occur as rapidly in the silicate melt (with a high impurity concentration). The lower SiO_2 growth kinetics leads to an increase in the proportion of $Y_2Si_2O_7$ in the silicate scale, with the partial depletion of the ceramic matrix phase occurring in the sub-surface material heat-treated at 1450°C for 100 hours. Matrix depletion arises via reaction between $Y_2Si_2O_7$ and the lower viscosity silicate scale, which leads to an enhancement of the Y^{3+} out-diffusion rate.

7.7. SUMMARY

The HIPed $Si_3N_4/Y_2Si_2O_7$ ceramics studied during the current programme exhibit excellent resistance to passive oxidation with a thin (8-10μm) oxide scale formed after heat-treatment for 100 hours at 1450°C. It is believed that the high purity of the scale formed at the cut-bulk ceramic produces rapid crystallisation of this scale so that it acts in a 'semi-protective' manner. It was apparent that a partial transformation of the α-$Y_2Si_2O_7$ matrix had occurred during relatively long term oxidation. Further study of

this effect upon the sub-oxide microstructural stability is required, paying specific attention to potential volume changes arising through polymorph transformation.

It is apparent that the surface oxidation resistance is not especially inferior to the bulk ceramic. Anomalous oxidation behaviour arose in regions where barium silicate contamination had occurred. Contamination is attributed to interaction with constituents of the encapsulating glass. Some post-HIP diamond machining will be necessary to remove the contaminated surface layer and to obtain the desired surface smoothness. However, the typical amount of material required to be removed would be less than 10μm in thickness to obtain a surface microstructure similar to the bulk material.

Comparison of the oxidation resistance of HIPed β-Si_3N_4/α-$Y_2Si_2O_7$ ceramics with other pressureless-sintered ceramics, for example the commercial Syalon type (eg. LCS 201), demonstrates a substantial increase in operating temperature. Generally, pressureless-sintered silicon nitride ceramics exhibit rapid oxidation at temperatures in excess of 1250°C due to matrix softening and increased ionic transport rates. This temperature limit is increased by approximately 50°C in the commercial β'-Si-Al-O-N/YAG ceramics, LCS 201, where the crystalline YAG matrix helps to reduce ionic transport rates. However at temperatures greater than 1320°C interaction between near-surface YAG and the silicate oxide scale produces oxidation rates comparable with β-Si_3N_4/glass materials [44]. The α-$Y_2Si_2O_7$ matrix, present in the HIPed ceramics studied during the current programme, is stable with respect to the surface silicate scale to temperatures in excess of 1450°C, offering the potential for component usage up to (and possibly exceeding) this temperature.

CHAPTER EIGHT

CONCLUSIONS AND SUGGESTIONS FOR FUTURE WORK

8.1. PROGRAMME GOALS

Several fabrication routes are currently available to the ceramic engineer for the manufacture of dense silicon nitride articles. Unfortunately hot-pressing and pressureless-sintering, the most widely used silicon nitride consolidation processes, both suffer from limitations inherent in the production route. Hot-pressing confines manufacture of densified materials to simple geometries, and pressureless-sintering requires the use of a relatively high volume, low viscosity liquid sintering medium (following the liquid phase sintering mechanism) which plays an important role in limiting the high temperature ceramic properties (eg. creep, oxidation resistance). The relatively new technique of hot-isostatic pressing (HIP) does not suffer from these drawbacks, and the fabrication and subsequent examination of HIPed silicon nitride has formed the focal point of the research presented in this thesis.

The principle aims of this work were to provide a greater insight into the HIP consolidation processes, as applied to silicon nitride based ceramics. The principle aspects that have been investigated are:

- Fabrication techniques for HIP silicon nitride, involving the development of glass encapsulation processes (Chapter 5).

- Microstructural assessment of HIP densified ceramics, paying particular attention to any surface microstructure modification arising from interaction with the glass encapsulant (Chapter 6).

- Examination of the oxidation behaviour of HIPed ceramics (Chapter 7).

- Microstructural and property comparison of pressureless-sintered silicon nitride ceramics with identical materials subjected to a post-sinter HIP treatment (Chapter 4).

The majority of HIPing has been conducted using a laboratory scale HIP system, with some additional samples densified in Sweden using the commercial ASEA process.

8.2. CONCLUSIONS

8.2.1. The Densification of Silicon Nitride by Glass Encapsulated HIPing

A range of encapsulation methods have been developed, generally based on the use of commercially available glass compositions:

a) The simplest of these techniques involves the encapsulation of cylindrical billets of 'green' state silicon nitride within either Pyrex or silica tubing.

Initial samples, encapsulated in silica, were not densified after HIP because of capsule failure during the cycle.

b) The use of Pyrex tube, with considering lower softening temperature, allowed greater flexibility for both the encapsulation process and the subsequent HIP cycle design.

A selection of silicon nitride compositions were HIPed to near theoretical density (> 97% TD) using this encapsulation route. Full densification was inhibited by the build-up of gas pressure within the capsule during the HIP cycle. It is proposed that the internal gas pressure arises from volatilization of the B_2O_3 component from Pyrex, producing gaseous O_2. Volatilization occurs from the internal face of the capsule because of the high capsule vacuum (2×10^{-5} Torr).

c) Glass tube encapsulation only allows the fabrication of relatively simple turned shapes. One solution to this problem involves placement of the shaped article within

Pyrex glass powder (contained in an oversize Pyrex tube).

This procedure was utilized for the densification of rectangular ceramic plates (of unspecified composition) for HIP Ltd., but has not been described in this thesis as the HIPed materials were not characterised at Warwick. A further development, allowing the densification of complex shaped articles, involved the use of particles of Pyrex glass in the form of a powder bed (or 'frit'). The 'green' state ceramic is packed in the glass powder, with both the encapsulation and HIP stages conducted in the HIP system. The final encapsulation stage, glass melting, was performed under partial atmospheric pressure. This was found to inhibit decomposition of the Pyrex glass and full densification (> 99.0% TD) was obtained.

d) A similar technique to the Pyrex powder/tube encapsulation method was developed, allowing encapsulation of silicon nitride within a selection of different glass compositions (whilst still sealed in a Pyrex ampoule and thus using a standard HIP cycle). The powdered compositions used were SiO_2, B_2O_3 and a tailored Y-Si-O-N glass (similar to the ceramic matrix phase composition). Near-theoretical densification was obtained with the SiO_2 encapsulant glass. Densification occurred using the Y-Si-O-N glass, although glass bloating and matrix volume enhancement were apparent in the bulk ceramic. B_2O_3-containing ampoules failed during the early HIP cycle stage through gas pressure build-up.

8.2.2. The Microstructure and Surface Interaction of Glass Encapsulated HIPed Ceramics

a) A generally fine β-Si_3N_4 grain structure was observed in all of the densified ceramics, with the grain scale being finer than equivalent pressureless-sintered materials (apparent for composition A1). Rapid cooling after HIP in the laboratory system prevented crystallisation of the matrix phase in all densified compositions. Conversely, complete crystallisation of the intergranular phase as yttrium disilicate was observed in specimens

HIPed as ASEA, where a slow furnace cool was used.

b) The level of interaction between the ceramic and Pyrex encapsulant was determined to be dependent on several factors.

The use of a boron nitride barrier layer is desirable to avoid surface reaction. No observable interaction was apparent with a BN layer thickness greater than 50μm, for all compositions. When a surface reaction layer had formed, the layer thickness was dependent upon the intergranular phase composition, specifically the glass viscosity. The greatest reaction layer thickness occurred at the surface of composition A1 (~80μm thick), with an Y-Mg-Si-O-N matrix phase, whilst only a thin interaction layer (~5μm) was present for ceramic B1, with a Y-Si-O-N matrix (both examples were measured with a nominal BN layer thickness of 8μm).

c) The mechanism of surface interaction for Pyrex encapsulated specimens was material transport of ionic species through the porous BN interlayer, most notably producing an increase in the SiO_2 concentration at the ceramic surface. The variation in the overall compositional balance at the ceramic surface leads to the preferred re-precipitation of α-Si_3N_4 as Si_2N_2O rather then β-Si_3N_4. Additionally, loss of ionic species from the ceramic matrix phase occurs during HIP, leading to the formation of a glass-free mono-phase Si_2N_2O layer.

d) The interaction occurring with SiO_2 and Y-Si-O-N encapsulant glasses involved penetration of the encapsulant, in the absence of a BN barrier layer, into the porous Si_3N_4 compact. The extent of ceramic/encapsulant interaction is dependent upon the porosity scale of the ceramic, with considerable matrix volume enhancement occurring into the bulk of the lower viscosity Y-Si-O-N glass encapsulated specimen. The penetration of the SiO_2 encapsulant glass produces a silica rich matrix phase and the subsequent formation of Si_2N_2O at the ceramic surface.

e) A similar surface microstructure to the bulk ceramic was observed for the ASEA HIPed materials, however Si_2N_2O formation was apparent, and a low level of Al substitution was detected at the as-received surface (arising from the encapsulant). The mechanism of interaction is identical to the Pyrex tube encapsulated ceramics. Further contamination of the ceramic was observed, with the formation of isolated barium (aluminium) silicate regions on the as-received surface.

The presence of boron within the sub-surface region of ASEA HIPed ceramics was qualitatively detected via the technique of inductively coupled plasma mass spectrometry (ICP/MS). It is currently difficult, however, to assess the location of boron within the ceramic microstructure.

8.2.3. The Oxidation of Fully Crystalline β-$Si_3N_4/Y_2Si_2O_7$ Ceramics

The ASEA HIPed ceramics, with a stable $Y_2Si_2O_7$ matrix phase, possess excellent resistance to (relatively) long term oxidation of the bulk ceramic at elevated temperature (~ 1450°C). Oxidation above 1350°C produces a thin coherent $SiO_2/Y_2Si_2O_7$ oxide scale on all ceramics in the series B1 to B7, with oxidation occurring by the mechanism of simultaneous in-diffusion of O^{2-} and out-diffusion of Y^{3+} and Si^{4+}. The rate-determining process is the out-diffusion of cationic species from the ceramic.

A greater oxidation rate (~ 2 to 3 times the bulk) is apparent at the as-received ceramic surface, where impurity Ba and Al aid the formation of a lower viscosity oxide scale which is largely amorphous, unlike the near fully crystalline bulk scale. Material transport rates are thus increased. It is believed that the presence of low concentrations of boron in the surface and sub-surface region does not greatly influence the surface oxidation rate.

8.2.4. Sinter-HIP Processing

The bulk microstructure of sinter-HIP processed ceramics was generally observed to be identical to the sintered materials. Only minimal grain-coarsening was apparent in any sinter-HIP compositions (LCS 201), contrary to the results of research conducted by Ziegler *et al* [147].

The proportion of α-Si_3N_4 in the pre-HIP material did not significantly influence the HIPed Si_3N_4 grain morphology, which was essentially identical for ceramics with initially <25% β-Si_3N_4 (>75% α-Si_3N_4) or 100% β-Si_3N_4.

Theoretical density was not obtained in any composition (A1, A2, or LCS 201) after sinter-HIP processing, with the greatest percentage density increases arising in specimens with the lowest starting density (and lowest β-Si_3N_4 level). The effective increase in density, after HIP, was observed to reduce with increasing sintered density, such that only minimal improvements were detected when ρ_{sinter} > 98% TD. A similar failure to attain complete densification was observed by Ziegler [147].

8.3. THE BENEFITS OF HIP FLEXIBILITY

Although HIP is a relatively expensive fabrication technique it allows a degree of compositional choice that is not possible with other silicon nitride densification methods. Glass encapsulated HIP can be utilized to consolidate complex-shaped ceramic components with tailored, 'single' additive based matrix compositions, such as $Y_2O_3(-SiO_2)$ or $Nd_2O_3(-SiO_2)$. Post-HIP annealing can be used to crystallise this matrix phase (ideally to a stable disilicate form). Although only a minimal improvement in room temperature strength is obtained for these materials, a high percentage of strength is retained to 1400°C [76]. The oxidation resistance of HIPed β-$Si_3N_4/Y_2Si_2O_7$ is considerably superior to the current commercially available silicon nitride ceramics, with only a minimal oxide scale formed after extended heat-treatment at 1450°C.

8.4. SUGGESTIONS FOR FUTURE WORK

8.4.1. HIP Densification Conditions

The HIP densification of Si_3N_4 based ceramics during the current program has involved the use of a set of 'standard' HIP processing conditions (ie. a temperature of 1700°C - 1750°C, and pressure 100 - 200MPa). Further study of the densification behaviour and kinetics of a selection of silicon nitride based materials is of particular interest. This work should include an investigation of the effects of each of the HIP process variables, so that a database-matrix of densification behaviour can be constructed for compositional variables.

The use of an increased heating rate, between 1500°C and the holding temperature, for example, may help to counteract the heterogeneous β-Si_3N_4 nucleation that was typically observed during the current programme, producing a finer grained microstructure. This may be in conjunction with a higher HIP temperature and shorter cycle duration.

8.4.2. Sinter-HIP Processing

Sinter-HIP consolidation has gained wide acceptance in the powder metallurgy field, particularly for flaw/pore removal, however very little has been documented regarding the sinter-HIP processing of silicon nitride based ceramics. Further studies of the densification behaviour of various silicon nitride ceramics is required, paying particular attention to refining the processing cycle to give greater improvements in the post-sinter densification.

8.4.3. Encapsulation Techniques

The current commercial ASEA encapsulation technique has been thoroughly developed since the late 1970s. Certain drawbacks are apparent, however. A considerable decrease in high temperature strength was observed for Si_3N_4 HIPed using the ASEA process

when compared to identical compositions HIPed in a refractory metal can [200]. The encapsulant/ceramic reaction occurring during HIP at ASEA does not appear to be consistent from one specimen to another. The quantification of boron levels in ASEA (and standard Pyrex) encapsulated samples is therefore required, in addition to a study of any potential consequences with regard to high-temperature material properties.

The potential of compositionally tailored encapsulant glasses is high, but for successful implementation the use of a diffusion barrier is required. Each variation in glass composition would also require a different encapsulation cycle as each glass would have a different melting temperature. This processing technique would generally be more expensive than the ASEA commercial glass and comparison of the various techniques, including refractory metal canning, is required to assess the commercial viability of each encapsulation/HIP method.

REFERENCES

1. Moulson A.J., *J.Mat.Sci.*, 14, p.1017 (1979)

2. Sorrel C.C. and McCartney E.R., *Materials Forum*, 9, p.149 (1986)

3. Probst H.B., *Am.Cer.Soc.Bull.*, 59, p.206 (1980)

4. Katz R.N., *Science*, 208, p.841 (1980)

5. Wachtman J.B., in 'High Tech Ceramics' (ed. P. Vincenzini), Elsevier, p.3069 (1987)

6. Mueller J.I., *Am.Cer.Soc.Bull.*, 61, p.588 (1982)

7. Hamano Y., Nakahara Y., Oizumi M., Yamaguchi K., and Matsuda R., in 'Ceramic Science and Technology at the Present and in the Future', p.131 (1981)

8. Seitz E., in 'High Tech Ceramics' (ed. P. Vincenzini), Elsevier, p.3037 (1987)

9. Maclean A.F., presented at '2nd Int. Symp. on Ceramic Materials and Components for Engines', Lübeck (1986)

10. Cassidy D.J. and Mclean A.F, in 'High Tech Ceramics' (ed. P.Vincenzini), Elsevier, p.2503 (1987)

11. Hardie D. and Jack K.H., *Nature*, 180, p.332 (1957)

12. Turkdogan E.T., Bills P.M., and Tippet V.A., *J.Appl.Chem.*, 8, p.296 (1958)

13. Jack K.H., *J.Mat.Sci.*, 11, p.1135, (1976)

14. Ruddlesden S.N. and Popper P., *Acta Crystallogr.*, 11, p.465 (1958)

15. Wild S., Grieveson P., and Jack K.H, *Special Ceramics*, 5, p.38 (1972)

16. Clancy W.P., *Microscope*, 22, p.279 (1974)

17. Prochazka S. and Greskovich C.D., 'Development of a sintering process for high performance silicon nitride', *AMMRC TR78-32*, (1978)

18. Lumby R.J., North B. and Taylor A.J., *Special Ceramics*, 6, p.283 (1974)

19. Jack K.H. and Wilson W.I., *Nature*, 238, p.28 (1972)

20. Rice R.W. and McDonough W.J., *J.Am.Cer.Soc.*, 58, p.264 (1975)

21. Yeh H.C. and Sikora P.F., *Am.Cer.Soc.Bull.*, 58, p.444 (1979)

22. Drew P. and Lewis M.H., *J.Mat.Sci.*, 9, p.261 (1974)

23. Lange F.F., *Int.Met.Rev.*, 1, p.1 (1980)

24. Kingery W.D., *J.Appl.Phys.*, 30, p.301 (1959)

25. Lewis M.H., Heath G.R., Winder S.M., and Lumby R.J., in 'Deformation of Ceramics II' (eds. R.E.Tressler and R.C.Bradt), Plenum Press, p.605 (1984)

26. Lange F.F., *J.Am.Cer.Soc.*, 56, p.518 (1973)

27. Ziegler G., Bentsen L.D., and Hasselman D.P.H., *Comm.Am.Cer.Soc.*, 64, p.C-35 (1981)

28. Terwilliger G.R. and Lange F.F., *J.Mat.Sci.*, 10, p.1169 (1975)

29. Mitomo M., *J.Mat.Sci.*, 11, p.1103 (1976)

30. Priest H.F., Priest G.L. and Gazza G.E., *J.Am.Cer.Soc.*, 60, p.81 (1977)

31. Giachello A., Martinegro P.C., Tommasini G., and Popper P., *J.Mat.Sci.*, 14, p.2825 (1979)

32. Mangels J.A. and Tennenhouse G.J., *Am.Cer.Soc.Bull.*, 59, p.1216 (1980)

33. Pompe R., Eklund L., and Hermasson L., *Special Ceramics*, 7, p.97 (1980)

34. Hampshire S. and Jack K.H., *Special Ceramics*, 7, p.439 (1980)

35. Jack K.H., in 'Processing of crystalline ceramics II' (ed. Hayne-Parlmour III), Plenum, New York, p.561 (1978)

36. Smith J.T. and Quackenbush C.L., in Proc.Int.Symp. on Densification and Sintering of Oxide and Non-Oxide Ceramics', Japan, p.126 (1978)

37. Masaki H. and Kamigato O., *J.Cer.Soc.Japan*, 84, p.508 (1976)

38. Oyama Y., *Jap.J.Appl.Phys.*, 10, p.1637 (1971)

39. Lewis M.H., Powell B.D., Drew P., Lumby R.J., North B., and Taylor A.J., *J.Mat.Sci.*, 12, p.61 (1977)

40. Lumby R.J., North B., and Taylor A.J., *Special Ceramics*, 6, p.283 (1974)

41. Bhatti A.R., *M.Phil Thesis*, University of Warwick (1979)

42. Butler E., Lewis M.H., Lumby R.J. and Szweda A., in 'Proc. 1st Int. Symp. on Ceramic Components for Engines' (eds. S.Somiya, E.Kanai and K.Ando), KTK Scientific Press, Japan (1983)

43. Winder S.M., *PhD Thesis*, University of Warwick (1985)

44. Heath, G.R., *PhD Thesis*, University of Warwick (1985)

45. Lange F.F., *J.Amer.Cer.Soc.*, 62, p.428 (1979)

46. Wotting G. and Zeigler G., *Ceramurgia Int.*, 10, p.18 (1984)

47. Greskovich C.D. and O'Clair C., *Am.Cer.Soc.Bull.*, 57, p.1055 (1978)

48. Engel W., *Powder Met.Int.*, 10, p.124 (1978)

49. Evans A.G., in 'Progress in Nitrogen Ceramics' (ed. F.L.Riley), Martinus-Nijhoff, p.595 (1983)

50. Mori M., Inoue H., and Ochiai T., in 'Progress in Nitrogen Ceramics' (ed. F.L.Riley), Martinus-Nijhoff, p.149 (1983)

51. Yamate T., Kawahito T., and Iwai T., in 'Proc. 1st Int. Symp. on Ceramic Components for Engines' (eds. S.Somiya, E.Kanai and K.Ando), KTK Scientific Press, Japan (1983)

52. Wagner C., *Z.Phys.Chem.*, 21B, p.25 (1933)

53. Horton R.M., *J.Amer.Cer.Soc.*, 52, p.121 (1969)

54. Cubbicciotti D. and Lau K.H., *J.Amer.Cer.Soc.*, 61, p.512 (1978)

55. Lewis M.H. and Barnard P., *J.Mat.Sci.*, 15, p.443 (1980)

56. Clarke D.R. and Lange F.F., *J.Amer.Cer.Soc.*, 63, p.586 (1980)

57. Babini G.N. and Vincenzini P., in 'Progress in Nitrogen Ceramics' (ed. F.L.Riley), Martinus-Nijhoff, p.427 (1983)

58. Babini G.N, Bellosi A., and Vincenzini P., *J.Mat.Scl*, 18, p.231 (1983)

59. Wu C.C., McKinney K.R., Rice R.W., McDonough W.J., and Freidman S.W., *J.Mat.Sci.*, 16, p.3099 (1981)

60. Lange F.F., *Int.Met.Rev.*, 25, p.1 (1980)

61. Inglis C.E., *Trans.Inst.Naval.Archit.*, 55, p.219 (1913)

62. Griffith A.A., *Phil.Trans.Roy.Soc.London*, 211A, p.163 (1920)

63. Irwin G.R., *J.Welding*, 31, p.450 (1952)

64. Lawn B.R. and Marshall D.B., *J.Am.Cer.Soc.*, 62, p.342 (1979)

65. Antis G.R., Lawn B.R., Marshall D.B., and Chantikul P., *J.Am.Cer.Soc.*, 64, p.539 (1981)

66. Miranzo P. and Moya J.S., *Ceramurgia Int.*, 10 (4), p.147 (1984)

67. Lewis M.H., Fung R., and Taplin D.M.R., *J.Mat.Sci.*, 16, p.3437 (1981)

68. Brown W.F. and Srawly J.E., *ASTM Special Tech. Paper*, p.410 (1966)

69. Lawn B.R. and Wilshaw T.R., 'Fracture of Brittle Solids', Cambridge Press (1975)

70. Lange F.F., *J.Am.Cer.Soc.*, 57, p.84 (1974)

71. Heinrich J. and Böhmer M., *Science of Ceramics*, 11, p.439 (1981)

72. Simpson L.A., *J.Am.Cer.Soc.*, 56, p.610 (1973)

73. Bowen L.J. and Carruthers J.G., *J.Mat.Sci.*, 13, p.684 (1978)

74. Faber K.T. and Evans A.G., *Acta Metall.*, 31, p.565 (1983)

75. Faber K.T. and Evans A.G., *Acta Metall.*, 31, p.577 (1983)

76. Tuersley I.P.T., Leng-Ward G., and Lewis M.H., Presented at '3rd Int. Symp. on Ceramic Materials and Components for Engines', Las Vegas (1988)

77. Knoch H. and Ziegler G., *Science of Ceramics*, 9, p.494 (1977)

78. Knoch H. and Gazza G.E., *Ceramurgia Int.*, 6, p.51 (1980)

79. Wotting G. and Ziegler G., *Science of Ceramics*, 12, p.361 (1983)

80. Paremore E.M., Spriggs R.M. and Vasilos T., *J.Am.Cer.Soc.*, 48, p.1 (1965)

81. Mussler B., Swain M. and Claussen N., *J.Am.Cer.Soc.*, 64, p.566 (1981)

82. Lumby R.J., Butler E. and Lewis M.H., in 'Progress in Nitrogen Ceramics', (ed. F.L. Riley), Martinus-Nijhoff, p.683 (1983)

83. Zimmerman F.X. and Walker W.H., in 'Isostatic Pressing Technology', (ed. P.J. James), Applied Science Pub., (1983)

84. Gay P., *British Patent* 5255, (1883)

85. Larker H.T., in 'High Pressure Science and Technology', (ed. Timmerhaus & Barber), p.329, Pergamon Press (1979)

86. Madden H.D., *U.S. Patent* 1 081 618, (1913)

87. Jeffrey B.A., *U.S. Patent* 1 863 854, (1932)

88. Jeffrey B.A., *U.S. Patent* 1 864 365, (1932)

89. Daubenmeyer H.W., *U.S. Patent* 1 983 602, (1934)

90. James P.J., in 'Isostatic Pressing Technology', (ed. P.J. James), Applied Science Pub., (1983)

91. Saller H.A., Paprocki S.J., Dayton R.W. and Hodge E.S., *U.S. Patent* 687 842 (pending) and *Canadian Patent* 680 160, (1964)

92. Saller H.A, Paprocki S.J., and Hodge E.S., 'Cladding of Zirconium-Uranium Alloys with Zirconium', BMI-960 (1954)

93. Paprocki S.J., Hodge E.S. and Boyer C.B., presented at '2nd Int. Conf. on Peacetime Uses of Atomic Energy', Geneva (1958)

94. Boyer C.B., presented at '2nd Int. Conf. on Isostatic Pressing', Stratford-upon-Avon, (1982)

95. Paprocki S.J., Hodge E.S. and Boyer C.B., 'The Cladding of Delta-Phase Zirconium Hydride', BMI-1244 (1957)

96. Boyer C.B., Orcutt F.D. and Conway R.M., *Chem. Eng. Progress*, 62, p.99 (1966)

97. Adlerborn J. and Larker H.T., *U.S. Patent* 4 455 275, (1984)

98. Schwartz N.B., *Iron Age*, 206, p.78 (1970)

99. Hodge E.S., Gripshouer P.J., and Hanes H.D., presented at '2nd. Int. Conf. AIME', Philadelphia (1964)

100. Larker H.T., *SAE Tech. Paper* 770335, (1977)

101. Larker H.T., in 'Progress in Nitrogen Ceramics', (ed. F.L.Riley), Martinus-Nijhoff (1983).

102. Adlerborn J. and Larker H.T., *British Patent* 1 522 705, (1978)

103. Adlerborn J., Larker H.T. and Nilsson J., *British Patent* 2 024 866 A, (1979)

104. Adlerborn J., *U.S. Patent* 4 081 272, (1978)

105. Larker H.T., in 'High Pressure Science and Technology', vol.2 (ed. Timmerhaus and Barber), (1979)

106. Böhmer M. and Heinrich J., *German Patent* DE 3 047 237 (1980)

107. Heinrich J., Henn N. and Böhmer M., *Mat.Sci. and Eng.*, **71**, p.131 (1985)

108. Heinrich J. and Böhmer M., *Cer. Forum Int.*, **61**, p.399 (1984)

109. Yamada T., Shimada M. and Koizumi M., *Am.Cer.Soc.Bull.*, 60, p.1225 (1981)

110. Shimadu M., Uchida N. and Koizumi M., in 'Emergent Process Methods for High-Technology Ceramics', vol.17 (eds. R.F. Davis, H. Parlamour III and R.L. Porter), p.583, Plenum Publishing (1984)

111. Shimada M., Tanihata K., Kaba T. and Koizumi M., in 'Emergent Process Methods for High-Technology Ceramics', vol.17 (eds. R.F. Davis, H. Parlamour III and R.L. Porter), p.591, Plenum Publishing (1984)

112. Miyamoto Y., Tanaka K., Shimada M. and Koizumi M., presented at '2nd Int. Symp. on Ceramic Materials and Components for Engines', Lubeck (1986)

113. Adlerborn J. and Larker H.T., *US Patent* 4 112 143, (1978)

114. Adlerborn J. and Larker H.T., *Canadian Patent* 1 091 907, (1983)

115. Isaksson S.-E. and Larker H.T., *US Patent* 4 339 271, (1982)

116. Adlerborn J., Larker H.T. and Nilsson J., *US Patent* 4 256 688, (1981)

117. Adlerborn J., Larker H.T., Mattsson B., and Nilsson J., *US Patent* 4 446 100, (1984)

118. Adlerborn J., Larker H.T., Mattsson B., and Nilsson J., *US Patent* 4 478 789, (1984)

119. Adlerborn J., Larker H.T., Mattsson B., and Nilsson J., *European Patent* EP 0 118 702 A1, (1984)

120. Adlerborn J., Larker H.T., Mattsson B., and Nilsson J., *US Patent* 4 568 516, (1986)

121. Larker H.T., *Asea J.*, 54 (4), p.85 (1981)

122. Larker H.T., in 'Emergent Process Methods for High-Temperature Ceramics', vol. 17, (eds. R.F.Davis, H.Parlamour III and R.L.Porter), p.571, Plenum Publishing (1984)

123. Larker H.T., *Mat.Sci. and Eng.*, **71**, p.329 (1985)

124. Adlerborn J., Burström M., Hermansson L. and Larker H.T., *Mat. and Design*, 8 (4), p.229 (1987)

125. Heinrich J. and Böhmer M., *European Patent* EP 151472 A2, (1986)

126. Leng-Ward G., Plucknett K.P., Ketchion S., and Lewis M.H., presented at '91st Annual Meeting of the American Ceramic Society', Indianapolis, (1989)

127. Ingelström and Ekström T., in 'Proc. Int. Conf. on Hot Isostatic Pressing', p.307, Lulea (1987)

128. Ekström T., Käll P-O., Nygren M. and Olsson P-O., *Mat.Sci. and Eng.*, A109, p.161 (1988)

129. Ekström T., *Mat. Sci. and Eng.*, **A109**, p.341 (1988)

130. Ekström T., Käll P-O., Nygren M. and Olsson P-O., *J.Mat.Sci*, **24**, p.1853 (1989)

131. Lundberg R., Nyberg B., Willander K., Persson M. and Carlsson R., in 'Proc. Int. Conf. on Hot Isostatic Pressing', (ed. T.Garvare), p.323, Lulea (1987)

132. Kandori, T., *et al*, *J.Mat.Sci.Lett.*, **6**, p.1356 (1987)

133. Buljan, S.T. and Sarin, V.K., *Composites*, **18**, p.99 (1987)

134. Takemura H., Miyamoto Y. and Koizumi M., in 'Proc. Int. Conf. on Hot Isostatic Pressing', (ed. T.Garvare), p.329, Lulea (1987)

135. Larker H.T. and Adlerborn J., presented at '3rd Int. Symp. on Ceramic Materials and Components for Engines', Las Vegas (1988)

136. Butler N.D., Hepworth M.A., Iturriza I., and Catro F., presented at '1st European Ceramic Society Conf.', Maastricht (1989)

137. Pejryd L., *Mat.Sci. and Eng.*, **A105/106**, p.169 (1988)

138. Nezuka K., Miyamoto Y. and Koizumi M., in 'Proc. Int. Conf. on Hot Isostatic Pressing', (ed. T.Garvare), p.359, Lulea (1987)

139. Burström M., Adlerborn J. and Hermansson L., in 'Proc. Int. Conf. on Hot Isostatic Pressing', (ed. T.Garvare), p.383, Lulea (1987)

140. Homma K., Okada H., Fujikawa T. and Tatuno T., *Yogyo Kyokai-Shi*, **95** (2), p.91 (1987)

141. Adlerborn J., Hermansson L., Larker H.T., Matsson B., and Nilsson J., *US Patent* 4 717 535 (1988)

142. Wills R.R. and Brockway M.C., *Special Ceramics*, **7**, p.233 (1981)

143. Wills R.R., Brockway M.C., and Bansal G.K., *Mat. Sci. Res.*, **17**, p.597 (1984)

144. Yeheskel O., Gefen Y. and Talianker M., *J.Mat.Sci.*, **19**, p.745 (1984)

145. Yeheskel O., Gefen Y. and Talianker M., *Mat. Sci. and Eng.*, **78**, p.209 (1986)

146. Wötting G. and Ziegler G., in 'Proc. 1st Int. Symp. on Ceramic Materials and Components for Engines', Hakone, KTK Scientific Publ. (1983)

147. Ziegler G. and Wötting G., *Int. J. of High Tech. Ceramics*, **1**, p.31 (1985)

148. Hirota K., Ichikizaki T., Hasegawa Y., and Suzuki H., in 'Proc. 1st Int. Symp. on Ceramic Materials and Components for Engines', Hakone, KTK Scientific Publ. (1983)

149. Wusirika R., *Comm. Am. Cer. Soc.*, **67**, p.232 (1984)

150. Furukawa M., Misumi K., Nagano M., and Takano Y., *Nippon Tungsten* Rev., **17**, p.127 (1984)

151. Goto Y., Ohta H., Komeya K. and Fukikawa T., *J. Electron Microsc.*, 35 (4), p.365 (1986)

152. Iturriza I., Echeberria J. and Castro F., in 'Proc. Int. Conf. on Hot Isostatic Pressing of Materials: Applications and Developments', Antwerp (1988)

153. Iturriza I., Castro F., and Fuentes M., *J.Mat.Sci.*, 24, p.2047 (1989)

154. Tegman R., *Interceram*, 34 (1), p.22 (1985)

155. Arzt E., Ashby M.F., and Easterling K., *Met. Tans. A*, 14A, p.211 (1983)

156. Li W-B., Ashby M.F., and Easterling K.E., *Acta Metall.*, 35, p.2831 (1987)

157. Arén B. and Navara E., *Powder Metall.*, 3 (2), p.101 (1988)

158. Arén B. and Navara E., in 'Proc. Int. Conf. on Hot Isostatic Pressing', (ed. T.Garvare), p.107, Lulea (1987)

159. Ashby M.F., in 'Proc. Int. Conf. on Hot Isostatic Pressing', (ed. T.Garvare), p.29, Lulea (1987)

160. Asby M.F., in 'Proc. Int. Conf. on Hot Isostatic Pressing of Materials: Applications and Developments', Antwerp, p.1 (1988)

161. Kolaska H., Dreyer K. and Schaaf G., *Powder Metall. Int.*, 21 (1), p.22 (1989)

162. Amberg S. and Doxner H., *Powder Metall.*, 20, p.1 (1977)

163. Sheppard L.M., *Advanced Materials and Process*, 3, p.24 (1986)

164. Anon (ASEA-AB), *Interceram*, 5, p.66 (1986)

165. Hermansson L., Holmström T., and Larker H.T., presented at '3rd Int. Conf. on Isostatic Pressing', London (1986)

166. Larker H.T., *Interceram*, 36 (1), p.27 (1987)

167. Leng-Ward G., *Internal Interim Report*, University of Warwick, (1988)

168. Butler N.D., *Personal Communications*, (1987-89)

169. Bayliss R.W., *PhD Thesis*, University of Warwick, (1986)

170. Gauckler L.J., Hohnke H., and Tien T.Y., *J.Am.Cer.Soc.*, 63, p.35 (1980)

171. Butler N.D., *Internal Interim Report*, University of Warwick, (1983)

172. Cain M.G., *Internal Interim Report*, University of Warwick, (1987)

173. Klug H.P. and Alexander L.E., 'X-ray Diffraction Procedures', Wiley (1954)

174. Weibull W., *J.Appl.Mech.*, 18, p.239

175. Smith H.R. and Piper D.E., in 'Stress Corrosion Cracking in High Strength Steels and in Ti and Al Alloys', (ed. B.F.Brown), Naval Research Labs, Washington, p.17 (1972)

176 Fujikawa T., Moritoki M., Kanda T., Homma K., and Okada H., in 'Proc. 1st Int. Symp. Comp. on Ceramic Components for Engines', (eds. S.Somiya, E.Kanai and

K.Ando), KTK Scientific Press, Japan (1983)

177. Richerson D.W. and Wimmer J.M., *Comm.Amer.Ceram.Soc.*, *66*, p.173 (1983)

178. Bunting E.N., in 'Phase Diagrams for Ceramists', vol.1, p.130 (1964)

179. Negita K., *J.Mat.Sci.Lett.*, 3, p.755 (1985)

180. Pasto A.E., *Comm.Am.Ceram.Soc.*, 67, p.178 (1984)

181. Arias A., *NASA Technical Paper* TP 1382-1979, (1979)

182. Jack K.H., in 'Progress in Nitrogen Ceramics', (ed. F.L.Riley), Martinus-Nijhoff, p.45 (1983)

183. Mason S., *PhD Thesis*, University of Warwick (1988)

184. Kennard F.L., *Cer.Eng.Sci.Proc.*, 7, p.1095 (1986)

185. Hoffman M.J., Nagel A., Greil P. and Petzow G., *J.Am.Ceram.Soc.*, 72, p.765 (1989)

186. Ketchion S., *Internal Interim Report*, University of Warwick (1989)

187. Sheppard L.M., *Am.Cer.Soc.Bull.*, 67, p.1649 (1988)

188. Butler N.D., Dawson D.J., and Wordsworth R.A., presented at 'Institute of Ceramics Convention', Swansea (1989)

189. Moulson A.J., *J.Mat.Sci.*, 14, p.1017 (1979)

190. Messier D.R., Riley F.L., and Brook R.J., *J.Mat.Sci.*, 13, p.341 (1978)

191. Torpov N.A., in 'Phase Diagrams for Ceramists', vol.2, p.107 (1969)

192. Leng-Ward G., *Internal Interim Report*, University of Warwick (1987)

193. Drew R.A., Hampshire S., and Jack K.H., in 'Progress in Nitrogen Ceramics', (ed. F.L.Riley), Martinus-Nijhoff, p.323 (1983)

194. Landolt-Bornstein, 'Numerical Data and Functional Relationships in Science and Technology', vol.7d. (?)

195. Portwood D. and Eagles J., *Int. Analyst*, 2(2), p.21 (1988)

196. Barnes R.M., *Materials Sci. Res.*, 19, p.131 (1985)

197. Gray A.L., *Analyst*, 110, p.551 (1985)

198. Liddel K. and Thompson D.P., *Br.Ceram.Trans.J.*, 85, p.17 (1986)

199. Smith J.T., *J.Am.Cer.Soc.*, 60, p.465 (1977)

200. Yeh H., Fang H. and Teng K., *Cer.Eng.Sci.Proc.*, 9 (9-10), p.1333 (1988)